2016

Application of the Variational Fracture Model to Hydraulic Fracturing in Poroelastic Media

Chukwudi Chukwudozie
Louisiana State University and Agricultural and Mechanical College, chdozie@gmail.com

Recommended Citation

Chukwudozie, Chukwudi, "Application of the Variational Fracture Model to Hydraulic Fracturing in Poroelastic Media" (2016). *LSU Doctoral Dissertations*. 788.
https://digitalcommons.lsu.edu/gradschool_dissertations/788

APPLICATION OF THE VARIATIONAL FRACTURE MODEL TO HYDRAULIC FRACTURING IN POROELASTIC MEDIA

A Dissertation

Submitted to the Graduate Faculty of the
Louisiana State University and
Agricultural and Mechanical College
in partial fulfillment of the
requirements for the degree of
Doctor of Philosophy

in

The Craft & Hawkins Department of Petroleum Engineering

by
Chukwudi P. Chukwudozie
B. Eng., Federal University of Technology, Minna, 2006
M.S., Louisiana State University, 2011
M.S., Louisiana State University, 2015
August 2016

Acknowledgments

I wish to extend my deepest gratitude to my supervisors, Dr. Blaise Bourdin and Dr. Mayank Tyagi for all their guidance and support throughout my studies. I am particularly indebted to Dr. Blaise Bourdin for the opportunity to be part of this project which has exposed me to the beautiful world of scientific computations. I have always had a keen interest in numerical computations and Dr. Blaise has set me on the right track. During the course of this project and through our numerous interactions, I have gained from him in so many ways that cannot be quantified by just the success of this project. I am convinced that the skills and knowledge gained will be invaluable in my career.

I would like to thank Dr. Richard Hughes and Dr. Krishnaswamy Nandakumar for graciously accepting to serve in the committee. I also will like to thank Dr. Chris White for the role he played in getting me involved with this project.

I am grateful to Chevron Energy Technology Company (ETC) and in particular, the Rock Mechanics team for the financial support of this project and for the numerous internship opportunities. I would like to specially thank Dr. Keita Yoshioka for facilitating the sponsorship of this project by Chevron and for all his inputs and insightful comments. I am also grateful to Dr. Peter Connolly and Dr. Jose Adachi of Chevron ETC.

Finally, I am eternally indebted to my family, Paulina and Chibuikem, my parents and siblings for their endless support and patience during the course of this dissertation.

All numerical algorithms were programmed using the Portable Extensible Toolkit for Scientific Computation (PETSc). In addition, all numerical computations were performed on high performance computing resources at the Louisiana State University (LSU), the Texas Advanced Computing Center (TACC) at the University of Texas at Austin and the National Institute for Computational Sciences (NICS) at the University of Tennessee at Knoxville.

Table of Contents

APPENDIX

List of Tables

List of Figures

Abstract

Hydraulic fracturing has persisted through the use of simple numerical models to describe fracture geometry and propagation. Field tests provide evidence of interaction and merging of multiple fractures, complex fracture geometry and propagation paths. These complicated behaviors suggest that the simple models are incapable of serving as predictive tools for treatment designs. In addition, other commonly used models are designed without considering poroelastic effects even though a propagating hydraulic fracture induces deformation of the surrounding porous media. A rigorous hydraulic fracturing model capable of reproducing realistic fracture behaviors should couple rock deformation, fracture propagation and fluid flow in both the fracture and reservoir.

In this dissertation, a fully coupled hydraulic fracturing simulator is developed by coupling reservoir-fracture flow models with a mechanical model for reservoir deformation. The reservoir-fracture deformation is modeled using the variational fracture model which provides a unified framework for simultaneous description of fracture deformation and propagation, and reservoir deformation. Its numerical implementation is based on a phase-field regularized model. The phase field technique avoids the need for explicit knowledge of fracture location and permits the use of a single computational domain for fracture and reservoir representation. The first part of this work involves verification of the variational fracture model by solving the classical problem of fracture propagation in impermeable reservoirs due to injection of an inviscid fluid. Thereafter, the developed reservoir-fracture model is coupled to the mechanical model. Iterative solution of the variational fracture model and the coupled flow model provides a simplified framework for simultaneous modeling of rock deformation and fluid flow during hydraulic fracturing. Since the phase field technique for fracture representation removes the limitation of knowing a priori, fracture direction, the numerical solutions provide a means of evaluating the role of reservoir and fluid properties on fracture geometry and propagation paths. The developed coupled hydraulic fracturing model is first validated for scenarios for which closed form solutions exist in the literature.

Further simulations highlight the role of fluid viscosity and reservoir properties on fracture length, fracture width and fluid pressure. Numerical results show stress shadowing effect on the propagation of multiple hydraulic fractures. Finally, the effect of in situ stress on fracture propagation direction is reproduced while the role of varying reservoir mechanical properties on fracture height growth is investigated.

Chapter 1
Introduction

1.1 Introduction To Hydraulic Fracturing

Hydraulic fracturing is traced to the 1860s when liquid nitroglycerin (NG) was used to simulate shallow, hard rock formations in Pennsylvania, New York, Kentucky and West Virginia (Montgomery and Smith 2010). Not until 1949 was it introduced to the petroleum industry and since then over 2.5 million fracture treatments have been performed worldwide and about 60% of all wells drilled today are fractured (Montgomery and Smith 2010). These numbers underscore the increasing value of hydraulic fracturing to the petroleum industry and continued interest has galvanized its evolution from a simple low volume technique using gasoline gelled with napalm to a highly complex engineering procedure that uses improved fluids like delayed cross-linkers, improved mathematical models and imaging methods for post fracture analysis. Fundamentally, hydraulic fracturing is the process of fracture initiation and propagation in the subsurface, driven by hydraulic loading or fluid pressure of viscous fluids acting on the surfaces of the fracture (Barter et al. 2000; Sarris and Papanastasiou 2012). It is the primary technique used in the oil industry to increase recovery in production declining wells and to enable production in low permeable and tight formations of unconventional resources, like shale gas. The high permeable paths created by fractures extend the reach of wellbores beyond damaged areas around the bottomhole and improve productivity by changing reservoir fluid flow patterns from radial to linear. Apart from productivity increase, it finds utility in other areas including measurement of fracture gradient and in situ stresses necessary for wellbore stability analysis, and for increasing heat transfer areas through fully engineered geothermal reservoirs for heat extraction from hot dry rocks (Smith 1979; Zyvoloski 1985; Fomin et al. 2003; Albright and Pearson 1982). Its use for stress measurements is particularly attractive since knowledge of the elastic properties of the earth region is not required.

Hydraulic fracturing procedure involves first pumping a pad, which in most cases is a clean fluid like water, at pressures and rates high enough to initiate and extend fractures. Although fracture initiation pressure is hugely influenced by the least principal in-situ stress, it also depends on the mechanical properties and tensile strength of the formation. During fluid injection, fractures are kept open by the increasing pressure of the injected fluid. Once injection stops, pressure depletion occurs and the fractures start to close as fracturing fluid is lost either due to fluid leak-off into the formation or fluid flow back into the wellbore. To keep the fractures open and permeable for formation fluid flow to the wellbore, a slurry, which is fluid mixed with proppant, is injected following the pad.

Engineering design of a fracture treatment involves estimates of fluid volume, injection rate, volume and concentration of proppants, surface and bottomhole injection pressures and hydraulic horsepower requirement at the surface for a proposed fracture geometry. The major post treatment task is prediction of the dimensions of the created fracture. According to Hubbert and Willis (1957) and supported by numerous field evidence, most subsurface fractures are vertical, they propagate perpendicular to the least principal stress direction and their geometries are quantified by height, half length/radius and width. Fracture half length is the distance from wellbore to one of the fracture tips, fracture width is the separation between the two faces of the fracture while fracture height is the distance between the top and bottom of the fracture, for vertical fractures. These parameters are crucial in estimating how much production gains are derivable from the fracturing process. The major task for engineers is how to infer these geometric quantities for any given hydraulic fracturing treatment and reservoir mechanical properties. This is where hydraulic fracturing modeling and simulation comes into play.

1.1.1 Importance of Hydraulic Fracturing

Even though hydraulic fracturing has been in existence for over a century, the reason for the present renewed interest in the method is to enable production in unconventional reservoirs. This interest is facilitated by advances in drilling and completion technologies and advanced production strategies that have allowed hydraulic fractures to be used in horizontal wells to create large drainage areas in unconventional reservoirs. Unconventionals have been identified as very viable alternatives to conventional oil and gas reservoirs because of their abundance around the world. For example, the US has significant shale resources which the Energy Information Administration (EIA) (Kuuskraa, Stevens, and Moodhe 2013) estimates to be about 58 billion barrels of technically recoverable shale oil and 665 trillion cubic feet of technically recoverable shale gas. These resources are contained in several discovered shale plays scattered around the United States, including important ones like the Marcellus, Haynesville, Fayetteville, Barnett, Eagle Ford and Bakken as shown in Figure 1.1. The shale boom is a global phenomena, with resources existing in about 41 other countries. Those with significant resources includes Russia, China, Argentina, Algeria, Canada and Mexico. China with 1115 trillion cubic feet of recoverable shale gas tops the list of countries with shale gas resources while Russia tops shale oil countries with 75 billion barrels of recoverable oil. Despite the relative abundance of shale oil and gas resources, a common feature of all shale plays around the world is low formation permeability which makes economic production of their resources almost impossible. The key, therefore, to unlocking and tapping the enormous resources contained in shale is hydraulic fracturing.

The benefits of hydraulic fracturing of shale resources is already reaping dividends in the US as shale gas contributes significantly to meeting the growing demand for gas. As a result, the US economy is experiencing rapid growth in domestic natural gas supplies and significant decreases in prices. In fact, the EIA projects that natural gas from shale formations will be the primary driver of growth in domestic natural gas production through 2035, growing from 16% of supply in 2009 to 49% in 2035 as shown in Figure 1.2, and more than offsetting declining production from other sources (EIA 2014). Given these statistics, it is obvious that hydraulic fracturing has a huge role to play in bringing these projections to fruition. Thus, improvements in hydraulic fracturing technology through continuous research is necessary to provide the industry with better knowledge on how to make the process even more efficient.

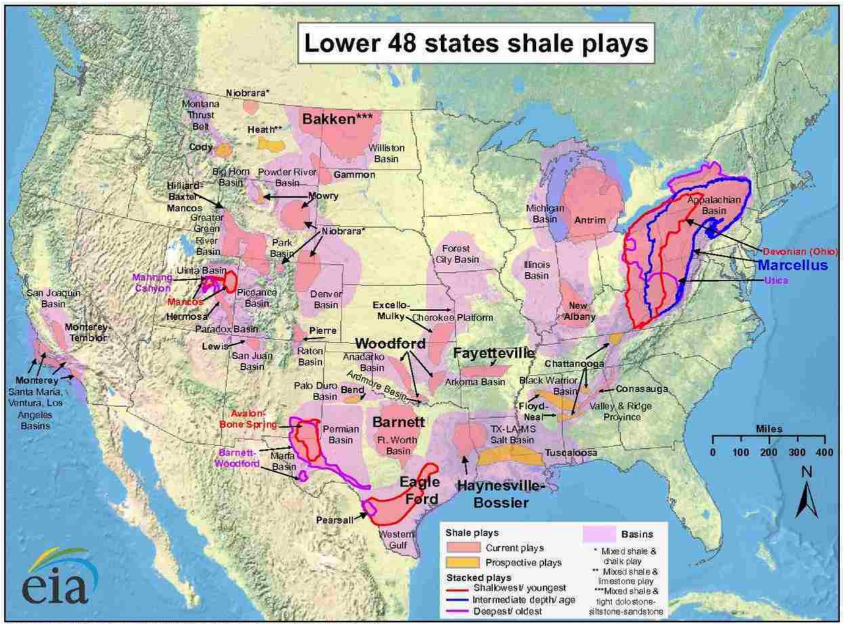

Source: Energy Information Administration based on data from various published studies.
Updated: May 9, 2011

Figure 1.1: Over 58 billion barrels and 665 trillion cubic feet of recoverable shale oil and gas reserves in the Lower 48 shale formations

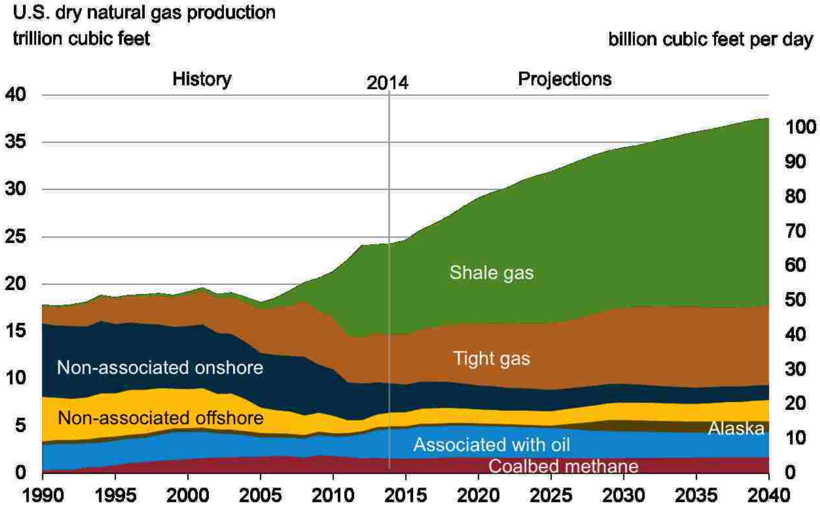

Source: EIA, Annual Energy Outlook 2014 Early Release

Figure 1.2: Shale gas production to drastically increase beyond the contribution of other sources, becoming the dominant source of dry gas in the US and eventually resulting in lower natural gas prices.

1.2 Motivation and Objective

Realistic hydraulic fracture behaviors are characterized by interaction and merging of multiple fractures, complicated fracture geometries from non-planar propagation and complex propagation paths due to insitu stresses and heterogeneity in reservoir properties. Modeling and computational challenges have hindered the development of robust numerical models capable of reproducing this complicated fracture behaviors. To simplify modeling of the hydraulic fracturing process, many previous works have made numerous assumptions including simplifying fracture geometries, constraining fracture propagation paths to known directions and assuming propagation of single planar fractures. In addition, fracture fluid loss is normally assumed unidirectional while the coupled effect of fluid loss and reservoir compaction on fracture propagation is rarely considered. The computational challenges stem from the fact that fracture propagation is a moving boundary problem in which fractures are considered as surfaces. For hydraulic fracturing applications, the issues are unique since it is not a trivial task developing efficient ways to numerically represent fractures and reservoir domains in the same computational framework while still ensuring hydraulic and mechanical coupling between both subdomains. Where attempt has been made to represent both fracture and reservoir, the computational cost is expensive and the numerics cumbersome, characterized by continuous remeshing to provide grids that explicitly match the evolving fracture surface (Gupta and Duarte 2014). Some of these challenges can be overcome by using a phase field representation for fractures.

The primary objective of this dissertation is to develop a hydraulic fracture simulation model using the variational approach to fracture as the mechanical model. The variational fracture model is a phase field based approach to fracture simulation. It was proposed by Francfort and Marigo (1998) and further developed by Bourdin, Francfort, and Marigo (2000). Fracture representation in the model is implemented using a smooth scalar field, often called the v-field. The v-field allows for a single computational domain to be used for both fracture and reservoir representation and removes the necessity for explicit identification of fracture and propagation directions. Other advantages of the model are summarized as follows.

1. It uses a fixed computational grids to represent fractured domain and to discretize model equations. Computational domains may be composed of simple elements like triangles, rectangles and cuboids.
2. It can handle propagation of multiple fractures since explicit fracture representation is not required.
3. Heterogeneity in material properties are easily handled by the model.
4. It is easy to incorporate thermal and hydraulic energy contributions to fracturing, leading to applications in thermal and hydraulic fracturing.
5. The numerical algorithm is parallelizable. Therefore, can be run on high performance computing resources to speed up fracture simulations.
6. No additional modeling cost for fracture propagation in two or three dimensional domains.

Although the variational fracture model is relatively new, it has found application in thermal fracturing (Bourdin et al. 2014) and thin film fracturing (Mesgarnejad 2014). Application in hydraulic fracturing (Bourdin, Chukwudozie, and Yoshioka 2012; Chukwudozie, Bourdin, and Yoshioka 2013; Wick, Singh, and Wheeler 2014; Mikelic, Wheeler, and Wick 2013) is at an early stage and this work aims to push the frontier in this area even further. This dissertation solves the hydraulic fracturing problem by coupling the variational fracture model to a coupled model for fluid flow in both fracture and reservoir. The fracturing fluid pressure, hydraulic fracture geometry and propagation paths are solutions of the coupled flow and mechanical models. A three dimensional numerical solution of the coupled model is implemented and can be applied to two dimensional cases under plain stress/strain conditions. To improve numerical stability of the solution algorithm, dimensionless forms of the variational fracture and coupled flow models are solved. Dimensional analysis of both the flow and mechanical models yield scaling parameters that can be used to convert the dimensionless numerical solutions and parameters to their respective dimensional values. The specific objectives of this dissertation are therefore:

1. To develop and implement a parallel hydraulic fracturing simulation that couples reservoir and fracture fluid flow to the variational fracture model that describes reservoir and fracture deformation. The variational fracture model used in this dissertation is a finite element implementation. The coupled flow model will be solved using the standard finite element method on structured grids and implemented within the PETSc (Portable, Extensible Toolkit for Scientific Computation) (Balay et al. 2011) framework. PETSc also provides the framework for parallel implementation.
2. To derive fracture width equation using the mechanical variables and develop numerical algorithm for its computation. The fracture width is an important component of the fracture flow model since it defines fracture permeability and volume.
3. To analyze fluid pressure and fracture geometric properties like length, radius, width, volume and propagation paths for different reservoir and fluid properties.
4. To highlight effect of insitu stresses on hydraulic fracture propagation, understand interaction between multiple propagating fractures and investigate the role of reservoir layers on fracture height growth.

1.3 Fundamentals of Hydraulic Fracturing Modeling

Given that hydraulic fractures do not exist in isolation but propagate in deformable porous media, hydraulic fracturing is the result of several complex processes occurring simultaneously in the subsurface. A comprehensive mathematical model for hydraulic fracturing requires incorporation of all of the following five mechanisms (Yuan 1997; Ghassemi 1996; Boone and Ingraffea 1989); fracture fluid flow, fluid flow in reservoir, fracture mechanics, solid deformation and poroelasticity.

1.3.1 Fracture Fluid Flow Modeling

An appropriate flow model is required to predict the fluid pressure that drives fracture propagation for given fluid rheological properties with the possibility of fluid loss. Fractures are considered to be planar objects since their widths are much less than their lengths i.e $w << L$. This assumption implies that fluid flow is only in the plane of the fracture with no component across the fracture face. In addition, laminar flow is commonly assumed so that with the planar geometry assumption, fluid flow follows the cubic law of Poiseuille's equation and is also governed by Reynolds equation from lubrication theory (Batchelor 1967). For a two dimensional fracture in the $x-y$ plane, the cubic law and Reynold's equation are shown below.

$$
\begin{aligned}
q_{f_x} &= -\frac{w^2}{12\mu}\frac{\partial p_f}{\partial x} \\
q_{f_y} &= -\frac{w^2}{12\mu}\frac{\partial p_f}{\partial y}
\end{aligned}
\tag{1.1}
$$

$$
\frac{\partial w}{\partial t} + \frac{\partial (w q_{f_x})}{\partial x} + \frac{\partial (w q_{f_y})}{\partial y} - q_\ell = q_{fs} \tag{1.2}
$$

q_{f_x}, q_{f_y} are the x and y components of fluid flux, q_{fs} and q_ℓ are injection flow rate and leak-off rate respectively while w is fracture aperture.

Equation 1.1 is similar to Poiseuille equation for fluid flow between parallel plates. Therefore, fracture permeability is $k_f = \frac{w^2}{12}$. Equation 1.2 is the continuity equation describing local mass conservation in the fracture. Considering that a fracture can have different orientations along different points on its surface, surface gradient and surface divergence are necessary to project the classical gradient and divergence in $\mathbb{R}^d$ onto the plane of the fracture in $\mathbb{R}^{d-1}$. This will eliminate the contribution of the normal component of these operators that are perpendicular to the fracture faces. Thus, using these operators, the fracture flow equations can be represented in a general form for any fracture surface orientation as given below (see Serres et al. (2002), Martin, Jaffré, and Roberts (2005)).

$$\vec{q}_f = -\frac{w^2}{12\mu}\nabla_\Gamma p_f \tag{1.3}$$

$$\frac{\partial w}{\partial t} + \nabla_\Gamma \cdot (w\vec{q}_f) + q_l = q_{fs} \tag{1.4}$$

$\nabla_\Gamma p_f$ and $\nabla_\Gamma \cdot w\vec{q}_f$ are surface pressure gradient and surface divergence of fluid flux.

Leak-off is a complex process (Fakoya and Shah 2013; Fakoya and Shah 2014) and mathematical description of its behavior is not a trivial task. The widely used Carters' model assumes leak-off is one-dimensional and perpendicular to the fracture face. According to Adachi, Siebrits, and Desroches (2007), this approximation is reasonable provided fracture is propagating sufficiently rapidly that non-orthogonal leak-off is negligible. Although Carter's model works well in low-permeability formations, van de Hoek (2000) notes that in high permeability formations, leak-off rates may be high compared to fracture propagation rates. Under this conditions, the 1D leak-off model will be insufficient to capture the full dimensional fluid loss pattern.

1.3.2 Reservoir Fluid Flow, Reservoir Deformation and Poroelasticity

Fluid loss from fracture to reservoir has significant consequences on hydraulic fracturing beyond reducing fluid efficiency. As fluid source term to the surrounding medium, it induces what is called poroelastic effects. Poroelastic effects reflect the interaction between deformation of the porous solid matrix and diffusion of pore fluid and their mutual effects on hydraulic fracturing. The major implication of poroelastic effects on fracturing is an increase in wellbore pressure than is obtained when poroelasticity is not considered (Smith 1985; Vandamme and Detournay 1989; Kovalyshen 2010). This is due to the fact that fluid loss to the region adjacent to fractures cause dilation of the poroelastic media which then generates compressive stress that acts against the fracture. The result is an increase in fluid pressure for a given injected fluid volume. In hydraulic fracturing literature, this generated compressive stress is called back stress. According to Aghighi (2007), the back stress also decelerates fracture growth and the resulting higher treatment pressure leads to more fluid loss. Other effects of poroelasticity on hydraulic fracturing include, increase in rock breakdown pressure (Kovalyshen 2010), fracture pressure higher than minimum in situ stress (Smith 1985; Kovalyshen 2010; Ghassemi 1996) and a reduction in fracture aperture which is a direct consequence of the back stresses acting on the fractures. It is important to note that poroelastic effects are less significant when fracturing is carried out with high viscous fluids and in deforming media with low permeability since fluid loss is minimized under these conditions.

The mutual interaction between fluid diffusion and reservoir deformation is handled by linear poroelasticity theory developed by Biot (1941). The theory consists of a set of two equations: the equilibrium equation with constitutive relations for solid deformation and the continuity equation with Darcy's law for fluid diffusion in the reservoir. The equations can be written as an elastic Navier equation with a coupling term for pore pressure and as a diffusion equation for pore pressure with a coupling term for the dilation.

$$G\nabla^2 u_i + \frac{G}{1-2\nu} u_{k,ki} = \alpha p_{r,i} - F_i \tag{1.5}$$

$$\frac{\partial p_r}{\partial t} - kM\nabla^2 p_r = -\alpha M \frac{\partial \epsilon_{vol}}{\partial t} + Mq_{rs} \tag{1.6}$$

G, ν, F_i, α and $\vec{u}$ are shear modulus, Poisson ratio, body force, Biot's coefficient and displacement respectively while k, M, ϵ_{vol}, q_{rs} and p_r are permeability, Biot's modulus, volumetric strain, fluid source term and reservoir pressure respectively. Equations 1.5 and 1.6 are incorporated into hydraulic fracturing modeling to account for the effect of poroelasticity on hydraulic fracturing.

Solution Methods for Coupled Flow and Deformation in Poroelastic Media

Coupled numerical solution of Equations 1.5 and 1.6 is necessary to obtain accurate solutions of pressure and displacement in a poroelastic domain. Based on the level of coupling in the numerical technique, the approaches can be broadly classified into fully coupled, explicit coupling, loose coupling and sequential coupling (Kim 2010; Kim, Tchelepi, and Juanes 2009; Kim, Tchelepi, and Juanes 2011; Jha and Juanes 2006; Wan 2002; Hameyer et al. 1999). Sequential approaches are further divided into iterative, explicit and loose coupling.

Fully Coupling Approach

In the fully coupled approach, $\vec{u}$ and p_r are solved for simultaneously by generating a single matrix that contains coefficients of Equations 1.5, 1.6 and their coupling terms. It is common practice to use a single numerical technique to discretize the poroelasticity equations and generate the single matrix. Lewis (1998) has described a consistent way of doing this using the finite element method and numerical implementation of the finite element discretization has been carried out by several authors (Jha and Juanes 2006; Zheng, Burridge, and Burns 2003). Different numerical methods can also be used to discretize the equations. For example, Wan (2002) used stabilized the finite element method for the force balance equation and the finite difference method for the flow equation. The fully coupled approach is unconditional stable but requires sophisticated mathematical techniques and development of robust geomechanical simulators for all problems even if the contribution of one of the phenomena (deformation or flow) is not important in describing the overall behavior of the reservoir system.

Partial Coupling Approach

In this method, Equations 1.5 and 1.6 are decoupled to allow them to be solved separately. The coupling terms are passed between the two solvers. Depending on the degree of numerical coupling, these techniques are further classified as sequential/iterative, explicit and loose coupling.

Sequential/Iterative Coupling

This techniques involve successive solution of Equations 1.5 and 1.6 during which $\vec{u}$ and p_r are exchanged to update the coupling terms in each model. Both equations are solved iteratively at each time step until the solution converges. Since each equation is solved separately, sequential methods allow for the possibility of different numerical techniques for discretizing the equations. In addition, different grids over the computational domain can be used for the different equations but with a platform for mapping from one grid to another, variables/quantities that are shared between the models. As a result of this flexibility, numerical implementation of each model can be developed as standalone packages. If the numerical solution of each model is reliable and the coupling algorithm properly implemented, sequential solutions converge to the fully coupled solution.

Sequential solution methods for poroelasticity are further categorized into drained split, undrained split, fixed strain and fixed stress methods depending on whether Equation 1.5 is solved before Equation 1.6 during the iteration, or vice versa (Kim 2010; Kim, Tchelepi, and Juanes 2009). In drained and undrained split coupling methods, Equation 1.5 is first solved and then $\vec{u}$ is transferred to Equation 1.6 to update the volumetric strain rate contribution to flow. As the names suggest, during the solution of Equation 1.5, changes in p_r over the computational domain is frozen in the drained split while no change in fluid content is imposed in the undrained split method. Conversely, the flow model is first solved in the fixed stress and fixed strain techniques to obtain the reservoir pressure which is then transferred to the mechanics equation. Changes in volumetric strain rate and mean stress are frozen in the fixed strain and fixed stress methods respectively.

Stability analysis carried out by Kim (2010) show fixed strain and drained split methods are conditionally stable while fixed stress and undrained split are unconditionally stable.

Loose coupling

In this method, either a fixed number of iterations is carried out at each time step or the coupled problem is not solved at every time step but only after a specified time in the computation (Minkoff et al. 1999; Settari and Walters 2001; Minkoff et al. 2003).

Explicitly coupling

This is a non iterative approach as only a single solution of the flow and deformation equations are carried out at each time step (Dean et al. 2006). The solutions from this method are obviously not accurate but can offer computational savings if the contribution of flow to deformation or vice versa is not strong.

1.3.3 Solid Deformation and Fracture Mechanics

Fracture mechanics aspect deals with fracture propagation by predicting when (initiation), where (direction) and how (stable or unstable) fractures propagate. The widely used theory in this regard is linear elastic fracture mechanics (LEFM) which is based on the work of Griffith (1921). According to this theory, the elastic energy of a material that contains a fracture dissipates during fracture creation. An energy release rate, G, is defined which quantifies the rate of change of the elastic energy ($\mathcal{E}$) with length/area for fracture propagating along a pre-existing path.

$$G = -\frac{d\mathcal{E}}{d\ell} \tag{1.7}$$

Fracture will propagate in a stable manner when the energy release rate reaches a critical value, G_c, called the fracture toughness. i.e.

$$G = G_c \tag{1.8}$$

For mixed mode deformation

$$G = G_I + G_{II} + G_{III} \tag{1.9}$$

Fracture toughness is a material property and measures the resistance of the material to grow fractures.

$$\begin{aligned} G_I &= \frac{K_I^2}{E'} \\ G_{II} &= \frac{K_{II}^2}{E'} \\ G_{III} &= \frac{(1+\nu)K_{III}^2}{E} \end{aligned} \tag{1.10}$$

Considering that fracture toughness is related to the stress intensity factor by Irwin's formula (Irwin 1957) of Equation 1.10, the propagation criteria can also be expressed in terms of stress intensity factor i.e.

$$K = K_c \tag{1.11}$$

where K_c is the critical stress intensity factor. Again, superposition of all modes leads to

$$K = K_I + K_{II} + K_{III} \tag{1.12}$$

K_I, K_{II}, K_{III} are mode-**I**, **II** and **III** stress intensity factors. $E' = E$ for plane stress and $E' = \frac{E}{(1-\nu^2)}$ for plane strain problems. Formulas for stress intensity factors for different fracture configurations and loading conditions have been derived in the literature (Tada, Paris, and Irwin 2000). By using Equation 1.10, the corresponding fracture toughness can be obtained.

Another approach for predicting fracture propagation is based on the cohesive zone model (Barenblatt 1962; Dugdale 1960). This model does not use the parameters (stress intensity factor) employed by LEFM since it avoids stress singularity at fracture tip by adding a zone of vanishing thickness, called the cohesive zone, ahead of the crack tip. The zone which also acts as a transition region between the open fracture and the intact material ahead of the fracture tip as shown in Figure 1.3, consists of upper and lower surfaces held by a cohesive traction. According to the general model, as fractures are subjected to external loading, the separation between the cohesive surfaces increases until it reaches a critical value at which

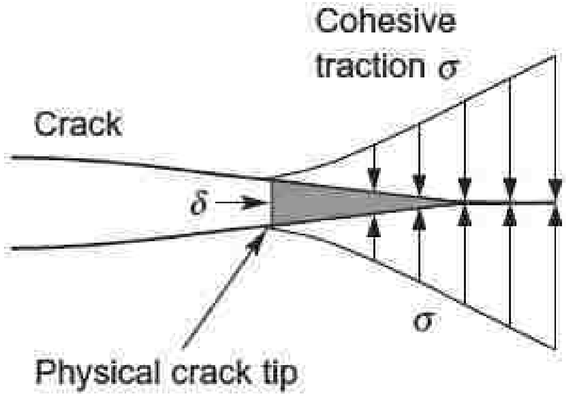

Figure 1.3: cohesive element

point the fracture grows. A cohesive law describes the behavior of the cohesive fracture by defining the relationship between cohesive traction and separation of the cohesive surfaces in terms of their respective critical values. The material properties in these laws are the critical stress/traction, critical separation and cohesive energy. Only two of these properties are necessary to completely define a cohesive law.

Solving the mathematical models of each of the phenomena described above is not a trivial task by any means. This invariably means that hydraulic fracturing based on the coupling of all the mechanisms described above will even be more daunting. The complexity is increased by the non-linear relationship between fracture permeability and fracture aperture. More often than not, one or more of the mechanisms are left out during hydraulic fracturing modeling. On the basis of the complexity of the interaction between diffusion of fracturing fluid into the reservoir and rock deformation modeled by poroelasticity, Vandamme and Detournay (1989) has classified hydraulic fracturing into uncoupled, partial coupling and fully coupled.

In the uncoupled approach (Perkins and Kern 1961; Kristianovic and Zheltov 1955; Nordgren 1972; Adachi, Siebrits, and Desroches 2007; Geertsma and de Klerk 1969; Detournay and Garagash 2003), poroelasticity is not incorporated as the rock is considered to be elastic and experiences no fluid diffusion and the associated deformation. Fracture opening as a function of fracturing fluid pressure and insitu stress is modeled using the elasticity equation while fracture fluid flow is modeled using Reynold's equation and the cubic law. However, models in this category acknowledge that some fluid is lost during hydraulic fracturing. The fluid loss is assumed to be unidirectional and modeled using law. The non consideration of poroelasticity in this type of approach means that fluid loss only accounts for volume balance and has no role in activating the influence of rock dilation on hydraulic fracturing.

Partial coupling has some of the features of the uncoupled approach, including the assumption of linear elasticity for the rock and Reynolds equation for fracture flow modeling. However, leak-off is modeled more rigorously by assuming linear diffusion from fracture to reservoir. Although these methods (Tran, Settari, and Nghiem 2013; Settari and Price 1984; Kovalyshen 2010) consider interaction between fluid flow and solid deformation initiated by the fluid loss, poroelasticity is not rigorously modeled using Biot's theorem. Rather, the additional stress generated due to rock dilation is calculated and applied to the elasticity equation in the form of the back stress.

Fully coupled approach accounts for solid deformation and fluid interaction using Biot's poroelasticity theory. The models in this category (Mohammadnejad and Khoei 2013; Boone and Ingraffea 1990; Carrier and Granet 2012) make no assumption about the dimensionality of the fluid loss. Instead, fluid loss is a consequence of the coupling between fracture and reservoir flow and is modeled according to linear diffusion. The flow coupling introduces a time scale in the fracturing problem and allows the effects of reservoir properties like permeability and Biot's coefficient on hydraulic fracturing to be investigated.

1.4 Review of Hydraulic Fracture Modeling

The difficulty of hydraulic fracturing modeling posed by the need to incorporate several processes simultaneously and the need to extract properties for an unknown geometry has been highlighted. To keep the problem tractable, engineers simplified fracture geometry to 2D, pseudo-3D (P3D) and 3D and considered hydraulic fracturing as the propagation of these geometries in a permeable or impermeable media. Consequently, fracture design is based on analytically calculating geometric parameters of these simple models for given treatment parameters and fluid/rock properties. Although these models are approximate solutions for certain fracture problems (Savitski and Detournay 2002), recently, they have had limited success in field treatment designs due to their inability to reproduce realistic behaviors that are prevalent in the widely fractured unconventional reservoirs. A number of such approximated geometries have been in existence since the onset of hydraulic fracture study and the history of fracture development will be incomplete without alluding to the works of the pioneers (Perkins and Kern 1961; Kristianovic and Zheltov 1955; Nordgren 1972; Geertsma and de Klerk 1969). In proposing their fracture model, Perkins and Kern (1961) considered that some conditions such as zones with horizontal stress higher than in the pay zone are sometimes found above and below the pay zone cause vertical fractures to be limited in growth in the vertical direction. Given these conditions, fracture will grow until it reaches the boundary zones and then will be restricted in vertical growth. Although fracture continues to extend laterally away from the wellbore, the high stresses at the top and bottom layers tend to close the fracture in those locations. The result is a fracture geometry with length far greater than height, as shown in Figure 1.4a. The fracture width in this model has an elliptical cross-section on a horizontal plane. For Newtonian fluid flow under laminar flow conditions, the width of this model on a horizontal plane through its center has been calculated using the crack opening equation by Sneddon and Elliott (1946) and is shown in Equation 1.13. No estimate of the fracture length was proposed.

$$w(x) = \frac{2(1-\nu^2)Hp}{E} \tag{1.13}$$

$w(x)$ is fracture width profile through the middle of the fracture. ν, E, p are Poisson's ratio, Young's modulus and fluid pressure respectively while x_f is the fracture half length and x is location along the fracture length. Nordgren (1972) extended the work of Perkins and Kern (1961) to include the effects of fluid loss through a continuity equation to calculate fracture length. For all their significant contributions, the model is today called the PKN (Perkins-Kern-Nordgren) model.

A complementary two dimensional hydraulic fracture geometry is the KGD (Kristinovic-Geertsma-de Klerk) model shown in Figure 1.4b. Again, it assumes a constant fracture height equal to the height of the oil bearing formation it propagates in. It was proposed by (Kristianovic and Zheltov 1955; Geertsma and de Klerk 1969) with a closed form solution of the fracture width given by

$$w(x) = \frac{4(1-\nu^2)Lp}{E} \tag{1.14}$$

The constant height of both KDG and PKN models, constrained by thickness of the fracturing layer, limits their ability to predict vertical propagation of hydraulic fractures. In addition, rigorous fracture mechanics is not captured in the formulations since fracture geometry is predetermined, independent of fluid flow and variations in reservoir properties. On the positive side, however, they have been used to verify new hydraulic fracture simulators because of the simplicity of their geometries and analytical solutions. Pseudo-3D models (P3D), the evolutionary step after 2D modeling were introduced (Settari and Cleary 1986; Advani, Lee, and Lee 1990; Morales 1989) to remove the constant and uniform height assumptions of the 2D models. By extending these 2D models, particularly the PKN geometry, to include in-situ stress variation in the top and bottom bounding layers, variation in fracture height during hydraulic fracturing were modeled.

General three dimensional fracture modeling considers fractures as planar objects that are oriented orthogonal to the minimum in situ stress. These models place no restriction on fracture length and height growth. In addition, they allow fluid flow along the fracture length and height directions. Given the two dimensional nature of fluid flow, modeling requires coupling between equations for fluid flow and linear elasticity. Three dimensional fracture modeling can be grouped into two categories. The first category involves analytical and numerical solution to a coupled model that includes integral equations for fracture width as a function of fluid pressure and the fracture fluid flow model (Clifton and Abou-Sayed 1981; Barree 1983; Savitski and Detournay 2002; Detournay and Garagash 2003; Bunger, Detournay, and Garagash 2005; Adachi, Siebrits, and Desroches 2007; Ribeiro and

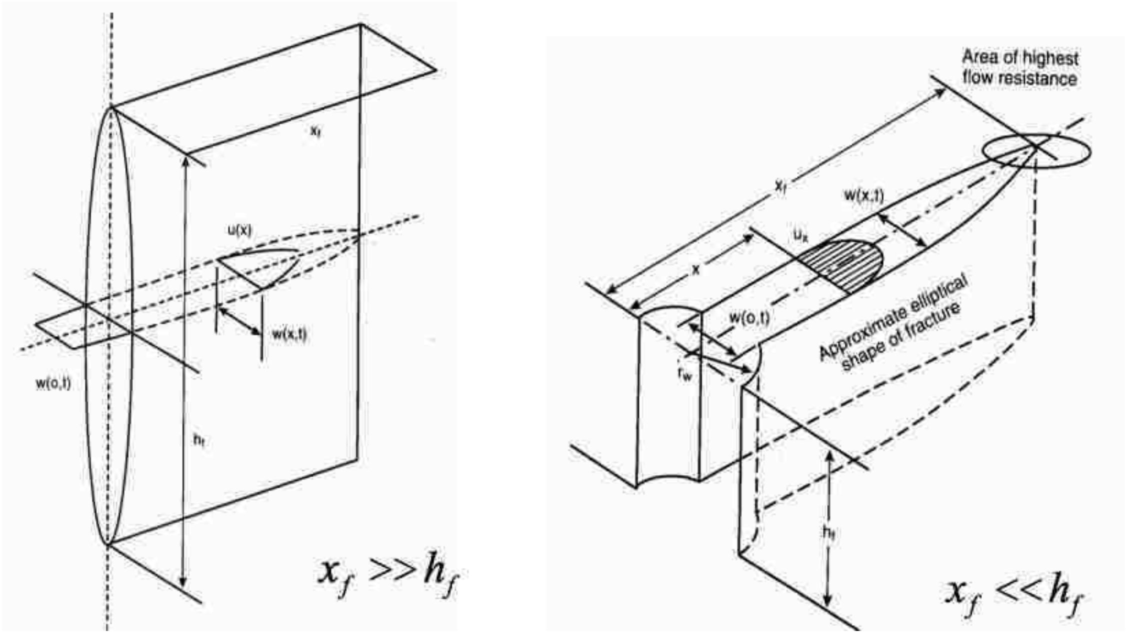

(a) Perkin-Kern-Nordgren (PKN) fracture model geometry for $x_f >> h_f$

(b) Kristianovic-Geertsma-de Klerk (KGD) fracture model geometry for $x_f << h_f$

Figure 1.4: 2D PKN and KGD hydraulic fracture geometry

Sharma 2012; Kovalyshen 2010; Yuan 1997; Bui 1977; Ghassemi 1996). Equation 1.15 is the commonly used elasticity integral for fracture width computation, where $R(t)$ is the domain of the fracture, σ_c is the local minimum in situ stress while C contains all the elastic properties of the layered rock. As evident in Equation 1.15, these methods only solve for fracture opening displacement and height along planes perpendicular to the propagation direction without describing deformation in the poroelastic media outside the fracture.

$$\int_{R(t)} C(x,y,\xi,\eta)\, w(\eta,t)\, d\xi d\eta = p(x,y,t) - \sigma_c(x,y) \tag{1.15}$$

In the second group, fracture width is not explicitly calculated from some integral equations like in the previous group, but is inferred from displacement solution of the hydromechanical models. Solution of coupled flow and mechanical problem requires specialized computational grids which not only permits solution of the fracture flow model at discrete points along the fracture but also allows application of this fracture fluid pressure on the boundary of the reservoir at the fracture/reservoir interface. Early attempts simply treated the fractures as external boundaries of the reservoir computational domain (Ji, Settari, and Sullivan 2009; Dean and Schmidt 2009). Initiation and propagation of the fracture were achieved by gradual release of the original fixed nodes on the fracture boundary plane and the fracture width then became the displacement of the released node. Some authors have used special interface elements called zero-thickness elements to handle fluid flow in fractures embedded in continuum media (see Carrier and Granet (2012), Segura and Carol (2004), Segura and Carol (2008a), Segura and Carol (2008b), Boone and Ingraffea (1990), Lobão et al. (2010)). An example is shown in Figure 1.5 and was proposed by Carrier and Granet (2012). It is a degenerate 8-node quadrangle. Fracture flow equation is discretized and solved on the mid-plane nodes. This means that fracture fluid pressure, p_f, is defined on nodes 6 and 8. The outer segments of the element defined by lines through nodes 4-7-3 and through nodes 1-5-2 are the connection between fracture and reservoir. This outer edges also serve as the reservoir-fracture interface for the mechanical model. Fracture aperture defined in the middle edge, is the difference between the displacement of the upper and the lower segments. Hydraulic continuity is ensured by specifying that fracture fluid pressure in the mid-plane nodes is equal to the reservoir fluid pressure on the outer segments. i.e p_f on node 6 is equal to p on node 2 and 3 and p_f on node 8 is equal to p on 1 and 4. The use of this type of elements allow for explicit fracture representation and easy solution of reservoir and fracture models on their respective computational domains. However, since the interface elements for fracture representation are inserted along the edges of continuum grids, the fracture propagation direction is known a priori and limited to the edges of grids, which in most cases is one of the principal coordinate directions of the computational grid. In addition, three dimensional computations using this meshes have not been reported.

The extended finite element method (XFEM) and the generalized finite element method (GFEM) have also been used to facilitate fracture representation in the reservoir domain. In the XFEM, the level set method or any of its variants is used to track the fracture location. Mohammadnejad and Khoei (2013) modeled hydraulic fracturing propagation in poroelastic media with the XFEM. The coupled effect of fluid flow and deformation in the surrounding reservoir was incorporated. Dahi (2009) also used the XFEM for hydraulic fracturing model but did not consider poroelasticity. Both applications were for line fractures in two dimensional reservoirs. On the other hand, the GFEM uses separate computational grids for fracture and reservoir representation. In applying the GFEM for hydraulic fracturing modeling, Gupta and Duarte (2014) and Gupta and Duarte (2015) used fixed grids for the reservoir while the embedded mesh for fracture representation was updated and continuously refined during fracture propagation. For both XFEM and GFEM, the additional degrees of freedom due to the enrichment functions significantly increases the computational cost. In addition, the frequent interpolation of numerical data between reservoir and fracture meshes reduces the accuracy of the GFEM which affects convergence of the method. Recently, the phase field method has been applied to hydraulic fracturing. The seminal work by Bourdin, Chukwudozie, and Yoshioka (2012, Chukwudozie, Bourdin, and Yoshioka (2013) led developments in this area. Bourdin, Chukwudozie, and Yoshioka (2012) introduced the phase field based variational fracture model for hydraulic fracturing and verified it by simulating fracture propagation in elastic domains due to inviscid fluid injection. Chukwudozie, Bourdin, and Yoshioka (2013) extended the initial work to account for the effects of insitu stresses on propagation patterns. Hydraulic fracture propagation in two and three dimensional reservoirs were simulated in both publications. However, fracture and reservoir fluid flow were not considered. Following the initial works, interests in applying the phase field methods for hydraulic fracturing modeling has increased. Although Mikelic, Wheeler, and Wick (2013), Wick, Singh, and Wheeler (2014), Mikelic, Wheeler, and Wick (2015) have incorporated reservoir-fracture fluid flow in phase field hydraulic fracturing model, they considered fractures as being of the same dimension as the reservoir. As a result a single poroelastic flow model was developed, obtained by weighting and adding reservoir and fracture flow models. The phase field variable was used as the indicator function for weighting the flow models. In addition, fracture width was not computed to update fracture permeability. Rather, predefined values of permeability were assigned to fracture regions.

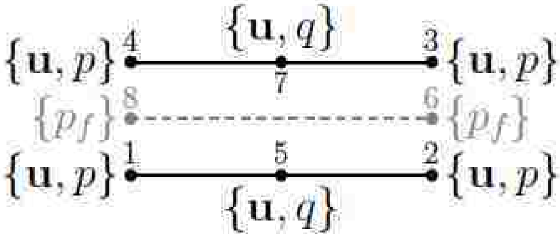

Figure 1.5: Zero-thickness interface element for solution of the coupled mechanical and flow models used in (Carrier and Granet 2012) for hydraulic fracturing modeling

1.4.1 Dissertation Outline

The previous sections introduced hydraulic fracturing, discussed the important phenomena that influence fracturing in deformable porous media and reviewed the important developments and contributions on the subject. The remaining part of this dissertation consists of four chapters with the following organization.

Chapter 2 focuses on the mechanical component. The variational fracture model is presented while fracture representation using the phase field approach is introduced. A phase field calculus is developed for converting surface integrals to volume integrals and examples of its application in fracture width and volume computations are shown. Thereafter, the variational fracture model is verified by solving the classical problem of hydraulic fracturing in impermeable media. This problem has been studied by several authors and is equivalent to injection of an inviscid fluid.

Chapter 3 introduces the flow component of the hydraulic fracturing model. The approach for coupling reservoir and fracture fluid flow models is presented while phase field calculus is used to regularize the developed coupled flow model. A modified fixed stress split algorithm for numerically coupling the flow and mechanical models is also presented. The numerical technique for fracture width computation is discussed in details. Thereafter, the classical Mandel's and Terzaghi's consolidation problems are solved to verify the geomechanics aspect of the coupling.

Chapter 4 solves hydraulic fracturing problems using the coupled model developed in Chapter 3. The model is first verified by solving problems with known solutions. Thereafter, the effects of reservoir properties on fracture path and geometry is studied. In situ stresses are incorporated while hydraulic fracture propagation in layered reservoirs is simulated.

Chapter 5 concludes the dissertation and recommends directions for continued research.

Chapter 2
Variational Fracture Modeling

2.1 Introduction

Fracture deformation and propagation make up the mechanical components of a hydraulic fracturing simulation while the flow component consists of reservoir and fracture fluid flow modeling. The objective of this chapter is to review and verify the general formulation of the variational fracture model used as the mechanical component of this dissertation. First, fracture representation using the phase field approach is described while the associated phase field calculus that accounts for cracks in integral quantities is presented. Some basic features of the numerical variational fracture code will be highlighted and results from numerical verification experiments for fluid driven fractures and natural fractures will be presented and discussed.

2.2 General Fracture and Deformation Models in Poroelastic Media

Reservoir deformation is traditionally modeled according to the theory of linear poroelasticity developed by Biot (1941). The theory addresses coupling between deformation of fluid saturated porous media and transient fluid diffusion using two equations for solid deformation and fluid flow (Lewis 1998). Since fractures are boundaries of poroelastic domains, their deformation also follow the poroelasticity theory. In its basic form, solid deformation is modeled by the equilibrium equation derived from momentum conservation with linear elastic stress-strain constitutive relation. The mathematical formulation of poroelastic reservoir deformation and fracture propagation are described as follows.

A poroelastic media, Ω in $\mathbb{R}^d$; $d = 2$ or 3, containing a fracture is shown in Figure 2.1, where $\Omega \setminus \Gamma \subset \mathbb{R}^d$ is the unfractured part of the reservoir while $\Gamma \subset \mathbb{R}^{d-1}$ is the fracture. Although the domain of the poroelastic media is bounded externally by $\partial\Omega = \partial_D\Omega \cup \partial_N\Omega$, where $\partial_D\Omega$ and $\partial_N\Omega$ are the displacement and traction boundaries respectively, the fracture can also be considered as part of its boundary. Therefore, in principle, $\partial\Omega = \Gamma \cup \partial_D\Omega \cup$

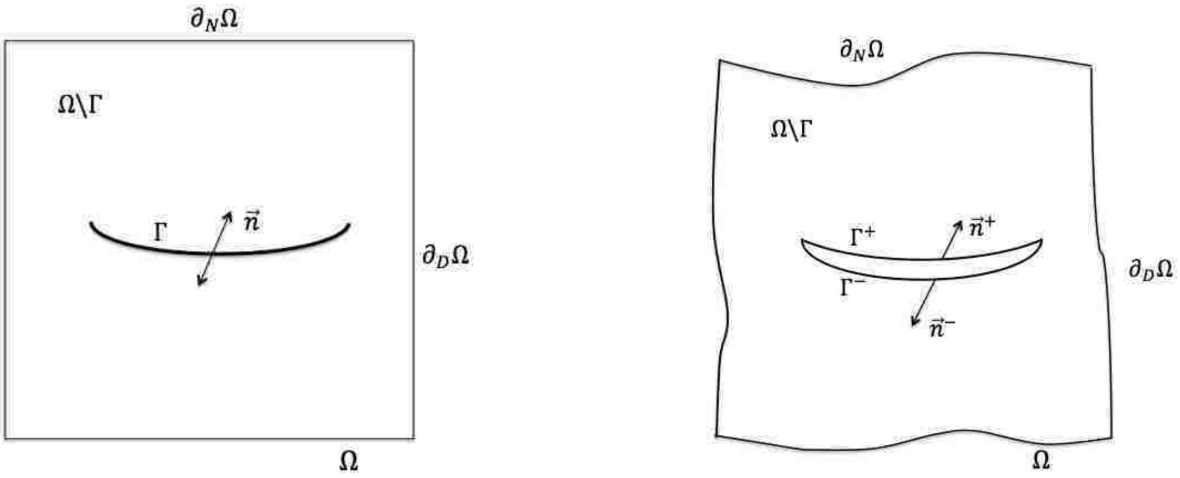

(a) Reference configuration for a poroelastic medium containing a fracture. The fracture, Γ is a surface defined by a single normal, $\vec{n}_\Gamma$

(b) Deformed configuration for a poroelastic medium containing a fracture. The crack has two surfaces defined by Γ^+ and Γ^-. The spacing between both fracture faces is the fracture width

Figure 2.1: Schematic of reservoir and fracture as components that make up the poroelastic media. The fracture is an internal boundary of the porous media with normal $\vec{n}_\Gamma$

$\partial_N\Omega$. In linearized elasticity, the reference configuration (e.g Figure 2.1a) is always used for mathematical modeling. However, in the deformed geometry (Figure 2.1b) of the poroelastic medium, the fracture is considered as a discontinuity with two surfaces Γ^+ and Γ^-, where $\pm$ represent the top and bottom of the fracture with normals $\vec{n}^+$ and $\vec{n}^-$ pointing away from the fracture and into the reservoir. Geometrically, these surfaces are assumed to coincide in the reference configuration so that $\vec{n}^+ = -\vec{n}^- = \vec{n}_\Gamma$.

Linear poroelasticity is applied to $\Omega \setminus \Gamma$ in Figure 2.1a. Application of traction forces on the fracture deforms it, creating displacement discontinuity across its surfaces. In hydraulic fracturing, the traction force is the fluid pressure of the injected fracturing fluid. Since fluid flow occurs in $\Omega \setminus \Gamma$ and Γ, additional deformation as predicted by poroelasticity through Biot's coefficient (α) is experienced by both fracture and reservoir.

Reservoir Deformation Model

For effective stress, σ', defined as

$$\sigma' = \sigma - \alpha \, \mathbb{I} p_r \tag{2.1}$$

the stress-strain relationship from linear elasticity is

$$\sigma = \mathbf{A} \, \epsilon \tag{2.2}$$

where $\mathbf{A}$ is the elasticity tensor that contains the mechanical properties of the reservoir while ϵ is the small strain tensor defined as

$$\epsilon = \frac{(\nabla \, \vec{u} + \nabla \, \vec{u}^T)}{2}$$

Under quasi-static, small strain, isothermal equilibrium and negligible inertial assumptions, the governing equation is the result of linear momentum balance for the solid and liquid phases.

$$\nabla \cdot \sigma' - \rho_b \, \vec{g} = \vec{f} \quad \text{in} \quad \Omega \setminus \Gamma \tag{2.3}$$

where

$$\rho_b = (1 - \phi) \, \rho_s + \phi \, \rho_f$$

ρ_b, ρ_s, ρ_f are the bulk densities of the porous media, density of the solid grains and density of the fluid respectively. $\vec{f}$ is body forces while ϕ is the true porosity defined (relative to the deformed configuration) as the ratio of pore volume to the total volume of the porous media.

Boundary Conditions

The governing equation is completed with boundary conditions that specifies either a known displacement, $\vec{u}_d$ on $\partial\Omega_D$ or a known traction, $\vec{\tau}$ on $\partial\Omega_N$.

$$\begin{aligned} \vec{u} &= \vec{u}_d \quad \text{on} \quad \partial\Omega_d \\ \sigma' \cdot \vec{n} &= \vec{\tau} \quad \text{on} \quad \partial\Omega_N \end{aligned} \tag{2.4}$$

Fracture Deformation

Fractures are traction boundaries of the poroelastic domain, where the force is the fluid pressure. Therefore, the deformation equation is

$$\sigma' \cdot \vec{n}_\Gamma = -p_f \vec{n}_\Gamma \quad \text{in} \quad \Gamma \tag{2.5}$$

The models described above have been used by numerous authors to describe reservoir and fracture deformation in poroelastic media (Dahi 2009; Rungamornrat, Wheeler, and Mear 2005; Yuan 1997; Detournay 1991; Aghighi 2007; Shen 2014).

Propagation Criteria

Prediction of fracture extension in the variational fracture model is based on Griffith's energy criterion for fracturing of a brittle material. Thus, the use of variational fracture model in this work assumes the poroelastic material is brittle and experiences no plastic strains during deformation. According to Griffith's criterion, fracture extension occurs if the energy available for fracture growth (energy release rate, G) is equal to the fracture toughness (G_c). That is, fracture propagates if

$$G = G_c \tag{2.6}$$

The criterion above can also be stated in terms of the criticality of the stress intensity factor as

$$K = K_c \tag{2.7}$$

where G and K are related by (Irwin 1957).

$$\begin{aligned} G &= \frac{(1-\nu^2)}{E}\Big(K_I^2 + K_{II}^2 + \frac{K_{III}^2}{1-\nu}\Big) \quad \text{(plane strain)} \\ G &= \frac{1}{E}\Big(K_I^2 + K_{II}^2 + (1+\nu)K_{III}^2\Big) \quad \text{(plane stress)} \end{aligned} \tag{2.8}$$

2.3 Variational Fracture Model

Fracture and reservoir deformation in the variational fracture model is based on linear poroelasticity. The fracture model reformulates the fracture deformation, propagation and reservoir deformation models described above into a single variational form that is built on the foundation of Griffith's energy criterion. A brief review of the development of the model is presented below. However, for an in-depth analysis of the method, see Bourdin, Francfort, and Marigo (2008) ,Bourdin, Francfort, and Marigo (2000).

Griffith's theory for brittle fracture is at the heart of the variational fracture model. According to Griffith's criterion, the existence and propagation of cracks is dependent on the crack surface energy and the competition between that surface energy and change in potential (bulk) energy during an infinitesimal increase of the crack length.

$$G = -\frac{\partial \mathcal{P}}{\partial l}; \qquad \mathcal{P} : \text{potential energy} \tag{2.9}$$

The energy release rate G, which according to Equation 2.9, shows that the energy dissipated to propagate a crack is proportional to the length in two dimensions (area in three dimensions) of the crack and is supplied by the release of bulk energy. Using Equation 2.6 as propagation criteria, Griffith proposed that the quasi-static evolution of a brittle crack signified by an increasing function $\dot{l}(t)$ must obey the following criteria:

$$\dot{l}(t) \geq 0 \tag{2.10}$$

$$G \leq G_c \tag{2.11}$$

$$(G - G_c)\dot{l}(t) = 0 \tag{2.12}$$

$\dot{l}(t)$ is a rate of change of length with time.

According to Equation 2.10, the fracture can only grow, prohibiting fracture healing during deformation and propagation. Equation 2.11 is the stability criterion which states that the energy release rate is bounded by the fracture toughness. Stable fracture propagation is only possible if Equation 2.11 is satisfied while propagation will be unstable if Equation 2.11 is violated. Equation 2.12 is the energy balance. It is evident from this criterion that if $G < G_c$, which occurs when the fracture is static, then obviously $\dot{l}(t) = 0$. On the other hand, during fracture growth, $\dot{l}(t) \geq 0$ so that $G - G_c = 0$. Again, the stability is achieved. As simple as the theory seems, Griffiths criterion however is incomplete on a number of grounds. Foremost is the assumption of a known propagation path. In addition, it is unable to handle crack initiation in the absence of strong singularities (Francfort and Marigo 1998; Bourdin, Francfort, and Marigo 2000; Chambolle, Giacomini, and Ponsiglione 2008). To overcome the shortcomings of Griffith's, the variational approach (Francfort and Marigo 1998; Bourdin, Francfort, and Marigo 2000) recasts Griffiths criterion into a variational setting, as the minimization over any crack set (any set of curves in two dimensions or surfaces in three dimensions) and any kinematically admissible displacement field $\vec{u}$, of a total energy consisting of the sum of the stored elastic energy and a surface energy proportional to the crack length in two dimensions or area in three dimensions. Considering a perfectly brittle linear elastic material with Hooke's law $\mathbf{A}$ and critical energy release rate G_c occupying a region Ω, the total energy of this material for any arbitrary number of cracks (Γ) and any kinematically admissible displacement is

$$\mathcal{F}(\vec{u},\Gamma) = \int_{\Omega\backslash\Gamma} \mathbf{W}(\epsilon(\vec{u}))\,dV - \int_{\partial\Omega_N} \vec{\tau}\cdot\vec{u}\,ds - \int_{\Omega} \vec{f}\cdot\vec{u}\,d\Omega + G_c\mathcal{H}^{N-1}(\Gamma) \tag{2.13}$$

$\mathbf{W}$ is the elastic energy density function associated with the linearized strain field and is given by $\mathbf{W}(\epsilon(\vec{u})) = \frac{1}{2}\mathbf{A}\epsilon(\vec{u}) : \epsilon(\vec{u})$, $\mathcal{H}^{N-1}(\Gamma)$ is simply the fracture length for two dimensional problems or its volume for three dimensional problems.

In the variational fracture setting (Francfort and Marigo 1998; Bourdin, Francfort, and Marigo 2000), the unilateral minimization of the total energy (Equation 2.13) replaces Griffiths condition of criticality of energy release rate for a crack to propagate. The model makes no assumption on the number of cracks or the crack path and geometry. Instead, Equation 2.13 provides a unified setting that handles path determination, nucleation, activation and growth of arbitrary number of cracks in two and three dimensions.

2.3.1 Phase Field Approximation

The discontinuity of fracture displacement fields and the unknown location of the discontinuities present difficulties for numerical implementation of Equation 2.13. To solve this problem, a phase field representation of the fractures is introduced (Bourdin, Francfort, and Marigo 2000). Fracture location is represented by a phase field function, v, which takes a value of 0 close to the crack and 1 far away from the crack, as shown in Figure 2.2. A transition region around the fracture exists with $0 < v < 1$, the size of which depends on a regularization length, ε.

Using the phase field variable to regularize the total energy and based on the work of Ambrosio and Tortorelli (1990a) and Ambrosio and Tortorelli (1990b), Bourdin (1998) has shown that Equation 2.14 converges to Equation 2.13 as $\varepsilon \to 0$. Thus, Equation 2.14 is the form of the total energy that is minimized in the variational fracture model.

$$\begin{aligned}\mathbf{F}_\varepsilon(\vec{u}, v) = \int_\Omega \mathbf{W}(\epsilon(\vec{u}), v) dV - \int_{\partial_N\Omega} \vec{\tau} \cdot \vec{u}\, d\, s - \int_\Omega \vec{f} \cdot \vec{u}\, dV \\ + \frac{G_c}{4c_n} \int_\Omega \Big(\frac{(1-v)^n}{\varepsilon} + \varepsilon |\nabla v|^2 \Big) dV\end{aligned} \tag{2.14}$$

where

$$c_n = \int_0^1 (1-s)^{n/2} ds \tag{2.15}$$

Numerical solution of Equation 2.14 is carried out by an alternate minimization scheme in which the equation is successively minimized with respect to the $\vec{u}$ and v fields until convergence is achieved.

Two different variants of the variational fracture model have been proposed. The models are known as AT1 and AT2 obtained by setting $n = 1$ and $n = 2$ respectively in Equation 2.14. According to Bourdin, Francfort, and Marigo (2000), the equilibrium solution of the v-field of a fracture for AT1 and AT2 are as follows:

For AT1:

$$v\,(\vec{x}) := \begin{cases} 0 & \text{if } d_\Gamma(\vec{x}) \le d_{Th} \\ \frac{d_\Gamma}{\varepsilon}(1 - \frac{d_\Gamma}{4\varepsilon}) & \text{else if } d_\Gamma(\vec{x}) < 2\varepsilon - d_{Th} \\ 1 & \text{otherwise,} \end{cases} \tag{2.16}$$

For AT2:

$$v\,(\vec{x}) := \begin{cases} 0 & \text{if } d_\Gamma(\vec{x}) \le d_{Th} \\ 1 - e^{-d_\Gamma(\vec{x})/2\varepsilon} & \text{otherwise,} \end{cases} \tag{2.17}$$

where $d_\Gamma(\vec{x})$ is the distance of any point $\vec{x}$ from the fracture while d_{Th} is the thickness of the fracture region with $v = 0$.

The use of the regularized problem does not require explicit representation of fractures. Numerical computation can be carried out on structured or unstructured finite element fixed

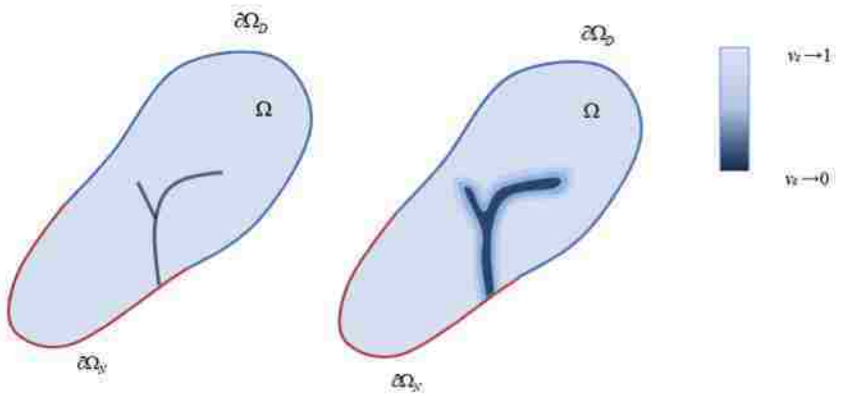

Figure 2.2: Phase field ($v-$field) fracture representation

meshes. The numerical algorithm is easy to parallelize and thus can take advantage of the availability of high performance computing resources to speed up computation for memory intensive problems.

2.3.2 Numerical Implementation

The variational fracture model used in this work is an implementation developed by Dr. Blaise Bourdin of the Mathematics department of LSU. It is a parallel, structured finite element code that is implemented using the PETSc library (Balay et al. 2011) and written in C programming language. Its implementation is in modules so that there is a V-step and a U-step to solve for fracture state (v) and displacement ($\vec{u}$) differently. This arrangement offers flexibility in implementing the alternate minimization scheme which as earlier stated, requires iteration between the V-step and U-step until a defined convergence level is achieved.

The structured finite element code uses the 8-node brick element type shown in Figure 2.3 and its associated shape function. Thus, it is a three dimensional code on for simulation on computational domains composed of regular parallelepiped. The code can also solve two dimensional problems by assuming plane strain conditions for the out-of-plane direction. The code has a handle for building the v-field of a pre-existing line fracture, penny shaped and rectangular shaped fractures in the computational domain using the equilibrium solution, Equation 2.17. With this feature, fractures of arbitrary sizes and orientation can be

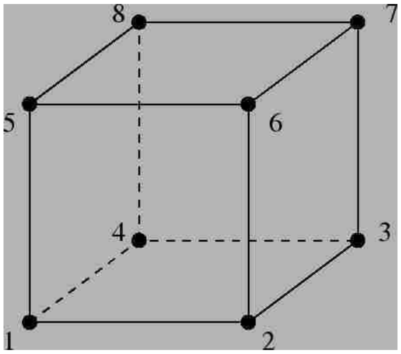

Figure 2.3: 8-node brick finite element used in variational fracture code

incorporated into a poroelastic domain for analysis.

Inputs to the fracture code are material properties and simulation parameters. The material properties include the geometry of the physical domain and the material elastic properties like E, ν, G_c. The simulation parameters include the resolution of the computation domain and the parameters of the fracture model like ε. The choice of ε is crucial in obtaining good numerical results for comparison with analytical or field data and in producing the correct propagation paths of the growing fracture. It also affects the actual value of fracture toughness used for simulation. According to Bourdin, Francfort, and Marigo (2008), asymptotic analysis of the surface energy term in Equation 2.14 shows that the fracture toughness is amplified, yielding an effective toughness given below.

$$G_{c,eff} = \begin{cases} G_c\big(1 + 3h/8\varepsilon\big) & \text{for } n = 1 \\ G_c\big(1 + h/2\varepsilon\big) & \text{for } n = 2 \end{cases} \tag{2.18}$$

Where h is structured grid with element. This amplification in the fracture toughness has to be accounted for in numerical simulations. This means that in any computation and for a material of fracture toughness value G_c, the input to the numerical simulation has to be scaled by a factor of $1/\big(1 + 3h/8\varepsilon\big)$ or $1/\big(1 + h/(2\varepsilon)\big)$. For example, using the $n = 2$ variational fracture model for a computation with fracture toughness $G_c = 1$ at resolution of $h = \varepsilon$, the actual input to the numerical simulator will be $G_c = 0.667$.

Since the variational approximation of the total potential energy (Equation 2.14) con-

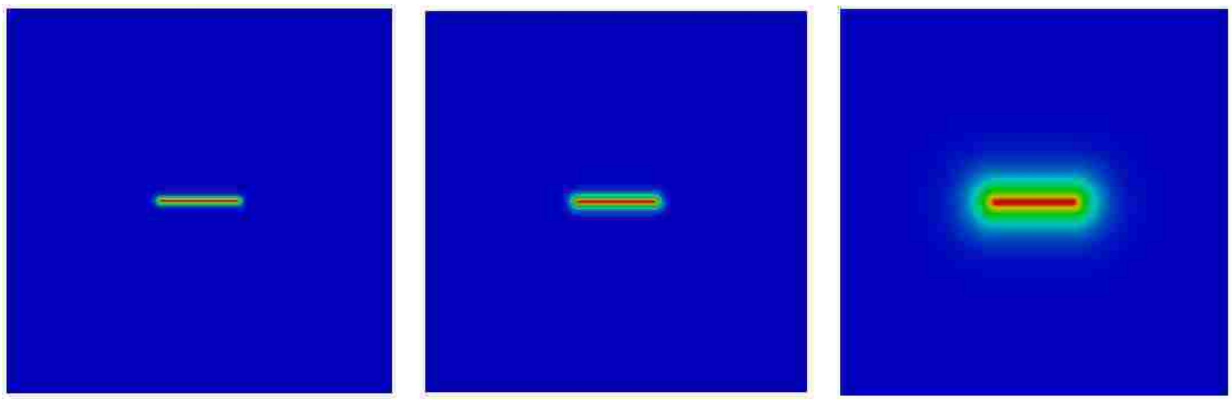

(a) Line fracture at $\varepsilon = 0.5h$ (b) Line fracture at $\varepsilon = h$ (c) Line fracture at $\varepsilon = 4h$

Figure 2.4: Profile of v-field for line at different ε/h values.

verges to the actual energy (Equation 2.13) as $\varepsilon \to 0$, an ideal choice will be to use a very small ε value. However, for a finite computation, ε is related to the element size, h so that $\varepsilon \approx h$ produces a sharp fracture profile as shown in Figures 2.4a and 2.4b for the phase field representation of a line fracture. Using this choice of ε will not reproduce the correct propagation paths for fractures inclined at an angle to any of the coordinate directions or for complex fractures that are branching, turning or merging. On the other hand, $\varepsilon > h$ produces a diffused fracture that creates softening effects in numerical simulation results. However, this range of ε is able to reproduce the correct behaviors associated with complex fractures. As seen in Figure 2.4c, the v-field representation of line fracture profile generated using $\varepsilon = 4\,h$ is diffused compared to those generated with smaller values of ε. A corresponding plot of the v-field across the line fracture at different ε values is shown in Figure 2.5. One observes that the profiles are sharper at small ε values while the profile at large ε values are diffused. In fact, for $\varepsilon = 8\,h$, the transition region spreads well into the unfractured region and will definitely have a large softening effect on numerical computations carried out at this resolution. With this understanding of the numerical behaviors associated with the use of extreme values of ε, the recommended trade-off is to use $h \leq \varepsilon \leq 4\,h$.

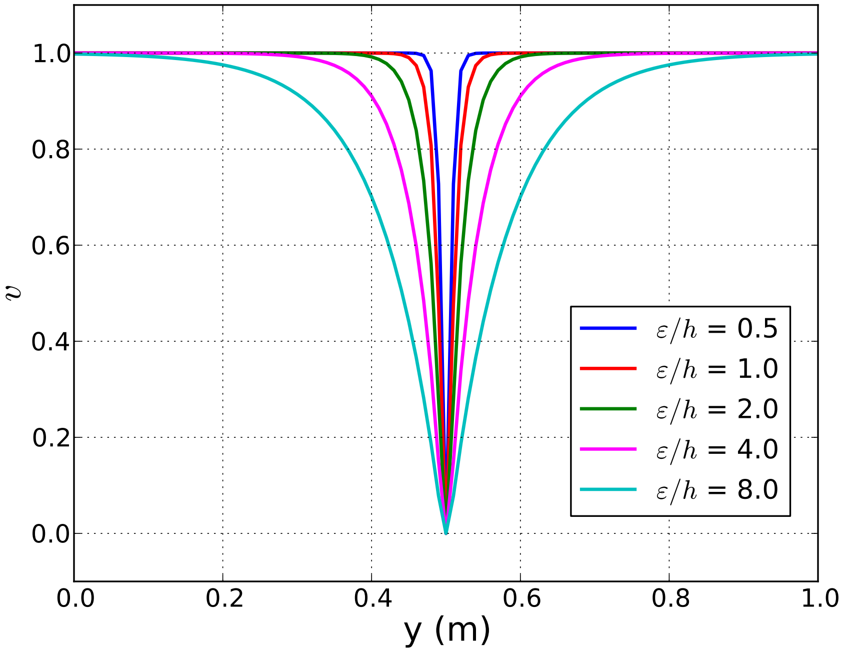

Figure 2.5: Plot of v-field across line fracture, at different ε/h values

2.3.3 Phase Field Calculus

The phase field representation simplifies integration over the fractured (Γ) and unfractured ($\Omega\backslash\Gamma$) subdomains by providing approximations for these integrals in terms of integrals over the whole computational domain. By using the approximate integrals, knowledge of the locations of Γ and $\Omega \setminus \Gamma$ is not required since all integrals can be computed over the whole domain as described below.

- Fracture normal, $\vec{n}_\Gamma$: The normal to the fracture is related to the gradient of the phase field. The gradient of the v-field is a vector quantity that points in the direction of the greatest rate of change of the v-field. The largest change in the v-field occurs in the transition region with $0 < v < 1$. Therefore, the fracture normal is computed as

$$\vec{n}_\Gamma \simeq \frac{\nabla v}{|\nabla v|} \tag{2.19}$$

- Integration over Γ: Let a discontinuous vector quantity $\vec{\psi}$ be defined on either side of the fracture Γ. The jump of the normal component of the discontinuous function ($[\![\vec{\psi}]\!] \cdot \vec{n}_\Gamma$) is the difference between its values on either side of the fracture face. The integral of the jump of the discontinuous function over Γ can be expressed in the form of an approximate integral over Ω using the phase field.

$$\int_\Gamma [\![\vec{\psi}]\!] \cdot \vec{n}_\Gamma \, ds \simeq \int_\Omega \vec{\psi} \cdot \vec{n}_\Gamma \, |\nabla v| \, dV = \int_\Omega \vec{\psi} \cdot \nabla v \, dV \tag{2.20}$$

Examples of the application of this formula are in the computation of fracture width (w), fracture volume (V_f) and leak-off volume (V_l) in the variational fracture framework.

- Fracture width, w: The width of the fracture at a point $\vec{x}$ on the fracture surface is the jump of the normal component of displacement at $\vec{x}$. In the variational phase field framework, fracture width is obtained by applying Equation 2.20 to integrate the jump of displacement along a line s, that runs orthogonal to the fracture face through $\vec{x}$.

$$w = -[\![\vec{u}]\!] \cdot \vec{n}_\Gamma \simeq \int_s \vec{u} \cdot \nabla v \, dx \tag{2.21}$$

- Fracture volume, V_f: Fracture volume is the integral of fracture width along the path of the fracture. Using Equation 2.20, the fracture volume is

$$V_f = \int_\Gamma w \, ds \simeq \int_\Omega \vec{u} \cdot \nabla v \, dV \tag{2.22}$$

- Leak-off volume, V_l: An important quantity during hydraulic fracturing is the amount of fluid loss. The fracturing fluid loss rate is a discontinuous quantity and assuming $\vec{q_r}$ is the flow velocity from the fracture, the total volume of fluid lost during fracturing is

$$V_l = -\int_0^t \int_\Gamma [\![\vec{q}_r]\!] \cdot \vec{n}_\Gamma \, ds \, d\tau \simeq \int_0^t \int_\Omega \vec{q}_r \cdot \nabla v \, dV \, d\tau \tag{2.23}$$

- Integration over $\Omega \backslash \Gamma$: The integral of a continuous/discontinuous function defined over the unfractured region, $\Omega \setminus \Gamma$, can be approximated by an integral over Ω as shown below.

$$\int_{\Omega \backslash \Gamma} \psi \, dV \simeq \int_\Omega v^2 \, \psi \, dV \tag{2.24}$$

2.3.4 Extension To Hydraulic Fracturing

During hydraulic fracture propagation, additional energy to extend fracture length is supplied to the poroelastic material, through the pressure of the injected fracturing fluid. To account for the fracturing fluid pressure, the total energy functional of the variational model presented in Equation 2.13 is extended to account for the contribution of the work done by pressure force in increasing fracture volume. The work done by the fracturing fluid pressure, p_f, in increasing the fracture volume is

$$\int_\Gamma p_f \, [\![\vec{u}]\!] \cdot \vec{n}_\Gamma \, ds \tag{2.25}$$

and when expressed using phase field calculus is

$$\int_\Omega p \, \vec{u} \cdot \nabla v \, dV \tag{2.26}$$

To obtain Equation 2.26 from Equation 2.25, the fracture fluid pressure p_f is replaced with p, where p is the fluid pressure acting in the whole computational domain. This is possible due to fluid pressure continuity from fracture to reservoir in poroelastic media so that p_f

and p_r are related to p as follows.

$$\begin{aligned} &p_r = p \quad \text{ in } \Omega \setminus \Gamma \\ &p_f = p_r = p \quad \text{ on } \Gamma \end{aligned} \tag{2.27}$$

where p_r is the fluid pressure in the reservoir. The work of the pressure forces (Equation 2.26) is added to Equation 2.13 to update the total energy formulation for hydraulic fracturing application.

$$\begin{aligned} \mathbf{F}_\varepsilon(\vec{u}, v) = &\int_\Omega \mathbf{W}(\epsilon(\vec{u}), v) dV - \int_{\partial_N \Omega} \vec{\tau} \cdot \vec{u}\, d\, s - \int_\Omega \vec{f} \cdot \vec{u}\, dV \\ &+ \frac{G_c}{4c_n} \int_\Omega \Big(\frac{(1-v)^n}{\varepsilon} + \varepsilon |\nabla v|^2 \Big) dV + \int_\Omega p\, \vec{u} \cdot \nabla v dV \end{aligned} \tag{2.28}$$

In addition, $\mathbf{W}(\vec{u}, v) = \frac{1}{2}\mathbf{A}\big(v\epsilon(\vec{u}) - \frac{\alpha}{3\kappa}\mathbb{I}p\big) : \big(v\epsilon(\vec{u}) - \frac{\alpha}{3\kappa}\mathbb{I}p\big)$ becomes the poroelastic energy density function since it accounts for pore pressure through the effective stress. κ is the drained bulk modulus of the material. It is important to note that the work of the pressure force is equivalent to applying a traction boundary condition on the fracture surface as described in Equation 2.5 of Subsec. 2.2 in the classical poroelastic fracture model.

2.3.5 Scaling of Variational Fracture Model

To apply the variational fracture model to any problem, the input parameters must be in consistent units. An example of a consistent measurement system is the SI units. The typical value for reservoir fracture toughness in SI units is ∼100 Pa m while the values for Young's modulus is $E < 100$ GPa. This means that several orders of magnitude exists between the E and G_c values for petroleum reservoirs. If one uses material parameters expressed in SI units in numerical simulations, numerical instability can sometimes arise. To circumvent this, a dimensionless form of the variational fracture model is used for numerical computations. This model is shown in Equation 2.29 and has the same form as the regular variational fracture model. The difference is that all inputs and variables are equipped with tilde to represent their non-dimensionality.

$$
\begin{aligned}
\mathbf{F}_{\varepsilon}(\vec{\tilde{u}}, v) = \frac{1}{2} \int_{\tilde{\Omega}} \tilde{\mathbf{A}} \big(v\epsilon(\vec{\tilde{u}}) - \frac{\alpha}{3\tilde{\kappa}} \mathbb{I}\tilde{p} \big) : \big(v\epsilon(\vec{\tilde{u}}) - \frac{\alpha}{3\tilde{\kappa}} \mathbb{I}\tilde{p} \big) d\tilde{V} - \int_{\partial_N \tilde{\Omega}} \vec{\tilde{\tau}} \cdot \vec{\tilde{u}} \, d\,\tilde{s} \\
- \int_{\tilde{\Omega}} \vec{\tilde{f}} \cdot \vec{\tilde{u}} \, d\tilde{V} + \frac{\tilde{G}_c}{4c_n} \int_{\tilde{\Omega}} \Big(\frac{(1-v)^n}{\tilde{\varepsilon}} + \tilde{\varepsilon} |\tilde{\nabla} v|^2 \Big) d\tilde{V} + \int_{\tilde{\Omega}} \tilde{p} \, \vec{\tilde{u}} \cdot \tilde{\nabla} v \, d\tilde{V}
\end{aligned}
\tag{2.29}
$$

From the numerical solutions of the dimensionless fracture model, the numerical results can be scaled to realistic reservoir input values using Equation 2.30. The derivation of the dimensionless variational fracture model and the scaling parameters for all the parameters and inputs can be found in Appendix A. The subscript o represents conversion factors from the dimensionless to the respective dimensional parameters.

$$
G_c = G_{c_o} \tilde{G}_c; \quad \vec{u} = u_o \vec{\tilde{u}}; \quad p = p_o \tilde{p}; \quad \kappa = E_o \tilde{\kappa} \tag{2.30}
$$

$$
\alpha = \alpha_o \tilde{\alpha}; \quad \mathbf{A} = E_o \tilde{\mathbf{A}}; \quad \vec{f} = f_o \vec{\tilde{f}}; \quad \vec{\tau} = p_o \vec{\tilde{\tau}}; \quad \Omega = x_o^N \tilde{\Omega} \tag{2.31}
$$

Where

$$
\begin{aligned}
u_o &= \sqrt{\frac{G_{c_o} x_o}{E_o}} \\
p_o &= \sqrt{\frac{G_{c_o} E_o}{x_o}} \\
f_o &= \sqrt{\frac{G_{c_o} E_o}{x_o^3}} \\
\alpha_o &= 1
\end{aligned}
\tag{2.32}
$$

2.4 Verification of Fracture Model

One of the simplest cases of hydraulic fracturing is injection of a zero viscosity fluid in an infinite conductivity fracture. The implication of this assumption is that no pressure losses are encountered inside the fracture as all the fluid energy is expended in mechanically deforming the material. With no fluid pressure gradient inside the fracture, the fracturing fluid does not flow and its pressure everywhere is uniform. Analytical solutions for this problem have been derived and can be found in Sneddon and Lowengrub (1969), Detournay and Garagash (2003).

The variational fracture model for hydraulic fracturing is verified by solving the elastic deformation and propagation of fractures due to injection of an inviscid fluid. Specifically, the crack opening displacements (COD), fracturing fluid pressure and fracture propagation paths will be computed for the fluid injection process. The effect of in-situ stress on the numerical results is also studied. Since the poroelastic material is assumed to be impermeable, fluid loss in the form of fluid exchange between fracture and poroelastic material is not considered. The numerical simulation results are compared against analytical expressions derived from Sneddon and Lowengrub (1969), for fracture propagating in an impermeable domain when $G = G_c$. First, the COD of a non propagating fracture acted upon by a known fluid pressure is computed. Thereafter, pressure and volume driven hydraulic fracture propagation are simulated. For all cases, spatially invariant fluid pressure is used, which implies that both $p_f(\vec{x})$ and $p_r(\vec{x})$ are constant in space. A zero initial fluid pressure is assumed while the reservoir is considered impermeable. These requirements are implemented by setting $\alpha = 0$ for the computations.

2.4.1 Application To Static Fractures in Two and Three Dimensions

This section simulates the deformation of a static line crack (Γ) of length $2l_o$ in an infinite two dimensional domain (Ω) in the $x - y$ plane as shown in Figure 2.6. This is the classic problem solved by Sneddon and Lowengrub (1969). The material is composed of a homogeneous isotropic, linear elastic material with Young's moduli E, Poisson's ratio ν, fracture toughness G_c. The domain is under plain strain conditions and the boundary conditions on the material is such that displacement and stresses vanish at infinity while the crack surface is acted upon by a uniform pressure p.

Line Fracture in a Two Dimensional Domain

The pre-existing line crack is non propagating and the objective is to obtain the fracture opening displacement and the fracture volume for a uniform pressure, p, acting on the

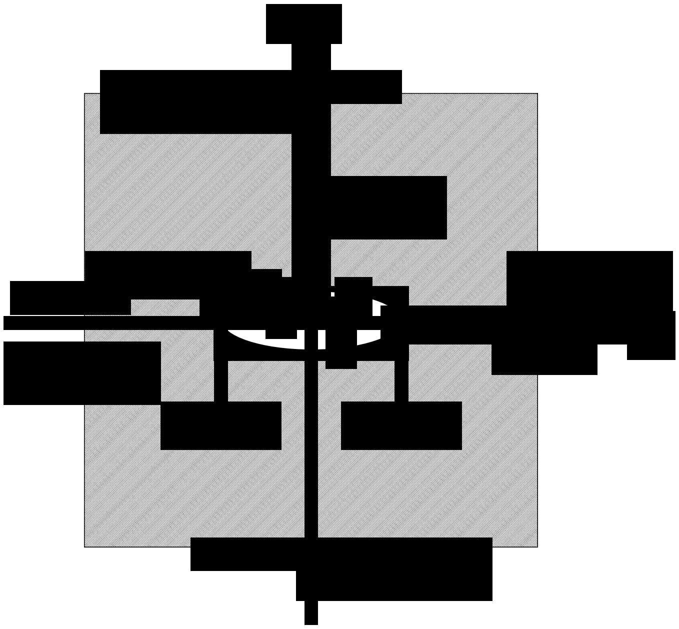

Figure 2.6: Schematic of deformed line crack in a two dimensional domain

crack surface. For the condition where the crack is found in the region defined by $y = 0$, $-l_o \leq x \leq l_o$ as in Figure 2.6, Sneddon and Lowengrub (1969) derived the following analytical expression for the crack opening displacement in the y-direction.

$$u_y(x, 0) = b\sqrt{1 - \frac{x^2}{l_o^2}} \tag{2.33}$$

where

$$\begin{aligned} b &= \frac{2\Delta p l_o}{E'} \\ \Delta p &= p - \sigma_{min} \end{aligned} \tag{2.34}$$

and

$$E' = \frac{E}{(1 - \nu^2)} \tag{2.35}$$

The fracture displacement profile is elliptic as evident from Equation 2.33. Thus, the fracture volume is

$$V_f = \pi b l_o \tag{2.36}$$

It is assumed that the reservoir domain and parameters are the same as in the dimensionless model. Therefore, all conversion factors with subscript o are equal to 1. The static fracture deformation experiment is reproduced using the variational fracture model on a computational domain of $\Omega = 4$ m × 4 m with pre-existing line fracture of length $l_o = 0.2$ m placed centrally in the domain as in Figure 2.6. The mechanical properties of the material are $E = 1$ GPa and $\nu = 0$. Since Sneddon's case is for an infinite domain, a large computation domain size relative to the initial fracture length is used, to minimize the effects of the boundary condition on the numerical results. From numerical results of the variational fracture minimization algorithm, the opening displacement along the fracture length is computed using the relationship below

$$u_y(x,0) = \frac{1}{2}\int_{-\infty}^{\infty} \vec{u}\,(x,0)\cdot\nabla v\,(x,0)\,dy \tag{2.37}$$

while fracture volume is given by

$$V_f = \int_{-\infty}^{\infty} \vec{u}\,(x,y)\cdot\nabla v\,(x,y)\,dV \tag{2.38}$$

For $p = 1.0$ MPa, $l_o = 0.2$ m, Figures 2.7a, 2.7b, 2.7c show the v-field representation, the displacement field across the fracture face and the deformed configuration of the static fracture. In addition, Figures 2.8 a and 2.8 b show the fracture opening displacement obtained using Equation 2.37 for different combinations of ε and h, compared with the analytical model of Sneddon and Lowengrub (1969). The results at fixed $h = 6.7 \times 10^{-3}$ and varying ε of Figure 2.8 shows that numerical results deviate more from the analytical solution as h/ε increases while the small deviations observed for opening displacement around the fracture tip is due to the smoothening effect of the scalar crack v-field. On the other hand, there is a better match between the numerical and analytical soutions for fixed $\varepsilon = 1 \times 10^{-2}$ and varying h as shown inn Figure 2.8b, even though the effect of softening is still observed for large h/ε ratios. Table 2.1 presents the computed fracture volume. There is good agreement between the numerical values computed using Equation 2.38 at different values of h and that computed using Equation 2.36. It is important to note that even though h is orders

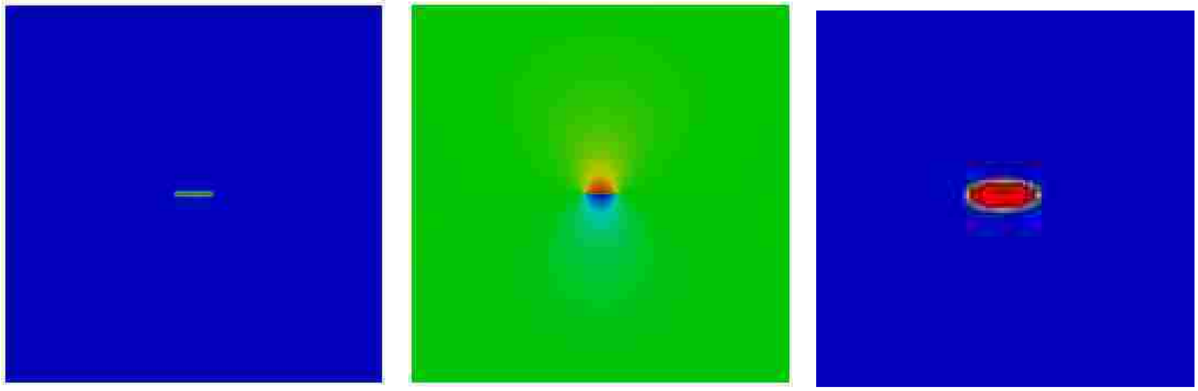

(a) Line fracture representation by scalar v-field

(b) Displacement field

(c) Deformed configuration of line crack in a two dimensional domain ($\times 150$)

Figure 2.7: v, displacement and deformed configuration of pressurized static line fracture

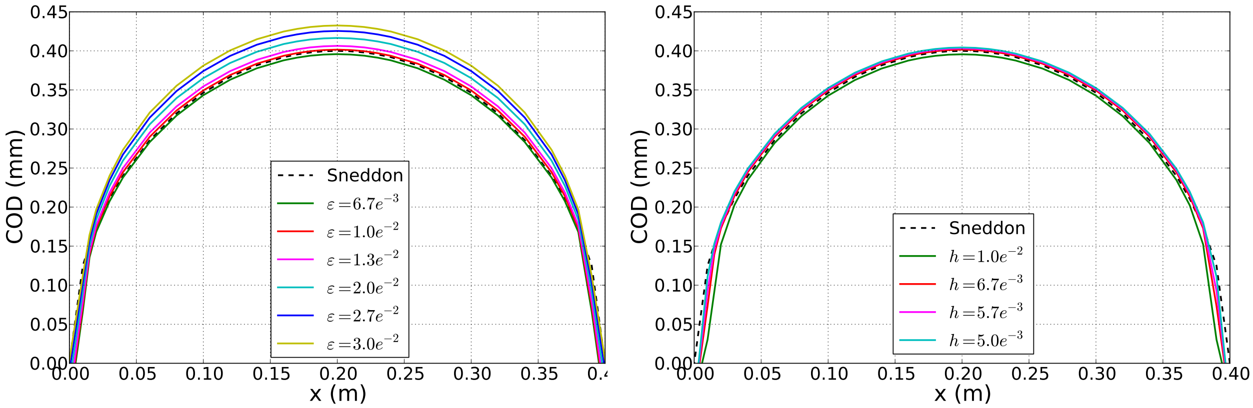

(a) Varying ε at $h = 6.7 \times 10^{-3}$ m

(b) Varying h at $\varepsilon = 1 \times 10^{-2}$ m

Figure 2.8: Line fracture opening displacement profile

of magnitude greater than the peak value of the crack opening displacement, the numerical solution still captures the correct profile of the fracture opening.

Although a null displacement boundary condition was used for all the presented results, the numerical simulation is insensitive to other types of displacement boundary conditions since the computational domain is large relative to the fracture length.

Penny-Shaped Fracture in a Three Dimensional Domain

Numerical simulation of the propagation of a penny-shaped fracture in a three dimensional computational domain is carried out. Again, the dimensionless parameters are as-

Table 2.1: Static fracture volume ($\varepsilon = 1 \times 10^{-2}$ m)

h (m)	1×10^{-2}	6.7×10^{-3}	5.7×10^{-3}	5×10^{-3}
Numerical fracture volume (m^2)	2.4×10^{-4}	2.47×10^{-4}	2.49×10^{-4}	2.51×10^{-4}
Analytical fracture volume (m^2)	2.513×10^{-4}			

sumed to be the same as the dimensional parameters. For this case, the analytical crack opening displacement and fracture volume for the static penny shaped fracture acted upon by a uniform pressure p have been derived by Sneddon and Lowengrub (1969) and are given below.

$$u_y(\rho, 0) = \epsilon\sqrt{(1-\rho)}; \qquad \rho = \frac{r}{R} \tag{2.39}$$

where

$$\epsilon = \frac{4\Delta pR}{\pi E'} \tag{2.40}$$

R is the radius of the penny fracture while r is the distance from the fracture inlet, of a point along the fracture axis. The fracture volume is

$$V = \frac{4}{3}\pi R^2 w_0 \tag{2.41}$$

w_0, opening displacement at fracture inlet ($\rho = 0$) is

$$w_0 = u_y(0,0) = \frac{4\Delta pR}{\pi E'} \tag{2.42}$$

Variational fracture simulation of the problem is carried out on $\Omega = 4$ m $\times$ 4 m $\times$ 4 m with an existing penny shaped fracture of $R_o = 0.2$ m, oriented with normal $(0,1,0)$ and placed in the center of the computational domain. Elastic properties of the material are $E = 1$ GPa and $\nu = 0$ with $p = 1.0$ MPa. Due to the large computation cost required for the three dimensional numerical simulations, only two cases with different domain resolutions were considered, and the results are shown in Figures 2.9 and 2.10. The computational domain is clipped in the center to reveal the penny shaped fractures. Figure 2.9a and Figure 2.9b are respectively the v-field of the fracture and the contour of the v-field taken at $v = 0.1$. For both

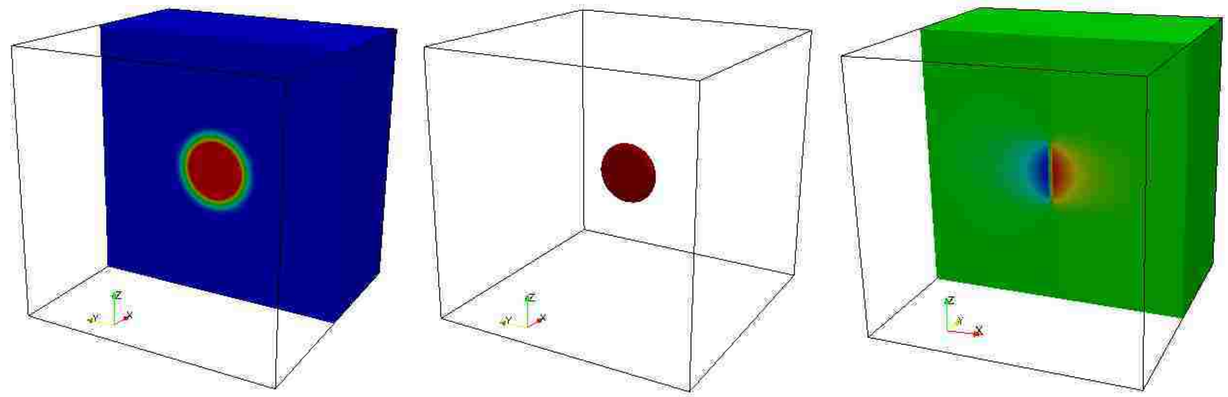

(a) v-field representation of fracture

(b) Fracture contour, taken at $v = 0.1$

(c) x-component of displacement. Note that the orientation here is different from that for the other two figures

Figure 2.9: v-field and displacement field for penny-shaped fracture in three dimensional computational grid

figures, the fracture surface is perpendicular to the normal to the clip plane. Also, Figure 2.9c shows the x-component of the displacement field on the domain that is clipped so that the fracture surface is parallel to the y-direction. As seen in Figure 2.10, good comparison is obtained between the numerically obtained opening displacement along a diameter of the fracture with that from the analytical formula (Equation 2.42). Since the material properties are homogeneous, the fracture opening displacements are isotropic and independent of the orientation of the diameter through the fracture, along which they were computed.

2.4.2 Pressure Driven Fracture Propagation in a Two Dimensional Domain

This section simulates propagation of a line fracture in an impermeable reservoir by specifying the pressure of the injected inviscid fluid. Given that fluid pressure is easy to specify, the simplest option for hydraulic fracturing is a pressure driven operation in which fluid pressure is monotonically ramped up to drive fracture propagation. However, analytical results show that this method of hydraulic fracturing propagation is unstable. The instability of the operation is also numerically confirmed using the fracture model.

Griffith's stability criteria provides the analytical basis that supports the instability of the pressure driven hydraulic fracture propagation. According to Equation 2.10, $G \leq G_c$

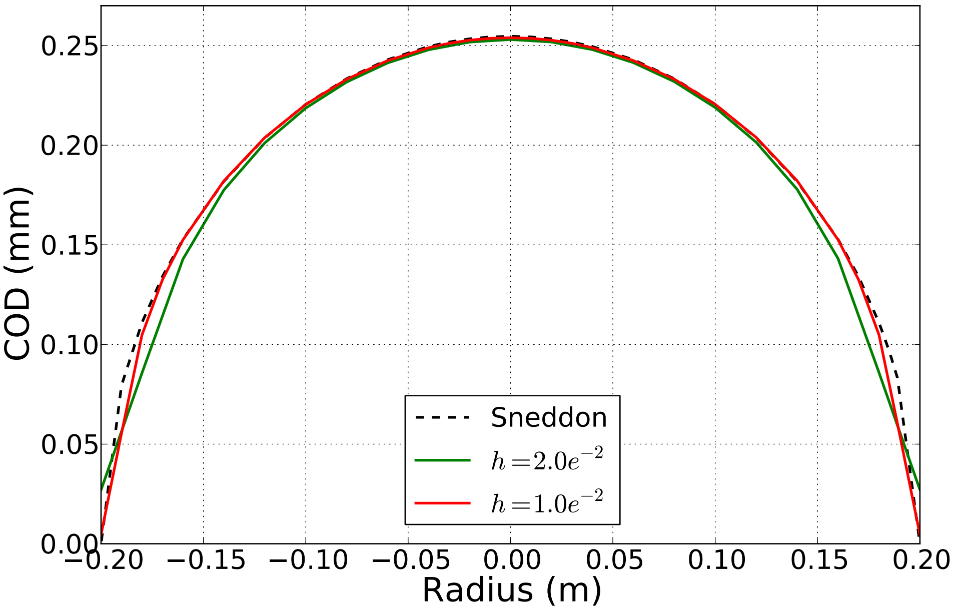

Figure 2.10: Penny-shaped fracture opening displacement for $\varepsilon = h$

must be satisfied at all times to guarantee stable fracture propagation. Violation of this will lead to unstable fracture propagation. Sneddon and Lowengrub (1969) derived the energy release rate a line fracture with initial half-length l_o, in an infinite two dimensional domain as

$$G = \frac{\pi \Delta p^2 l_o}{E'} \tag{2.43}$$

For a linearly increasing pressure modeled by $p = p_{ini}t$, where t is time and p_{ini} is the rate of increase in pressure with time, Equation 2.43 becomes

$$G = \frac{\pi \Delta p_{ini}^2 t^2 l_o}{E'} \tag{2.44}$$

Therefore, the critical time to reach Griffith's propagation criterion ($G = G_c$) is

$$t_c = \sqrt{\frac{G_c E'}{\pi \Delta p_{ini}^2 l_o}} \tag{2.45}$$

On examining Equation 2.44, one observes that for $t \leq t_c$, G will be less than G_c. Hence, the fracture will be static (i.e. $l = l_o$). However, for $t > t_c$, Equation 2.44 shows that G will be greater than G_c. This condition fails the stability requirement of Equation 2.11, leading to unstable hydraulic fracture propagation. Therefore, beyond the critical points, the analytical solutions are undefined.

The instability of a pressure driven hydraulic fracture propagation is numerically confirmed using the parameters in Table 2.2. The reservoir parameters are shown in the last column of the table while the second column (D) shows the numerical/dimensionless simulation inputs. The third column (o) contains the scaling factors used for converting the dimensionless properties to their respective reservoir quantities. The dimensionless computational domain is $\tilde{\Omega} = 4 \times 4$ while $\Omega = 100$ m $\times$ 100 m. For $p_{ini} = 0.0141$ MPa/s, the analytical solutions are $t_c = 25.8$, $p_c = 0.357$ MPa and $V_c = 0.0028$ m^2 from Equations 2.45, 2.43 and 2.36. At each time step, the dimensionless fluid pressure is applied to the fracture model to compute $\vec{\tilde{u}}$, v and the corresponding fracture volume, $\tilde{V}_f$. Thereafter, the quantities are scaled using Equation 2.30. Figure 2.11 plots the fluid pressure versus the computed fracture volume for both numerical simulation and the analytical solution. One observes from the numerical results that as the fluid pressure approaches the critical value, the numerical simulation becomes unstable and completely breaks down. This behavior is highlighted in Figure 2.12 which shows the v-field of the fracture after 1 s, 24 s and 25 s respectively. The critical pressure from the numerical simulation is reached after 24 s of pressure increase. At 25 s, which is beyond the critical time, the unstable fracture propagation leads to a complete breakdown of the v-field in the computational domain as seen in Figure 2.12c. This confirms the analytical proposition that pressure driven hydraulic fracture propagation is unstable and cannot be used to simulate the hydraulic fracturing process.

2.4.3 Volume Driven Fracture Propagation in Two and Three Dimensional Domains

The variational fracture model of Equation 2.28 assumes that the fracturing fluid pressure is known. As shown in the previous subsection, the pressure driven deformation leads to

Table 2.2: Reservoir parameters and numerical inputs for pressure driven hydraulic fracturing simulation. Column D is the dimensionless inputs to the numerical model while column o is the scaling for converting dimensionless parameters to physical values

Parameter	D	o	Physical
x	4	25 m	100 m
u	-	3.54×10^{-4} m	-
p		0.283 MPa	
p_{ini}	0.05/s	0.283 MPa/s	0.0141 MPa
E	1	20 GPa	20 GPa
G_c	1	1×10^{-7} GPa m	100 Pa m
ν	0	1	0
α	0	1	0
l_o	0.2	25 m	5 m

unstable fracture propagation. On the other hand, field hydraulic fracturing treatments are volume driven since an important requirement is that the sum of the fracture volume and fluid lost to the surrounding reservoir must equal the amount of fluid injected. In this volume driven operation, the fluid pressure is unknown and its computation must ensure volume conservation. Solution of the problem for injection of an inviscid fluid in an impermeable reservoir requires computing the uniform fluid pressure that deforms the fracture to create a fracture volume equal to the volume of injected fluid. Ordinarily, this is achievable by randomly sampling pressure values to find the one which when applied to the deformation model, creates a fracture that satisfies volume conservation. This crude technique, however, will require an infinite number of steps to find the correct pressure value. A solution technique is derived for minimizing the energy subject to a volume constraint. Considering only the U-step, the solution proceeds as follows: For $\alpha = 0$, find $\vec{\tilde{u}}$ that minimizes

$$\mathcal{E}(\vec{\tilde{u}}) = \frac{1}{2}\int_{\tilde{\Omega}\backslash\tilde{\Gamma}} \tilde{\mathbf{A}}'\epsilon(\vec{\tilde{u}}) : \epsilon(\vec{\tilde{u}})\, d\tilde{V} - \int_{\partial_N\tilde{\Omega}} \vec{\tilde{\tau}} \cdot \vec{\tilde{u}}\, d\tilde{s} \tag{2.46}$$

subject to

$$-\int_{\tilde{\Gamma}} [\![\vec{\tilde{u}}]\!] \cdot \vec{n}_\Gamma\, d\tilde{s} = \tilde{V}_{inj} = \tilde{Q}\,\tilde{t} \tag{2.47}$$

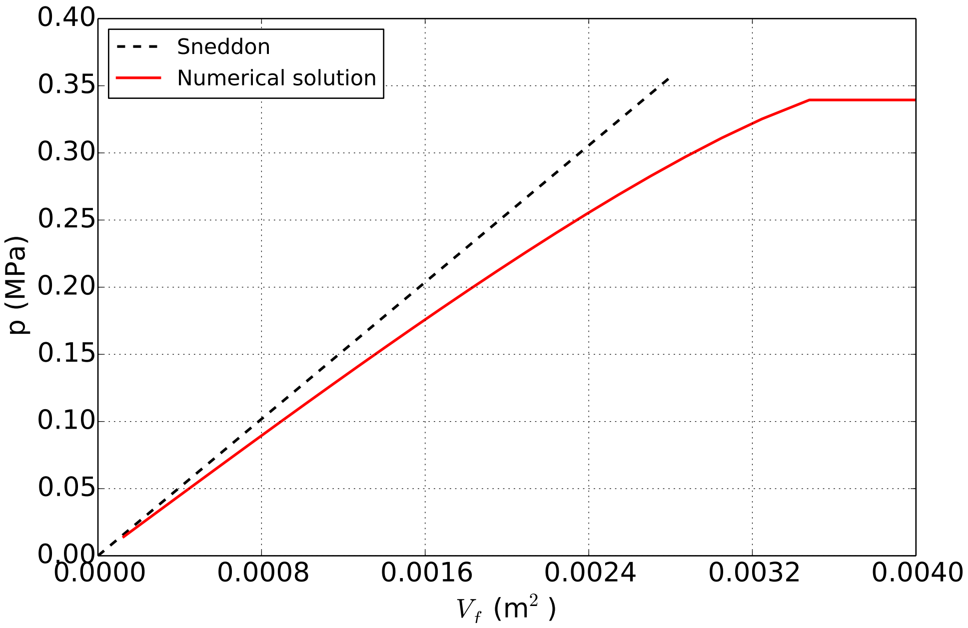

Figure 2.11: Numerical results for pressure driven experiment

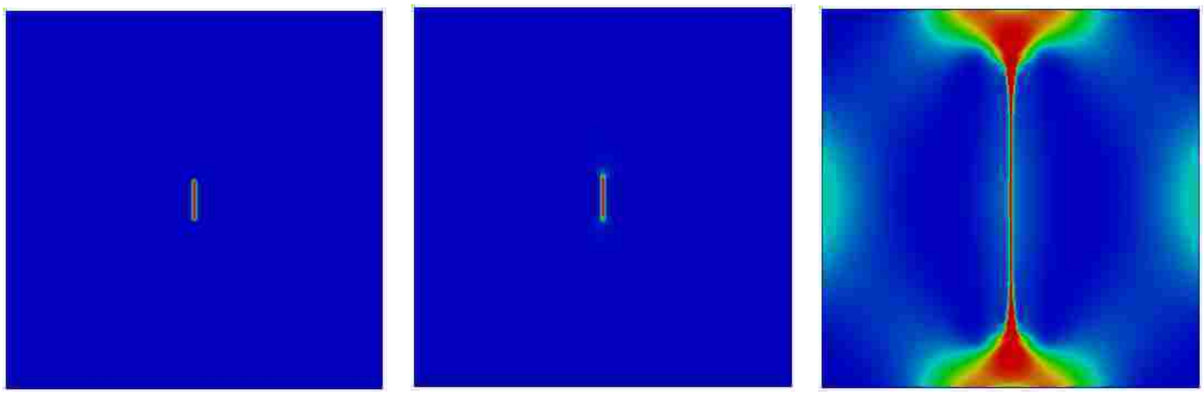

(a) Fracture at t = 1 s

(b) Fracture after 24 s, just before critical pressure is reached

(c) Fracture after 25 s. The completely broken v-field is the result of unstable fracture propagation

Figure 2.12: Fracture evolution during pressure driven experiment. The hydraulic fracture is incapable of propagating in a stable manner when a pressure beyond the critical value is imposed

To solve the constrained optimization problem, a lagrangian multiplier, λ, is introduced and a Lagrangian, $\mathcal{L}(\vec{\tilde{u}}, \lambda)$, is constructed to remove the volume constraint. Therefore, the problem becomes: Find $(\vec{\tilde{u}}, \lambda)$ that minimize

$$\mathcal{L}(\vec{\tilde{u}}, \lambda) = \frac{1}{2}\int_{\tilde{\Omega}\backslash\tilde{\Gamma}} \tilde{\mathbf{A}}'\epsilon(\vec{\tilde{u}}) : \epsilon(\vec{\tilde{u}})\, d\tilde{V} - \int_{\partial_N\tilde{\Omega}} \vec{\tilde{\tau}} \cdot \vec{\tilde{u}}\, d\tilde{s} - \lambda\Big(- \int_{\tilde{\Gamma}} [\![\vec{\tilde{u}}]\!] \cdot \vec{n}_\Gamma\, d\tilde{s} - \tilde{V}_{inj}\Big) \tag{2.48}$$

The first order optimality condition requires that the derivatives of $\mathcal{L}$ with respect to $\vec{\tilde{u}}$ and λ be equal to zero. $\partial_\lambda \mathcal{L} = 0$ is simply the volume balance (Equation 2.47) which has to be satisfied. On the other hand, $\partial_{\vec{\tilde{u}}}\mathcal{L}$ is

$$\begin{aligned}
\delta_{\vec{\tilde{u}}}\mathcal{L}(\vec{\tilde{u}}, \lambda; \phi) &= \int_{\tilde{\Omega}\backslash\tilde{\Gamma}} \tilde{\mathbf{A}}'\epsilon(\vec{\tilde{u}}) : \epsilon(\vec{\phi})\, d\tilde{V} - \int_{\partial_N\tilde{\Omega}} \vec{\tilde{\tau}} \cdot \vec{\phi}\, d\tilde{s} + \lambda \int_{\tilde{\Gamma}} [\![\vec{\phi}]\!] \cdot \vec{n}_\Gamma\, d\tilde{s} \\
&= \int_{\tilde{\Omega}\backslash\tilde{\Gamma}} \tilde{\sigma}' : \epsilon(\vec{\phi})\, d\tilde{V} - \int_{\partial_N\tilde{\Omega}} \vec{\tilde{\tau}} \cdot \vec{\phi}\, d\tilde{s} + \lambda \int_{\tilde{\Gamma}} [\![\vec{\phi}]\!] \cdot \vec{n}_\Gamma\, d\tilde{s} \\
&= - \int_{\tilde{\Omega}\backslash\tilde{\Gamma}} \tilde{\nabla} \cdot \tilde{\sigma}' \cdot \vec{\phi}\, d\tilde{V} + \int_{\partial_N\tilde{\Omega}} \tilde{\sigma}' \cdot \vec{n} \cdot \vec{\phi}\, ds + \int_{\partial_N\Omega} \vec{\tilde{\tau}} \cdot \vec{\phi}\, d\tilde{s} \\
&\qquad + \int_{\tilde{\Gamma}} \tilde{\sigma}' \cdot \vec{n}_\Gamma \cdot [\![\vec{\phi}]\!]\, d\tilde{s} + \lambda \int_{\tilde{\Gamma}} [\![\vec{\phi}]\!] \cdot \vec{n}_\Gamma\, d\tilde{s} \\
&= 0
\end{aligned} \tag{2.49}$$

The corresponding weak form is

$$\begin{aligned}
-\tilde{\nabla} \cdot \tilde{\sigma}' &= \quad in \quad \tilde{\Omega} \\
\tilde{\sigma}' \cdot \vec{n} &= \vec{\tilde{\tau}} \quad on \quad \partial_N\tilde{\Omega} \\
\tilde{\sigma}' \cdot \vec{n}_\Gamma &= -\lambda\, \vec{n}_\Gamma \quad in \quad \tilde{\Gamma}
\end{aligned} \tag{2.50}$$

On comparing the third part of Equation 2.50 with Equation 2.5, one notices that the lagrangian multiplier is really the fracturing fluid pressure. That is $\tilde{p} = \lambda$. If $\vec{\tilde{u}}_p$ is the solution to

$$\begin{aligned} -\tilde{\nabla}\cdot\tilde{\sigma}' &= 0 \quad in \quad \tilde{\Omega} \\ \tilde{\sigma}'\cdot\vec{n} &= 0 \quad on \quad \partial_N\tilde{\Omega} \\ \tilde{\sigma}'\cdot\vec{n}_\Gamma &= -\vec{n}_\Gamma \quad in \quad \tilde{\Gamma} \end{aligned} \tag{2.51}$$

and $\vec{\tilde{u}}_s$ is the solution to

$$\begin{aligned} -\tilde{\nabla}\cdot\tilde{\sigma}' &= 0 \quad in \quad \tilde{\Omega} \\ \tilde{\sigma}'\cdot\vec{n} &= \vec{\tilde{\tau}} \quad on \quad \partial_N\tilde{\Omega} \\ \tilde{\sigma}'\cdot\vec{n}_\Gamma &= 0 \quad in \quad \tilde{\Gamma} \end{aligned} \tag{2.52}$$

then by superposition, $\vec{\tilde{u}}_s + \tilde{p}\,\vec{\tilde{u}}_p$ is the solution to Equation 2.50. Therefore,

$$\vec{\tilde{u}} = \vec{\tilde{u}}_s + \tilde{p}\,\vec{\tilde{u}}_p \tag{2.53}$$

Upon substituting Equation 2.53 into Equation 2.47, one obtains

$$-\int_{\tilde{\Gamma}} [\![\vec{\tilde{u}}_s]\!]\cdot\vec{n}_\Gamma\, d\tilde{s} - \tilde{p}\int_{\tilde{\Gamma}} [\![\vec{\tilde{u}}_p]\!]\cdot\vec{n}_\Gamma\, d\tilde{s} = \tilde{V}_{inj} \tag{2.54}$$

Therefore, the fluid pressure is computed as

$$\tilde{p} = \frac{\tilde{V}_{inj} - \tilde{V}_{f_s}}{\tilde{V}_{f_p}} \tag{2.55}$$

where

$$\begin{aligned} \tilde{V}_{f_p} &= -\int_{\tilde{\Gamma}} [\![\vec{\tilde{u}}_p]\!]\cdot\vec{n}_\Gamma\, d\tilde{s} \\ \tilde{V}_{f_s} &= -\int_{\tilde{\Gamma}} [\![\vec{\tilde{u}}_s]\!]\cdot\vec{n}_\Gamma\, d\tilde{s} \end{aligned} \tag{2.56}$$

$\tilde{V}_{f_p}$ and $\tilde{V}_{f_s}$ are the fracture volumes created due to application of unit fluid pressure and in-situ stresses respectively. Using the phase field calculus

$$\begin{aligned} \tilde{V}_{f_p} &= \int_{\tilde{\Omega}} \vec{\tilde{u}}_p \cdot \tilde{\nabla} v \, d\tilde{V} \\ \tilde{V}_{f_s} &= \int_{\tilde{\Omega}} \vec{\tilde{u}}_s \cdot \tilde{\nabla} v \, d\tilde{V} \end{aligned} \tag{2.57}$$

An overview of the developed algorithm to simulate volume driven hydraulic fracture propagation is shown in Figure 2.13. The numerical solution algorithm requires alternating between solving for $\vec{\tilde{u}}$ and v fields respectively. The fluid pressure is updated and iteration is carried until concurrent convergence in U-V-P step is achieved. Convergence is measured using the two quantities defined in Equations 2.58 and 2.59.

$$\varepsilon_{\mathbf{v}} = \parallel v^{n,k+1} - v^{n,k} \parallel_{\infty} \tag{2.58}$$

$$\varepsilon_p = \left| \frac{\tilde{p}^{n,k+1} - \tilde{p}^{n,k}}{\tilde{p}^{n,k+1}} \right| \tag{2.59}$$

Scaling of the dimensionless fracture volume to reservoir scale is derived as follows

$$\begin{aligned} \int_{\Omega} \vec{u} \cdot \nabla v \, dV &= V_{inj} = Qt \\ u_o x_o^{N-1} \int_{\tilde{\Omega}} \vec{\tilde{u}} \cdot \tilde{\nabla} v \, d\tilde{V} &= V_o \tilde{V}_{inj} = Q_o \tilde{Q} t_o \tilde{t} \end{aligned} \tag{2.60}$$

Therefore

$$\int_{\tilde{\Omega}} \vec{\tilde{u}} \cdot \tilde{\nabla} v \, d\tilde{V} = \frac{V_o}{u_o x_o^{N-1}} \tilde{V}_{inj} = \frac{Q_o t_o}{u_o x_o^{N-1}} \tilde{Q} \tilde{t} \tag{2.61}$$

By setting the coefficients to 1, one obtains

$$V_o = u_o x_o^{N-1} = Q_o t_o \tag{2.62}$$

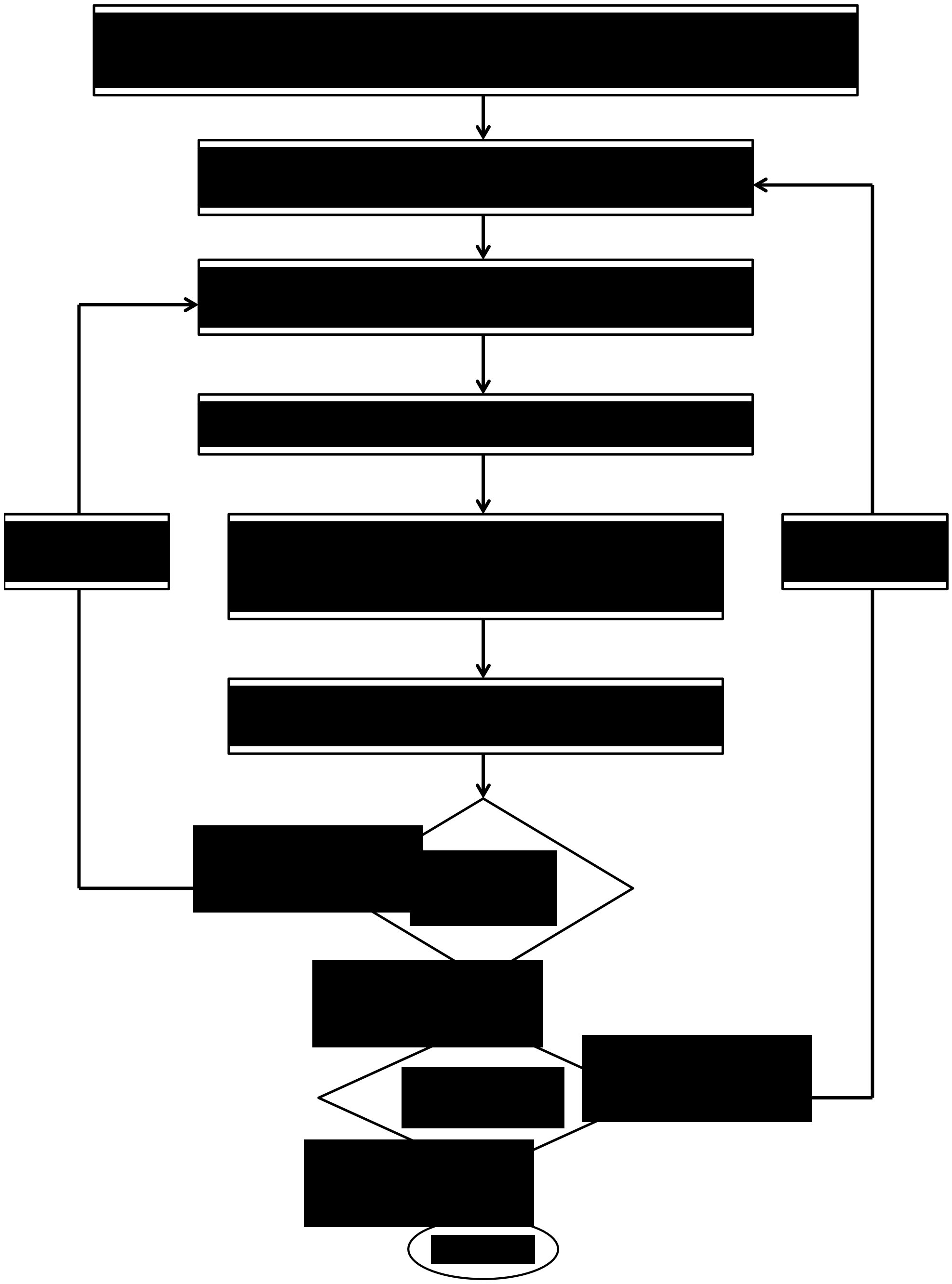

Figure 2.13: Numerical algorithm for hydraulic fracturing in impermeable rock

Line Fracture Propagation

This case extends the static fracture formulation of Sneddon and Lowengrub (1969) to account for quasi-static crack evolution under an injected fluid volume with no fluid loss to the elastic material. This problem is formulated following Griffith's criterion of stable crack propagation at critical energy release rate. The critical fracture volume at the onset of propagation is obtained by coupling the critical pressure, Equation 2.43, with the analytical solution for crack opening displacement, Equation 2.33, to obtain

$$V_{f_c} = \sqrt{\frac{4\pi l_o^3 G_c}{E'}} \tag{2.63}$$

Using Equation 2.63, the propagation criterion is expressed in terms of injected fluid volume. According to the volume criterion, the hydraulic fracture remains in its initial static condition if the injected fluid volume is less than the critical value but propagates in a stable manner when the injected fluid volume exceeds the critical value, i.e.

$$\text{criteria} = \begin{cases} \text{if} \quad V_{inj} < V_{f_c}: & \text{no propagation} \\ \text{if} \quad V_{inj} \geq V_{f_c}: & \text{stable propagation} \end{cases} \tag{2.64}$$

The fracture length and injected fluid pressure as a function of the injected fluid volume are therefore

$$\begin{aligned} p(V_{inj} < V_{f_c}) &= \frac{E' V_{inj}}{2\pi l_o^2} + \sigma_{min}; \qquad l(V_{inj} < V_{f_c}) = l_o \\ p(V_{inj} \geq V_{f_c}) &= \sqrt[3]{\frac{2G_c^2 E'}{\pi V_{inj}}} + \sigma_{min}; \quad l(V_{inj} \geq V_{f_c}) = \sqrt[3]{\frac{E' V_{inj}^2}{4 G_c \pi}} \end{aligned} \tag{2.65}$$

One observes from Equation 2.65 that prior to fracture propagation, fluid pressure increases linearly with injected volume at constant fracture length. On the other hand, fluid pressure decreases as fracture propagates. The derivation of Equations 2.63 and 2.65 can be found in Appendix C.

Numerical solution of this problem to compute fluid pressure and fracture length as functions of injected fluid volume makes use of the algorithm in Figure 2.13. An initial fracture of length $l_o = 12.5$ m is contained in a computational domain of size of $\Omega = 100$ m × 100 m. The reservoir properties, simulation inputs and dimensional scaling parameters are shown in Table 2.3. Fluid is injected at a constant rate into the fracture. Figure 2.14 compares the fracture fluid pressure obtained from the variational hydraulic fracture model at $h = \varepsilon$ with the analytical solution (Equation 2.65). It is observed that fluid pressure increases linearly prior to the fracture propagation at critical pressure and volume values of 0.52 MPa and 9.3×10^{-4} m^2 respectively, beyond which the pressure decreases as more fluid is injected to propagate the fracture. The numerical solution compares favorably with the analytical results, with some differences observed around the fracture propagation region. As the computational resolution increases, the differences between numerical and analytical results reduces. In fact, from the plots for different resolutions, one can infer that the numerical results will match the analytical model as $h \to 0$. The numerical results are the same as the analytical solution of Savitski and Detournay (2002) for the case of no fluid leak-off in the toughness dominated hydraulic fracturing regime.

As the fracture propagates, its length increases to give a positive change in fracture length as shown in Figure 2.15. Prior to fracture propagation however, the fracture is static and experiences no change in length. For both pre- and post-fracture propagation, a good match is obtained between the numerical simulation and analytical solution. The slight deviation of numerical results from the analytical formula observed in both Figures 2.14 and 2.15 at high injection volumes during the fracture propagation is attributed to the fact that the analytical solution is derived for an infinite domain while the variational hydraulic fracture solution was carried out on a finite computation domain. Thus, as the fracture increases in length, the numerical result becomes increasingly affected by the boundary conditions used.

Table 2.3: Reservoir parameters and numerical inputs for simulation of line fracture propagation. Column D is the dimensionless inputs to the numerical model while column o is the scaling for converting dimensionless parameters to physical values

Parameter	D	o	Physical
x	8	12.5 m	100 m
u	-	2.5×10^{-4} m	-
p	-	0.4 MPa	-
V_o	-	3.125×10^{-3} m^2	-
Δt	1	1 s	1 s
Q	0.02	3.125×10^{-3} m^2/s	6.25×10^{-5} m^2/s
E	1	20 GPa	20 GPa
G_c	1	1×10^{-7} GPa m	100 Pa m
ν	0	1	0
α	0	1	0
l_o	0.2	12.5 m	2.5 m

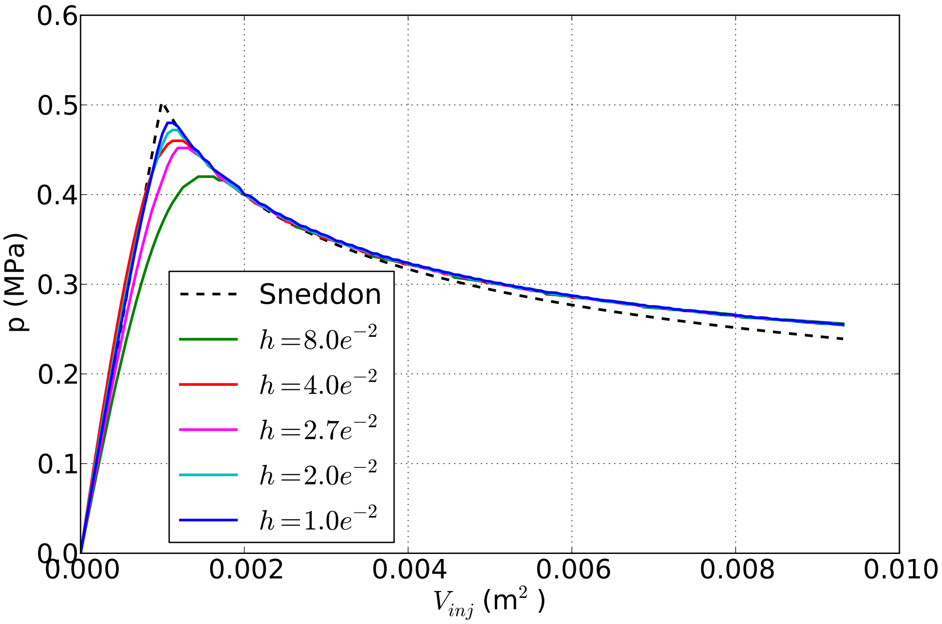

Figure 2.14: Line fracture fluid pressure as a function of injected volume for h/ϵ = 1.0

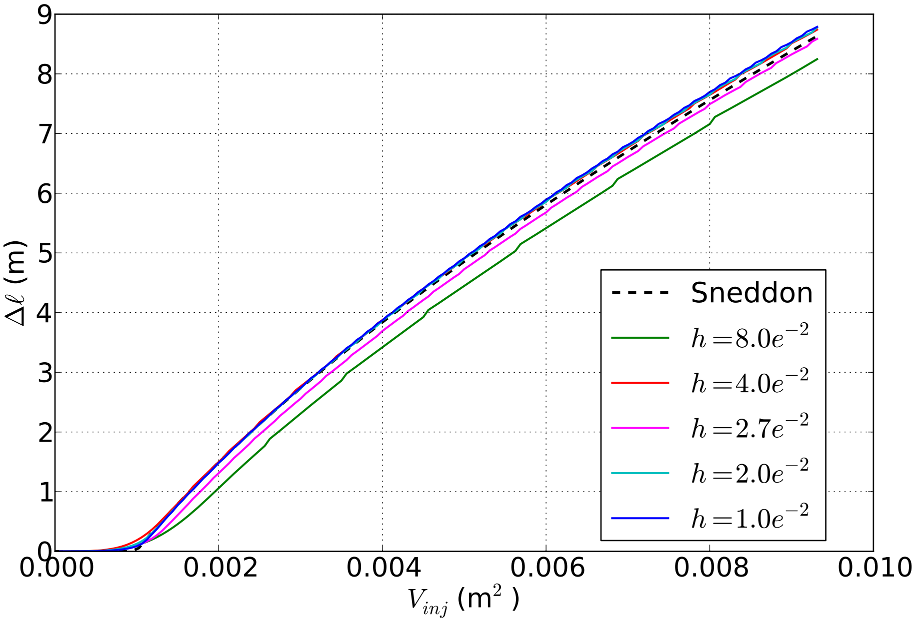

Figure 2.15: Change in line fracture length as a function of injected volume for computations at $\epsilon = h$

Grid Orientation Impact

To simplify the complexities associated with unknown propagation paths of hydraulic fractures, several authors have assumed a known propagation path that is limited to a coordinate direction of the computational grid (Carrier and Granet 2012; Boone and Ingraffea 1990) while some others have used massive mesh refinement and/or adaptation implemented after each time step to track the known path of the hydraulic fractures (Gupta and Duarte 2015). All of these are done at large computational expense.

One attraction of the variational fracture method is the use of a fixed mesh throughout the computations, irrespective of the number of fractures, their orientation with respect to the mesh grids and their propagation paths. This is possible since the continuous v-field is defined on the fixed mesh and evolves on it as fracture deforms and propagates. In this subsection, it is shown that using a fixed mesh, the hydraulic fracturing numerical results and propagation paths are the same irrespective of fracture orientation with respect to the computational grid. The two dimensional hydraulic fracturing experiment is repeated

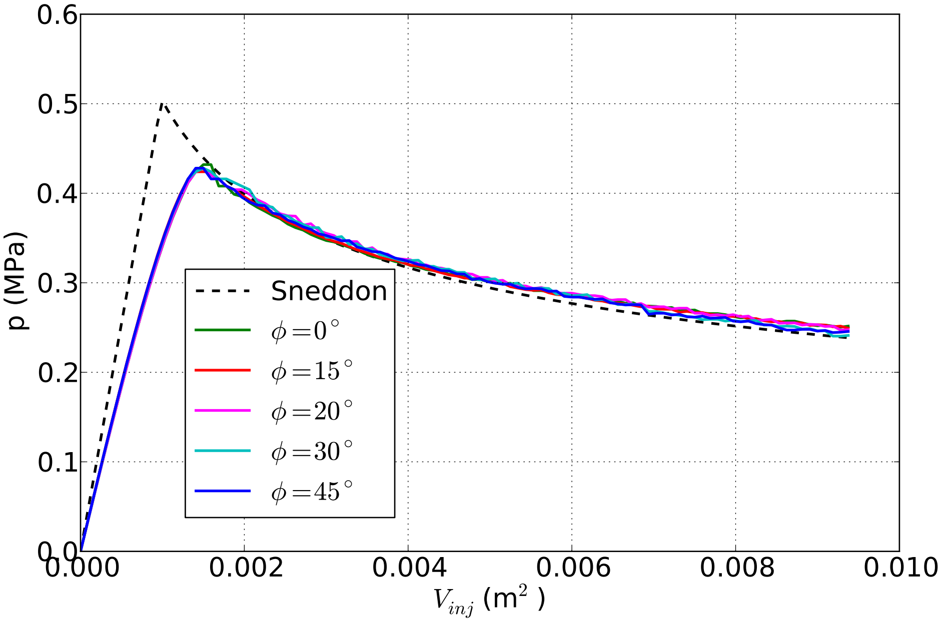

Figure 2.16: Fracturing fluid pressure as a function of injected fluid volume for line fracture at different orientations. Computations for $h = 0.01$ and $\varepsilon = 4\,h$

using the same material properties but with pre-existing fractures inclined at $\phi = 0°$, 15°, 20°, 30° and 45° with respect to the x-direction of the grid. However, $h = 0.01$ and $\varepsilon = 4h$. Figures 2.16 and 2.17 show results for fluid pressure and fracture length change. The numerical results are very similar for all fracture orientations and compare fairly well with the analytical solution. Figure 2.18 shows snapshots of some of the fractures before and after propagation. For all the orientations considered, propagation continued along initial fracture paths. This results show that the variational model is independent of the grid orientation used for hydraulic fracture computations.

Penny-Shaped Fracture Propagation

Similar to the line crack propagation example, this section considers the propagation of a penny-shaped fracture in a three dimensional, impermeable and elastic domain as studied in Sneddon and Lowengrub (1969). The analytical solution for the propagation of a penny-shaped fracture have also been derived in Appendix C. The critical fluid pressure and fluid volume for fracture propagation are

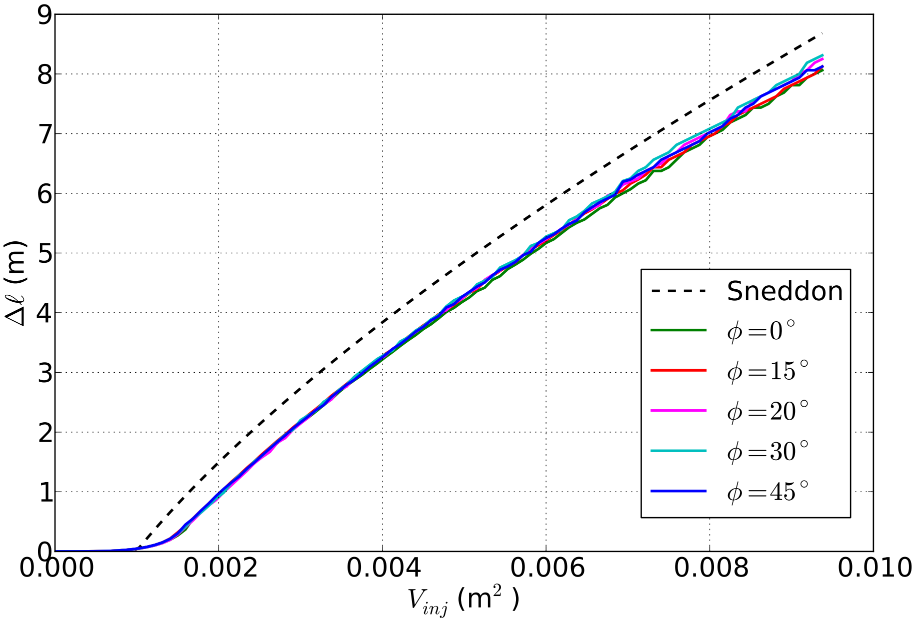

Figure 2.17: Change in fracture length as a function of injected fluid volume for line fracture at different orientations. Computations for $h = 0.01$ and $\varepsilon = 4\,h$

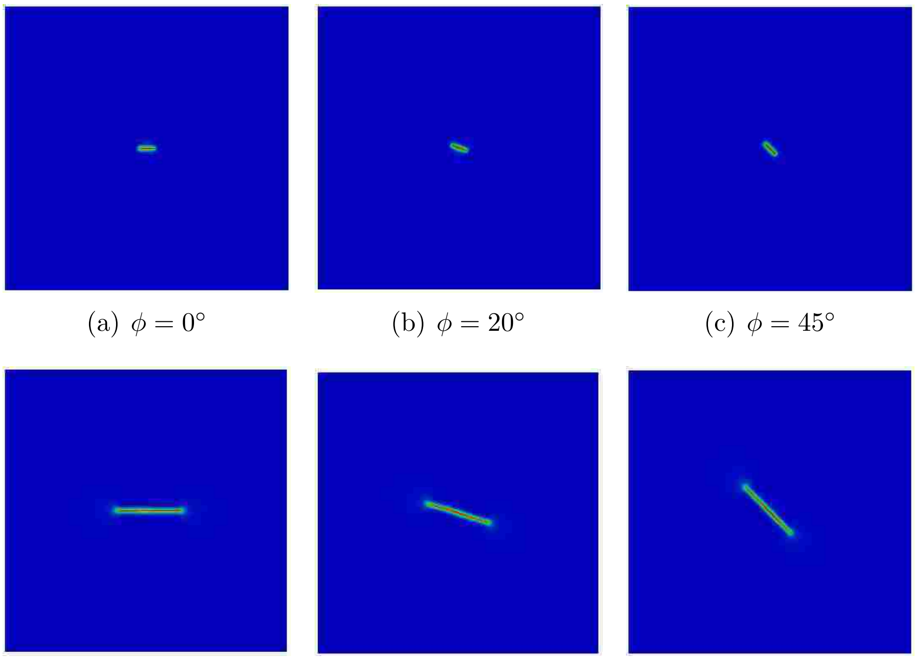

(a) $\phi = 0^\circ$ (b) $\phi = 20^\circ$ (c) $\phi = 45^\circ$

(d) $\phi = 0^\circ$ (e) $\phi = 20^\circ$ (f) $\phi = 45^\circ$

Figure 2.18: Propagation of line fracture at 0°, 20° and 45° with respect to x-axis of the fixed computational grid in a two dimensional domain elastic domain $(h = 0.01, \varepsilon = 4\,h)$

$$\Delta p_c = p_c - \sigma_{min} = \sqrt{\frac{\pi G_c E'}{4R_o}} \tag{2.66}$$

$$V_{f_c} = \frac{8}{3}\sqrt{\frac{\pi R_o^5 G_c}{E'}} \tag{2.67}$$

The propagation criteria in terms of injected volume is the same as Equation 2.64, so that the corresponding pressure (p) and fracture radius (R) relationships in terms of injected fluid volume are

$$\begin{aligned} p(V_{inj} < V_{f_c}) &= \frac{3E'V_{inj}}{16R_o^3} + \sigma_{min}; \qquad R(V_{inj} < V_{f_c}) = R_o \\ p(V_{inj} \geq V_{f_c}) &= \sqrt[5]{\frac{\pi^3 G_c^3 E'^2}{12V_{inj}}} + \sigma_{min}; \quad R(V_{inj} \geq V_{f_c}) = \sqrt[5]{\frac{9E'V_{inj}^2}{64\pi G_c}} \end{aligned} \tag{2.68}$$

The three dimensional reservoir domain is $\Omega = 100$ m × 100 m × 100 m, with a pre-existing penny-shaped fracture of initial radius, $R_o = 10$ m. The reservoir properties and numerical simulation inputs are contained in Table. 2.4. Numerical and analytical results of fracture fluid pressure at different injected fluid volumes are shown in Figure 2.19 while the change in penny-shaped fracture radius as a function of fluid volume is shown in Figure 2.20. Like in the two dimensional examples, fluid pressure increases linearly prior to the critical injected fluid volume. Within this regime, the fracture radius does not change since the fracture does not grow. At the critical injected volume of about 0.11 m^3, the fluid assumes the critical pressure of 0.4 MPa, beyond which fluid pressure decreases and fracture radius increases as more fluid is injected into the fracture during propagation. Figure 2.21a shows the fracture prior to fluid injection while Figure 2.21b is the fracture profile at the end of the simulation.

Fracture Propagation Under In-Situ Stresses

It is commonly accepted that hydraulic fractures propagate in the direction orthogonal to minimum in-situ stress in the subsurface. Considering their importance in determining hydraulic fracture propagation paths, the ability to handle these in-situ stresses is a necessary requirement for robust hydraulic fracturing models. The variational fracture model easily

Table 2.4: Reservoir parameters and numerical inputs for simulation of penny-shaped fracture propagation. Column D is the dimensionless inputs to the numerical model while column o is the scaling for converting dimensionless parameters to physical values

Parameter	D	o	Physical
x	2	50 m	100 m
u	-	5×10^{-4} m	-
p	-	0.2 MPa	-
V_o	-	1.25 m^3	-
Δt	1	1 s	1 s
Q	0.002	1.25 m^3/s	0.0025 m^3/s
E	1	20 GPa	20 GPa
G_c	1	1×10^{-7} GPa m	100 Pa m
ν	0	1	0
α	0	1	0
R_o	0.2	50 m	10 m

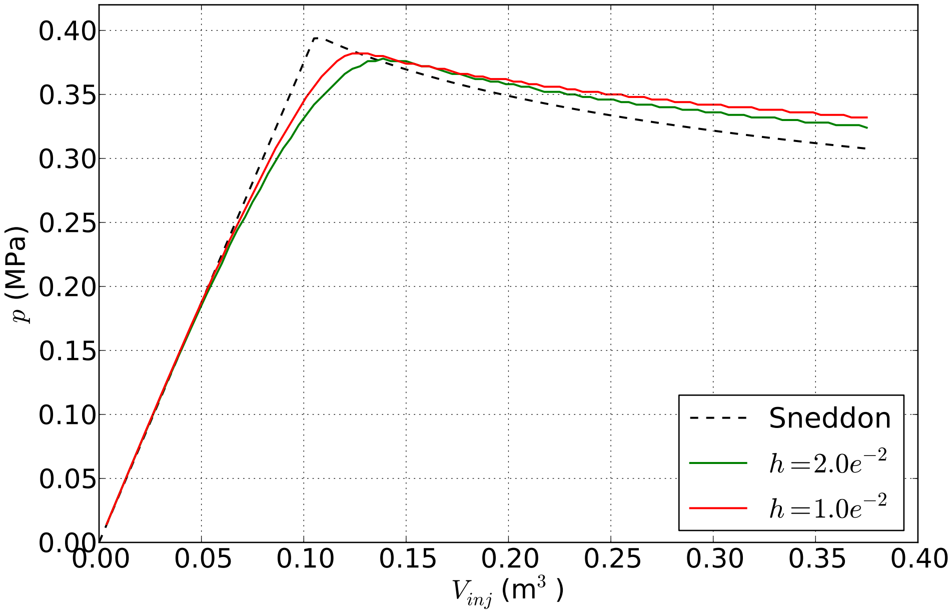

Figure 2.19: Penny-shaped fracturing fluid pressure as a function of injected volume for numerical computation at $\varepsilon = h$

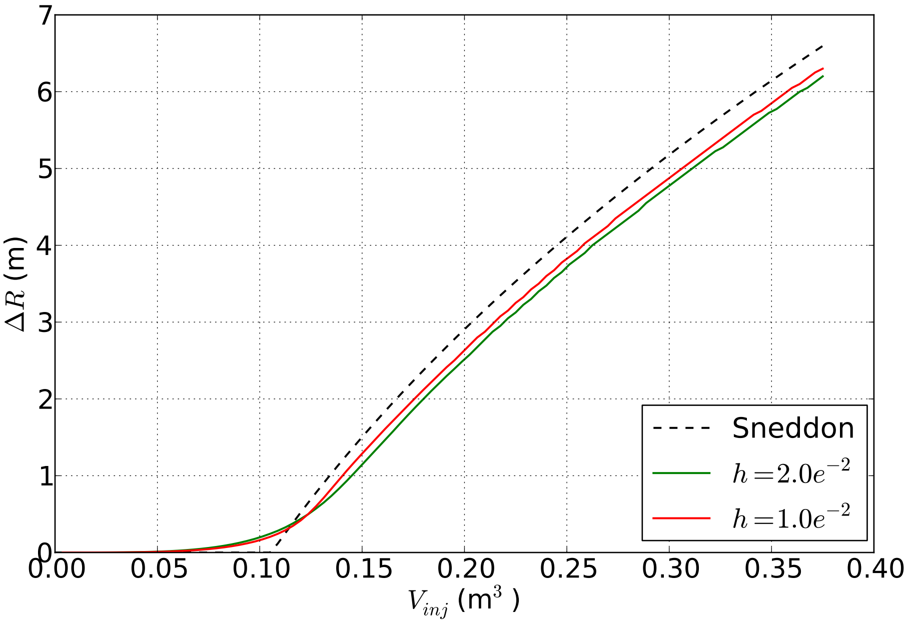

Figure 2.20: Change in penny-shaped fracture radius as a function of injected fluid volume for numerical computation at $\varepsilon = h$

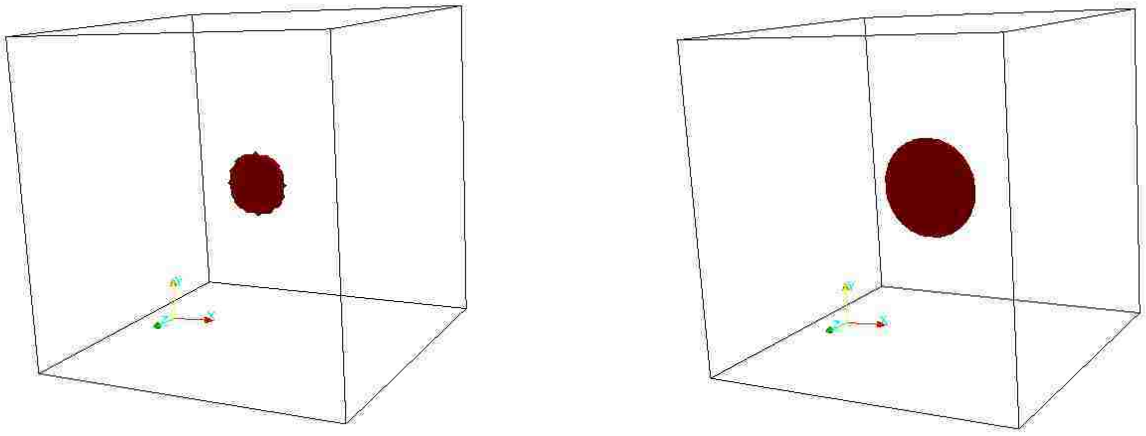

(a) Initial fracture geometry before fluid injection

(b) Final fracture geometry after injection of 0.3 m^3 of fluid

Figure 2.21: Snap shots of penny shaped fracture before and after fluid injection. Contour plot is at $v = 0.1$

accounts for these stresses as either tractions or specified displacements on boundaries of the computational domain. To investigate their effect on fracture propagation and to validate the numerical results against the analytical solution and the widely held orthogonal-to-minimum stress propagation direction, the previous volume driven fracture propagation is repeated but with in-situ stresses implemented as traction forces on all or some of the computation boundaries. The analytical solution (Equations 2.65 and 2.68) shows that fluid pressure at all injected fluid volumes in the presence of in-situ stresses is increased by an amount equal to the minimum in-situ stress compared to the fluid pressure for propagation without in-situ stresses. The numerical simulation uses isotropic in-situ stresses so that $\sigma_{zz} = \sigma_{xx} = -0.12$ MPa for the two dimensional computation and $\sigma_{zz} = \sigma_{yy} = \sigma_{xx} = -0.06$ MPa for the three dimensional computation. This means that $\sigma_{min} = \sigma_{max}$. The two dimensional computation is in plane strain where the y-coordinate is out-of plane while the x- and z-coordinates are the vertical and horizontal axes of the computational domain. Using the material properties in the previous computations without in-situ stresses, the numerically obtained fluid pressure compared with the analytical solution for the two and three dimensional computations are shown in Figures 2.22 and 2.23. As predicted by the analytical solution, the numerical fluid pressure is increased by the minimum in-situ stress and compares well with the analytical solution for both the two and three dimensional computations. The value of the intercept of the pressure plot with fluid volume axis is the minimum in-situ stress and this means that the fracture fluid pressure has to overcome the in-situ stress in the material before fracture faces can open.

To verify that fractures propagate orthogonal to the minimum stress directions, numerical computations were carried out in both two and three dimensions with inclined pre-existing fractures in the presence of different combinations of in-situ stresses. Figure 2.24 shows the two dimensional results while the three dimensional results are shown in Figure 2.25. The two dimensional computation has fracture defined at 30° and 45° to the x-axis and both subjected to four different in-situ stress combinations given as $\sigma_{xx} = -0.12$ MPa, $\sigma_{zz} = -0.12$ MPa, $\sigma_{xx} = -0.12$ MPa & $\sigma_{zz} = -0.06$ MPa and $\sigma_{xx} = -0.06$ MPa & $\sigma_{zz} = -0.12$ MPa re-

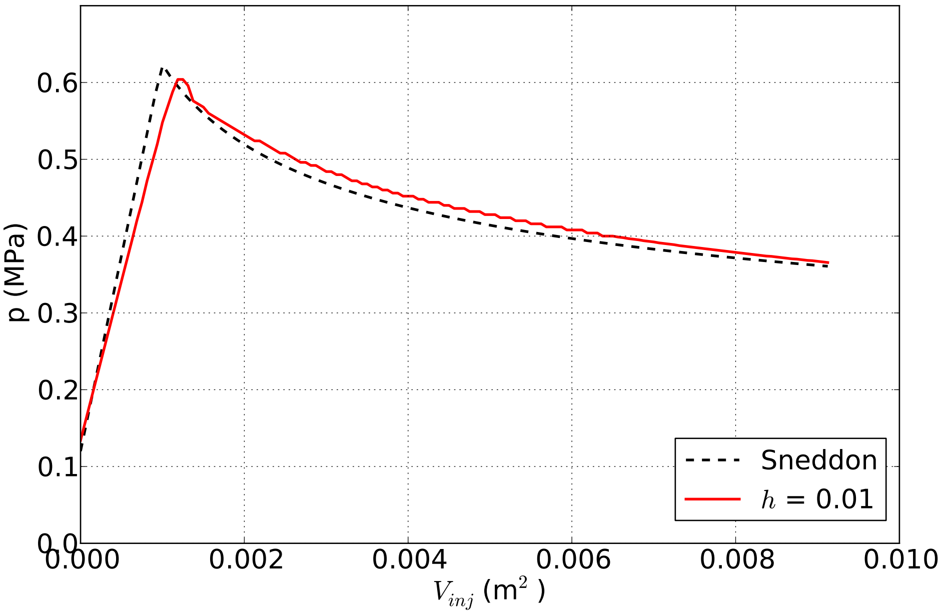

Figure 2.22: Two dimensional numerical result of fracture fluid pressure as a function of injected fluid volume for fracture propagation in the presence of $\sigma_{zz} = \sigma_{xx} = -0.12$ MPa in-situ stresses

spectively. Compared to the straight line propagation paths for the fractures under no in-situ stresses shown in Figure 2.18, it is observed in Figure 2.24 that different fracture configurations are obtained for each in-situ stress combination. In all the computations, however, fractures re-orient to propagate along complex paths perpendicular to the minimum in-situ stress directions.

For the three dimensional computations, only one initial penny-shaped fracture configuration at $\phi = 30°$ and $\theta = 0°$ is considered with in-situ stress combinations of $\sigma_{zz} = -0.06$ MPa, $\sigma_{xx} = -0.06$ MPa & $\sigma_{yy} = -0.06$ MPa, $\sigma_{yy} = -0.06$ MPa & $\sigma_{zz} = -0.06$ MPa, $\sigma_{xx} = -0.03$ MPa & $\sigma_{yy} = -0.06$ MPa & $\sigma_{zz} = -0.06$ MPa and $\sigma_{xx} = -0.04$ MPa & $\sigma_{yy} = -0.03$ MPa & $\sigma_{zz} = -0.06$ MPa respectively. Similar results as in the two dimensional computations are obtained as the fractures re-orient during propagation to lie in directions orthogonal to the minimum in-situ stress directions.

Although the fractures generally re-orient to propagate normal to the minimum in-situ stress direction, stress anisotropy has a huge effect on how sharply the fracture turns

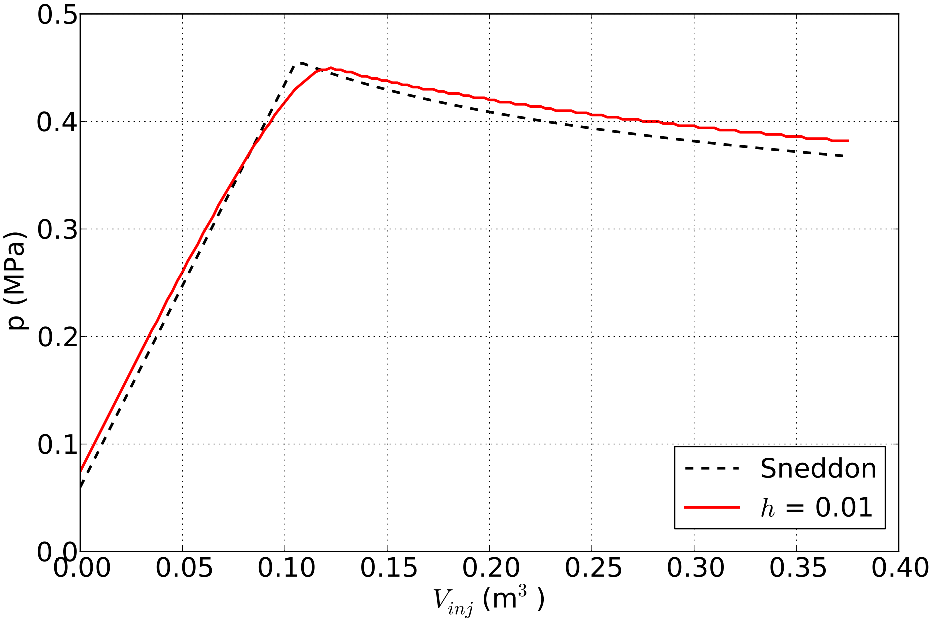

Figure 2.23: Three dimensional numerical result of fracture fluid pressure as a function of injected fluid volume for fracture propagation in the presence of $\sigma_{zz} = \sigma_{yy} = \sigma_{xx} = -0.06$ MPa in-situ stresses

during re-orientation. One can observe that larger stress anisotropy creates sharp fracture turns compared to those from lower stress anisotropies. This is obvious if one compares the propagation paths for Figures 2.24b with Figure 2.24d, Figure 2.24f with Figure 2.24h and Figure 2.25b with Figure 2.25c.

The possible combinations of in-situ stress values to obtain complex fracture propagation paths is exhaustive. Only a few to have been chosen to illustrate the ability of the variational fracture model to handle in-situ stresses and to reproduce complex propagation paths without the need for remeshing and/or the use of complex grids to track the path of the propagating fractures.

2.4.4 Multiple Hydraulic Fracture Propagation in Two and Three Dimensions

One of the most important features of the variational fracture model is its ability to handle multiple fractures without additional computational or modeling effort than required for single fractures. Once the existence of multiple fractures is defined by the phase field, their propagation and interaction is inherently defined by numerical solution of the alternate

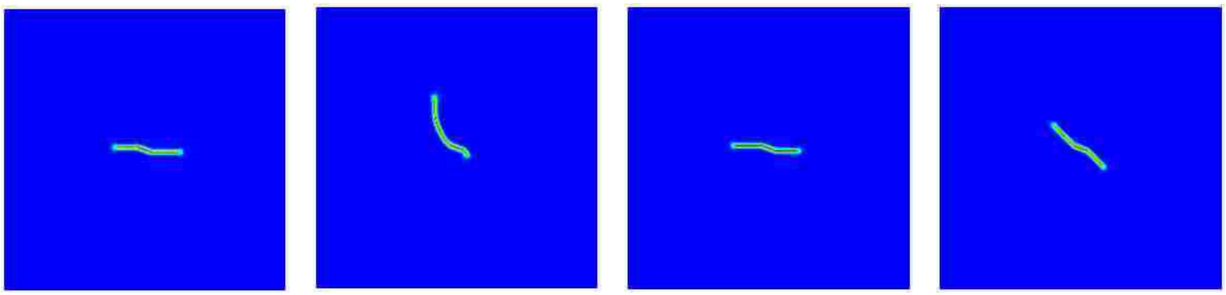

(a) $\phi = 20°$, $\sigma_{xx} = -0.12$ MPa

(b) $\phi = 20°$, $\sigma_{zz} = -0.12$ MPa

(c) $\phi = 20°$, $\sigma_{xx} = -0.12$ MPa, $\sigma_{zz} = -0.06$ MPa

(d) $\phi = 20°$, $\sigma_{xx} = -0.06$ MPa, $\sigma_{zz} = -0.12$ MPa

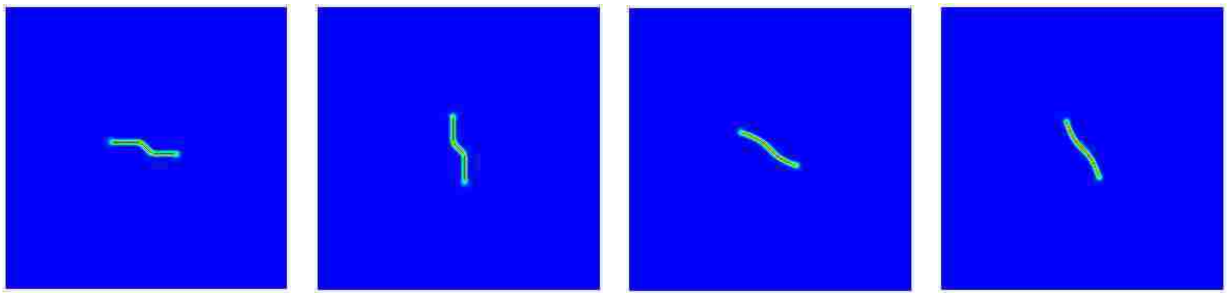

(e) $\phi = 45°$, $\sigma_{xx} = -0.12$ MPa

(f) $\phi = 45°$, $\sigma_{zz} = -0.12$ MPa

(g) $\phi = 45°$, $\sigma_{xx} = -0.12$ MPa, $\sigma_{zz} = -0.06$ MPa

(h) $\phi = 45°$, $\sigma_{xx} = -0.06$ MPa, $\sigma_{zz} = -0.12$ MPa

Figure 2.24: Propagation paths for inclined line fractures under prescribed injected fluid volume in a two dimensional elastic medium subject to in-situ stresses

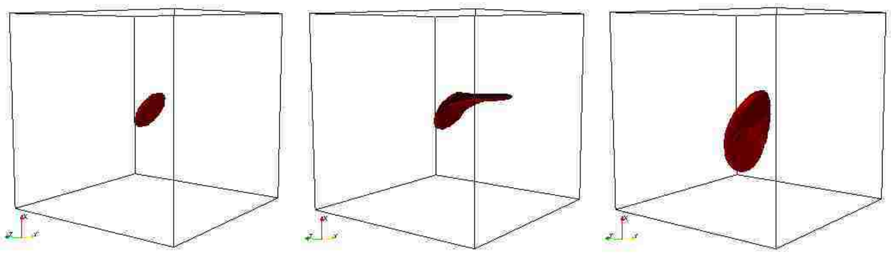

(a) Pre-existing penny-shaped fracture at $\phi = 30°$, $\theta = 0°$

(b) $\sigma_{zz} = -0.06$ MPa

(c) $\sigma_{xx} = -0.06$ MPa, $\sigma_{yy} = -0.06$ MPa

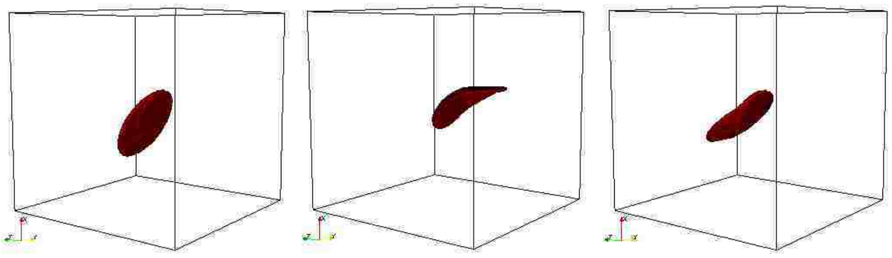

(d) $\sigma_{yy} = -0.06$ MPa, $\sigma_{zz} = -0.06$ MPa

(e) $\sigma_{xx} = -0.03$ MPa, $\sigma_{yy} = -0.06$ MPa, $\sigma_{zz} = -0.06$ MPa

(f) $\sigma_{xx} = -0.04$ MPa, $\sigma_{yy} = -0.03$ MPa, $\sigma_{zz} = -0.06$ MPa

Figure 2.25: Propagation paths for volume driven penny-shaped fracture inclined at $\phi = 30°$ and $\theta = 0°$ in a three dimensional elastic medium subject to in-situ stresses

minimization scheme. This capability is highlighted by considering the propagation of two fractures in two dimensional ($\tilde{\Omega} = 8 \times 8$) and three dimensional ($\tilde{\Omega} = 2 \times 2 \times 2$) domains. The fractures are inclined at an angle to each other and are close enough for interaction to occur. Both fractures experience to the same uniform pressure determined by the balance between their cumulative fracture volume and total injected fluid volume. Fracture evolution and interaction is depicted in Figure 2.26 for the two dimensional problem and Figure 2.27 for the three dimensional case. For both two and three dimensional computations, propagation initiated in the larger fractures since according to the analytical solution, the critical pressure for propagation is inversely proportional to fracture length. As more fluid is injected, the larger fracture propagates towards the smaller one and connects to it along a curved path to create one big fracture. Further fluid injection leads to propagation of both tips of the single large fractures.

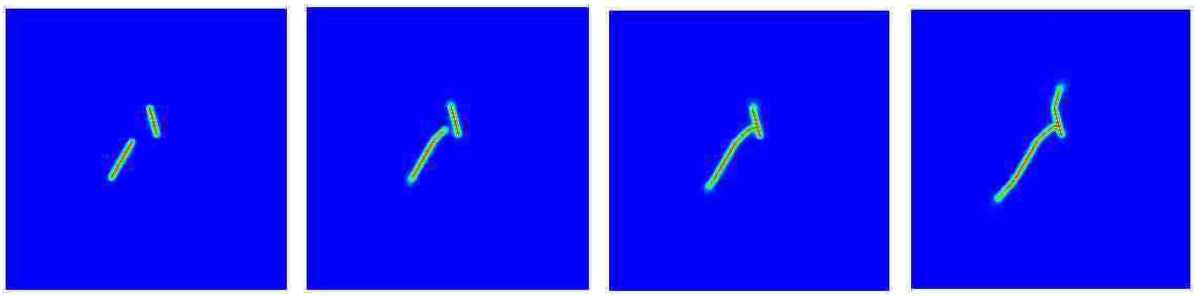

Figure 2.26: Multiple hydraulic fracture geometry and propagation in two dimensions

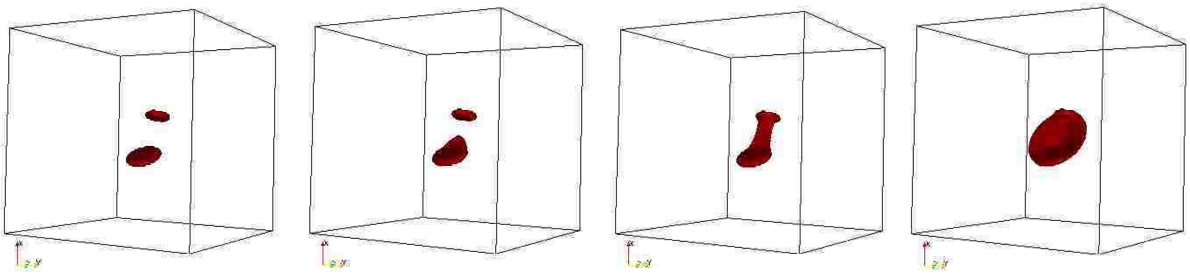

Figure 2.27: Multiple hydraulic fracture geometry and propagation in 3D

2.4.5 Joint Sets in Multi-Layered Rocks

This section compares the patterns of natural fractures generated using the variational fracture model against those reported in literature and outcrop patterns observed in nature. To achieve this, the propagation of fractures in a two-dimensional layered domain is simulated. Similar numerical experiments have been carried out and can be found in Chukwudozie et al. (2013), Guo, Xiang, and Lei (2013), Ladeira and Price (1981), Hobbs (1967), Gross, Fischer, and Engelder (1995).

Natural fractures are an important component of fractured reservoirs and have significant impacts on reservoir fluid flow characteristics and overall geomechanical properties of the formation. It is therefore important to incorporate the effect of natural fractures at the outset of field developments as ignoring their influence may have significant consequences in field production planning. Understanding the characteristics of natural fractures is a first step towards incorporating fractures into a field development design. It is widely understood that natural fracture characteristics are dependent on the mechanical stratigraphy of the sedimentary layers that make up the rock i.e. on the combination of different mechanical

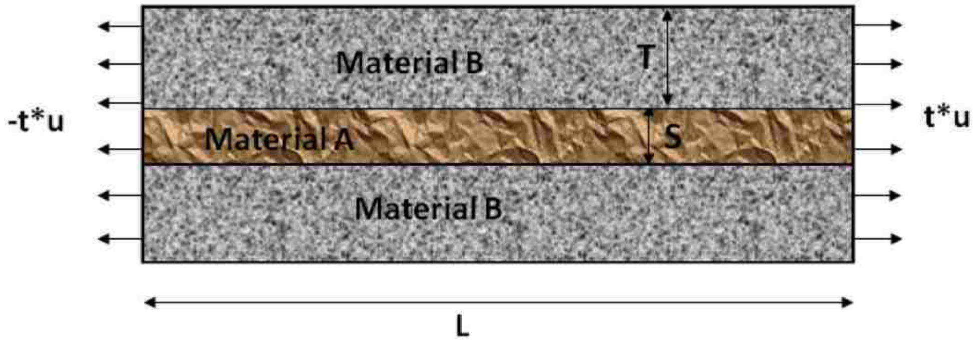

Figure 2.28: Geometry of domain for natural fracture simulation

properties and thickness of the layers that make up the formation (Underwood et al. 2003; Ladeira and Price 1981; Huang and Angelier 1989; Becker and Gross 1996). Thus, the interesting these numerical test are the fracture patterns generated for a set of mechanical properties in a layered system subjected to tensile loading.

The computational domain for simulating the fracturing process is shown in Figure 2.28. It is a 3-layer rectangular domain with a middle brittle layer bounded by two elastic layers. The length of domain is L while the thickness of the middle layer and the two bounding layers are S and T respectively. Quasi-static loading is achieved by keeping the top and bottom stress free while the sides are pulled with a monotonically increasing displacement given by

$$\begin{aligned} \vec{u}\,(0,t) &= -t\,u \\ \vec{u}\,(L,t) &= t\,u \end{aligned} \tag{2.69}$$

t is an increasing parameter taking on values from $1, 2, 3 \ldots$. The simulation was carried out with the material properties shown in Table 2.5 and with $\varepsilon = h$ and $h = 0.01$. Simulation results showing fracture patterns during the deformation process are shown in Figures 2.29. The important features observed during and after the propagation of the fractures are summarized below.

1. Sequential infilling of fractures: Fractures fill up the brittle layer in a sequential manner

Table 2.5: Material properties for natural fracture simulation

Parameter	Value
E	$40.0, 40.0, 40.0$
ν	0.25,0.01,0.25
G_c	4.0,0.2,4.0
L,S	5.0,0.9

as documented in Hobbs (1967), Gross (1995) and Tang (2008). Average fracture spacing decreases with increasing strain as new fractures nucleate to infill spaces between pre-existing fractures.

2. Stress build-up between fractures: Upon the formation of a set of two fractures, stress builds-up between the existing fracture sets. For the variational fracture simulation results in Figures 2.29, this is represented by regions with large transition values for the v-field as in Figures 2.29a and 2.29b. From this region of increased stress, new fractures are formed and the stress is subsequently released. This phenomena is related to the stress shadow behavior that is well documented in literature.

3. Parallel fractures, perpendicular to layers: As noted in Underwood (2003), Ruf (1998), Wennberg (2012), Bai (2002), Tang (2008) and Gross (1995) for homogeneous distribution of material properties, the simulated fractures form in parallel sets that are perpendicular to the mechanical layers.

4. Layer debonding: Layer delamination is observed as the vertical fractures are formed. This affects fracture spacing as additional vertical fracture formation is inhibited (Tang 2008) since energy is expended in propagating the fractures along the interface, rather than in forming new fractures.

An example of joint patterns observed in an outcrop rock in nature is shown in Figure 2.30. In the image, one can clearly identify some of the features obtained from the numerical simulation. These include parallel joint sets that are perpendicular to the rock layers

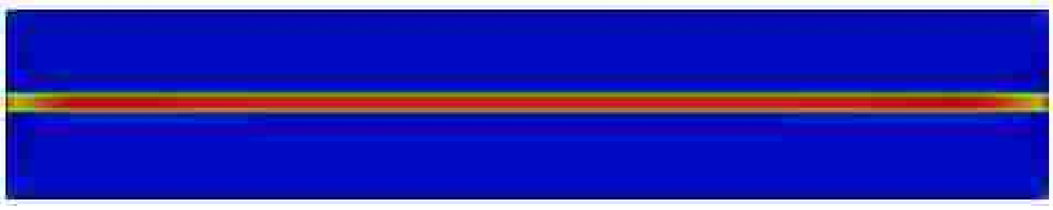

(a) High stress region in brittle layer prior to fracture formation

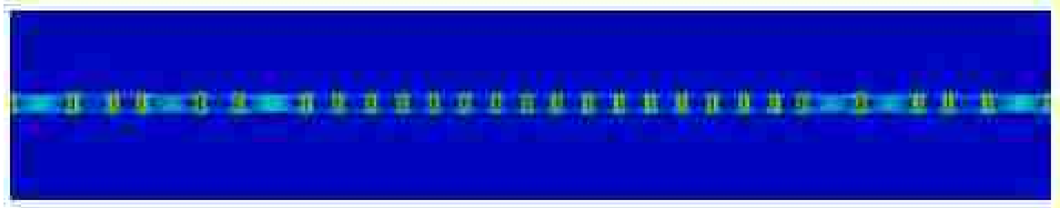

(b) High stress region between fracture set

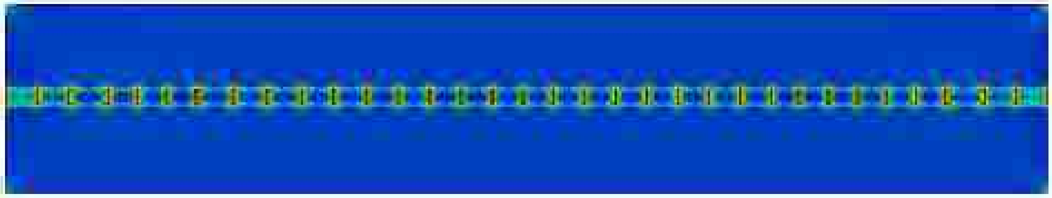

(c) Parallel fracture sets at fracture saturation

Figure 2.29: Joint sets simulated using variational fracture model

and terminating at the layer interfaces. Traverse fractures that debond and separate the horizontal layers are also observed.

Figure 2.30: Example of joint sets observed in nature

Chapter 3

Coupled Model for Fracture Fluid Flow and Deformation

3.1 Introduction

Earlier, it was explained that hydraulic fracturing simulation requires coupling between a mechanical model and a flow model. The relationship between both models is summarized in Figure 3.1. In this work, the variational fracture model is used as the mechanical model and it was introduced and verified in Chapter 2. The fluid flow component of the hydraulic fracturing model highlighted by the red box in Figure 3.1 is introduced in this chapter. This component solves for flow in both reservoir and fracture unlike some other hydraulic fracturing simulations which only model fracture fluid flow and use Carter's model to account for fluid loss to the surrounding medium. Single phase, Newtonian flow is assumed in both the fracture and the reservoir. Coupling of the models for flow in the fracture and reservoir is achieved through hydraulic communication between both subdomains to provide a single integral equation for fluid flow in the whole domain. With the fully coupled single flow model, interaction between solid deformation and fluid flow in the adjoining region caused by fluid loss is more realistically modeled while the mutual effect of poroelasticity on hydraulic fracture propagation is captured.

The governing equations are introduced and no attempt is made to derive them since they are well established. Rather, the flow models will be analyzed in the context of the phase field since the individual equations apply to different subdomains which are distinguished using the v-field presented in Chapter 2. Finite element analysis of the individual flow equations and the coupling strategy will be discussed in detail and verified against classical consolidation examples. Thereafter, coupling between flow and mechanical components of the hydraulic fracturing model will be introduced and example cases presented.

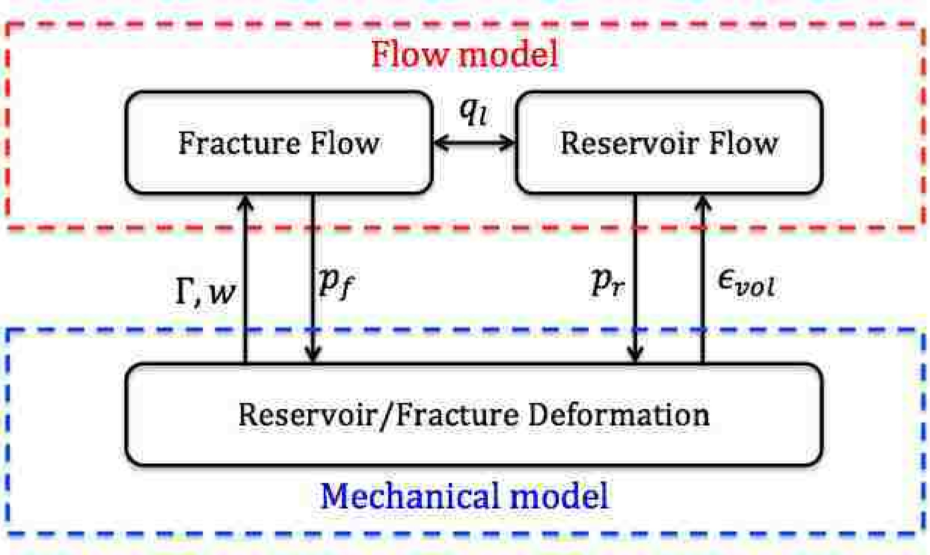

Figure 3.1: Geometry of important components used for fracture width computation

A poroelastic domain as shown in Figure 3.2a consists of two non overlapping subdomains, $\Omega \setminus \Gamma$ and Γ represented by Figures 3.2b and 3.2c respectively. Ω is the poroelastic medium while $\Omega \setminus \Gamma$ and Γ are the reservoir and fracture subdomians with same geometric properties as described in Sec. 2.2 for Figure 2.1 in Chapter 2. It is important to point out that the fracture is only an internal boundary of the poroelastic domain. This implies that $\partial\Omega = \Gamma \cup \partial_D\Omega \cup \partial_N\Omega$. On the other hand, it is also assume that the fracture does not reach the external boundaries. Therefore, $\Gamma \cap (\partial_D\Omega \cup \partial_N\Omega) = \emptyset$. The governing equations for coupled flow in $\Omega \setminus \Gamma$ and Γ are different and are described in the following sections.

3.2 Reservoir Flow Model: Single Phase Flow

The framework for incorporating interaction between deformation and fluid flow was first introduced by Biot (1941) and has seen increasing application in petroleum reservoir fluid production (Zheng, Burridge, and Burns 2003; Lewis 1998). According to the model, coupling is introduced through Biot's effective stress concept in the momentum conservation equation and through volumetric strain contribution to flow in the conservation of fluid mass. This coupled framework is applied to the variational hydraulic fracturing model through the effective stress in the elastic energy term in the variational fracture energy functional of

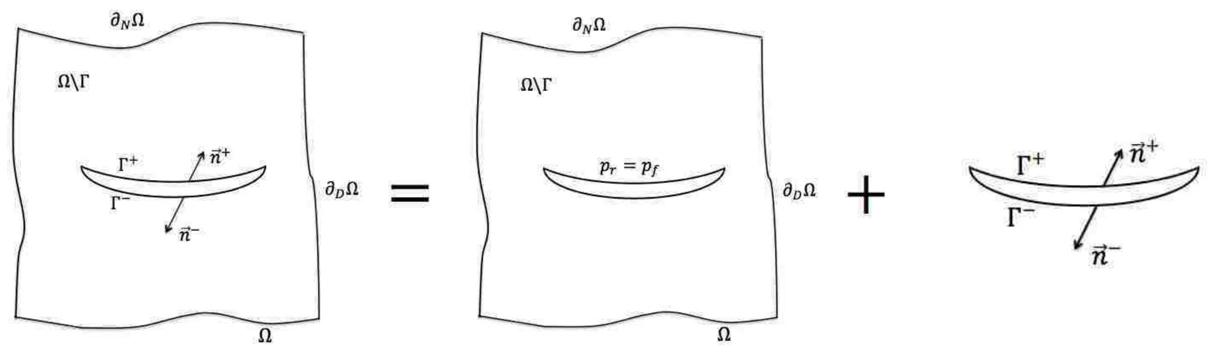

(a) Poroelastic domain containing reservoir and fracture

(b) Reservoir domain without fracture

(c) Fracture domain isolated from reservoir

Figure 3.2: Schematic of reservoir and fracture as components that make up the poroelastic media.

Equation 2.14 and in the mass balance equation developed from Biot's poroelastic theory for slightly compressible single phase, flow in a deformable medium. In the poroelasticity model, the increment of fluid content in a poroelastic media is given by

$$\zeta = \alpha \nabla \vec{u} + \frac{p_r}{M} \tag{3.1}$$

α, $\vec{u}$, p_r and M are Biot's constant, solid displacement, reservoir fluid pressure and Biot's modulus respectively. M is further given by the relationship

$$\frac{1}{M} = \frac{\alpha - \phi}{K_s} + \frac{\phi}{K_f} \tag{3.2}$$

where,

$$\alpha = 1 - \frac{K_T}{K_s} \tag{3.3}$$

K_T, K_s and K_f are the bulk modulus of the overall skeleton, bulk modulus of the grain/rock matrix and bulk modulus of the fluid. ϕ is the porosity of the rock.

Mass balance on the fluid content in the compressible (Biot 1941; Lewis 1998; Zheng, Burridge, and Burns 2003) media is

$$\begin{aligned}\frac{\partial \zeta}{\partial t} + \nabla \cdot \vec{q_r} = q_{rs} \\ \frac{1}{M}\frac{\partial p_r}{\partial t} + \alpha \frac{\partial \epsilon_{vol}}{\partial t} + \nabla \cdot \vec{q_r} = q_{rs}\end{aligned} \tag{3.4}$$

ϵ_{vol} is the volumetric strain which couples reservoir fluid flow with reservoir deformation as shown in Figure 3.1. q_{rs} is the source or sink term and it has a unit of volumetric flow rate per unit volume. $\vec{q_r}$ is the flow rate described by Darcy's law below

$$\vec{q_r} = -\frac{K}{\mu}\nabla p_r \tag{3.5}$$

K, μ are permeability tensor and fluid viscosity respectively. Upon substituting Equation 3.5 into Equation 3.4, the reservoir continuity equation below is obtained.

$$\frac{1}{M}\frac{\partial p_r}{\partial t} + \alpha \frac{\partial \epsilon_{vol}}{\partial t} - \nabla \cdot \frac{K}{\mu}\nabla p_r = q_{rs} \tag{3.6}$$

Initial and Boundary Conditions

The initial condition is such that $p_r = p_o$, where p_o is the initial reservoir pressure. A pressure or a flux boundary condition is also applied on the reservoir boundaries so that

$$\partial_D \Omega \cap \partial_N \Omega = \emptyset \quad \text{and} \quad \partial_D \Omega \cup \partial_N \Omega = \partial \Omega \tag{3.7}$$

where $\partial_D \Omega$ and $\partial_N \Omega$ are the pressure and flux boundaries respectively.

1. For pressure boundary condition

$$p_r = \bar{p} \quad \text{on} \quad \partial_D \Omega \tag{3.8}$$

2. For flux boundary condition

$$\vec{q}_r \cdot n = q_n \quad \text{on} \quad \partial_N \Omega \tag{3.9}$$

where $\vec{n}$ is the normal vector to the boundaries, q_n is the specified velocity component normal to $\partial_N \Omega$ while $\bar{p}$ is the boundary pressure specified on $\partial_D \Omega$.

The consequence of hydraulic communication between reservoir and fracture is that fluid pressure is continuous in the poroelastic domain. Since fracture is a boundary of the reservoir, this condition implies that fracture fluid pressure is the reservoir pressure at the reservoir-fracture interface.

$$p_r = p_f \quad \text{in } \Gamma \tag{3.10}$$

Although pressure is continuous in the poroelastic domain, its gradient is discontinuous across the fracture. This means that the fluid flux across the fracture face is discontinuous, as fluid flows either into or out of the fracture from both faces. On the basis of mass conservation, fluid flux from the fracture into the reservoir really accounts for loss of injected fluid during fracturing. Therefore in this work, leak-off will be modeled as the jump of fluid flux from both fracture faces.

$$q_l = -[\![\vec{q}_r]\!] \cdot \vec{n}_\Gamma \text{ across } \Gamma \tag{3.11}$$

3.2.1 Fixed Stress Split Solution for Coupled Flow and Deformation in Poroelastic Media

For a fixed fracture geometry, coupled numerical solution of Equations 2.14 and 3.6 is carried out to obtain p and $\vec{u}$ in the poroelastic domain. For this work, the fixed stress split technique is used to solve this coupled reservoir flow and deformation problem in the region of the computational domain with $v = 1$. This method is chosen for two reasons.

1. Its unconditional stability is needed for this complex problem with multiple levels of couplings; reservoir/fracture flow coupled to reservoir/fracture deformation.

2. The variational fracture solver which also models reservoir deformation is an exter-

nal standalone package. The main input to the mechanical model is fluid pressure defined over the computational domain. Thus, it does not have modifications to the deformation equations that will enable drained and undrained split solution methods.

In the fixed stress method, the continuity equation is first solved to compute fluid pressure, p_r. Thereafter, p_r is transferred to the variational fracture model to solve for $\vec{u}$. During the pressure solution step, reservoir deformation is decoupled from fluid flow by keeping the volumetric stress constant. The fixed stress method proceeds as follows: Let σ_{vol} and ϵ_{vol} be the volumetric stress and volumetric strain defined by

$$\begin{aligned} \sigma_{vol} &= \frac{\sigma_x + \sigma_y + \sigma_z}{3} \\ \epsilon_{vol} &= \nabla \cdot \vec{u} = \epsilon_x + \epsilon_y + \epsilon_z \end{aligned} \tag{3.12}$$

so that from linear poroelasticity

$$\sigma_{vol} + \alpha\, p_r = \kappa \epsilon_{vol} \tag{3.13}$$

κ is the drained bulk modulus of the reservoir rock related to E and ν by

$$\kappa = \begin{cases} \frac{E\,(1-\nu)}{(1+\nu)(1-2\,\nu)}; & 1D \\ \frac{E}{2\,(1+\nu)(1-2\,\nu)}; & 2D \\ \frac{E}{3\,(1-2\,\nu)}; & 3D \end{cases} \tag{3.14}$$

The volumetric strain in Equation 3.6 is eliminated by using Equation 3.13 to obtain

$$\Big(\frac{1}{M} + \frac{\alpha^2}{\kappa}\Big)\frac{\partial p_r}{\partial t} - \nabla \cdot \frac{K}{\mu} \nabla p_r - = q_{rs} - \frac{\alpha}{\kappa}\frac{\partial \sigma_{vol}}{\partial t} \quad \text{in } \Omega \setminus \Gamma \tag{3.15}$$

Equation 3.15 is the flow model solved in the fixed stress iterative coupling approach. As observed from the right hand side, the flow model is decoupled from deformation. On the left hand side, however, volumetric stress acts as an additional source term and represents contribution of reservoir deformation to fluid diffusion. Given that one of the primary variables in the mechanical model is $\vec{u}$, it is necessary to consider σ_{vol} contributions in terms of $\vec{u}$. To achieve this, for Equation 3.15 solved at a given iteration level $k+1$, the σ_{vol} obtained from the previous iteration level k is used. Therefore,

$$\Big(\frac{1}{M} + \frac{\alpha^2}{\kappa}\Big)\frac{\partial p_r^{k+1}}{\partial t} - \nabla \cdot \frac{K}{\mu}\nabla p_r^{k+1} = q_{rs} - \alpha\frac{\partial \epsilon_{vol}^k}{\partial t} + \frac{\alpha^2}{\kappa}\frac{\partial p_r^k}{\partial t} \quad \text{in } \Omega \setminus \Gamma \tag{3.16}$$

Superscripts represent iteration levels so that mechanical variables lag behind flow variables by one iteration. As the coupled numerical solution converges $p_r^{k+1} \to p_r^k$ and $\epsilon_{vol}^{k+1} \to \epsilon_{vol}^k$.

3.2.2 Weak Formulation of Single Phase Reservoir Flow Equation

Let $\psi_r \in H^1(\Omega)$ be a test function so that $\psi_r = 0$ on $\partial_D\Omega$. The weak form of the flow model is obtained by multiplying Equation 3.16 with ψ_r and integrating over the applicable domain. Since Equation 3.16 only applies to the unfractured part of the poroelastic domain (i.e. Figure 3.2b), the integration is carried out over $\Omega \setminus \Gamma$.

$$\begin{aligned}\int_{\Omega\setminus\Gamma}\Big(\frac{1}{M} + \frac{\alpha^2}{\kappa}\Big)\frac{\partial p_r^{k+1}}{\partial t}\psi_r\,dV - \int_{\Omega\setminus\Gamma}\nabla \cdot \frac{K}{\mu}\nabla p_r^{k+1}\psi_r\,dV = \int_{\Omega\setminus\Gamma} q_{rs}\psi_r\,dV \\ - \alpha\int_{\Omega\setminus\Gamma}\frac{\partial \epsilon_{vol}^k}{\partial t}\psi_r\,dV + \frac{\alpha^2}{\kappa}\int_{\Omega\setminus\Gamma}\frac{\partial p_r^k}{\partial t}\psi_r\,dV\end{aligned} \tag{3.17}$$

Upon carrying out integration by parts on the second term of the equation above, one obtains

$$\begin{aligned}\int_{\Omega\setminus\Gamma}\nabla \cdot \frac{K}{\mu}\nabla p_r^{k+1}\psi_r\,dV = -\int_{\Omega\setminus\Gamma}\frac{K}{\mu}\nabla p_r^{k+1}\nabla\psi_r\,dV \\ + \int_{\partial_N\Omega}\frac{K}{\mu}\nabla p_r^{k+1}\cdot\vec{n}\,\psi_r\,ds + \int_{\Gamma^+}\frac{K}{\mu}\nabla p_r^{k+1}\cdot\vec{n}_\Gamma^+\,\psi_r\,ds \\ + \int_{\Gamma^-}\frac{K}{\mu}\nabla p_r^{k+1}\cdot\vec{n}_\Gamma^-\,\psi_r\,ds\end{aligned} \tag{3.18}$$

Applying Equations 3.9 and 3.11 and considering that $\vec{n}_\Gamma^+ = -\vec{n}_\Gamma^- = \vec{n}_\Gamma$, then

$$\int_{\Omega\backslash\Gamma} \nabla \cdot \frac{K}{\mu} \nabla p_r^{k+1} \psi_r \, dV = - \int_{\Omega\backslash\Gamma} \frac{K}{\mu} \nabla p_r^{k+1} \nabla \psi_r \, dV \\ - \int_{\partial_N \Omega} q_n \, \psi_r \, ds - \int_\Gamma [\![q_r]\!] \cdot \vec{n}_\Gamma \psi_r \, ds \quad (3.19)$$

Upon substituting Equation 3.19 into Equation 3.17

$$\int_{\Omega\backslash\Gamma} \Big(\frac{1}{M} + \frac{\alpha^2}{\kappa}\Big) \frac{\partial \, p_r^{k+1}}{\partial t} \, \psi_r \, dV + \int_{\Omega\backslash\Gamma} \frac{K}{\mu} \nabla p_r^{k+1} \cdot \nabla \psi_r \, dV = \int_{\Omega\backslash\Gamma} q_{rs} \, \psi_r \, dV - \alpha \int_{\Omega\backslash\Gamma} \frac{\partial \epsilon_{vol}^k}{\partial t} \, \psi_r \, dV \\ + \frac{\alpha^2}{\kappa} \int_{\Omega\backslash\Gamma} \frac{\partial p_r^k}{\partial t} \, \psi_r \, dV - \int_{\partial_N \Omega} q_n \, \psi_r \, ds + \int_\Gamma q_l \, \psi_r \, ds \quad (3.20)$$

The emergence of the last integral term containing q_l is a natural consequence of the integration by parts of the flow model. Therefore, leak-off is implicitly incorporated with no need for models like Carter's.

3.3 Fracture Fluid Flow Model

The mathematical model for fluid flow in the fracture is as follows.

$$\frac{\partial w}{\partial t} + \nabla_\Gamma \cdot (w \, \vec{q}_f) + q_l = q_{fs} \quad \text{in } \Gamma \quad (3.21)$$

$$w \vec{q}_f = - \frac{w^3}{12 \mu} \nabla_\Gamma p_f \quad \text{in } \Gamma \quad (3.22)$$

$$q_l = - [\![\vec{q}_r]\!] \cdot \vec{n}_\Gamma \quad \text{on } \Gamma \quad (3.23)$$

$$\vec{q}_f \cdot \vec{m}_\Gamma = 0 \quad \text{on } \partial\Gamma \quad (3.24)$$

$$w = - [\![\vec{u}]\!] \cdot \vec{n}_\Gamma \quad (3.25)$$

Equations 3.21, 3.22 are the volume balance and the cubic law that relates fluid flux and pressure gradient. As shown in Figure 3.1, coupling between the mechanical model and fracture fluid flow is through the fracture width (w), fracture geometry (Γ) and fracturing fluid pressure (p_r). In addition, reservoir and fracture fluid flow are coupled through the fluid loss (Equation 3.23) from fracture to reservoir. Equation 3.23 ensures that fluid leak-off is a consequence of the solution of the full dimensional fluid diffusion in the reservoir. For mathematical convenience and to complete the boundary conditions for the fracture problem, no fluid loss is allowed from the fracture tip, as described by Equation 3.24. $\vec{m}_\Gamma$ is the tangential direction at the fracture tip, $\partial\Gamma$. Surface gradient and surface divergence operators are defined in Appendix D. Using the definition for surface divergence in Equation D.4, Equation 3.21 is expressed as

$$\frac{\partial w}{\partial t} + [\vec{n}_\Gamma \times \nabla \cdot (\vec{n}_\Gamma \times w\vec{q}_f)] + q_l = q_{fs} \qquad \text{(from Equation } D.2\text{)} \tag{3.26}$$

The fracture continuity equation in terms of fracture fluid pressure is obtained by substituting Equation 3.22 into the above equation.

$$\frac{\partial w}{\partial t} - \big[(\vec{n}_\Gamma \times \nabla) \cdot \frac{w^3}{12\mu}(\vec{n}_\Gamma \times \nabla_\Gamma p_f)\big] + q_l = q_{fs} \tag{3.27}$$

3.3.1 Weak Form of Fracture Flow Equation

Similar to Subsec. 3.2.2 for reservoir flow model, Equation 3.26 is multiplied by a test function ψ_f and integrated over Γ.

$$\begin{aligned} \int_\Gamma \quad {}_f \big(q_{fs} - \frac{\partial w}{\partial t} - q_l\big) ds &= \int_\Gamma \big((\vec{n}_\Gamma \times \nabla) \cdot (\vec{n}_\Gamma \times w\vec{q}_f)\big)\psi_f \, ds \\ &= \int_\Gamma \quad {}_f \big[\nabla \times \ (\vec{n}_\Gamma \times w\vec{q}_f)\big] \cdot \vec{n}_\Gamma \, ds \end{aligned} \tag{3.28}$$

Applying Equation D.1, the right hand side of Equation 3.28 can be expressed as

$$\begin{aligned} \int_\Gamma \big[(\nabla \times \psi_f \, (\vec{n}_\Gamma \times w\vec{q}_f)\big] \cdot \vec{n}_\Gamma \, ds = &\int_\Gamma \quad {}_f \, \big[(\nabla \times \ (\vec{n}_\Gamma \times w\vec{q}_f)\big] \cdot \vec{n}_\Gamma \, ds \\ &+ \int_\Gamma \big[\nabla\psi_f \times (\vec{n}_\Gamma \times w\vec{q}_f)\big] \cdot \vec{n}_\Gamma \, ds \end{aligned} \tag{3.29}$$

Stoke's theorem defined in Appendix D is applied to the left hand side of Equation 3.29 to obtain

$$\int_\Gamma \left[(\nabla \times \psi_f \, (\vec{n}_\Gamma \times w\vec{q}_f) \right] \cdot \vec{n}_\Gamma \, ds = \oint_{\partial\,\Gamma} \psi_f \, w\vec{q}_f \cdot \vec{m}_\Gamma \, ds \tag{3.30}$$

Equation 3.29 becomes

$$-\int_\Gamma \quad {}_f \left[(\nabla \times \; (\vec{n}_\Gamma \times w\vec{q}_f) \right] \cdot \vec{n}_\Gamma \, ds = -\oint_{\partial\,\Gamma} \psi_f w\vec{q}_f \cdot \vec{m}_\Gamma \, ds + \int_\Gamma \left[\nabla\psi_f \times (\vec{n}_\Gamma \times w\vec{q}_f) \right] \cdot \vec{n}_\Gamma \, ds \tag{3.31}$$

Since $\vec{q}_f \cdot \vec{m}_\Gamma = 0$ on $\partial\,\Gamma$, the first component on the right hand side of Equation 3.31 is equal to zero and it becomes

$$-\int_\Gamma \quad {}_f \left[(\nabla \times \; (\vec{n}_\Gamma \times w\vec{q}_f) \right] \cdot \vec{n}_\Gamma \, ds = \int_\Gamma \left[\nabla\psi_f \times (\vec{n}_\Gamma \times w\vec{q}_f) \right] \cdot \vec{n}_\Gamma \, ds \tag{3.32}$$

Substituting Equation 3.32 back into Equation 3.28 and applying some of the vector algebra identities in Appendix D

$$\begin{aligned}
\int_\Gamma \quad {}_f \left(q_{fs} - \frac{\partial w}{\partial t} - q_l \right) ds &= -\int_\Gamma \left[\nabla\psi_f \times (\vec{n}_\Gamma \times w\vec{q}_f) \right] \cdot \vec{n}_\Gamma \, ds \\
&= -\int_\Gamma \left[(\vec{n}_\Gamma \times \nabla\psi_f) \cdot (\vec{n}_\Gamma \times w\vec{q}_f) \right] ds \\
&= \quad \int_\Gamma \frac{w^3}{12\mu} \left[(\vec{n}_\Gamma \times \nabla_\Gamma \, p_f) \cdot (\vec{n}_\Gamma \times \nabla\psi_f) \right] ds \\
&= -\int_\Gamma \frac{w^3}{12\mu} \left[(\nabla_\Gamma \, p_f \times \vec{n}_\Gamma) \cdot (\vec{n}_\Gamma \times \nabla\psi_f) \right] ds \\
&= -\int_\Gamma \frac{w^3}{12\mu} \left[\nabla_\Gamma \, p_f \cdot \left(\vec{n}_\Gamma \times (\vec{n}_\Gamma \times \nabla\psi_f) \right) \right] ds \\
&= \quad \int_\Gamma \frac{w^3}{12\mu} \left[\nabla_\Gamma \, p_f \cdot \nabla_\Gamma \, \psi_f \right] ds
\end{aligned} \tag{3.33}$$

3.4 Reservoir and Fracture Flow Coupling

3.4.1 Weak Formulation of Scaled Model

Reservoir and fracture flow equations obtained from finite element analysis are here presented as Equations 3.34 and 3.35 respectively. Similar to the computation of p_r in the reservoir flow model, p_f is computed at one iteration level above the mechanical model. Hence, the fracture width has the superscript k.

$$\int_{\Omega\setminus\Gamma}\left(\frac{1}{M}+\frac{\alpha^2}{\kappa}\right)\frac{\partial\, p_r^{k+1}}{\partial t}\,\psi_r\,dV+\frac{K}{\mu}\int_{\Omega\setminus\Gamma}\nabla p_r^{k+1}\cdot\nabla\psi_r\,dV=\int_{\Omega\setminus\Gamma}q_{rs}\,\psi_r\,dV-\alpha\int_{\Omega\setminus\Gamma}\frac{\partial\epsilon_{vol}^k}{\partial t}\,\psi_r\,dV$$
$$+\frac{\alpha^2}{\kappa}\int_{\Omega\setminus\Gamma}\frac{\partial p_r^k}{\partial t}\,\psi_r\,dV-\int_{\partial_N\Omega}q_n\,\psi_r\,ds+\int_\Gamma q_l\,\psi_r\,ds \quad (3.34)$$

$$\int_\Gamma\frac{(w^k)^3}{12\mu}\left[\nabla_\Gamma\, p_f^{k+1}\cdot\nabla_\Gamma\,\psi_f\right]ds=-\int_\Gamma\frac{\partial w^k}{\partial t}\,\psi_f\,ds+\int_\Gamma q_{fs}\,\psi_f-\int_\Gamma q_l^k\,\psi_f\,ds \quad (3.35)$$

The leak-off component is eliminated by adding Equations 3.34 and 3.35 to obtain

$$\int_{\Omega\setminus\Gamma}\left(\frac{1}{M}+\frac{\alpha^2}{\kappa}\right)\frac{\partial\, p_r^{k+1}}{\partial t}\,\psi_r\,dV+\frac{K}{\mu}\int_{\Omega\setminus\Gamma}\nabla p_r^{k+1}\cdot\nabla\psi_r\,dV+\int_\Gamma\frac{(w^k)^3}{12\mu}\left[\nabla_\Gamma\, p_f^{k+1}\cdot\nabla_\Gamma\,\psi_f\right]ds$$
$$=\int_{\Omega\setminus\Gamma}q_{rs}\,\psi_r\,dV-\alpha\int_{\Omega\setminus\Gamma}\frac{\partial\epsilon_{vol}^k}{\partial t}\,\psi_r\,dV+\frac{\alpha^2}{\kappa}\int_{\Omega\setminus\Gamma}\frac{\partial p_r^k}{\partial t}\,\psi_r\,dV$$
$$-\int_{\partial_N\Omega}q_n\,\psi_r\,ds-\int_\Gamma\frac{\partial w^k}{\partial t}\,\psi_f\,ds+\int_\Gamma q_{fs}\,\psi_f\,ds \quad (3.36)$$

Integrals over $\Omega\setminus\Gamma$ are contributions from the reservoir flow model while those over Γ are fracture flow components. Since location of fracture, Γ, is unknown, it is difficult to numerically integrate components of Equation 3.36 over their respective domains. The fracture is represented as in the variational fracture framework and a regularized formulation is introduced using the phase field calculus to convert integrals over $\Omega\setminus\Gamma$ and Γ to integrals over Ω, irrespective of the location of Γ. For Equation 3.17, this is achieved by multiplying by v^2 the integrands of integrals over $\Omega\setminus\Gamma$, as introduced in Equation 2.24. Similarly, using Equation 2.20, integrals over Γ are converted to full domain integrals over Ω by multiplying their integrands by $|\nabla v|$. Since fracture region is represented by $v = 0$, this formulation uses v as an indicator function to distinguish between integrals over the two subdomains.

So far, two pressures are identified in the flow model: reservoir fluid pressure, p_r and fracture fluid pressure, p_f. Hydraulic communication between fracture and reservoir stipulates pressure continuity so that a single pressure variable is used to represent the fluid pressure. Therefore, if p is the pressure in the whole computational domain, then

$$\begin{aligned} p_r &= p; \quad \psi_r = \psi \text{ in } \quad \Omega \setminus \Gamma \\ p_f &= p; \quad \psi_f = \psi \text{ on } \quad \Gamma \end{aligned} \tag{3.37}$$

According to Equation 3.37, fracture pressure is the fluid pressure on Γ and reservoir pressure is fluid pressure in $\Omega \setminus \Gamma$. Mathematically, p can be considered a weighted combination of p_r and p_f so that both variables can be replaced with p in the volume integral of Equation 3.36. Similarly, due to continuity of the domain for both fracture and reservoir flow in the variational fracture framework, the test functions are also continuous and replaced with ψ, as described by Equation 3.37. After applying all the above concepts, Equation 3.36 becomes

$$\begin{aligned} \int_\Omega v^2 \Big(\frac{1}{M} + \frac{\alpha^2}{\kappa}\Big) \frac{\partial p^{k+1}}{\partial t} \psi \, dV + \frac{K}{\mu} \int_\Omega v^2 \nabla p^{k+1} \cdot \nabla \psi \, dV + \int_\Omega \frac{(w^k)^3}{12\mu} \big(\nabla_\Gamma p^{k+1} \cdot \nabla_\Gamma \psi\big) |\nabla v| \, dV \\ = \int_\Omega v^2 \, q_{rs} \, \psi \, dV - \alpha \int_\Omega v^2 \frac{\partial \epsilon^k_{vol}}{\partial t} \psi \, dV + \frac{\alpha^2}{\kappa} \int_\Omega v^2 \, \frac{\partial p^k}{\partial t} \psi \, dV \\ - \int_{\partial_N \Omega} q_n \, \psi + \int_\Omega \psi \, q_{fs} |\nabla v| \, dV - \int_\Omega \psi \frac{\partial w^k}{\partial t} |\nabla v| \, dV \end{aligned} \tag{3.38}$$

Where

$$\begin{aligned} \vec{n}_\Gamma &\simeq \frac{\nabla v}{|\nabla v|} \\ \nabla_\Gamma p &\simeq \nabla p - (\nabla p \cdot \vec{n}_\Gamma) \, \vec{n}_\Gamma \end{aligned} \tag{3.39}$$

A careful analysis of Equation 3.38 shows that it degenerates to zero everywhere inside the fracture, since $v = 0$ and $|\nabla v| = 0$ inside the fracture. This breakdown in the model creates an ill-conditioned system of equations which is almost impossible to solve. To improve the stability of the resultant numerical model, a modification similar to the approach used in deriving the fixed stress model is proposed. The proposed modification which is shown in Equation 3.40, uses Biot's compressibility ($\frac{1}{M}$) as a stabilizing term. Furthermore, to prevent the v-field from affecting the flow model in the absence of fracture opening (i.e. $w \leq 0$, for example, prior to fracture opening under in situ stresses), the minimum permeability in every grid block is the reservoir permeability.

$$\begin{aligned}\int_\Omega \Big(\frac{1}{M} + v^2\,\frac{\alpha^2}{\kappa}\Big)\frac{\partial\, p^{k+1}}{\partial t}\,\psi\, dV + \frac{K}{\mu}\int_\Omega \nabla p^{k+1}\cdot\nabla\psi\, dV + \int_\Omega \frac{(w^k)^3}{12\mu}\big(\nabla_\Gamma\, p^{k+1}\cdot\nabla_\Gamma\,\psi\big)|\nabla v|\, dV \\ = \int_\Omega v^2\, q_{rs}\,\psi\, dV - \alpha\int_\Omega v^2\frac{\partial\epsilon^k_{vol}}{\partial t}\,\psi\, dV + \frac{1}{M}\int_\Omega (1-v^2)\,\frac{\partial p^k}{\partial t}\,\psi\, dV \\ + \frac{\alpha^2}{\kappa}\int_\Omega v^2\,\frac{\partial p^k}{\partial t}\,\psi\, dV - \int_{\partial_N\Omega} q_n\,\psi\, dV \\ + \int_\Omega \psi\, q_{fs}|\nabla v|\, dV - \int_\Omega \psi\frac{\partial w^k}{\partial t}|\nabla v|\, dV \end{aligned} \tag{3.40}$$

3.4.2 Well Flow Rate Representation in Regularized Fracture

$\tilde{q}_{rs}$ and $\tilde{q}_{fs}$ are the reservoir and fracture fluid sources/sinks in the coupled flow model. As in conventional reservoir well modeling, both can be modeled either as constraints on flow rates or constraints on bottom hole pressures. In this work, constant flow rate condition is used as the only constraint for both reservoir and fracture wells. Mathematically, reservoir well flow rate conditions are modeled as point sources/sinks using the dirac delta function as shown below.

$$\tilde{q}_{rs} = \Sigma_{i=1}^{n}\tilde{Q}_{r,i}\,\delta(\vec{\tilde{x}} - \vec{\tilde{x}}_{r,i}) \tag{3.41}$$

On the other hand, modeling well flow rate for fracture wells is different from that for reservoir wells. Since fracture locations in the variational approach are not identified by specific points but by a smooth phase field, a regularized representation of the fracture well rate is used.

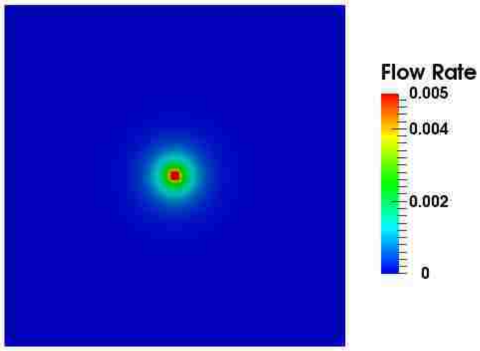

Figure 3.3: Regularized well rate representation for a two dimensional domain

For two dimensional domain

$$\tilde{q}_{fs} \simeq \begin{cases} \Sigma_{i=1}^{m} \frac{\tilde{Q}_{f,i}}{2\pi\tilde{\varepsilon}^2} & \text{if } |\tilde{\vec{x}} - \tilde{\vec{x}}_{f,i}| \leq th/2 \\ \Sigma_{i=1}^{m} \frac{\tilde{Q}_{f,i} \exp^{-|\vec{x}-\vec{x}_{f,i}|/\tilde{\varepsilon}}}{2\pi\tilde{\varepsilon}^2} & \text{if } |\tilde{\vec{x}} - \tilde{\vec{x}}_{f,i}| \geq th/2 \end{cases} \tag{3.42}$$

For three dimensional domain

$$\tilde{q}_{fs} \simeq \begin{cases} \Sigma_{i=1}^{m} \frac{\tilde{Q}_{f,i}}{4\pi\tilde{\varepsilon}^3} & \text{if } |\tilde{\vec{x}} - \tilde{\vec{x}}_{f,i}| \leq th/2 \\ \Sigma_{i=1}^{m} \frac{\tilde{Q}_{f,i} \exp^{-|\vec{x}-\vec{x}_{f,i}|/\tilde{\varepsilon}}}{4\pi\tilde{\varepsilon}^3} & \text{if } |\tilde{\vec{x}} - \tilde{\vec{x}}_{f,i}| \geq th/2 \end{cases} \tag{3.43}$$

$\tilde{Q}_r$ and $\tilde{Q}_f$ are dimensionless versions of Q_r and Q_f which are the volumetric injection rates with units of m^3/s for three dimensional problems and m^2/s for two dimensional problems. $\tilde{\vec{x}}_r$ and $\tilde{\vec{x}}_f$ are locations of n number of reservoir and m number of fracture wells. th is the thickness of the phase field fracture representation, i.e the thickness of the fracture region with $v = 0$. Figure 3.3 shows an example of regularized fracture flow rate representation. The peak strength is around the fracture region with large $|\tilde{\nabla} v|$ but diminishes as $v \to 1$ and $|\tilde{\nabla} v| \to 0$.

3.4.3 Scaling of Coupled Flow Model

Scaling of the coupled flow model is carried out to derive a dimensionless form which is consistent with, and is coupled to the dimensionless fracture model of subsec. 2.3.5. The important variables and parameters of the coupled flow model are p, w, K, $\vec{u}$, K, μ, t and

Q, and they are scaled as follows.

$$w = u_o \tilde{w}; \quad M = m_o \tilde{M}; \quad \mu = \mu_o \tilde{\mu}; \quad K = k_o \tilde{K}; \quad Q = Q_o \tilde{Q}; \quad t = t_o \tilde{t}; \tag{3.44}$$

Where $Q = Q_r + Q_f$ is the total injection rate. In addition,

$$\begin{aligned} t_o = \frac{u_o x_o^{N-1}}{Q_o} &= \sqrt{\frac{G_{c_o} x_o^{2N-1}}{E_o Q_o^2}} \\ \mu_o &= \frac{G_{c_o}^2 x_o^{N-2}}{E_o Q_o} \\ k_o &= \frac{u_o^3}{x_o} \\ m_o &= E_o \end{aligned} \tag{3.45}$$

Combining the scalings defined in Equation 3.44 and those of Equation 2.30, a dimensionless flow model is derived and is shown below.

$$\begin{aligned} &\int_{\tilde{\Omega}} \Big(\frac{1}{\tilde{M}} + v^2 \,\frac{\alpha^2}{\tilde{\kappa}}\Big) \frac{\partial \, \tilde{p}^{k+1}}{\partial \tilde{t}} \, \psi \, d\tilde{V} + \frac{\tilde{K}}{\tilde{\mu}} \int_{\tilde{\Omega}} \tilde{\nabla} \tilde{p}^{k+1} \cdot \tilde{\nabla} \psi \, d\tilde{V} + \int_{\tilde{\Omega}} \frac{(\tilde{w}^k)^3}{12\tilde{\mu}} \big(\tilde{\nabla}_\Gamma \, \tilde{p}^{k+1} \cdot \tilde{\nabla}_\Gamma \, \psi\big) |\tilde{\nabla} v| \, d\tilde{V} \\ &= \int_{\tilde{\Omega}} v^2 \, \tilde{q}_{rs} \, \psi \, d\tilde{V} - \alpha \int_{\tilde{\Omega}} v^2 \frac{\partial (\tilde{\nabla} \cdot \vec{\tilde{u}}^k)}{\partial \tilde{t}} \, \psi \, d\tilde{V} + \frac{1}{\tilde{M}} \int_{\tilde{\Omega}} (1 - v^2) \, \frac{\partial \tilde{p}^k}{\partial \tilde{t}} \, \psi \, d\tilde{V} \\ &\quad + \frac{\alpha^2}{\tilde{\kappa}} \int_{\tilde{\Omega}} v^2 \, \frac{\partial \tilde{p}^k}{\partial \tilde{t}} \, \psi \, d\tilde{V} - \int_{\partial_N \tilde{\Omega}} \tilde{q}_n \, \psi \, d\tilde{V} \\ &\quad + \int_{\tilde{\Omega}} \psi \, \tilde{q}_{fs} |\tilde{\nabla} v| \, d\tilde{V} - \int_{\tilde{\Omega}} \psi \frac{\partial \tilde{w}^k}{\partial \tilde{t}} |\tilde{\nabla} v| \, d\tilde{V} \end{aligned} \tag{3.46}$$

As seen in the first equation of Equation 3.45, Q_o and t_o are not independent and therefore cannot be arbitrarily specified. Only one of Q_o or t_o has to be given as an input to complete the scaling. The possible options are either Q and $\tilde{Q}$ are known and from which Q_o is computed or t and $\tilde{t}$ are known from which t_o is computed.

The numerical simulation solves the dimensionless flow model of Equation 3.46 while the respective conversion factors (with subscript o) given in Equation 3.45 are used to scale the numerical simulation results to dimensional quantities. Details of the derivation of Equations

3.46 and 3.45 can be found in Appendix B.

3.4.4 Finite Elements Discretization

The computational domain for the flow problem is the same structured grid as that for the mechanical problem. The standard Galerkin finite element method is used to solve Equation 3.40 and the test function, ψ, is a weighted sum of the shape functions, φ_i, defined on all the nodes.

$$\psi = \sum_{i=1}^{n} \psi_i \, \varphi_i \tag{3.47}$$

$\tilde{p}$ is also a weighted sum of all the nodal pressure values as shown below.

$$\tilde{p} = \sum_{i=1}^{n} \tilde{p}_i \, \varphi_i \tag{3.48}$$

n is the total number of nodes in the structured grid. Nodal values of φ_i for the 3D, 8-node brick element used in this work are well described in literature and can be found in Ern and Guermond (2004) and Elman, Silvester, and Wathen (2005). Reservoir permeability is assumed to be a diagonal tensor with principal values $\tilde{k}_x$, $\tilde{k}_y$ and $\tilde{k}_z$ so that upon substituting Equations 3.47 and 3.47 into Equation 3.40, the discrete equations generated from the finite element analysis can be written in the following matrix form.

$$\Big[\, \mathbf{S} \,\Big] \frac{d}{d\tilde{t}} \Big[\, \tilde{\mathbf{p}} \,\Big]^{k+1} + \Big[\, \mathbf{D}_r + \mathbf{D}_f^k \,\Big] \Big[\, \tilde{\mathbf{p}} \,\Big]^{k+1} = \Big[\, \mathbf{f}_r^k + \mathbf{f}_f^k \,\Big] \tag{3.49}$$

Where

$$\mathbf{S} = \int_{\tilde{\Omega}} \Big(\frac{1}{\tilde{M}} + v^2 \, \frac{\alpha^2}{\tilde{\kappa}} \Big) \varphi_i \varphi_j \, d\tilde{V} \tag{3.50}$$

$$\mathbf{D}_r = \int_{\tilde{\Omega}} \Big(\frac{\tilde{k}_x}{\tilde{\mu}} \frac{\partial \varphi_i}{\partial \tilde{x}} \frac{\partial \varphi_j}{\partial \tilde{x}} + \frac{\tilde{k}_y}{\tilde{\mu}} \frac{\partial \varphi_i}{\partial \tilde{y}} \frac{\partial \varphi_j}{\partial \tilde{y}} + \frac{\tilde{k}_z}{\tilde{\mu}} \frac{\partial \varphi_i}{\partial \tilde{z}} \frac{\partial \varphi_j}{\partial \tilde{z}} \Big) \, d\tilde{V} \tag{3.51}$$

$$\mathbf{D}_f^k = \frac{1}{12\tilde{\mu}} \int_{\tilde{\Omega}} (\tilde{w}^k)^3 \tilde{\nabla}_\Gamma \varphi_i \cdot \tilde{\nabla}_\Gamma \varphi_j |\tilde{\nabla} v| \, d\tilde{V} \tag{3.52}$$

$$\begin{aligned} \mathbf{f}_r^k = & \int_{\tilde{\Omega}} v^2 \, \tilde{q}_{rs} \, \varphi_i \, d\tilde{V} - \alpha \int_{\tilde{\Omega}} \frac{\partial(\tilde{\nabla} \cdot \vec{\tilde{u}}^k)}{\partial \tilde{t}} \varphi_i \, d\tilde{V} + \frac{1}{\tilde{M}} \int_{\tilde{\Omega}} (1 - v^2) \, \frac{\partial \tilde{p}^k}{\partial \tilde{t}} \, d\tilde{V} \\ & + \frac{\alpha^2}{\tilde{\kappa}} \int_{\tilde{\Omega}} v^2 \, \frac{\partial \tilde{p}^k}{\partial \tilde{t}} \varphi_i \, d\tilde{V} - \int_{\partial_N \tilde{\Omega}} \tilde{q}_n \, \varphi_i \, d\tilde{V} \end{aligned} \tag{3.53}$$

$$\mathbf{f}_f^k = \int_{\tilde{\Omega}} \tilde{q}_{fs} |\tilde{\nabla} v| \, \varphi_i \, d\tilde{V} - \int_{\tilde{\Omega}} \frac{\partial \tilde{w}^k}{\partial \tilde{t}} |\tilde{\nabla} v| \, \varphi_i \, d\tilde{V} \tag{3.54}$$

$\tilde{\mathbf{p}}$ is the vector of fluid pressure in the poroelastic domain. $\mathbf{S}$ and $\mathbf{D}$ are the finite element matrices generated for the coupled problem while the $\mathbf{f}$'s are the right hand side vectors containing the fluid sources. k superscripts represent iteration levels. $\mathbf{D}_r$ which is generated from the reservoir flow model is independent of fluid pressure and therefore has no k superscript. $\mathbf{D}_f$, on the other hand, depends on the displacement through the fracture width. Hence, $\mathbf{D}_f^k$ has the superscript k since mechanics lags behind flow by one iteration level.

Time Discretization and Numerical Solution

Using the θ-method, $\tilde{\mathbf{p}}$ and $\mathbf{f}$ are evaluated at intermediate time steps, $n + \theta$, according to Equations 3.55, where $0 \leq \theta \leq 1$. Consequently, Equation 3.49 is computed at $n + \theta$ to obtain Equation 3.56.

$$\begin{aligned} \Big[\tilde{\mathbf{p}}\Big]_{n+\theta}^{k+1} &= \theta \Big[\tilde{\mathbf{p}}\Big]_{n+1}^{k+1} + (1 - \theta) \Big[\tilde{\mathbf{p}}\Big]_n \\ \Big[\mathbf{f}\Big]_{n+\theta}^{k} &= \theta \Big[\mathbf{f}\Big]_{n+1}^{k} + (1 - \theta) \Big[\mathbf{f}\Big]_n \end{aligned} \tag{3.55}$$

$$\Big[\ \mathbf{S}\ \Big] \frac{d}{d\tilde{t}} \Big[\ \tilde{\mathbf{p}}\ \Big]_{n+\theta}^{k+1} + \Big[\ \mathbf{D}_r + \mathbf{D}_f^k\ \Big] \Big[\ \tilde{\mathbf{p}}\ \Big]_{n+\theta}^{k+1} = \Big[\ \mathbf{f}_r^k + \mathbf{f}_f^k\ \Big]_{n+\theta} \tag{3.56}$$

The time derivative of pressure in Equation 3.56 is approximated using finite difference of Equation 3.55 so that upon substituting Equations 3.55 and 3.57 into Equation 3.56, the time evolution of pressure in the whole computation domain is obtained by solving Equation 3.58

$$\frac{d}{d\tilde{t}} \Big[\tilde{\mathbf{p}}\Big]_{n+\theta}^{k+1} = \frac{\Big[\tilde{\mathbf{p}}\Big]_{n+1}^{k+1} - \Big[\tilde{\mathbf{p}}\Big]_n}{\Delta \tilde{t}} \tag{3.57}$$

$$\begin{aligned}\Big[\mathbf{S} + \theta\,\Delta\tilde{t}\,(\mathbf{D}_r + \mathbf{D}_f^k)\Big]\,\Big[\tilde{\mathbf{p}}\Big]_{n+1}^{k+1} = \Big[\mathbf{S} - (1-\theta)\,\Delta\tilde{t}\,(\mathbf{D}_r + \mathbf{D}_f^k)\Big]\,\tilde{\mathbf{p}}_n + \Delta\tilde{t}\,\Big[\theta\,[\mathbf{f}_r^k + \mathbf{f}_f^k]_{n+1} \\ + (1-\theta)\,\Big[\theta\,[\mathbf{f}_r^k + \mathbf{f}_f^k]_n\Big]\end{aligned} \tag{3.58}$$

One observes that Equation 3.58 is written in terms of θ. This offers the flexibility that different time discretization schemes can be obtained by using particular values of θ. For example, $\theta = 0$ gives the conditionally stable forward Euler scheme, $\theta = 1$ is the unconditionally stable backward Euler time scheme while $\theta = 0.5$ is the Crank-Nicholson scheme.

The system of equations in Equation 3.58 is solved iteratively using Newton's method. Since the set of equations are linear, the Jacobian ($\mathbf{J}$) for Newton's method is independent of pressure and is simply the coefficient matrix multiplying the unknown pressures. The residual $\mathbf{r}$ is

$$\begin{aligned}\mathbf{r}(\mathbf{x}) = \Big[\mathbf{S} + \theta\,\Delta\tilde{t}\,(\mathbf{D}_r + \mathbf{D}_f^k)\Big]\,\Big[\tilde{\mathbf{p}}\Big]_{n+1}^{k+1} - \Big[\mathbf{S} - (1-\theta)\,\Delta\tilde{t}\,(\mathbf{D}_r + \mathbf{D}_f^k)\Big]\,\tilde{\mathbf{p}}_n \\ - \Delta\tilde{t}\,\Big[\theta\,[\mathbf{f}_r^k + \mathbf{f}_f^k]_{n+1} + (1-\theta)\,\Big[\theta\,[\mathbf{f}_r^k + \mathbf{f}_f^k]_n\Big]\end{aligned} \tag{3.59}$$

Therefore,

$$\mathbf{J} = \mathbf{r}'(\mathbf{x}) = [\mathbf{S} + \theta\,\Delta t\,(\mathbf{D}_r + \mathbf{D}_f^k)] \tag{3.60}$$

3.4.5 Fracture Width Computation

The fracture width ($\tilde{w}$) is computed using Equation 3.61 which was introduced in Chapter 2. Like reservoir permeability, the fracture width is defined on all cells and $\tilde{w} \geq 0$ is enforced to prevent interpenetration of the fracture faces. Figure 3.4 highlights the necessary components used in the fracture width computation algorithm. Equation 3.61 suggests that three components are needed to compute $\tilde{w}$ for a particular cell, c. These are; the local fracture normal, $\vec{n}_\Gamma$, at the reference cell, the line s along which the integral is evaluated and half length, b, of the line s. The center of s is the center of the reference cell c. s has orientation $\vec{n}_\Gamma = \frac{\tilde{\nabla} v}{|\tilde{\nabla} v|}$ and extends to length b from the reference cell center in the $\pm\,\vec{n}_\Gamma$

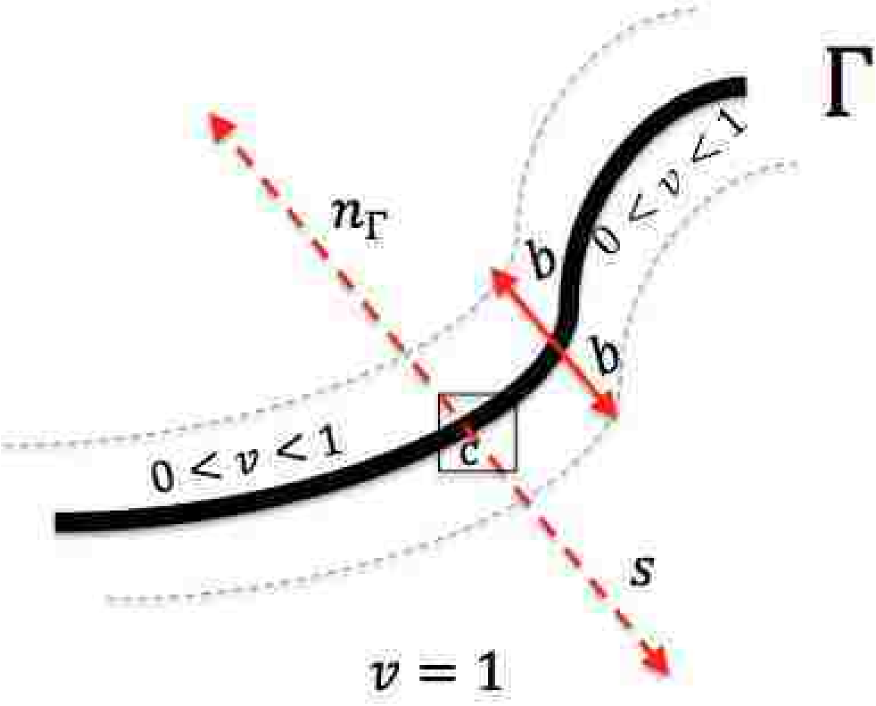

Figure 3.4: Geometry of important components used for fracture width computation

directions. The simplest choice of b is one that ensures s cuts across the whole computation domain. However, this is unnecessary since regions along s with constant v values do not contribute to the integral. In addition, this poses problems if s cuts across multiple fractures.

$$\tilde{w} = \int_{-b}^{b} \vec{\tilde{u}} \cdot \tilde{\nabla} v \, d\tilde{x} \tag{3.61}$$

For open fractures, $\tilde{w} > 0$ for cells in the v transition region while $\tilde{w} = 0$ for those cells with constant v value. Therefore, the numerical algorithm to implement Equation 3.61 is carried out only on cells with $0 < v < 1$ since cells outside this region do no contribute to the fracture flow model as they have $|\tilde{\nabla} v| = 0$. This means that b can be chosen so that for a reference cell at one end of the transition region with $v \approx 1$, s extends across the fracture face and covers the whole region with $v < 1$. Once b and s are determined, s is discretized so that $\vec{\tilde{u}} \cdot \tilde{\nabla} v$ is sampled at the discrete points for input to Equation 3.61.

The algorithm is verified for a simple case of a line fracture that cuts a rectangular

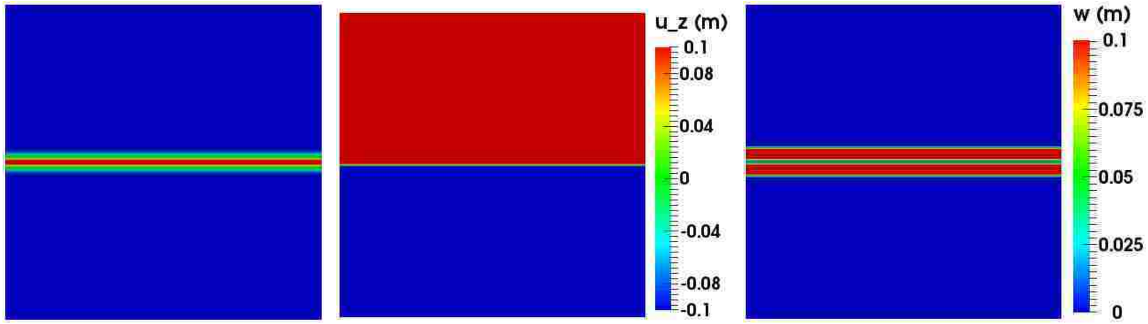

(a) v field for horizontal fracture that cuts the square domain (b) Vertical displacement field around the horizontal fracture (c) $\tilde{w}$ distribution around the fracture, in the cells with $0 < v < 1.0$

Figure 3.5: Horizontal fracture geometry for verification of fracture width computation

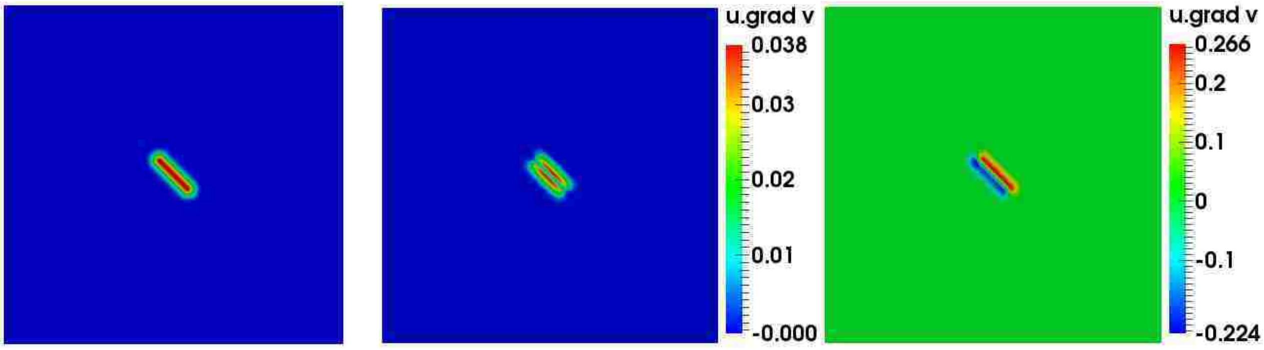

(a) v field (b) $\vec{u}\cdot\nabla v$ for domain with fixed boundaries (c) $\vec{u}\cdot\nabla v$ for translated domain

Figure 3.6: Pressurized inclined line fracture used to verify fracture width computation algorithm

domain into two equal parts as shown in Figure 3.5a. The fracture is opened by displacing the material in the vertical axis by 0.1 units at the top and -0.1 units at the bottom as shown in Figure 3.5b. This gives a total uniform fracture opening of 0.2 units across the fracture but with 0.1 units distributed on either side of the fracture faces. $\tilde{w}$ computed for this geometry using the algorithm described above is shown in Figure 3.5c. A uniform value of 0.1 is computed for cells in the region with average v value of less than 1 but greater than 0. Outside this region, $\tilde{w} = 0$.

Even though $\tilde{\nabla} v$ is one of the most important quantifies used for fracture width computation, it can also introduce numerical errors in the width especially around fracture tips. Considering that $\tilde{\nabla} v$ is defined everywhere around the fracture, the computed normal around the fracture tip is most likely going to be different from the actual fracture surface normal. Therefore, the use of the previously described algorithm around fracture tips results in integration lines that are far from being orthogonal to the fracture surface. Figure 3.7 shows the geometry of integration lines on cells around the fracture tip. One observes that on some cells, the line is either s_2 or s_3 while it is s_2 on cells that are on the fracture tip. In that region, however, the ideal line is s which is perpendicular to the fracture surface. Integration along s_1 or s_2 or s_3 picks up the wrong displacement fields, leading to distorted values for w around fracture tips. The effects of this error are highlighted by considering two different displacement boundaries for width computations for the pressurized fracture shown in Figure 3.5a. In the first computation, a fixed displacement is applied on all boundaries while in the second computation, the domain is translated by 0.2 and 0.1 units in the horizontal and vertical directions respectively. The quantity $\tilde{\vec{u}} \cdot \tilde{\nabla} v$ used in computing w is shown in Figures 3.5b and 3.5c for both computations. Due to the symmetric nature of the boundary condition for the first computation, its $\tilde{\vec{u}} \cdot \tilde{\nabla} v$ profile is uniformly distributed across the fracture faces unlike that for the second computation. Since the same amount of fluid pressure is applied to the fractures in both computations, one will expect the width profiles to be the same irrespective of the boundary type used. However, as shown in Figure 3.8, $\tilde{w}$ for the translated domain is different from that for the fixed domain due to the numerical errors accumulated around the fracture tips. Although one can faintly observe a uniformly distributed w around the interior of the fracture, the effect of the numerical error results in a maximum fracture width around the bottom tip which is four about times the actual maximum fracture width expected in the center of the fracture. If the error laden width profile in Figure 3.8b is used in the flow model, the pressure distribution obtained will be wrong.

Since fracture permeability depends on the fracture width, care must be taken to filter out this error from the width computation before incorporation into the flow model. The approach to filter out this error is based on two variables, fx and $\mathbf{I}$, defined everywhere in the computational domain. fx is a characteristic function computed using Equation 3.62 while

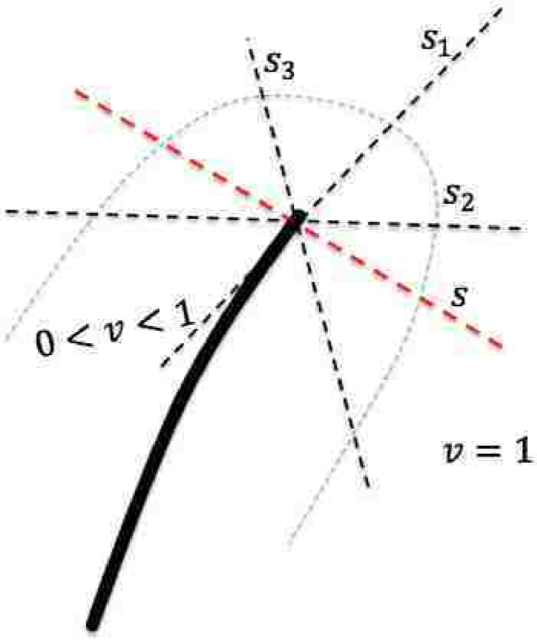

Figure 3.7: Integration lines used for fracture width computation around fracture tip regions

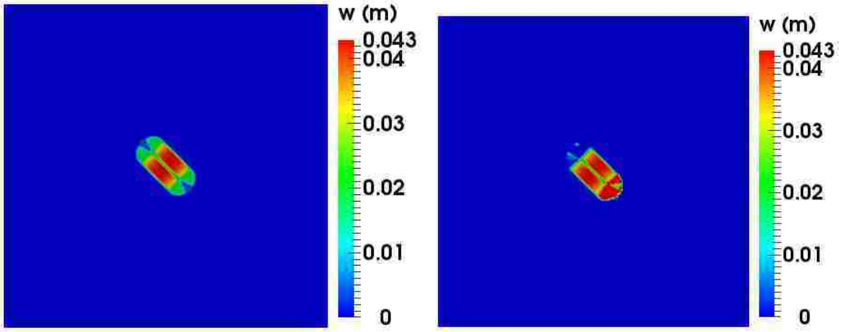

(a) $\tilde{w}$ for fixed domain (b) $\tilde{w}$ for translated domain

Figure 3.8: Computed fracture width for fractures in fixed and translated domains. Error in computed width due to application of the algorithm around fracture tips is obvious in the translated domain

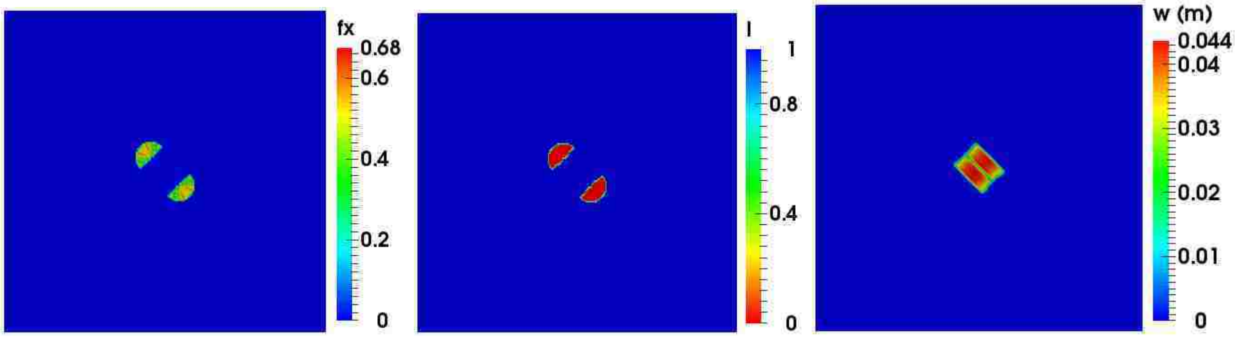

(a) Characteristic function, fx (b) Indicator function, $\mathbf{I}$ (c) Filtered w computed for fracture in translated domian

Figure 3.9: Fracture width computed after application of filtering algorithm to remove tip errors

$\mathbf{I}$ is an indicator function that takes a value of 1 around the fracture faces and 0 everywhere else, including the fracture tip. It depends on fx as shown in Equation 3.63.

$$fx = \left| \int_{-b}^{b} \tilde{\nabla} v \, d\tilde{x} \right| \tag{3.62}$$

f_{tol} is a pre-specified value that defines the threshold between fracture face and fracture tips.

$$\mathbf{I}(fx) := \begin{cases} 1 & \text{if } fx < f_{tol} \\ 0 & \text{otherwise ,} \end{cases} \tag{3.63}$$

Once $\mathbf{I}$ is computed, the fracture width is updated as

$$\tilde{w} = \mathbf{I}(fx) * \tilde{w} \tag{3.64}$$

It is important to note that the above ideas do not follow any rigorous mathematical theorem or proofs. Rather, it is based on intuition.

The above algorithm was used to filter out the tip error from the width computation for the translated domain. The results for fx, $\mathbf{I}$ and $\tilde{w}$ are shown in Figure 3.9. It is obvious that Equation 3.64 filters out the error around the bottom tip to create a more uniform width profile that compares fairly well with Figure 3.8a.

3.4.6 Numerical Algorithm for Hydraulic Fracturing Solution

Point wise convergence of the overall numerical solution to the fracture solution is impossible in the phase field approach since the fracture is not identified at any particular level set of the phase field, but in the transition region defined by $0 < v < 1$. This is why fracture width at a point is not given by displacement jump at that point in the computation domain. Rather, it is the sum (integral) of all the normal components of displacement along the line that cuts through the transition region or fracture face (see Equation 3.61). Making use of the same idea, the fracture pressure at any point, x_s, along the fracture length is computed as

$$\tilde{p}_f(x_s) = \frac{\int_s \tilde{p}\,\vec{\tilde{u}} \cdot \tilde{\nabla} v \, d\tilde{x}}{\int_s \vec{\tilde{u}} \cdot \tilde{\nabla} v \, d\tilde{x}} \tag{3.65}$$

where s is the integration line orthogonal to the fracture at point x_s.

Figure 3.10 shows the numerical algorithm for solution of the coupled hydraulic fracturing model. The core of the algorithm are two nested loops. The inner loop iterates between $\tilde{p}$ and $\vec{\tilde{u}}$ solvers until convergence while the outer loop solves the V-step only. The outer loop uses converged solutions of the inner loop to propagate the fracture, if the critical pressure is reached. The inner loop error is defined as the difference between consecutive values of a volume averaged pressure, $\bar{p}$ $\left(=\frac{\int_{\tilde{\Omega}} \tilde{p}\,\vec{\tilde{u}} \cdot \tilde{\nabla} v \, d\tilde{V}}{\int_{\tilde{\Omega}} \vec{\tilde{u}} \cdot \tilde{\nabla} v \, d\tilde{V}}\right)$, while the outer loop error is the difference between v values of consecutive fracture evolution steps. Once the evolution step converges, computation for a new time step starts and initial values for $\tilde{p}$, $\vec{\tilde{u}}$ and v for the first iteration are their respective converged solutions from the previous time steps.

3.5 Flow Model Verification I: Reservoir Fluid Flow

This section verifies the reservoir flow component of the coupled model by solving flow problems which have analytical solutions. Numerical implementation of different boundary condition types is tested as well. The mechanical component is decoupled by setting $\vec{u} = 0$ and $v = 0$ everywhere in the computational domain.The validation case is the same as in Masud and Hughes (2002), Nakshatrala et al. (2006) and Correa and Loula (2007) for a cube

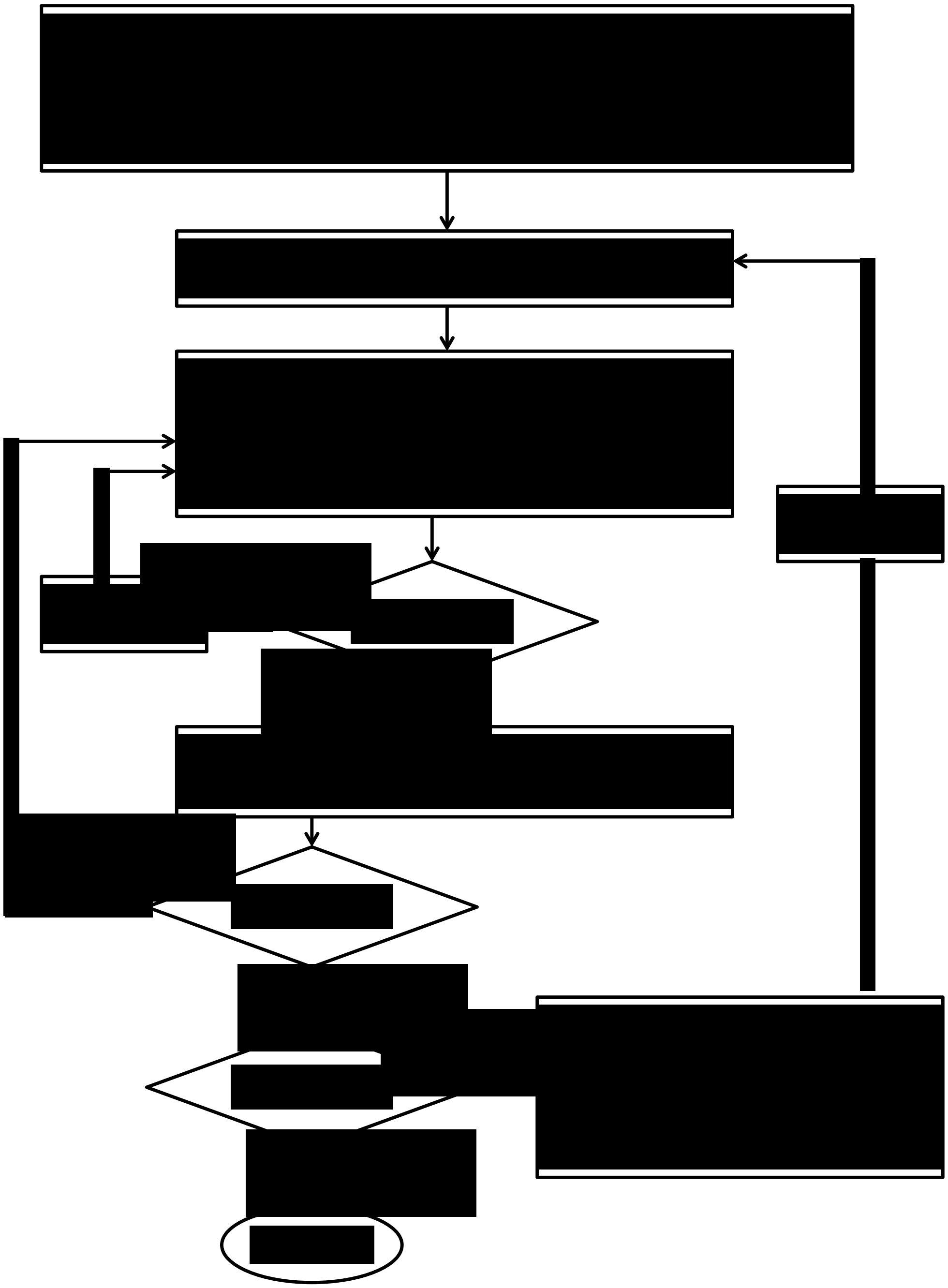

Figure 3.10: Numerical algorithm for solution of developed coupled model for hydraulic fracturing simulation

of unit length i.e. $\Omega = [1, 0] \times [1, 0] \times [1, 0]$. The exact pressure solution is given by

$$p(x, y, z) = \sin(2\pi x)\sin(2\pi y)\sin(2\pi z) \tag{3.66}$$

It is assumed that $K = I$, $\rho = 0$ and $\mu = 0$. I is the identity matrix. Substituting Equation 3.66 into Equation 3.5 and neglecting gravity, the fluid velocity is

$$\begin{aligned} q_x &= -2\pi\cos(2\pi x)\sin(2\pi y)\sin(2\pi z) \\ q_y &= -2\pi\sin(2\pi x)\cos(2\pi y)\sin(2\pi z) \\ q_z &= -2\pi\sin(2\pi x)\sin(2\pi y)\cos(2\pi z) \end{aligned} \tag{3.67}$$

The steady state problem is solved so that $\frac{1}{M} = 0$ and the source term becomes

$$\begin{aligned} q_{rs} = \nabla \cdot \vec{q} &= \Big(\frac{\partial u}{\partial x} + \frac{\partial v}{\partial y} + \frac{\partial w}{\partial z}\Big) \\ &= 12\pi^2\sin(2\pi x)\sin(2\pi y)\sin(2\pi z) \end{aligned} \tag{3.68}$$

Neunmann boundary condition is used by applying the normal component of Equation 3.67 on all boundaries of the domain. Fluid source is implemented as point sources by applying Equation 3.68 over all nodes in the computational domain. The numerical results are shown in Figure 3.11. There is good comparison between the numerical results in Figure 3.11 and exact solution obtained by applying Equations 3.66 and 3.67 on all nodes in the computational domain, as shown in Figure 3.12.

3.6 Flow Model Verification II: Coupled Reservoir Flow and Deformation

3.6.1 Terzaghi's One-Dimensional Consolidation Problem

The developed coupled flow and deformation finite element solution algorithm is first validated with the classical Terzaghi one dimensional consolidation problem. The physical model shown in Figure 3.13, consists of a homogeneous column of soil of dimensions $H \times L$, subjected to a constant load, σ_n, at the top. The sample is fixed at the bottom while the

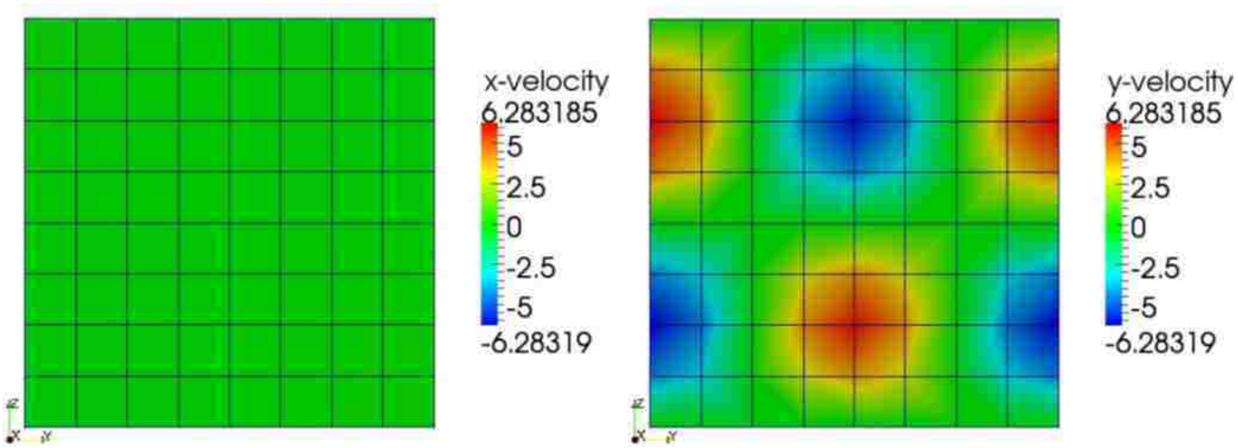

(a) x-velocity (b) y-velocity

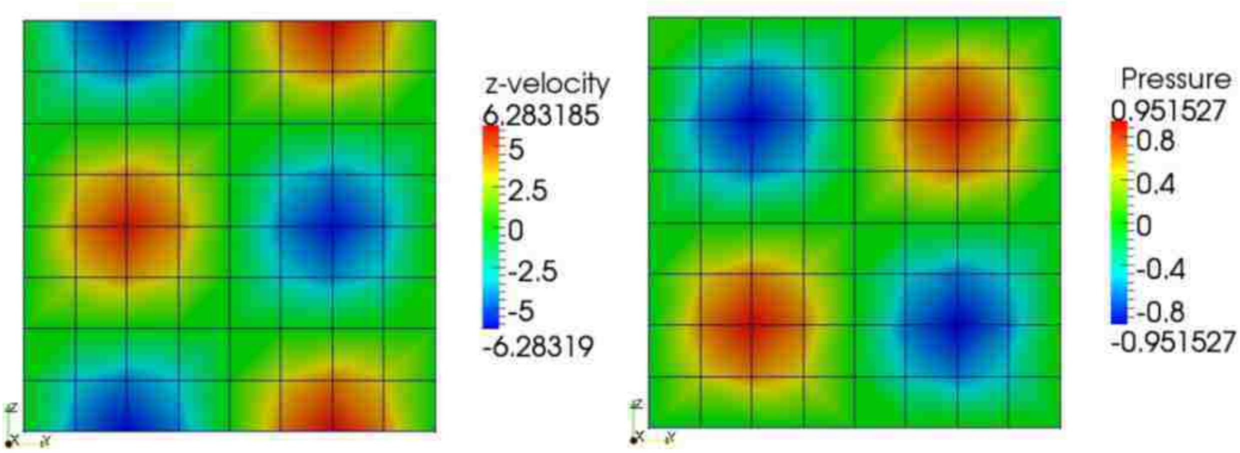

(c) z-velocity (d) pressure

Figure 3.11: Stabilized finite element solution for case 1 at $x = 0.25$.

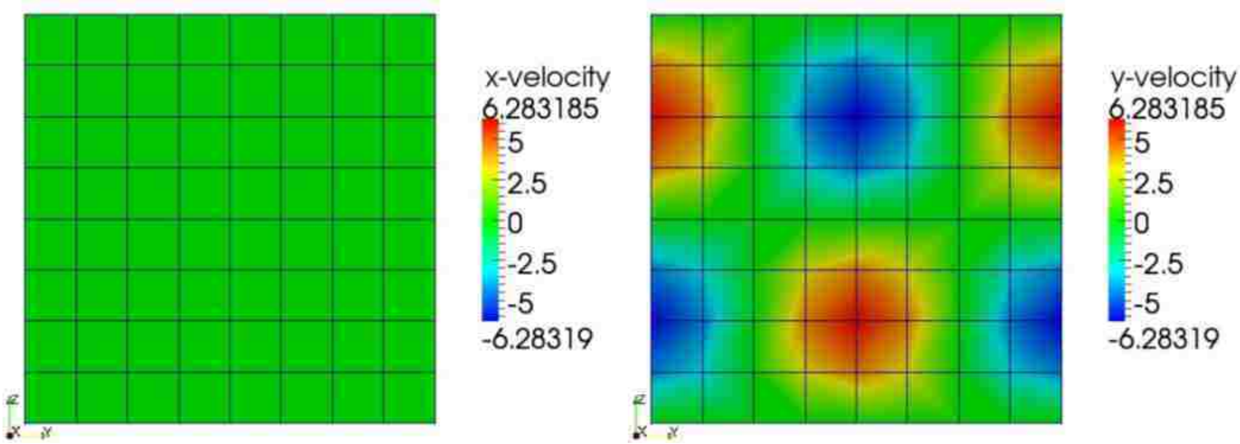

(a) x-velocity (b) y-velocity

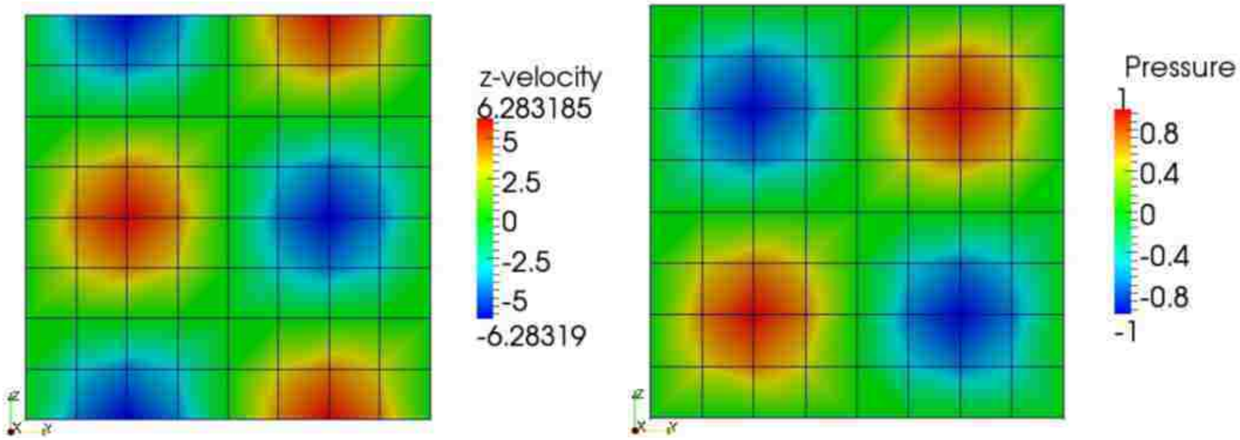

(c) z-velocity (d) pressure

Figure 3.12: Exact solution for case 1 at $x = 0.25$.

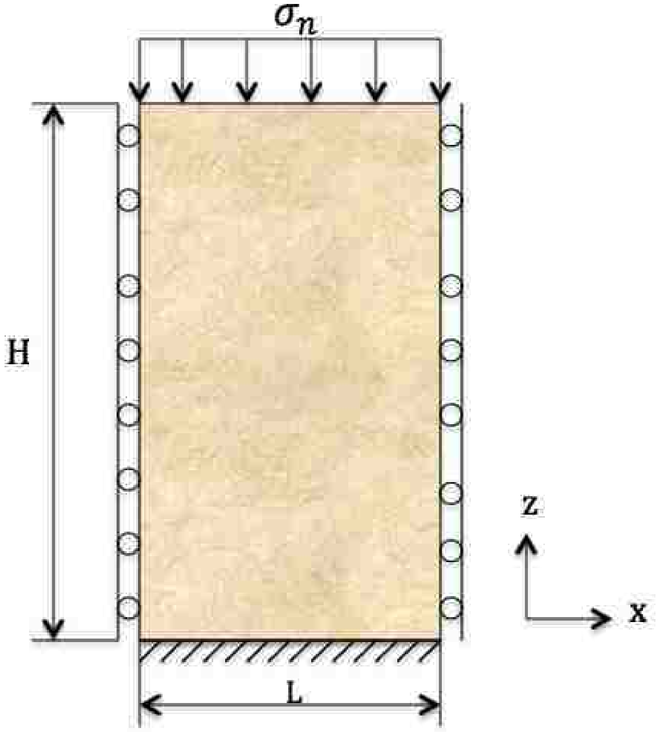

Figure 3.13: Uniaxial consolidation soil column

sides are free to move in the vertical direction. During consolidation, the bottom boundary is impermeable while the top is fully drained, allowing flow of fluid out of the sample. The initial condition for consolidation is the undrained sample state. That is, upon subjecting the soil column to the constant load and not allowing fluid flow through any of the boundaries, the vertical displacement and pore pressure developed are the initial conditions. Subsequent deformation is accompanied by fluid flow through the top and a zero pore pressure boundary condition. During this process, deformation progresses from the undrained to the fully drained state.

Analytical solutions for pore pressure, soil displacement and fluid velocity have been developed by Verruijt (2013), Jaeger, Cook, and Zimmerman (2007) and are summarized as Equations 3.69, 3.70, 3.71 and 3.72.

$$p_o = \frac{\alpha \, m_v}{S + \alpha^2 \, m_v} \sigma_n \tag{3.69}$$

$$p(h-z,t) = p_o \sum_{n=1,3,\dots}^{\infty} \frac{4}{n\pi} \sin(\frac{n\pi\, z}{2h}) \exp(-\frac{n^2\pi^2\, c_v t}{4h^2}) \tag{3.70}$$

$$q_z(h-z,t) = \frac{2\,k}{\mu} p_o \sum_{n=1,3,\dots}^{\infty} \cos(\frac{n\pi\, z}{2h}) \exp(-\frac{n^2\pi^2\, c_v t}{4h^2}) \tag{3.71}$$

$$u_z(h-z,t) = \frac{\sigma_n}{\kappa} \Big[(z-h) + \frac{\alpha\, p_o\, h}{\sigma_n} \sum_{n=1,3,\dots}^{\infty} \frac{8}{n^2\pi^2} \cos(\frac{n\pi\, z}{2h}) \exp(-\frac{n^2\pi^2\, c_v t}{4h^2})\Big] \tag{3.72}$$

Where

$$\begin{aligned} m_v &= \frac{1}{\kappa} \\ S &= \frac{1}{M} \\ c_v &= \frac{k}{\mu(S + \alpha^2\, m_v)} \end{aligned} \tag{3.73}$$

p_o is the initial pore pressure while $p(h-z,t)$, $q_z(h-z,t)$ and $u_z(h-z,t)$ are pressure, vertical fluid velocity and displacement in the soil sample during the consolidation stage.

The data in Table 3.1 were used in the numerical computation. The results are shown in Figures 3.14, 3.15, 3.16, where analytical solutions are lines while numerical results for a computational domain size of 5×21 and 1 s time steps are the circles. There is a good match between analytical solutions and the numerical results from the coupled solution algorithm. As seen in Figure 3.14, a constant initial pore pressure is developed in the sample in the undrained state and as drained deformation progresses, pore pressure diminishes gradually, maintaining a constant value of zero at the top as fluid flows out of the material. The long time solution is a uniform pore pressure of zero, the completely drained state for which all fluid has been expelled from the material. Soil displacement in Figure 3.15 increases as fluid is withdrawn from the material since the effective stress on the grains increases while fluid velocity in Figure 3.16 progressively decreases with pore pressure decrease, as less fluid is left in the soil.

Table 3.1: Parameters for one dimensional consolidation problem

Parameter	Value
E	1.44×10^4 MPa
ν	0.2
α	0.79
M	1.23×10^4 MPa
μ	122 cp
k	$2 \times 10^{-13}\ m^2$
σ_n	4 MPa
H	3 m
L	2 m

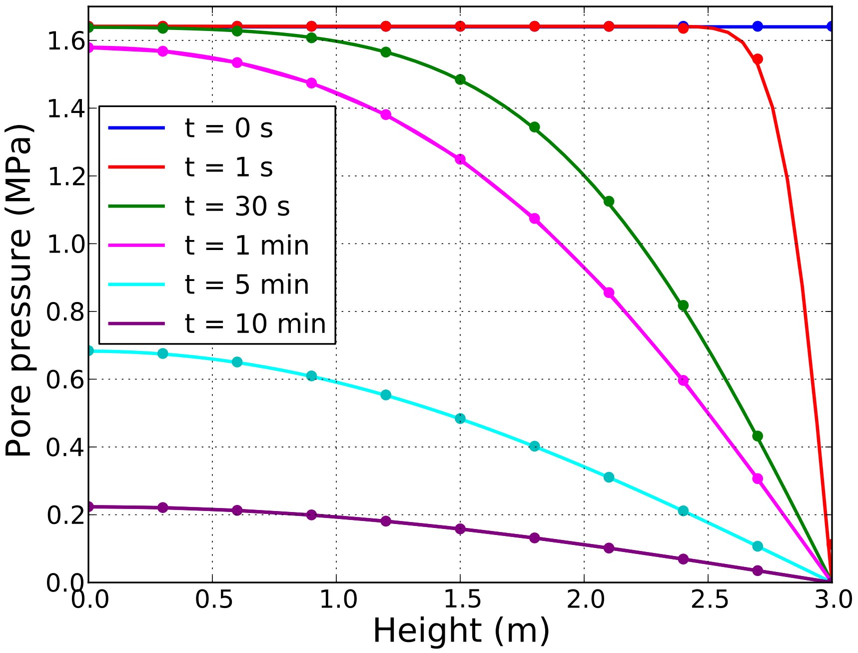

Figure 3.14: Uniaxial consolidation pore pressure

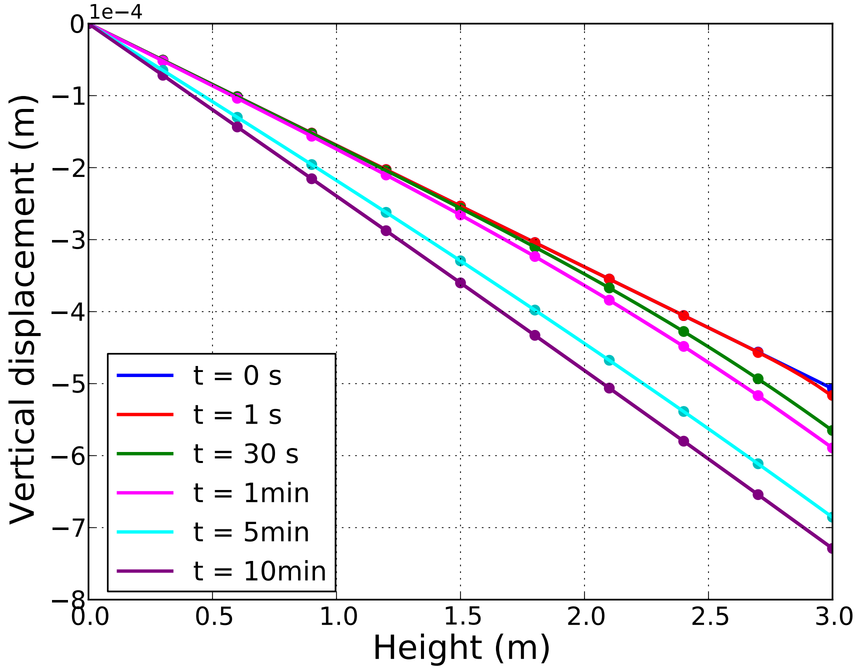

Figure 3.15: Uniaxial consolidation displacement

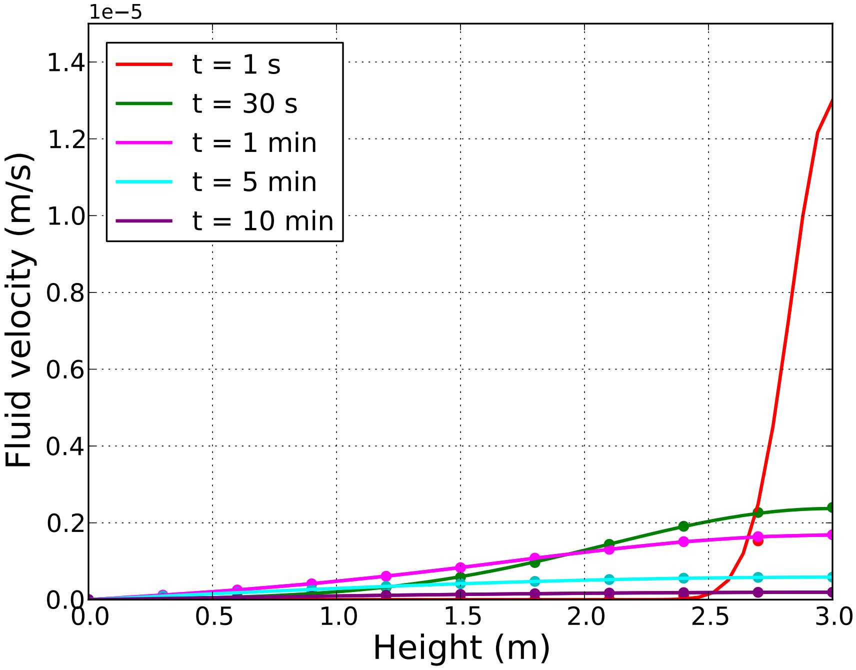

Figure 3.16: Uniaxial consolidation fluid velocity

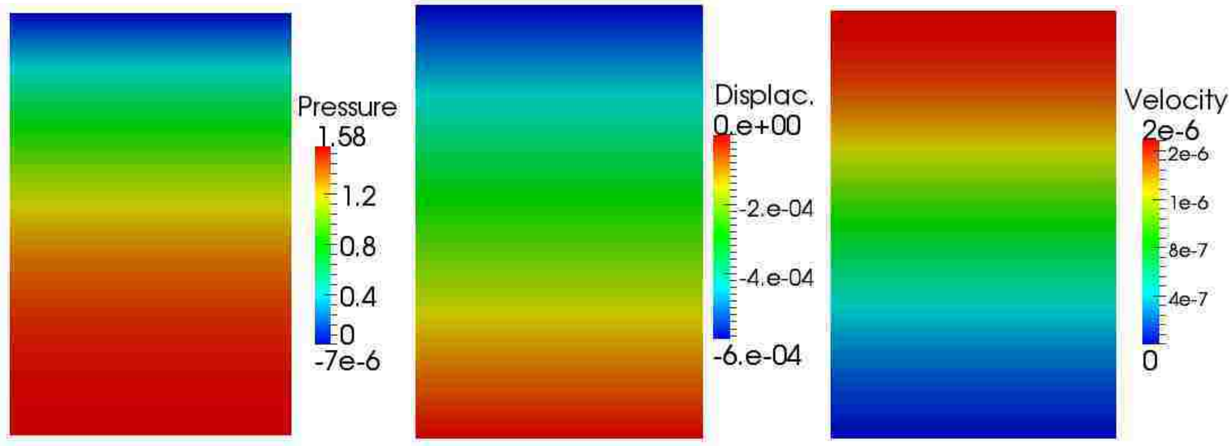

(a) Pressure (b) Vertical displacement (c) Vertical fluid velocity

Figure 3.17: Snapshot of pore pressure, vertical displacement and vertical velocity in Terzaghi's uniaxial consolidation problem

3.6.2 Case 2: Mandel Cryer Two-Dimensional Consolidation Problem

Mandel's problem (Mandel 1953) is commonly used to validate coupled flow and deformation algorithms since it admits an analytical solution (Abousleiman et al. 1996; Detournay and Cheng 1988; Phillips 2005; Lee 2008; Wang 2000; Coussy 2004) for a two dimensional problem on a finite domain. The physical model of the problem is shown in Figure 3.18. It consists of a long rectangular saturated soil sample with dimensions $2a \times 2b$ held between two rigid, frictionless and impermeable plates placed at the top and bottom of the sample. A constant force $2F$ is applied to the rigid plates under plane strain conditions while the lateral sides are free from stress and pore pressure. The initial conditions for consolidation are the instantaneous deformation condition at $t = 0$, obtained by applying the force $2F$ on the plates without allowing drainage from all sides of the sample. The rigid plates simplify the problem as all variables (pore pressure, vertical stress, vertical and horizontal displacements) are independent of the z-direction. In addition, it implies that the force $2F$ is distributed across the plate so that integral of the total stress on that part of the boundary is equal to 2F, as in Equation 3.80.

The numerical model assumes both fluid and solid are incompressible i.e $\frac{1}{M} = 0$, $B = 1$ and $\nu_u = 0.5$, as shown in Table 3.2 for fluid and rock properties. For this case, analytical

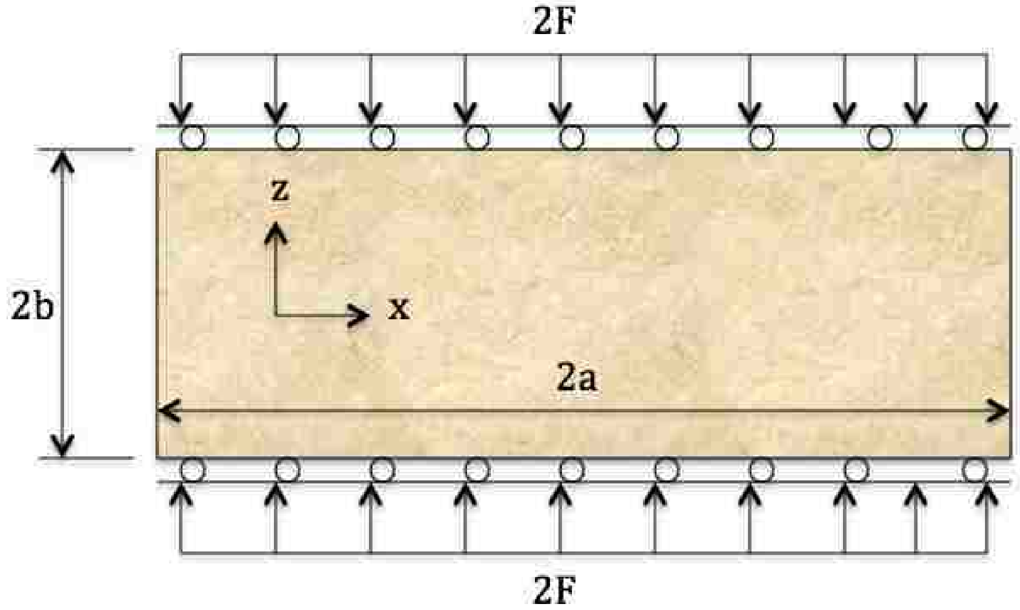

Figure 3.18: Model of Mandel's problem

solutions are taken from Mandel (1953) and Detournay and Cheng (1988) for comparison with the numerical solutions. Equations 3.74 and 3.75 gives the instantaneous pore pressure ($p(0^+)$) and vertical displacement ($u_z(x, b, 0^+)$) of the sample upon application of the confining forces while Equations 3.76 and 3.77 are the analytical pore pressure and vertical displacement during the consolidation stage.

$$\frac{a\,p(0^+)}{F} = \frac{B(1+\nu_u)}{3} \tag{3.74}$$

$$u_z(x, b, 0^+) = -\frac{F(1-\nu_u)b}{2Ga} \tag{3.75}$$

$$p(x,t) = \frac{2FB(1+\nu_u)}{3a} \sum_{i=1}^{\infty} \frac{\sin\alpha_i}{\alpha_i - \sin\alpha_i \cos\alpha_i} \Big(\cos\frac{\alpha_i x}{a} - \cos\alpha_i \Big) \exp\left(-\alpha_i^2 ct/a^2\right) \tag{3.76}$$

$$u_z = \left[-\frac{F(1-\nu)}{2Ga} + \frac{F(1-\nu_u)}{Ga} \sum_{i=1}^{\infty} \frac{\sin\alpha_i \cos\alpha_i}{\alpha_i - \sin\alpha_i \cos\alpha_i} \exp\left(-\alpha_i^2 ct/a^2\right) \right] z \tag{3.77}$$

Where

$$c = \frac{2kB^2G(1-\nu)(1+\nu_u)^2}{9\mu(1-\nu_u)(\nu_u-\nu)} \tag{3.78}$$

Table 3.2: Parameters for Mandel's problem

Parameter	Value
E	1 MPa
ν	0.2
α	1
M	∞ MPa
μ	1 MPa s
k	1 m^2
F	2.5 MN
a	2.5 m
b	1 m
B, ν_u	1, 0.5

$$\tan \alpha_i = \frac{1-\nu}{\nu_u - \nu} \alpha_i \tag{3.79}$$

Due to the symmetry of the problem geometry, only the top half of the physical model is used in the finite element simulation of the problem. It is discretized with 51 × 5 nodes with a time step size of 0.01 s. At $t = 0$, no flow boundary condition is implemented on all sides of the domain while the bottom is fixed. At $t > 0$, zero pressure is implemented on the lateral sides of the sample to allow for fluid drainage.

The variational fracture code is not capable of implementing a rigid motion boundary condition. As a result, a displacement boundary condition is used at the top to vertically displace the sample by an amount equivalent to applying the force $2F$. This displacement is given by Equation 3.84 which is derived as follows. From Equation 3.81 which is the strain-stress relationship from the theory of linear poroelasticity, the plane strain poroelasticity equation, Equation 3.82, is obtained by considering that $\epsilon_{yy} = 0$ and $\sigma_{xx} = 0$ everywhere in the sample (Detournay and Cheng 1993). Equation 3.83 is obtained by combining Equation 3.82 with Equation 3.81 applied to the z-direction. Finally, Equation 3.83 is integrated over [-a, a] range and after substituting Equation 3.80 into the integral, Equation 3.84 is obtained.

$$\int_{-a}^{a} \sigma_{zz} = 2F \tag{3.80}$$

$$2G\epsilon_{ij} = \sigma_{ij} - \frac{\nu}{1+\nu}\sigma_{kk}\delta_{ij} + \frac{\alpha(1-2\nu)}{1+\nu}p\delta_{ij} \tag{3.81}$$

$$\sigma_{yy} = \nu\sigma_{zz} + \alpha(1-2\nu)p \tag{3.82}$$

$$2G\epsilon_{zz} = (1-\nu)\sigma_{zz} + \alpha(1-2\nu)p \tag{3.83}$$

$$u_z(b,t) = \frac{b}{4Ga}\Big[2(1-\nu)F + \alpha(1-2\nu)\int_{-a}^{a} p(x,t)\Big] \tag{3.84}$$

The pore pressure and vertical displacement obtained from finite element numerical results are compared with the analytical solutions. In Figure 3.19, an instantaneous pore pressure value of 0.5MPa is developed through out the sample. As deformation progresses during the consolidation stage, pore pressure gradually diminishes in the sample, with a maximum value at the sample center and zero at the sides. The numerical pore pressures closely match the analytical results and it is evident from the plots that at large times, the pore pressure will eventually reduce to zero everywhere in the sample. At that stage, all the fluid would have been expelled from the soil. Figure 3.22 shows the pressure distribution over the computational domain at $t = 6$ s. The numerical result of the pressure in the sample center, shown in Figure 3.20, properly captures the well known Mandel Cryer effect in which the pore pressure at the center increases above the initial value of 0.5MPa for small times after initial application of the compression force. The reason for this behavior which is reported to have been observed in laboratory experiments (Verruijt 2013), is explained by Mandel (Mandel 1953). Numerical and analytical solution of the vertical displacement of the sample is shown in Figure 3.21. In this figure, the sample initially deforms in the undrained state with $u_z = -0.6$ m. Thereafter, it progressively deforms to the fully drained state with $u_z = -0.96$ m as $p \to 0$. Figure 3.22 highlights the pore pressure developed in the sample after 6 s of consolidation.

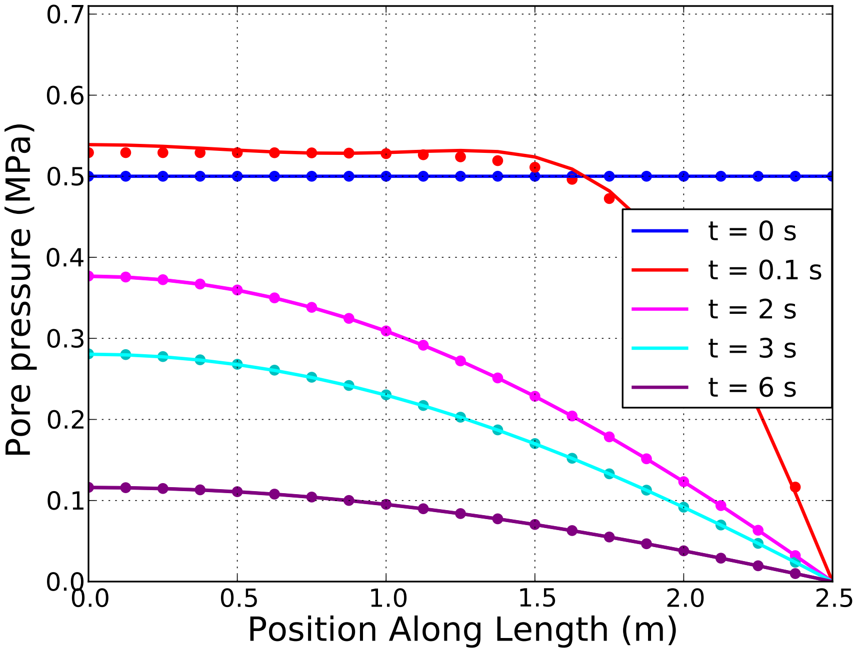

Figure 3.19: Mandel's problem pore pressure vs. time

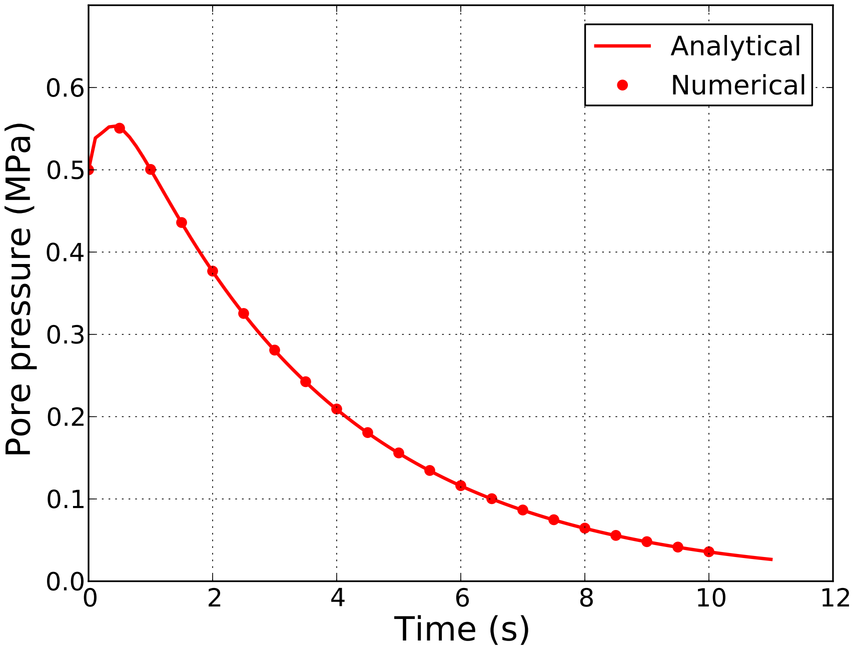

Figure 3.20: Pore pressure developed at the center of soil sample in Mandel's problem, during consolidation stage

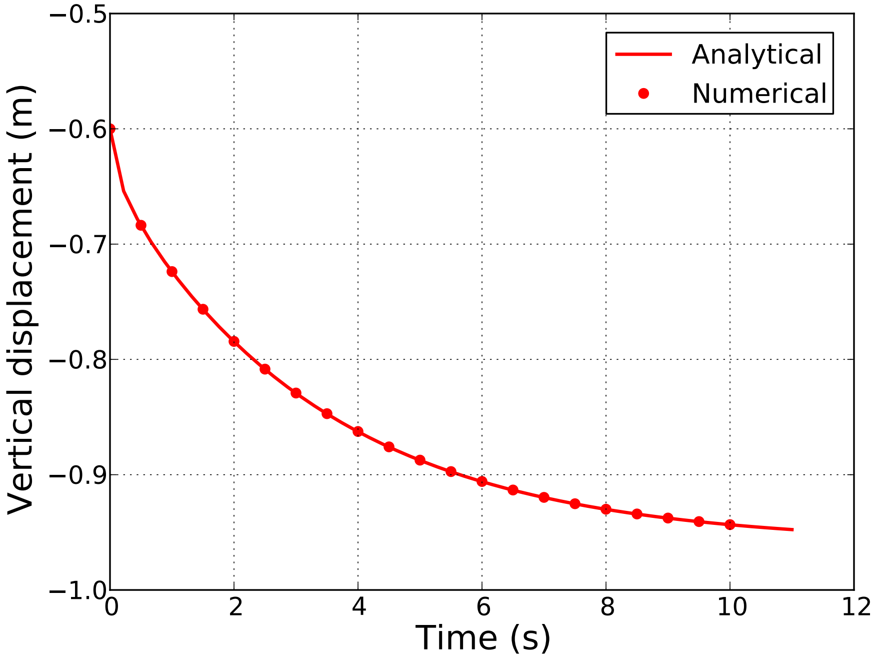

Figure 3.21: Vertical displacement of soil sample in Mandel's problem during, consolidation stage

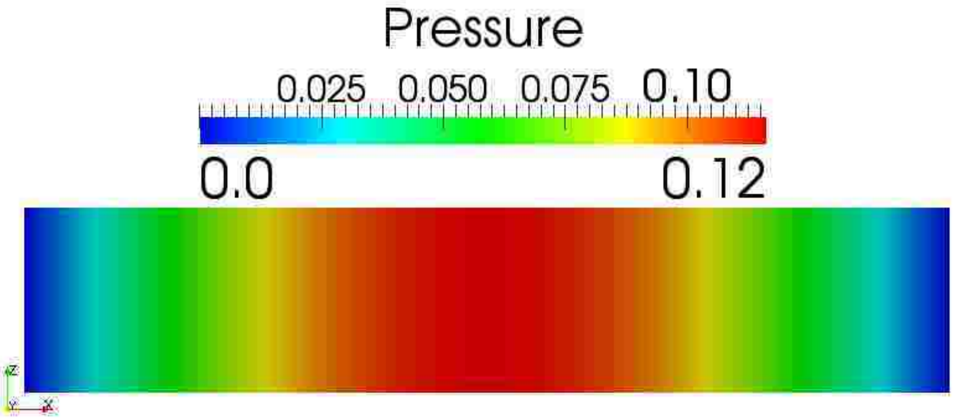

Figure 3.22: Developed pore pressure in soil sample in Mandel's problem at t = 6 s

Chapter 4
Numerical Hydraulic Fracturing Simulations

4.1 Introduction

With the coupled model developed in Chapter 3, it is easy to investigate the poroelastic effects and the contributions of fluid and reservoir properties on fracture propagation path, fracture geometry and fracturing fluid pressure. The focus of this chapter is to apply the developed coupled model to a variety of hydraulic fracture propagation problems. First, the numerical model is verified by solving the plane-strain fluid-driven fracture propagation problem under some of the scaling regimes defined by Detournay and Garagash (2003), Hu and Garagash (2010). The geometry of this category of fractures is the KGD model. This class of problems are ideal for verification of hydraulic fracturing numerical simulations since a wide range of analytical and/or semi analytical solutions exist for modeling the evolution of fracture opening displacement, fracture length and fluid pressure as functions of time. Thereafter, the effect of varying reservoir properties on hydraulic fracturing is studied while the propagation of multiple fractures is simulated to understand the stress shadow effect. Finally, penny-shaped fracture propagation in three dimensional reservoirs is simulated to investigate the factors that can affect hydraulic fracture height growth in layered reservoirs.

4.2 Verification of Coupled Model: KGD Fracture Propagation

According to Detournay and Garagash (2003), fracture propagation is governed by two competing energy dissipation mechanisms and two fluid storage mechanisms. The energy dissipation mechanisms are associated with viscous fluid flow and and rock deformation to create fractures, while the fluid storage mechanisms involve fluid storage in the fracture and fluid leak-off into the permeable reservoir. Based on the relative magnitude of the dissipation

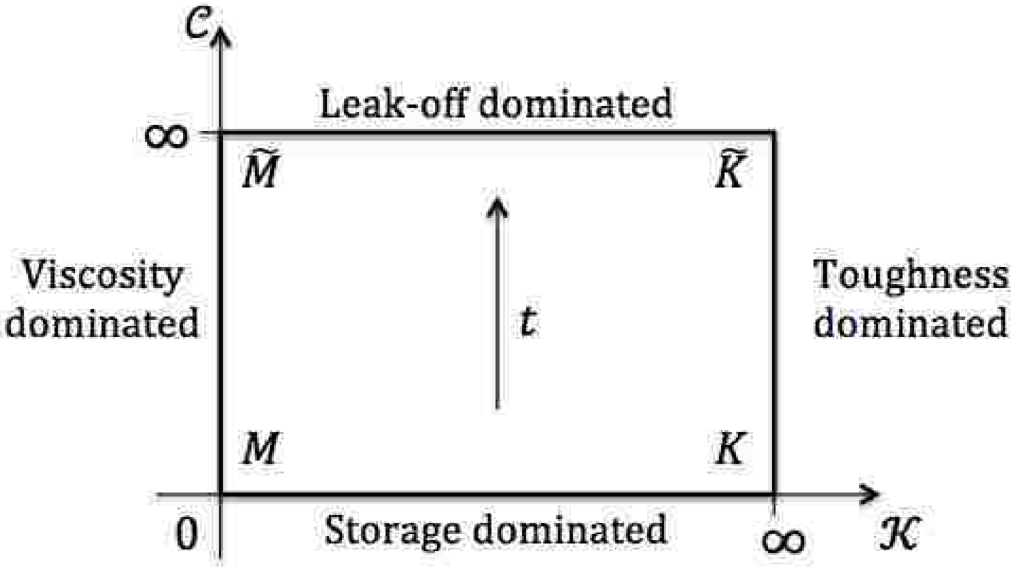

Figure 4.1: Hydraulic fracture parametric space, from Detournay and Garagash (2003)

processes and storage processes, a parametric space of the different propagation regimes was created and is shown in Figure 4.1. The vertices correspond to propagation regimes in which only one of the energy dissipation mechanisms and fluid storage mechanisms dominate. For example, M, K, $\tilde{M}$ and $\tilde{K}$ vertices are the storage-viscosity, storage-toughness, leak-off-viscosity and leak-off-toughness regimes respectively. The verification examples in this dissertation are in the toughness dominated regime (K-vertex) where the energy dissipated in the viscous fluid flow inside the fracture is negligible compared to the energy dissipated in fracturing the rock. The K-vertex is characterized by injection of an inviscid fluid into a fracture in an impermeable reservoir. Analytical and semi-analytical solutions for this regime have been derived in Sneddon and Lowengrub (1969), Hu and Garagash (2010), Bunger, Detournay, and Garagash (2005). The numerical solution for the volume driven propagation in Subsec. 2.4.3 also falls in this region. The coupled model uses finite values of mechanical and flow properties, including fluid viscosity and reservoir permeability. Therefore, to mimic the toughness dominated case, small values of fluid viscosity and reservoir permeability are used. Due to the finite but small fluid viscosity and permeability, the propagation mechanism is no longer characterized by the K-regime, but by the near K-regime. The semi-analytical solution by Garagash (2006) corrects for this deviation from the K-vertex due to small fluid viscosity, providing a good approximation for hydraulic fracturing propagation along the MK edge. For a constant injection rate, Q, the amount of deviation is characterized by a small dimensionless viscosity parameter, $\mathcal{M}$, defined as

$$\mathcal{M} = \frac{\mu' Q}{E'}\Big(\frac{E'}{K'}\Big)^4 \tag{4.1}$$

where $E' = \frac{E}{1-\nu^2}$, $\mu' = 12\mu$, $K' = \sqrt{\frac{32\,G_c E'}{\pi}}$. Given that $\mathcal{M}$ is a dimensionless quantity, its value should be the same even if the parameters in Equation 4.1 are replaced with their respective dimensionless quantities used in the numerical fracture and coupled flow model. Using the scalings of Equations 2.30 and 3.44, $K' = \tilde{K}'\sqrt{G_{c_o}E_o}$, where $\tilde{K}' = \sqrt{\frac{32\,G_c E'}{\pi}}$. Therefore $\mathcal{M}$ becomes

$$\mathcal{M} = \Big(\frac{\mu_o Q_o E_o}{G_{c_o}}\Big)\frac{\tilde{\mu}'\tilde{Q}}{\tilde{E}'}\Big(\frac{\tilde{E}'}{\tilde{K}'}\Big)^4 = x_o^{N-2}\frac{\tilde{\mu}'\tilde{Q}}{\tilde{E}'}\Big(\frac{\tilde{E}'}{\tilde{K}'}\Big)^4 \tag{4.2}$$

$N = 2$ for the line fracture problem. Therefore,

$$\mathcal{M} = \frac{\tilde{\mu}'\tilde{Q}}{\tilde{E}'}\Big(\frac{\tilde{E}'}{\tilde{K}'}\Big)^4 \tag{4.3}$$

It is obvious from Equations 4.1 and 4.3 that the dimensionless viscosity parameter is the same whether it is computed using dimensionless (simulation) or dimensional (physical) parameters. This findings supports the consistency of the derived dimensional analysis in Appendix A and B. It also shows that the conversion of the numerical simulation parameters and results to their respective dimensional equivalents does not change the hydraulic fracturing propagation regime. $\mathcal{M} = 0$ corresponds to the K-vertex for the injection of an inviscid fluid in a fracture in an impermeable reservoir. Hydraulic fracturing in the K-vertex regime has been numerically simulated in Chapter 2 and verified with Sneddon's solution.

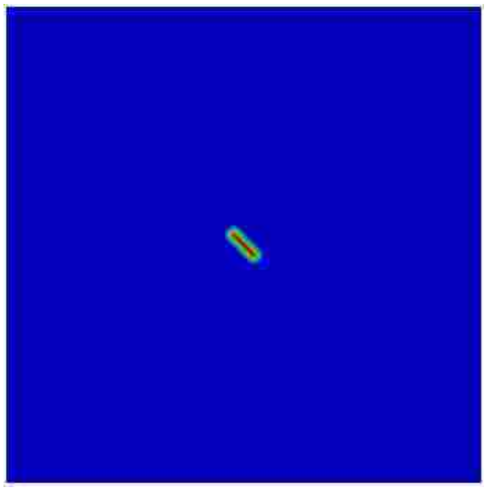

Figure 4.2: Phase field representation of pre-existing fracture used for verification of coupled model. Fracture is inclined at 45° and has initial fracture length of $l_o = 3$ m

Table 4.1: Reservoir properties for verification of coupled hydraulic fracture model. Column D is the dimensionless inputs to the numerical model while column o is the scaling for converting dimensionless parameters to physical values

Parameter	D	o	Physical
x	200	1 m	200 m
u	-	0.014 m	-
p	-	0.014 GPa	-
δt	0.2	1.41 s	0.283 s
E	17	1 GPa	17 GPa
ν	0.2	1	0.2
G_c	5×10^{-4}	2×10^{-4} GPa m	100 Pa m
K	1×10^{-16}	2.83×10^{-6} m^2	2.83×10^{-22} m^2
ϕ	0.2	1	0.2
α	1	1	1
K_s	10	1 GPa	10 GPa
K_f	0.625	1 GPa	0.625 GPa
μ	1×10^{-13}, 1×10^{-7}	4×10^{-6} GPa s	4×10^{-19} GPa s, 4×10^{-13} GPa s
Q_{fs}	0.05	0.01 m^2/s	5×10^{-4} m^2/s

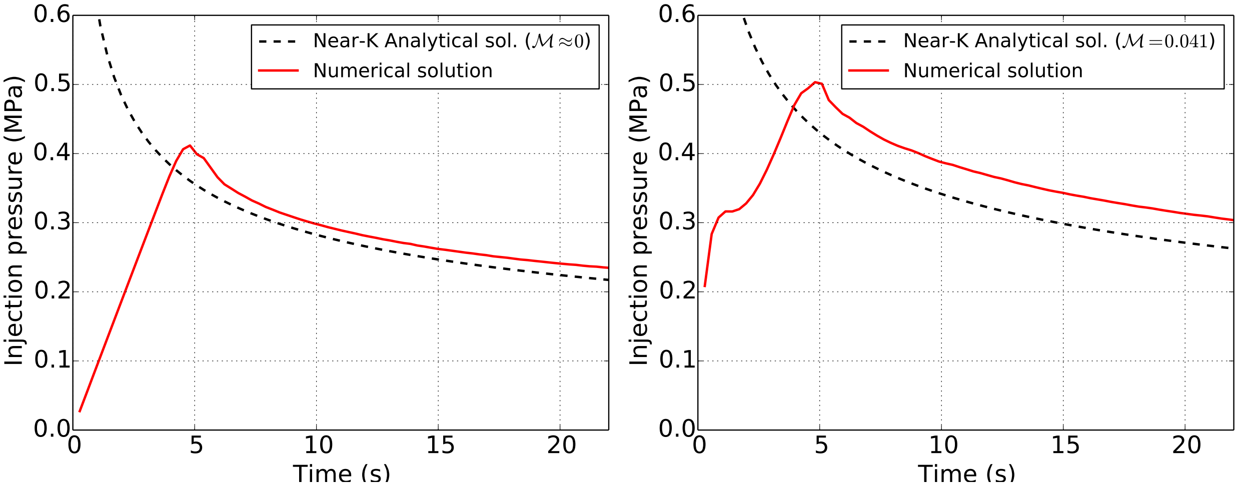

(a) $\mathcal{M} \approx 0$ (b) $\mathcal{M} = 0.041$

Figure 4.3: KGD injection fluid pressure for toughness dominated propagation regime

Figure 4.2 shows the problem domain for the verification case. It is a square of size 200 m × 200 m with an initial fracture of half-length of $l_o = 3$. The pre-existing fracture is inclined at 45° and is located at the center of the domain. Fluid is injected into the center of the fracture at a constant rate of 5×10^{-4} m^2/s. The initial pore pressure is zero everywhere while the boundary conditions are such that pore pressure is zero and displacements are fixed. The reservoir properties and numerical simulation parameters are given in Table 4.1. They are assumed homogeneous and isotropic where applicable.

Using a finite element grid size of 801×801, the numerically obtained fracturing pressure, fracture length and crack mouth opening displacement are compared with the semi-analytical solutions of Garagash (2006). Two fluid cases, $\mu = 4 \times 10^{-19}$ GPa s and 4×10^{-13} GPa s, corresponding to $\mathcal{M} \approx 0.0$ and $\mathcal{M} = 0.041$ are used. Numerical results for computed injection fluid pressure, fracture half length and fracture mouth width are shown in Figure 4.3a, 4.4a, 4.5a for $\mathcal{M} \approx 0.0$ and Figure 4.3b, 4.4b, 4.5b for $\mathcal{M} = 0.041$ respectively. As seen in Figure 4.3a and 4.3b, fracturing injection pressure increases until the critical value is reached and subsequently decreases as the fracture propagates. For $\mathcal{M} \approx 0.0$, a linear pressure evolution is observed prior to fracture propagation unlike the non-linear path for $\mathcal{M} = 0.041$. The deviation from linearity for $\mathcal{M} = 0.041$ is due to the larger fluid viscosity

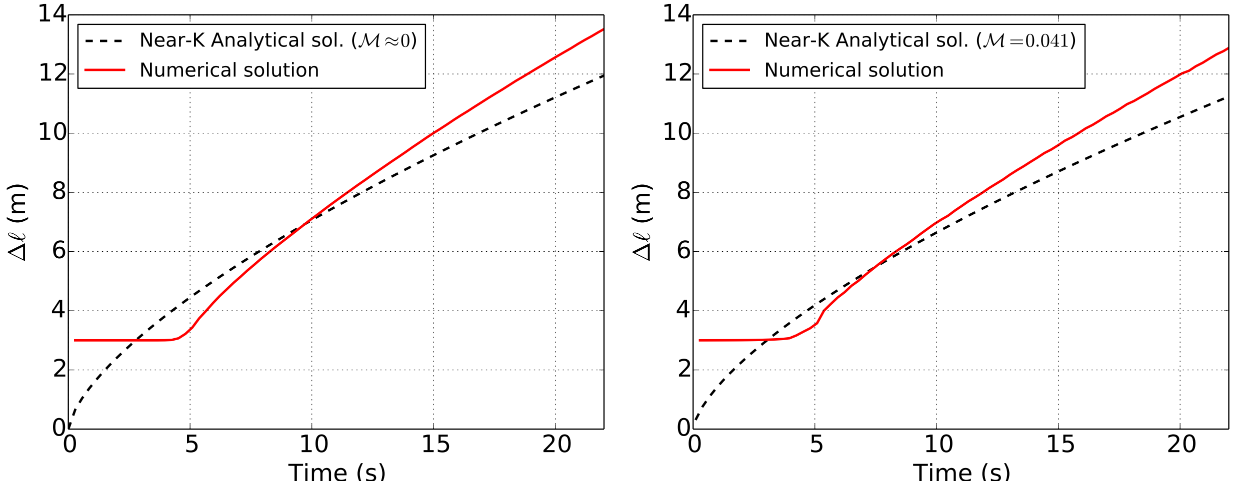

(a) $\mathcal{M} \approx 0$ (b) $\mathcal{M} = 0.041$

Figure 4.4: KGD fracture half length for toughness dominated propagation regime

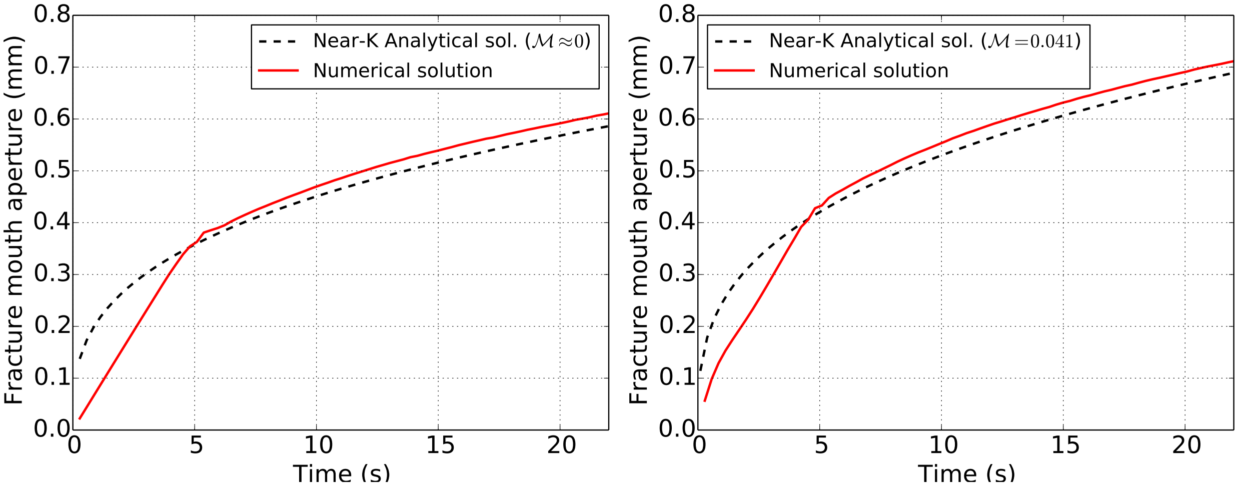

(a) $\mathcal{M} \approx 0$ (b) $\mathcal{M} = 0.041$

Figure 4.5: KGD fracture mouth width for toughness dominated propagation regime

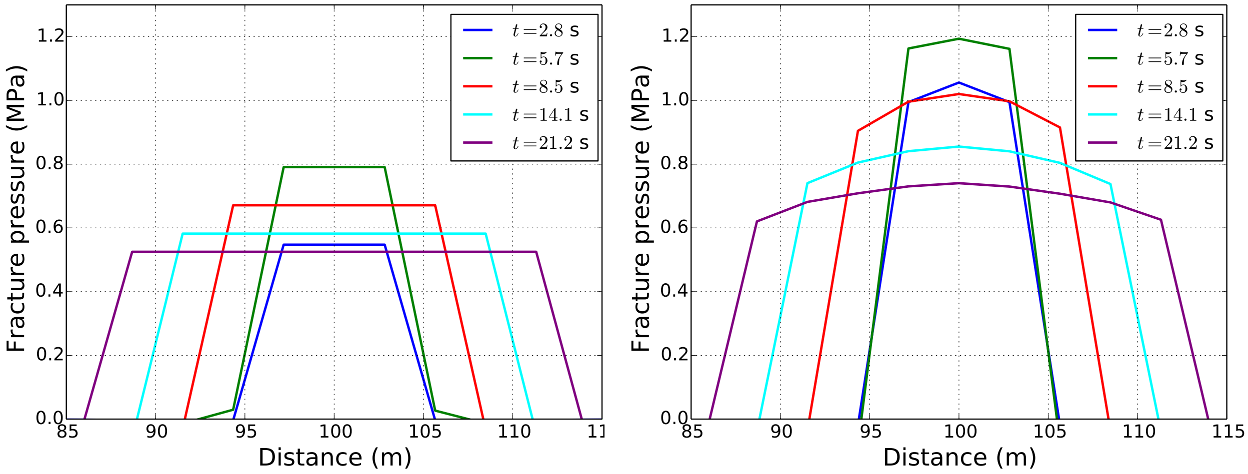

(a) $\mathcal{M} \approx 0$

(b) $\mathcal{M} = 0.041$

Figure 4.6: Fluid pressure profile along the fracture length, for KGD fracture in toughness dominated regime. The fluid pressure is taken on a line that cuts through the center of the fracture and runs across the entire fracture length

for this case. Figure 4.6a which plots time evolution of the pressure inside the fracture along its length, shows a uniform fluid pressure throughout the length of the fracture for $\mathcal{M} \approx 0$. This profile is in agreement with the basic assumption of a constant pressure used in deriving Sneddon's solution for fracture propagation due to injection of an inviscid fluid. On the other hand, Figure 4.6b for $\mathcal{M} = 0.041$ shows a non-uniform pressure with maximum values at the fracture mouth. The higher viscosity creates a pressure gradient inside the fracture which explains the deviation from linearity in the linear elastic regime prior to fracture propagation, as seen in Figure 4.3b. Comparing the results of Figure 4.3a and 4.3b, Figure 4.4a and 4.4b and Figure 4.5a and 4.5b, it is obvious that the larger fluid viscosity generates a shorter fracture with a larger fracture mouth width at a higher injection pressure compared to the same values for a lower fluid viscosity. The time evolution of the fracture opening displacement profile is shown in Figure 4.7a and 4.7b. In addition to a monotonous increase in the normal displacement of the fracture faces for both cases, the fracture opening displacement for $\mathcal{M} \approx 0$ is smaller than those for $\mathcal{M} = 0.041$.

All the plots show fairly good comparisons between the numerical results and the analytical and semi-analytical solutions of Sneddon and Lowengrub (1969) and Bunger, Detournay,

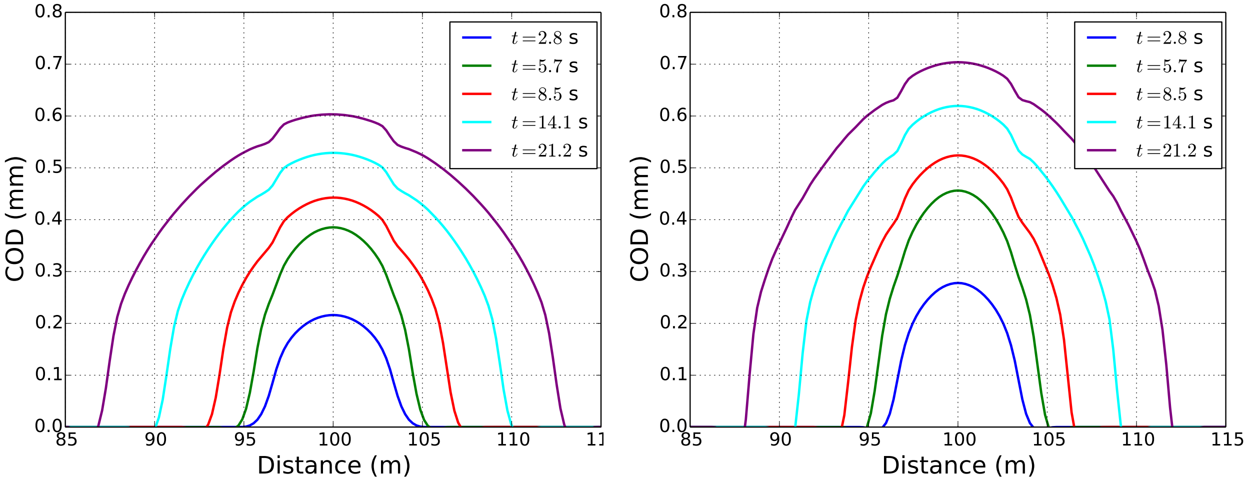

(a) $\mathcal{M} \approx 0$

(b) $\mathcal{M} = 0.041$

Figure 4.7: Opening displacement profile for KGD fracture under toughness dominated regime

and Garagash (2005). The differences between numerical and analytical solutions are acceptable if the following points are considered. First, the analytical solutions are derived for infinite computational domains while the numerical simulations use a finite domain size. To reduce boundary effects on the numerical simulation results, the large computational domain size (200 m × 200 m) relative to the initial fracture length (6 m) is selected. However, this reduces the numerical resolution of the fracture in the computational domain. More importantly, since the fracture location does not need to be known, the numerical flow model is only an approximation considering the various assumptions that have been made in the development of the regularized flow model and in the fracture width computation.

4.3 Effect of Biot's Coefficient on Fracture Propagation

The degree of coupling between reservoir deformation and fluid flow in reservoir during hydraulic fracturing is determined by Biot's coefficient, α. The dependence of fluid pressure and hydraulic fracture dimensions on α is studied by varying α between 0.4 and 1.0. The parameters used for this computation are the same as in Table 4.1 but with $x = 100$ m ($\tilde{x} = 100$), $\mu = 4 \times 10^{-19}$ GPa s, an initial fluid pressure of 0.14 MPa and finite element size of 401 × 401. The numerical results and the analytical solution for $\mathcal{M} = 0$ are shown

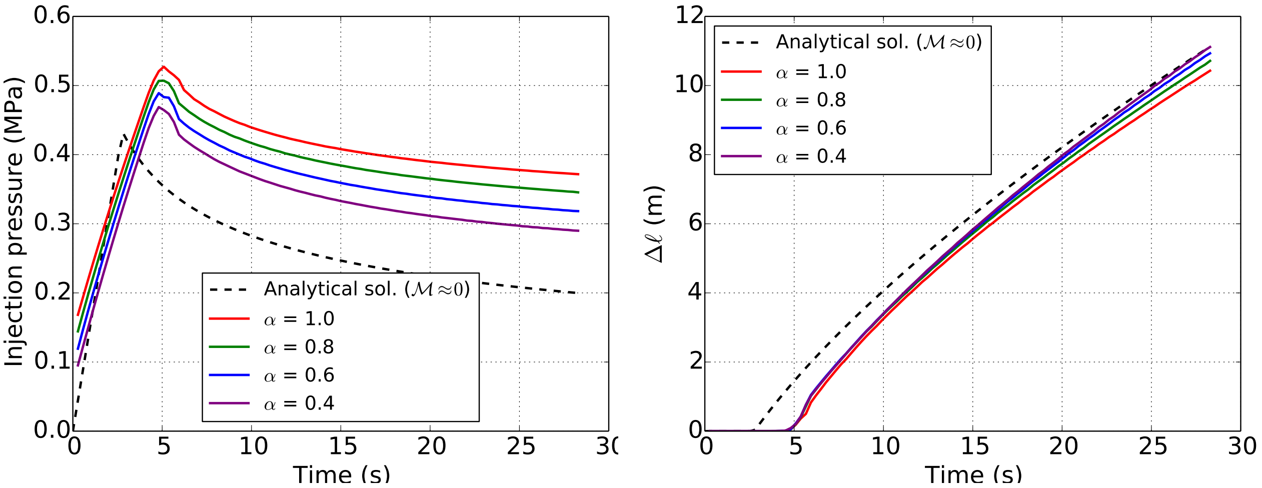

(a) Fracture mouth injection pressure

(b) Change in fracture half length

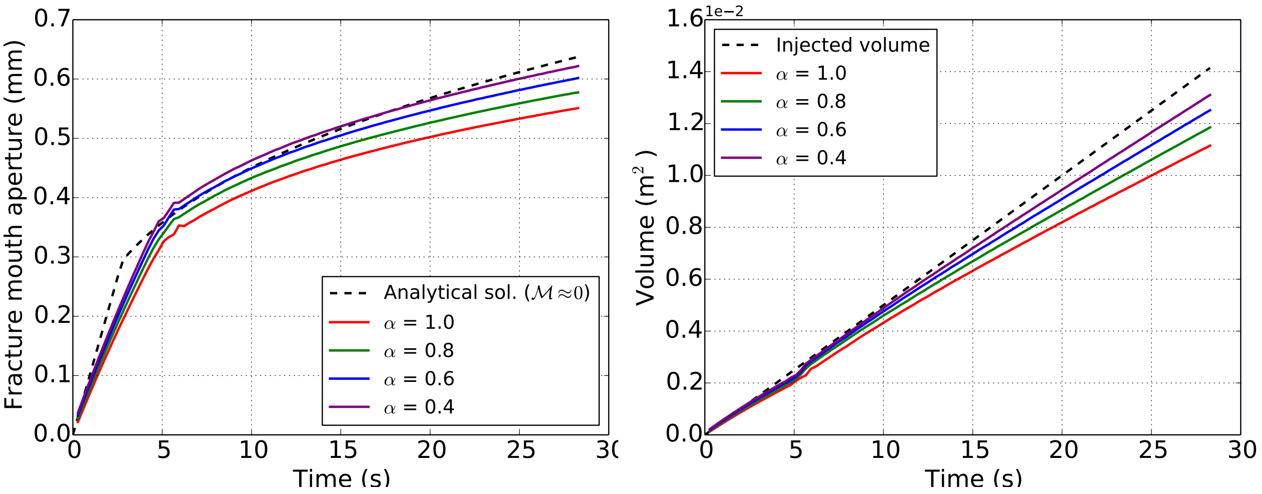

(c) Fracture mouth aperture

(d) Fracture volume

Figure 4.8: Plots of fracturing injection pressure, change in fracture length, fracture mouth aperture and fracture volume for different Biot's coefficients

in Figure 4.8. Figure 4.8a, 4.8b, 4.8c and 4.8d show the time evolution of the injection pressure, change in fracture half length, fracture mouth aperture and fracture volume respectively. The results in this subsection are better understood if one examines the role of poroelasticity. Poroelastic effects on fracture propagation depends on the level of flow and deformation coupling through α. As earlier mentioned, poroelastic effects result from back stresses generated in the region of the reservoir adjoining the fracture. These generated back stresses oppose the fracture deformation and propagation. They are the result of the volumetric expansion of the adjoining reservoir region and the fact that the injection pressure has to overcome the opposing force of the far field reservoir pressure for fracture to propagate. Thus, as α increases in the reservoir, the injection pressure as shown in Figure 4.8a increases, since the fracture fluid has to overcome the opposing reservoir pressure before the fracture starts deforming. In fact, if the fluid pressure plot for $\alpha = 1.0$ is extended to $t = 0$ s, an injection pressure of approximately 0.14 MPa is obtained. This means that fracture fluid injection pressure has to be at least equal to the far field pore pressure for fractures to open.

Biot's coefficient also affects the overall fracture geometry as seen in Figure 4.8b, 4.8c and 4.8d. The fracture half length, fracture mouth aperture and fracture volume all decrease with increasing α, since the increasing contribution of poroelastic effects due to reservoir deformation and far field pore pressure reduces the rate of fracture deformation and propagation. However, for all α values considered, the fractures propagated along the direction of initial orientation.

The numerical computations used small values of reservoir permeability and fluid viscosity while the analytical solutions are for the asymptotic case of zero permeability and inviscid fluid. From the injection pressure plot, one observes that the numerical results approaches the analytical solution as α decreases to zero. This is so since the analytical solution is derived without consideration of poroelastic coupling between the fracture and reservoir. Similarly, the numerical results for fracture length, width and volume tends towards the analytical solution as α decreases.

4.4 Effect of Reservoir Permeability on Fracture Propagation

During hydraulic fracturing operations, the amount of fracture fluid loss to the surrounding reservoir is dependent on the reservoir permeability. Using the phase field flow model, the leak-off coefficient is not required to quantify fluid loss. Rather, fluid loss is implicitly accounted for through the coupling between reservoir and fracture fluid flow. The effect of reservoir permeability on fluid pressure, fracture geometry and propagation direction is investigated in this subsection by two set of numerical simulations with the parameters in Table 4.1 but with $x = 100$ m ($\tilde{x} = 100$) and $\mu = 4 \times 10^{-19}$. In the first experiment, isotropic reservoir permeabilities of $k = 2.8 \times 10^{-21}$ m^2, 5.7×10^{-21} m^2, 1.1×10^{-20} m^2, 1.7×10^{-20} m^2 and 2.3×10^{-20} m^2 respectively are used. For $\mu = 4 \times 10^{-19}$ GPa s, this gives $\frac{k}{\mu} = 7 \times 10^{-3}$, 1.4×10^{-2}, 2.8×10^{-2}, 4.2×10^{-2} and 5.7×10^{-2} in units of m^{2}s^{-1}/GPa. The numerical results and analytical solutions ($\mathcal{M} = 0$) are shown in Figure 4.9 for injection pressure, change in fracture half length, fracture mouth aperture and fracture volume respectively. From Figure 4.9a for fracture mouth injection pressure, one observes that the critical pressures are not significantly affected by reservoir permeability for the chosen fluid viscosity. However, increasing reservoir permeability makes fracture propagation more difficult since the critical time for the onset of propagation is delayed. This delay is due to large fluid loss to the surrounding reservoir for higher permeability computations. As a result, a large amount of fluid will need to be injected to build up enough pressure to propagate the fracture. Correspondingly, the fracture propagation rate is slower for increasing reservoir permeability. In addition, the large fluid loss experienced in higher permeability computations lead to smaller fracture mouth opening and fracture volumes respectively. Increasing fluid leak-off with higher reservoir permeability means that the hydraulic fracture propagates more along the $K\tilde{K}$ edge in Figure 4.1. This deviation from the K-regime is responsible for differences between numerical and analytical results as reservoir permeability increases.

Figure 4.10 shows snapshots of the fracture and fluid pressure in the computational domain for different reservoir permeabilities at 42 s. The top row plots the v-field and

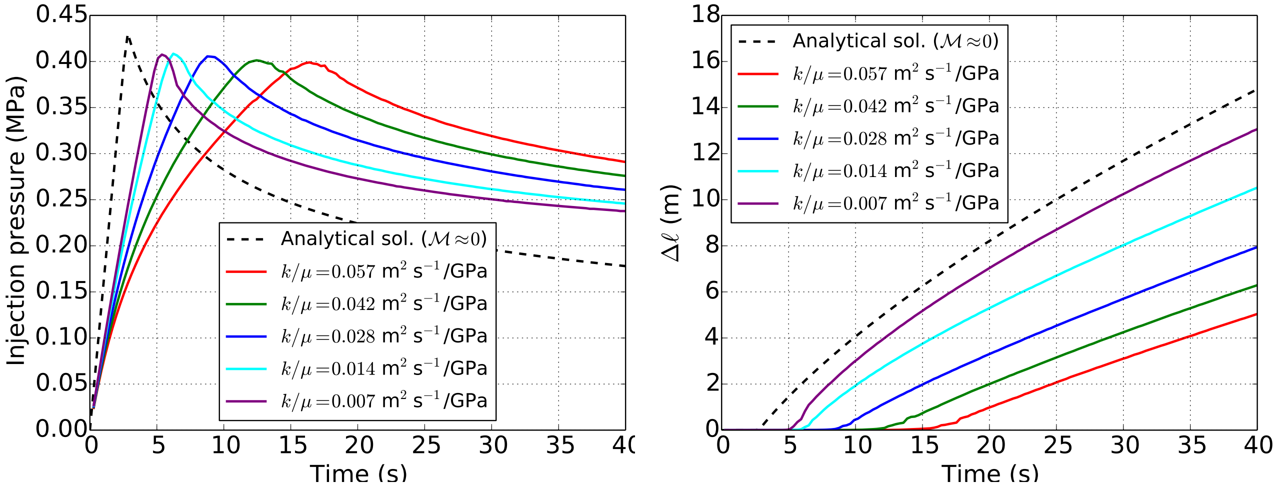

(a) Fracture mouth injection pressure

(b) Change in fracture half length

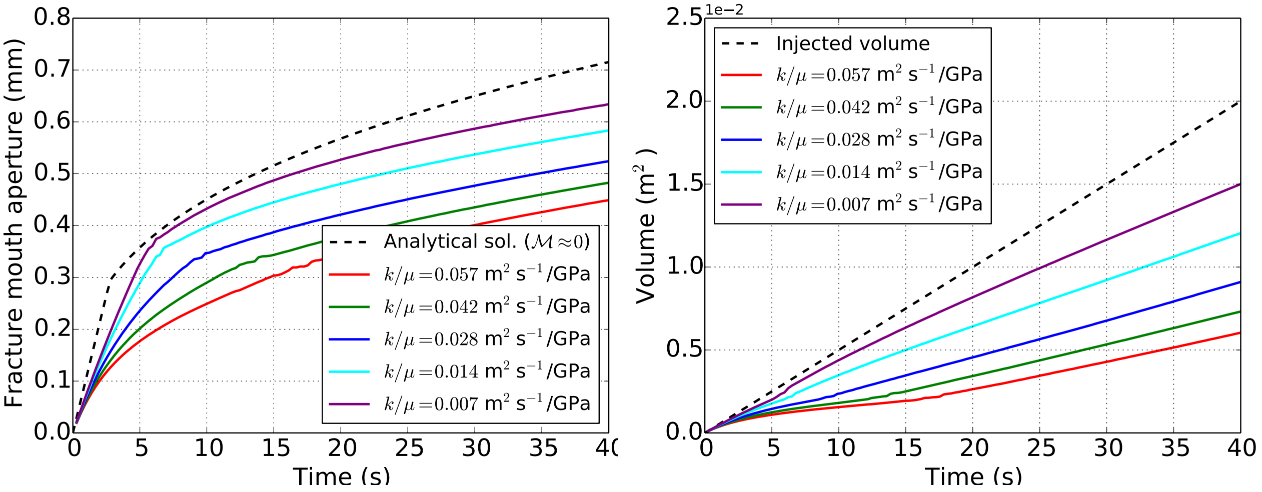

(c) Fracture mouth aperture

(d) Fracture volume

Figure 4.9: Plots of fracturing injection pressure, change in fracture length, fracture mouth aperture and fracture volume for different reservoir permeabilities

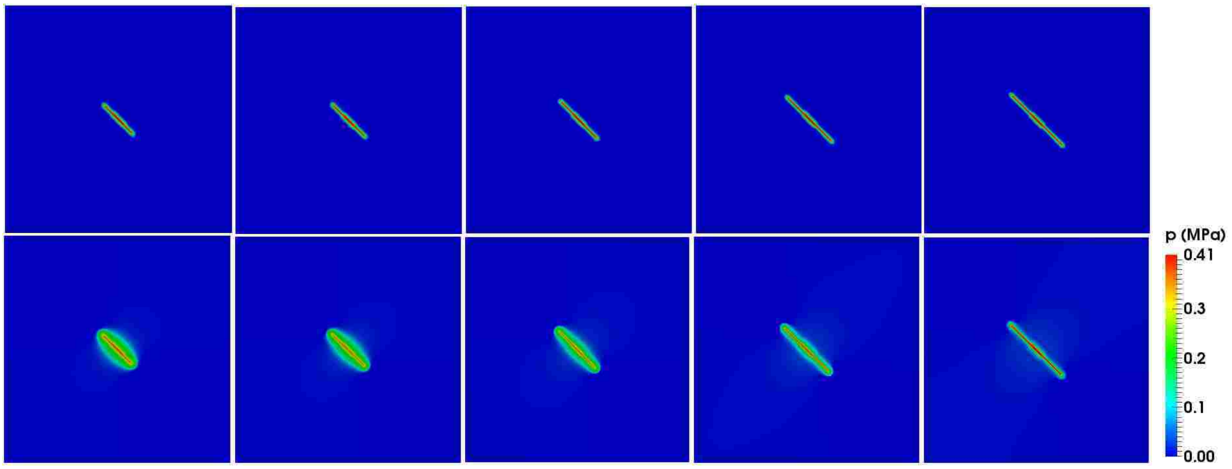

(a) k = 2.3×10^{-20} m^2 (b) k = 1.7×10^{-20} m^2 (c) k = 1.1×10^{-20} m^2 (d) k = 5.7×10^{-21} m^2 (e) k = 2.8×10^{-21} m^2

Figure 4.10: Effect of reservoir permeability on fracture propagation at $t = 42$ s. The top row shows the fracture v-field and one observes that fracture length after 42 s of fluid injection decreases with increasing reservoir permeability. The computed pressure distribution in the bottom row highlights the greater fluid diffusion into the reservoir as permeability increases.

clearly, the fracture length decreases as reservoir permeability increases for the same injection time. In addition, the fluid pressure plots at the bottom row highlights the effect of reservoir permeability on fluid loss. One observes greater pressure diffusion into the reservoir for higher permeabilities compared to those for lower permeabilities. The fluid pressure diffusion into the reservoir is an indication of fluid loss from the fracture to the reservoir.

The second set of numerical computations study the effect of directional variation in reservoir permeability on fracture propagation directions. Anisotropy in reservoir permeability is created by keeping k_z constant at 2.8×10^{-21} m^2 and varying k_x. The numerical results for fracture propagation are shown in Figure 4.11. As propagation initiates, the fracture kinks for anisotropic permeability ratio ($\frac{k_x}{k_z}$) greater than 10. The change in propagation direction occurs since fractures seek directions that offer the least resistance to fluid flow, which in this case, is the horizontal direction ($k_x > k_z$). The kinking angle increases with increasing $\frac{k_x}{k_z}$.

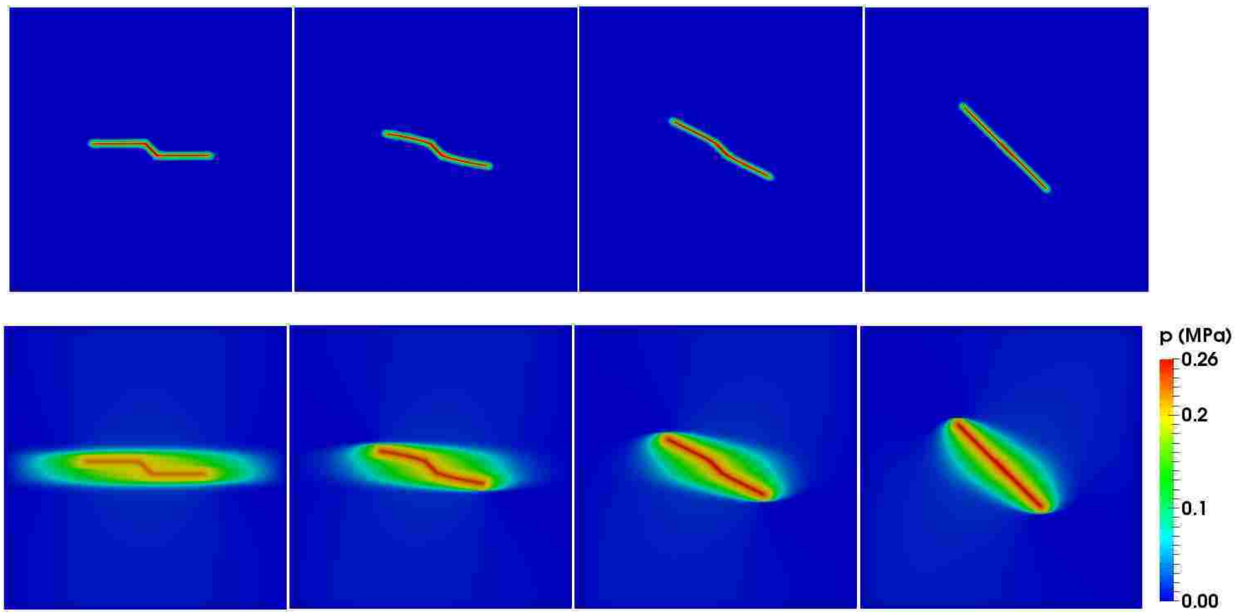

(e) p for $k_x = 5.7\times10^{-19}$ m^2 (f) p for $k_x = 2.3\times10^{-19}$ m^2 (g) p for $k_x = 1.1\times10^{-19}$ m^2 (h) p for $k_x = 5.7\times10^{-20}$ m^2

Figure 4.11: Effect of reservoir permeability anisotropy on fracture propagation patterns. For $k_z = 2.8\times10^{-21}$ m^2 and different k_x values, top row shows the v-field while the bottom row shows pressure distribution in and around fractures.

4.5 Effect of Fluid Viscosity on Fracture Propagation

The fracturing fluid viscosity is important in controlling the rate of fluid loss to the formation during hydraulic fracturing operations. A high viscosity fluid reduces leak-off to the formation. However, when compared to the use of low viscosity fluids, high viscosity fluids generate higher pressure gradients inside fractures. This subsection investigates the role of fluid viscosity on fracture fluid pressure, fracture geometry and fracture propagation. The computational domain, initial and boundary conditions and initial fracture geometry are the same as in Subsec. 4.4. The fluid viscosity used are $\mu = 4\times10^{-15}$ GPa s, 4×10^{-14} GPa s, 4×10^{-13} GPa s, 8×10^{-13} GPa s to 2×10^{-12} GPa s, which corresponds to $\frac{k}{\mu} = 2.5\times10^{-1}$, 2.5×10^{-2}, 2.5×10^{-3}, 1.25×10^{-3} and 5×10^{-4} in units of m^{2}s^{-1}/GPa for 2.8×10^{-21} m^2 reservoir permeability. Other parameters are the same as in Table 4.1. Remember that the e fracturing fluid and reservoir fluid are the same, with the same fluid viscosity. Therefore, the viscosity varied in this subsection is that of the fluid in the whole system.

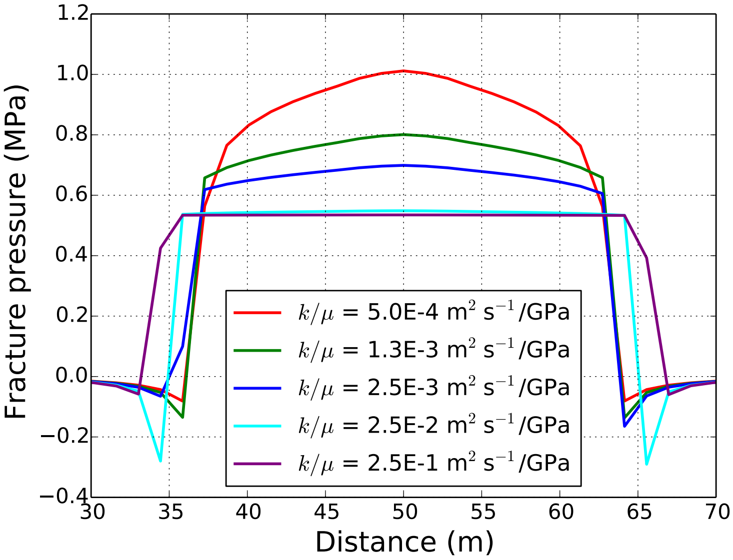

Figure 4.12: Fluid pressure on a line through the center of the fracture for different fluid velocities at $t = 28$ s

Figure 4.12 shows the fluid pressure plotted on a straight line along the fracture length (i.e. the region with $0 \leq v < 1.0$) for different fluid viscosities. The fracture mouth is at 50 m while the results are for t = 28 s. The pressure gradient inside the fracture increases with fluid viscosity, with peak pressure obtained at the fracture mouth followed by a gradual decrease in pressure towards the fracture tip. A uniform fluid pressure profile is obtained for low fluid viscosities, which agrees with the constant pressure assumption used in deriving Sneddon's (Sneddon and Lowengrub 1969) solution for fracturing due to injection of inviscid fluids.

Numerical results for injection pressure, change in fracture half-length, fracture mouth aperture and fracture volume are shown in Figure 4.13. The injection pressure increases with increasing fluid viscosity. As a result, the critical pressures for fracture propagation also increases with fluid viscosity. This means fracture propagation rate is slower with higher fluid viscosity. As the fluid viscosity decreases, the pressure plots tend towards an asymptotic limit. This limit is the K-regime solution for fracture propagation due to injection of inviscid fluid. High fluid viscosity also leads to reduction in fracture length as shown in Figure 4.13b. As shown in Figure 4.13c, for the smaller fracture lengths due to higher viscosity, the fracture

Table 4.2: Reservoir properties for multiple fracture propagation. Column D is the dimensionless inputs to the numerical model while column o is the scaling for converting dimensionless parameters to physical values

Parameter	D	o	Physical
x	200	1 m	200 m
u	-	0.014 m	-
p	-	0.014 GPa	-
δt	0.2	1.41 s	0.283 s
E	17	1 GPa	17 GPa
ν	0.2	1	0.2
G_c	5×10^{-4}	2×10^{-4} GPa m	100 Pa m
k	-	2.83×10^{-6} m^2	-
ϕ	0.2	1	0.2
α	1	1	1
K_s	2	1 GPa	2 GPa
K_f	0.125	1 GPa	0.125 GPa
μ	1×10^{-14}	4×10^{-6} GPa s	4×10^{-20} GPa s
Q_{fs}	0.05	0.01 m^2/s	5×10^{-4} m^2/s

mouth aperture increases. As a result, the fracture geometry created due to injection of high viscosity fluids tends towards a thick-short fracture i.e. short length but large aperture. The plot of Figure 4.13d shows created fracture volumes that are greater than the injected fluid volume. This is the product of numerical errors, due to inadequate computational resolution for the flow problem and for the hydraulic fracture propagation path.

4.6 Multiple Fractures

Field hydraulic fracturing operations involve propagation of multiple fractures from perforation clusters. The ability to model multiple fracture propagation is an attractive feature for any hydraulic fracturing simulation tool. In the variational model, fracture deformation and propagation are captured by evolution of the associated v-field defined over the whole computational domain. Hence, irrespective of the number of fractures, the fracture model easily handles multiple fractures without additional modeling effort than is required for a single fracture.

The coupled hydraulic fracture model leverages this important quality of the variational fracture model to simulate propagation of multiple hydraulic fractures. This capability is

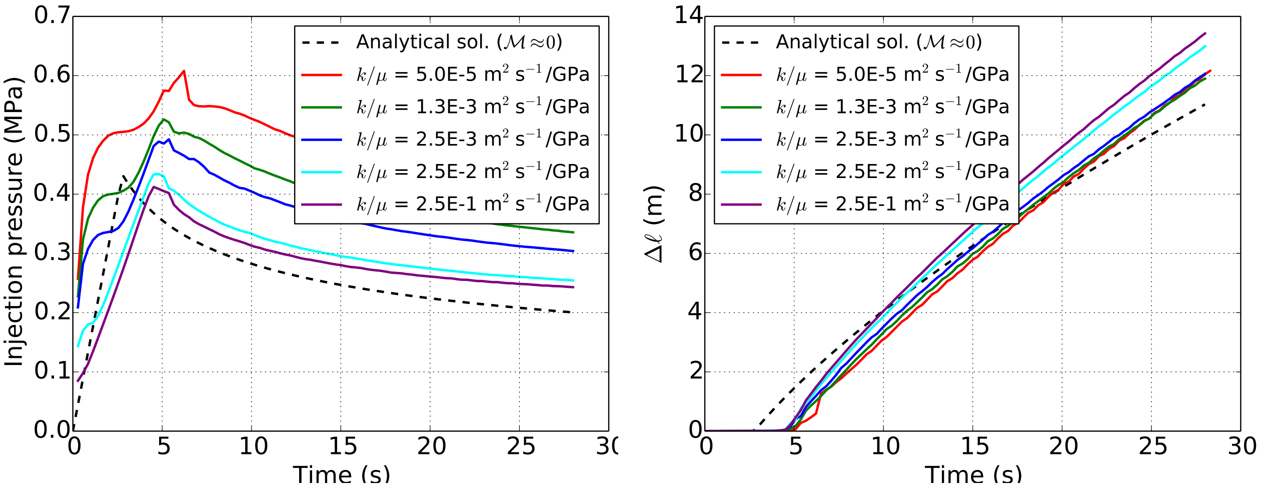

(a) Fracture mouth injection pressure (b) Change in fracture half length

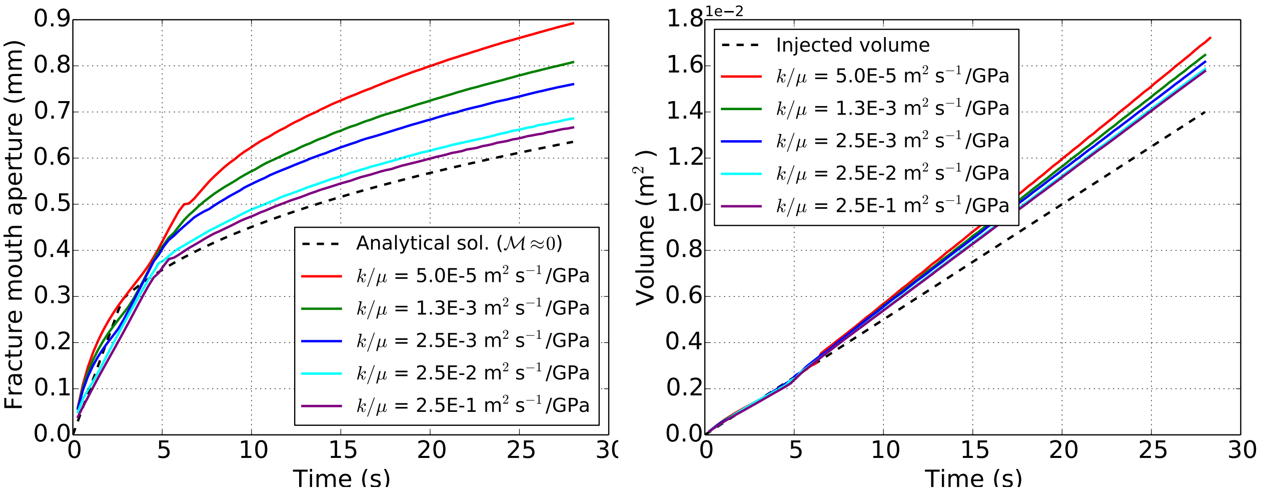

(c) Fracture mouth aperture (d) Fracture volume

Figure 4.13: Plots of fracturing injection pressure, change in fracture length, fracture mouth aperture and fracture volume for different fluid viscosities

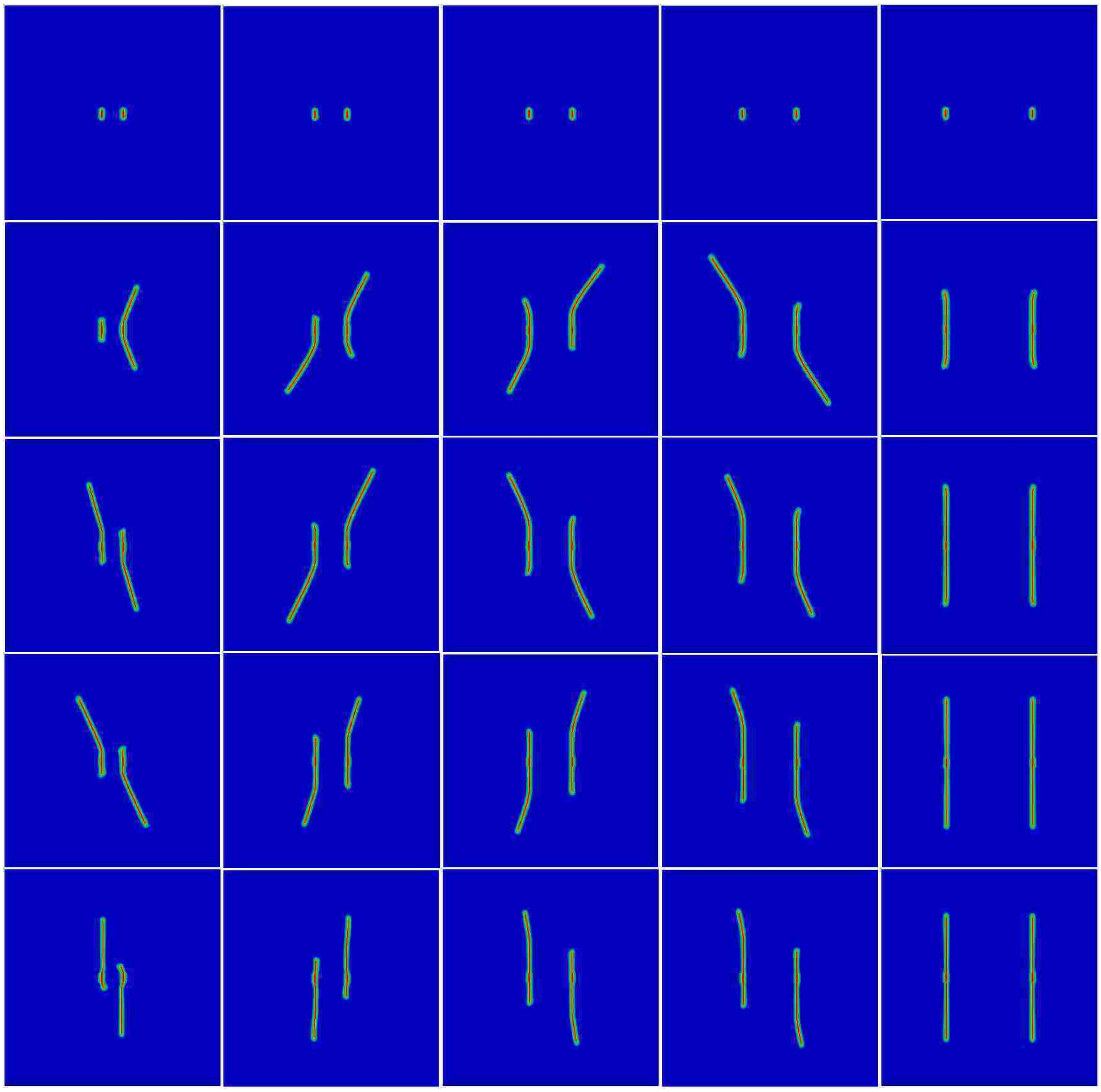

Figure 4.14: Propagation patterns of two pre-existing fractures with injection wells in the center of both fractures. The first to the last columns represent different fracture spacings of 20 m, 30 m, 40 m, 50 m and 80 m respectively. The top to the bottom rows are the v-field representations of the pre-existing fracture and propagated fractures for $k = 1.7\times10^{-20}$ m^2, 5.7×10^{-21} m^2, 2.8×10^{-21} m^2 and 1.4×10^{-21} m^2 respectively

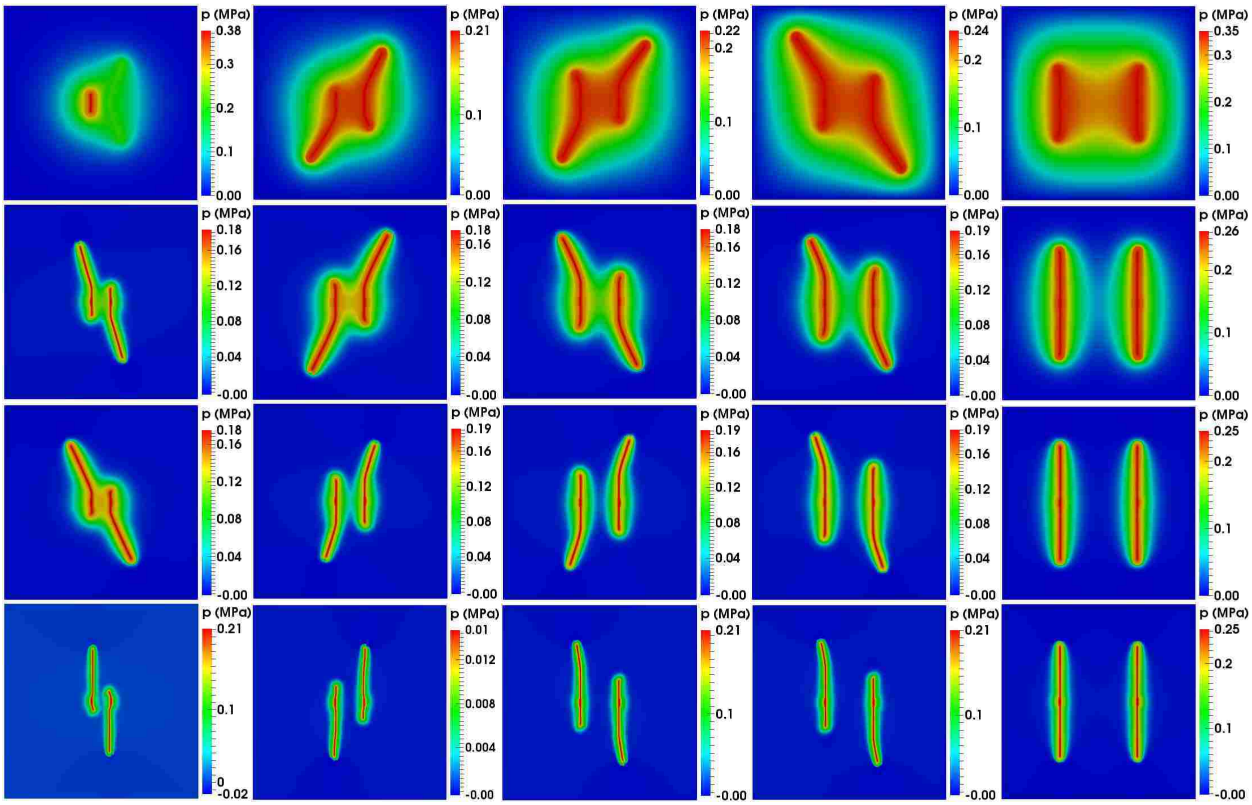

Figure 4.15: Computed fluid pressure for fractures in Figure 4.14. The first to the last columns represent different fracture spacings of 20 m, 30 m, 40 m, 50 m and 80 m respectively. The top to the bottom rows are $k = 1.7\times10^{-20}$ m^2, 5.7×10^{-21} m^2, 2.8×10^{-21} m^2 and 1.4×10^{-21} m^2 respectively

highlighted by considering cases with multiple initial fractures in a reservoir. The first case is for a computation with two initial vertical fractures of lengths of $l_o = 3$ m. Both fractures are centrally located in a computational domain of size 200 m × 200 m. Four different fracture spacings, are considered: 30 m, 40 m, 50 m and 80 m. For each spacing, the reservoir permeability is also varied to study the effect of the reservoir permeability on the propagation of both fractures. For this problem, $K_s = 2$ GPa, $K_f = 0.125$ GPa and $\mu = 1 \times 10^{-20}$ GPa s. Other fluid and material properties are as in Table 4.1. Fluid is injected in the center of both fractures at equal rates of $Q_{fs} = 5 \times 10^{-4}$ m^2/s. The numerical results for fracture patterns and fluid pressure are shown in Figure 4.14 and 4.15 respectively. The first row in Figure 4.14 is the phase field representation of the initial fractures at different fracture spacings while subsequent rows are computations for increasing reservoir permeability i.e. rows two, three, four and five are for $k = 1.7{\times}10^{-20}$ m^2, $5.7{\times}10^{-21}$ m^2, $2.8{\times}10^{-21}$ m^2 and $1.4{\times}10^{-21}$ m^2 respectively. For all computations, the fractures interact by propagating away from each other along curved paths, due to the stress shadow effect. The propagation patterns are such that after initiation, both tips propagate simultaneously along the initial direction for some time. After some length changes, only one fracture tip propagates and away from the other fracture. As fracture spacing increases, the length of the propagated vertical section of the both fractures increases. The curvature of propagation decreases as the fracture spacing increases. This is due to diminishing interaction between both fractures as the influence of the additional confining stresses generated by the presence of the other fracture is diminished by distance. On comparing the patterns from top to bottom for each column, that is for different permeabilities for a particular fracture spacing, one observes that decreasing reservoir permeability reduces fracture curvature and complexity. Note that even though most of the fracture patterns obtained are symmetric or close to been symmetric, the computation for 20 m spacing and $k = 1.7 \times 10^{-20}$ m^2 shows that non-symmetric hydraulic fracture propagations are possible even with uniform reservoir properties. For this particular computation, only the right fracture propagated, creating a shadow around the left fracture which completely inhibits its propagation. Numerically obtained fluid pressure

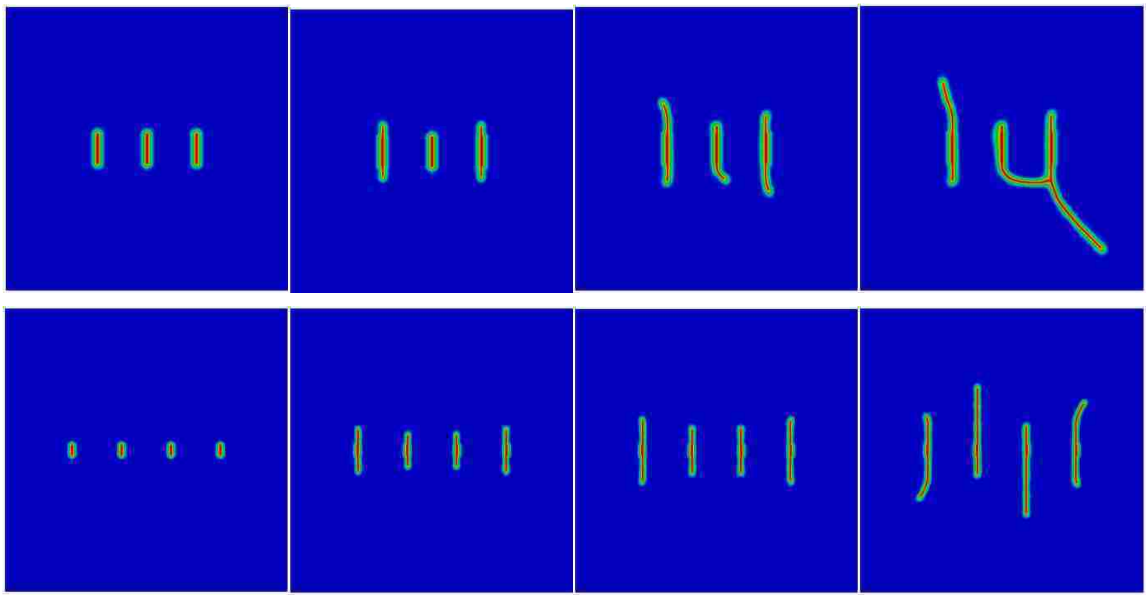

Figure 4.16: Evolution of propagation paths for three and four parallel fractures with fluid injection into the center of each fracture. The top row are snapshots of the v-field for three fractures at 28.3 s, 9.5 mins 14.1 mins and 16.5 mins. The bottom row shows snapshots of the v-field for four fractures at 7.1 s, 4.7 mins, 5.9 mins and 7.1 mins

for all computations are shown in Figure 4.15. According to the pressure diffusion patterns, the interaction between fluid injected in both wells increases with decreasing fracture spacing. With decreasing reservoir permeably, the injected fluid is constrained to both fractures with less leak-off into the surrounding formation.

Numerical simulations for fluid injection into three and four initial fractures were also carried out. The initial fracture half-lengths are 10 m and 3 m for the three and four fracture cases respectively. For both cases, the fracture spacing is 35 m while reservoir permeability is 2.8×10^{-21} m^2. Other parameters are the same as in the previous example for two initial fractures. The numerical results are shown in Figure 4.16 and 4.17. Figure 4.16 highlights the evolution of the propagation of the fractures while Figure 4.17 shows the corresponding fluid pressure distribution in the reservoir. For both examples, at early times, the outside fractures grow faster than the fractures in the center of the configuration. As the outer fractures propagate, they exert compressive stresses on the centrally located fractures which restricts their growth. During this time period, the fracture width of the compressed central fractures is less than those of the outside fractures. The reduced fracture width corresponds

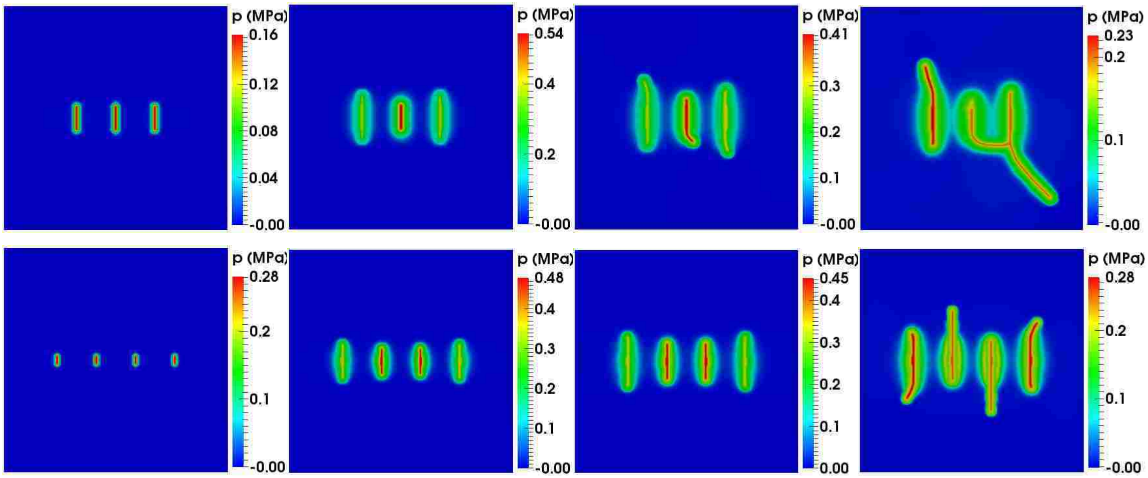

Figure 4.17: Reservoir fluid pressure during the evolution of propagation paths for three and four parallel fractures with fluid injection into the center of each fracture. Top row is snapshot of the pressure distribution during evolution of the three fractures at 28.3 s, 9.5 mins 14.1 mins and 16.5 mins. Bottom row is the snapshot of the pressure distribution during evolution of the four fractures at 7.1 s, 4.7 mins, 5.9 mins and 7.1 mins

to lower fracture permeability which leads to fluid pressure build up in the compressed fractures, as seen in the two middle columns of Figure 4.17. As fluid injection continues, the fluid pressure in the middle fractures builds up to a point that it eventually overcomes the opposing compressive stress exerted on them. This results in their rapid growth, leading to the final patterns observed on the right column of Figure 4.16, with merging of two fractures obtained for the three fracture case.

4.7 Well Shut-in After Fracture Propagation

Often times during a minifrac test, after the initial fractures are created and extended, the injection well is shut-in during which fluid pressure in the fracture declines. Pressure decline occurs because the fluid flows back into the well or leaks-off into the adjoining reservoir. The common reason for well shut-in is to collect the pressure decline data which when properly analyzed, yields useful information about the reservoir and fracture, like fracture geometry, formation closure pressure, minimum in situ stress, leak-off characteristics etc. However, as the fluid pressure drops, the fracture closes. Keeping the fracture open, especially after the main fracture stimulation treatment, is crucial in providing sufficient hydraulic pathway for formation fluid to flow from the reservoir to production wells. To ensure that fractures stay open, engineers typically inject proppants to hold the fracture faces.

To mimic the minifrac test, numerical experiments are performed during which the well is shut-in after a period of fluid injection and fracture propagation. The fluid pressure and fracture geometry changes are analyzed before and after the well shut-in. The reservoir model and initial fracture geometry are the same as in Subsec. 4.4. Fluid viscosity is $\mu = 1\times10^{-4}$ GPa s while other parameters are the same as in Table 4.1. Three different reservoir permeabilities of $k = 4 \times 10^{-15}$ m^2, 2×10^{-15} m^2 and 1×10^{-15} m^2 are considered. Fluid is injected into the fracture at a constant rate of $Q_{fs} = 0.05$ m^2/s for 42 s, after which the well is shut-in. The numerical results for fluid injection with well shut-in are shown in Figure 4.18 while the results without well shut-in are those in Figure 4.9. The pressure responses are such that after fluid injection stops at 42 s, there is additional reduction in injection pressure as fluid leaks-off into the reservoir. The rate of decline is directly proportional to the reservoir permeability. Similarly, fracture mouth aperture decreases with declining fluid pressure while fracture length remains constants after well shut-in, since the fluid pressure falls below the critical values necessary for continued fracture propagation. Figure 4.19 shows the evolution of fluid pressure in the reservoir at different times for $\frac{K}{\mu} = 0.028$ m^{2}s^{-1}/GPa. The fracture length increases until t = 42 s and remains constant thereafter. Fluid leak-off into the reservoir is highlighted by the decreasing pressure inside the fracture and increasing fluid diffusion into the reservoir as time progresses beyond the well shut-in time.

4.8 Effect of In-Situ Stresses on Propagation Directions

The effect of in-situ stresses on fracture propagation direction is simulated in this section. The reservoir-fracture geometry is similar to Figure 4.2 but with a reservoir size of 50 m × 50 m. In-situ stresses are implemented by by fixing the left and bottom boundaries of the reservoir while the traction forces are applied on the other boundaries. For $G_c = 100$ Pa m, $Q_{fs} = 5 \times 10^{-4}$ m^2/s, $\mu = 4 \times 10^{-14}$ GPa s, $k = 8.9 \times 10^{-24}$ m^2, 0.014 MPa initial reservoir pressure and other properties as in Table 4.1, the numerical results of fracture propagation patterns for different in-situ stresses are shown in Figure 4.20. Four different

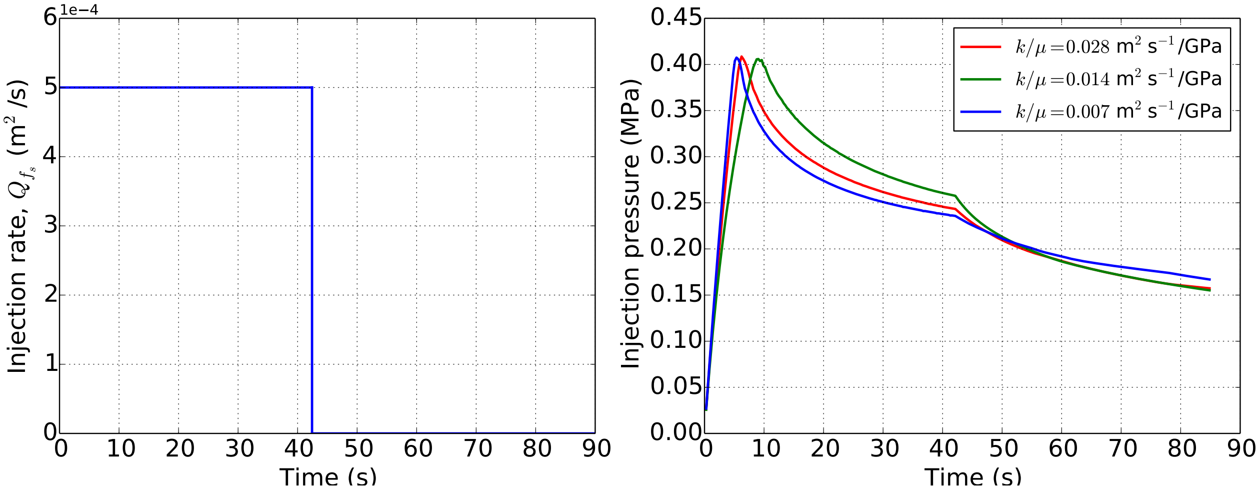

(a) Injection rate (b) Injection pressure

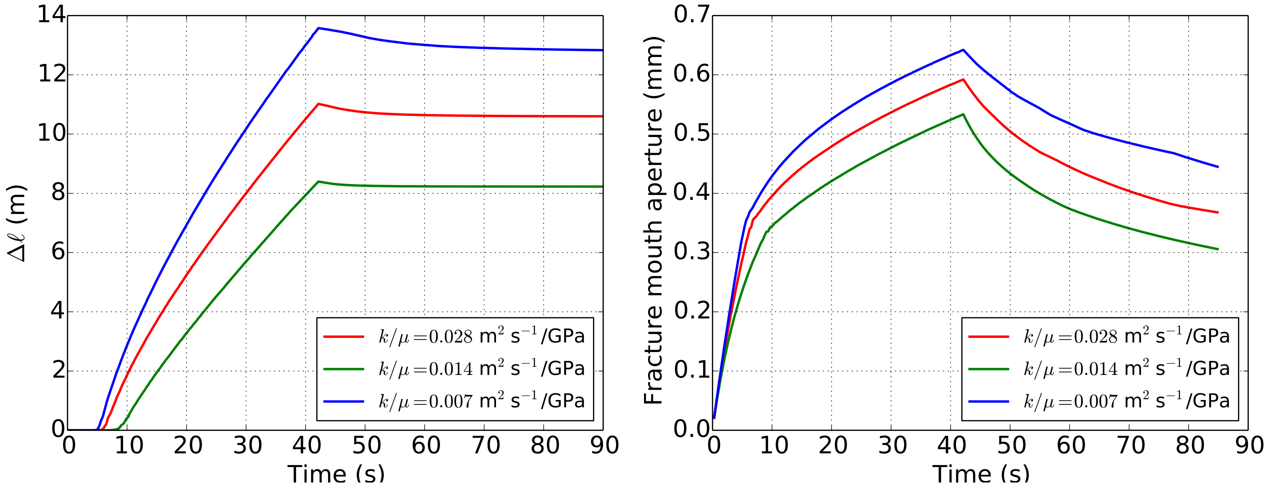

(c) Change in fracture half length (d) Fracture mouth aperture

Figure 4.18: Change in fracture length and fracture mouth aperture during well shut-in operation for different reservoir permeabilities. The well is shut-in after 42 s

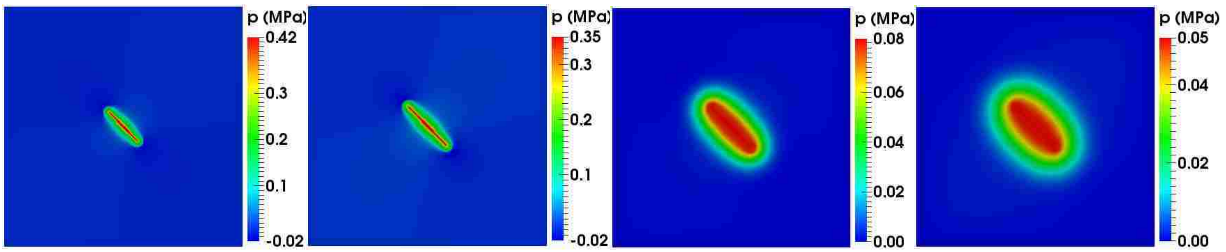

(a) t = 2.4 mins (b) t = 3.5 mins (c) t = 23.6 mins (d) t = 47.1 mins

Figure 4.19: Snap shots of pressure distribution in the reservoir with $\frac{K}{\mu} = 0.028$ m^{2}s^{-1}/GPa, during simulation injection well shut-in. The well is shut-in after 42 s

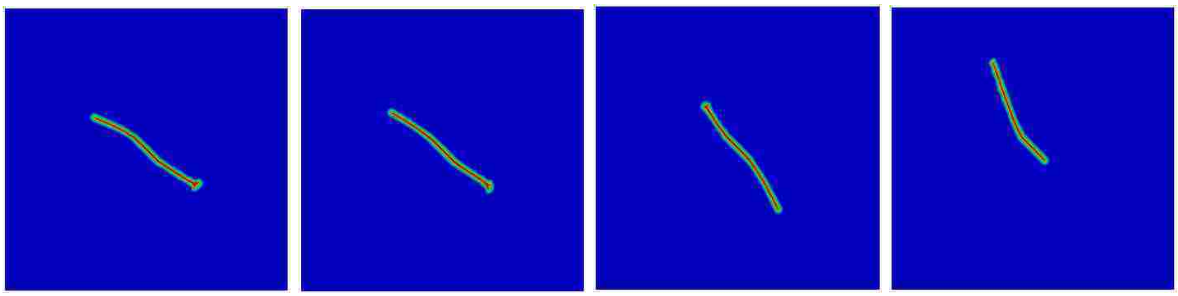

(a) σ_{xx}=-0.07 MPa and σ_{zz} = -0.04 MPa (b) σ_{xx}=-0.07 MPa and σ_{zz} = -0.057 MPa (c) σ_{xx}=-0.04 MPa and σ_{zz} = -0.07 MPa (d) σ_{xx}=-0.07 MPa and σ_{zz} = -0.1 MPa

Figure 4.20: Fracture propagation paths for different combination of in-situ stresses

combinations of in-situ stresses are considered: σ_{xx} = -0.07 MPa and σ_{zz} = -0.04 MPa, σ_{xx} = -0.07 MPa and σ_{zz} = -0.057 MPa, σ_{xx} = -0.04 MPa and σ_{zz} = -0.07 MPa, σ_{xx} = -0.07 MPa and σ_{zz} = -0.1 MPa. For all the cases, as one would expect, fractures reorient from their initial 45° configuration to propagate orthogonal to the minimum in-situ stress direction. However, as seen in Figure 4.20d, in-situ stresses can also lead to asymmetric hydraulic fracture propagation.

4.9 Hydraulic Fracture Propagation in Layered Reservoirs

Petroleum reservoirs are highly stratified which favors location of formation fluids within certain layers in the subsurface. Once a productive zone is identified, hydraulic fracturing is designed so that fracture growth is constrained within the layer of interest. Restricting fracture height growth is necessary to enable fractures reach far into productive formations and to prevent growth into adjoining formations that are non-productive. Considering the difficulty in modeling hydraulic fracture propagation even for simple formations, classical models have assumed that fracture height is defined by the formation thickness. Although this assumption may not be far from the reality, the reason for this is the differences in mechanical and flow properties of the reservoir layers. Hence, numerical simulations are performed in thus subsection to study fracture growth and propagation in multi-layered reservoirs. Layering is created by varying the values of E, G_c or k for different regions in the reservoir computational domain.

Computations for fracture propagation in two and three dimensions are carried out. The

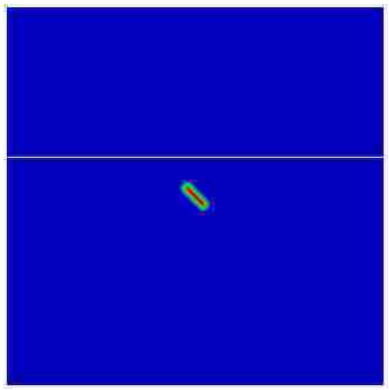

Figure 4.21: Initial fracture for the 2-layered, two dimensional reservoir. The layers are separated at 60 m in the vertical direction. The layer separation can be identified by the white line in the images

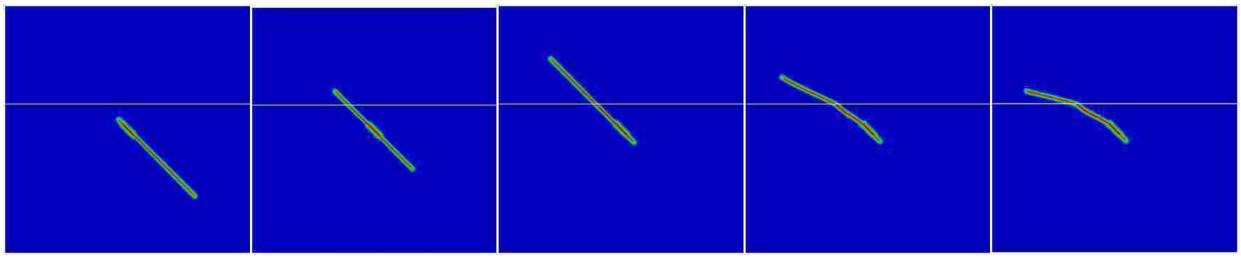

(a) $E_{top} = 85$ GPa (b) $E_{top} = 17$ GPa (c) $E_{top} = 8.5$ GPa (d) $E_{top} = 3.4$ GPa (e) $E_{top} = 1.7$ GPa

Figure 4.22: Hydraulic fracture propagation paths in two dimensional reservoir containing two layers separated by the white line

two dimensional reservoir-fracture model is shown Figure 4.21. It has a size of 100 m × 100 m and contains two layers separated along the vertical direction at 60 m. The Young's modulus, E, of the bottom layer is fixed at 17 GPa while that for the top layer is varied. All other properties are the same through out the reservoir as in Table 4.1. The numerical results for fracture propagation and fluid pressure distribution for five cases for different values of E_{top} (85, 34, 17, 3.4 and 1.7 GPa) are shown in Figure 4.22 and 4.23. A symmetric propagation of both tips is obtained for the single layer case with $E_{top} = E_{bottom} = 17$ GPa. Since fracture toughness and other parameters are the same for both layers, the effect of higher modulus in the top layer is a reduction in reservoir deformation and fracture opening compared to the situation where the modulus is smaller in that layer. Thus, for $E_{top} > 17$ GPa, the hydraulic fracture propagates away from the top layer since it is more difficult to open the fractures in that layer compared to the bottom layer. Correspondingly, for $E_{top} < 17$ GPa, the fractures propagate into the top layer since its lower modulus compared to that of the bottom layer means that fracture width opens easily in the top layer. One also observes that for $\frac{E_{top}}{E_{bottom}} < 0.2$, the hydraulic fractures experience kinks as they enter the top layer.

The three dimensional computations highlight the role of varying mechanical properties of reservoir layers on hydraulic fracture height growth. The reservoir parameters, fluid properties and numerical simulation inputs are shown in Table 4.3 while the computational geometry showing the contour of the fracture domain at $v = 0.1$ is shown in Figure 4.24a. The reservoir is a cube of size 50 m × 50 m × 50 m. The fracturing fluid is injected into an initial penny shaped fracture of 5 m radius located in the center of domain. The reservoir is divided into three vertical layers with interfaces at 17 m and 25 m respectively. This means that the fracture is located in the middle layer. The top and bottom layers are assumed similar, with the same values for reservoir properties as highlighted by the color contrast in Figure 4.24a. Layering in the reservoir is created by differences in either E, G_c or k between the layers. Otherwise, all other properties are the same for all the layers. The base reservoir properties without variation between layers are as in Table 4.3. For a reservoir with uniform properties (base values) in all layers, the hydraulic fracture has a uniform geometry as shown

Table 4.3: Reservoir properties for fracture propagation in a three layered, three dimensional reservoir. Column D is the dimensionless inputs to the numerical model while column o is the scaling for converting dimensionless parameters to physical values

Parameter	D	o	Physical
x	50	1 m	50 m
u	-	1.4×10^{-4} m	-
p	-	1.4×10^{-4} GPa	-
δt	10	1.4×10^{-2} s	0.14 s
E	17	1 GPa	17 GPa
ν	0.2	1	0.2
G_c	5	2 $\times 10^{-8}$ GPa m	100 Pa m
k	1×10^{-12}	2.83×10^{-12} m^2	2.83×10^{-24} m^2
ϕ	0.2	1	0.2
α	1	1	1
K_s	2	1 GPa	2 GPa
K_f	0.125	1 GPa	0.125 GPa
μ	1×10^{-13}	$4{\times}10^{-14}$ GPa s	$4{\times}10^{-27}$ GPa s
Q_{fs}	5	0.01 m^3/s	$5{\times}10^{-2}$ m^3/s

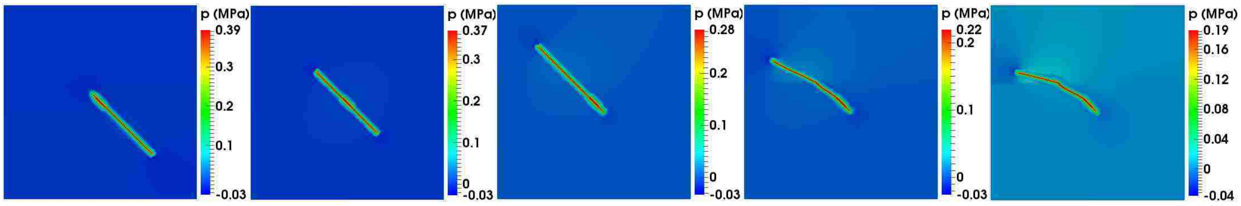

(a) E_{top} = 85 GPa (b) E_{top} = 17 GPa (c) E_{top} = 8.5 GPa (d) E_{top} = 3.4 GPa (e) E_{top} = 1.7 GPa

Figure 4.23: Hydraulic fracturing fluid pressure distribution in two dimensional reservoir containing 2 layers separated by the white line

in Figure 4.24b. The penny shape remains unchanged throughout fracture propagation.

Numerical results for fracture propagation in reservoir with varying G_c between the layers are shown in Figure 4.25. Higher fracture toughness of the external layers favors hydraulic fracture growth in the middle layer. The fracture geometry in this conditions grows more in length than in height. In fact, for very high $\frac{G_{c,ext}}{G_{c,mid}}$ ratio, the fracture is completely restricted to the middle layer as seen in Figure 4.25c. As a result, it has a constant height that is approximately equal to the thickness of the middle layer. On the other hand, a reduction in $\frac{G_{c,ext}}{G_{c,mid}}$ favors fracture growth into the top and bottom layer, with a geometry that is longer

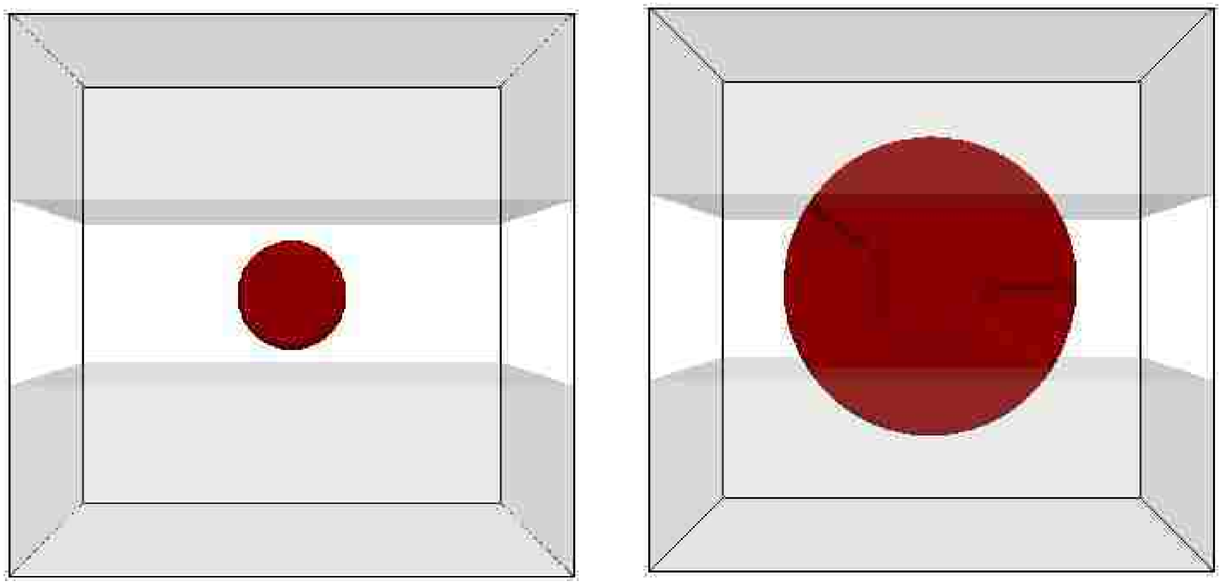

(a) Initial penny shaped fracture

(b) Geometry of propagated fracture in the layered reservoir with uniform properties. The fracture shape remains unchanged throughout propagation

Figure 4.24: Penny shaped fracture in a three dimensional reservoir with 3 layers. Fracture shape is taken as the contour at $v = 0.1$. The layers are identified by different colors. Top and bottom layers have the same properties, hence the same color representation

in the vertical direction than in the horizontal direction.

Figure 4.26 shows the propagated hydraulic fracture geometry in the layered reservoir for different Young's modulus. Higher Young's modulus in the surrounding layers impedes fracture growth out of the middle layer while lower modulus in the surrounding layers encourages fracture growth out of the middle layer.

Lastly, the effect of varying reservoir permeability in the layered reservoir on the fracture geometry is shown in Figure 4.27. The large fluid losses associated with high reservoir permeability delays the onset of fracture propagation since pressure build up towards the critical value is delayed. For higher permeability in the middle layer, the fluid pressure in the region of the fracture in that layer builds up slower due to high leak-off while the fracture region closest to the adjoining layers experience higher fluid pressure. Given that fracture toughness is the same in all layers, the fracture propagates more in the vertical direction than in the horizontal direction. On the other hand, lower permeability in the middle encourages

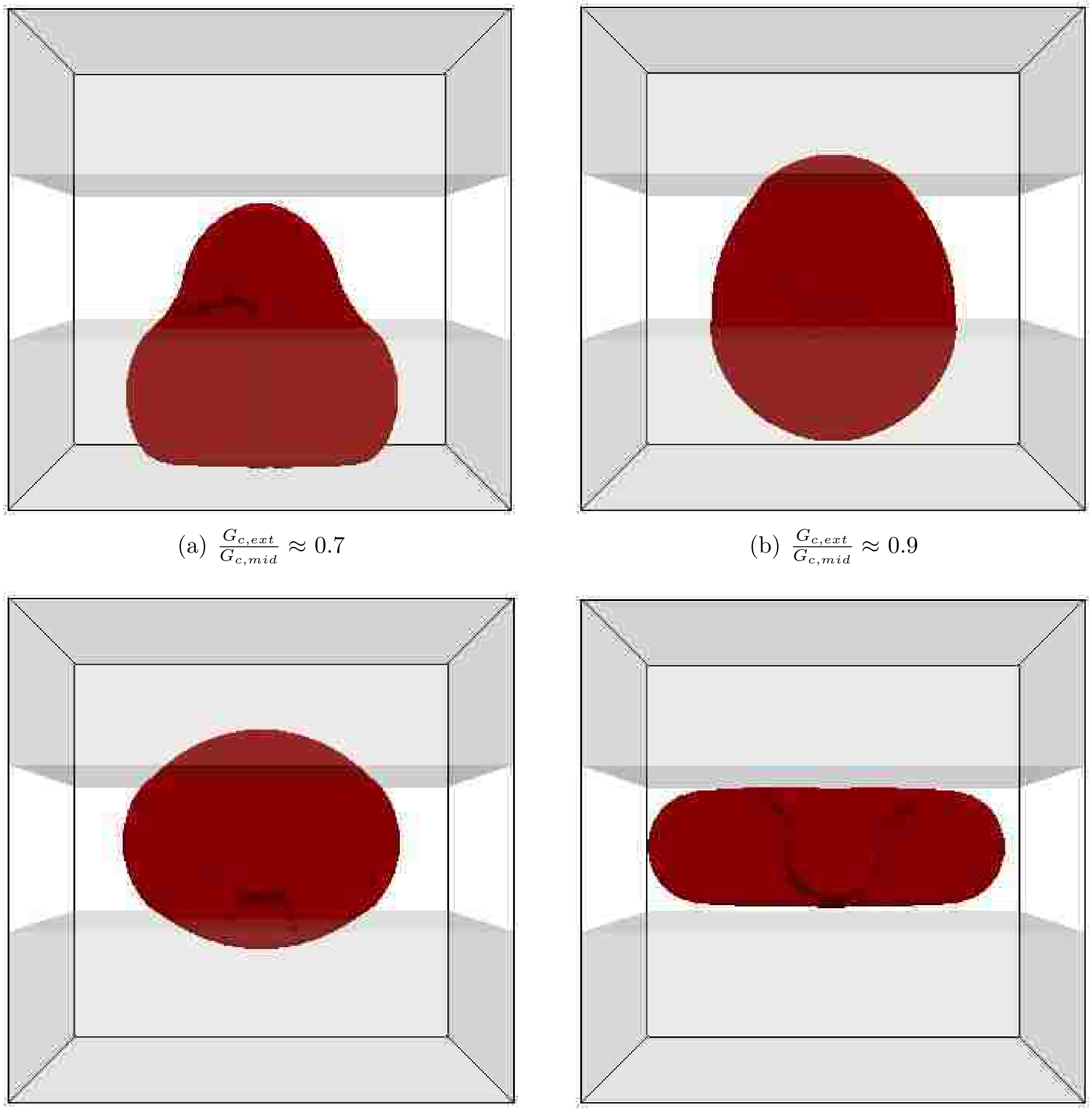

(a) $\frac{G_{c,ext}}{G_{c,mid}} \approx 0.7$

(b) $\frac{G_{c,ext}}{G_{c,mid}} \approx 0.9$

(c) $\frac{G_{c,ext}}{G_{c,mid}} \approx 1.2$

(d) $\frac{G_{c,ext}}{G_{c,mid}} = 10$

Figure 4.25: Propagated hydraulic fracture in the three layered reservoir with different fracture toughness

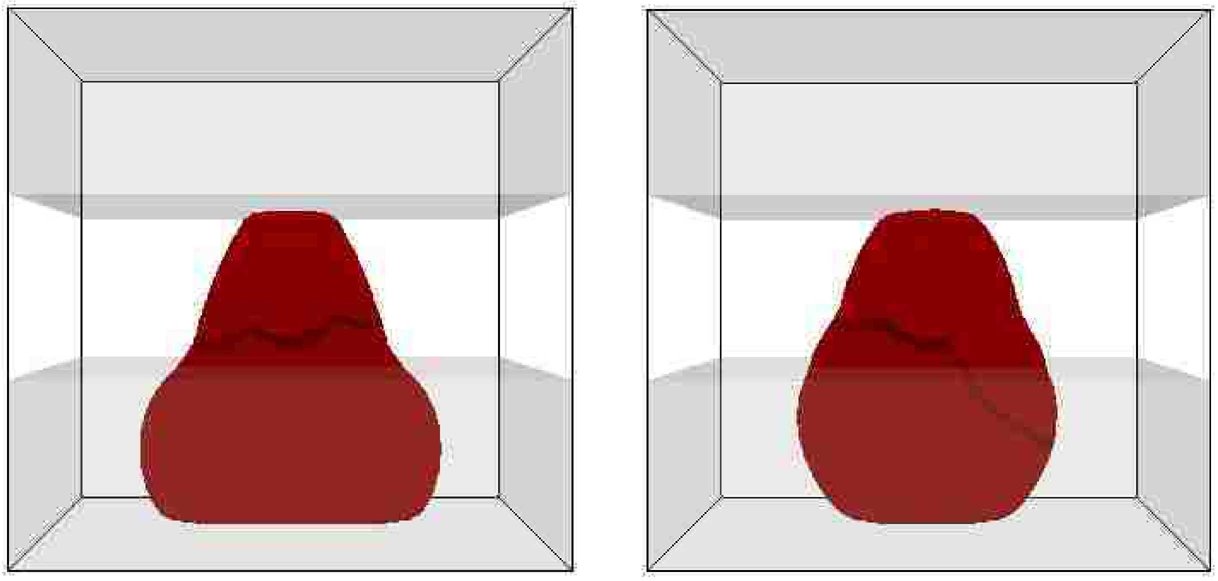

(a) $\frac{E_{ext}}{E_{mid}} = 0.1$ (b) $\frac{E_{ext}}{E_{mid}} = 0.2$

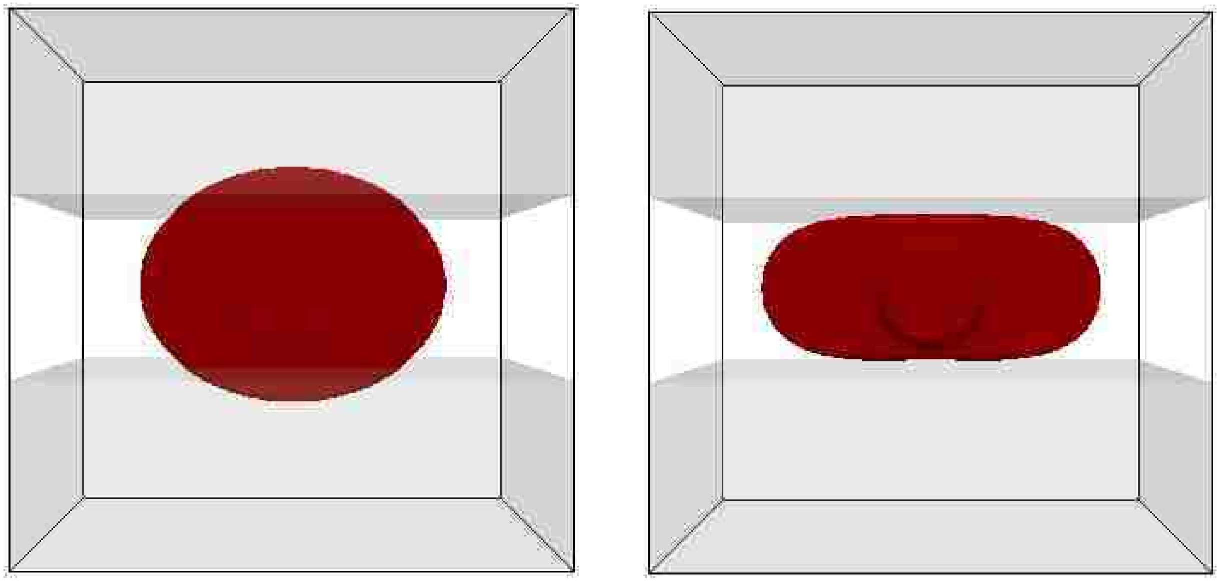

(c) $\frac{E_{ext}}{E_{mid}} = 2$ (d) $\frac{E_{ext}}{E_{mid}} = 5$

Figure 4.26: Propagated hydraulic fracture in the three layered reservoir with different Young's modulus

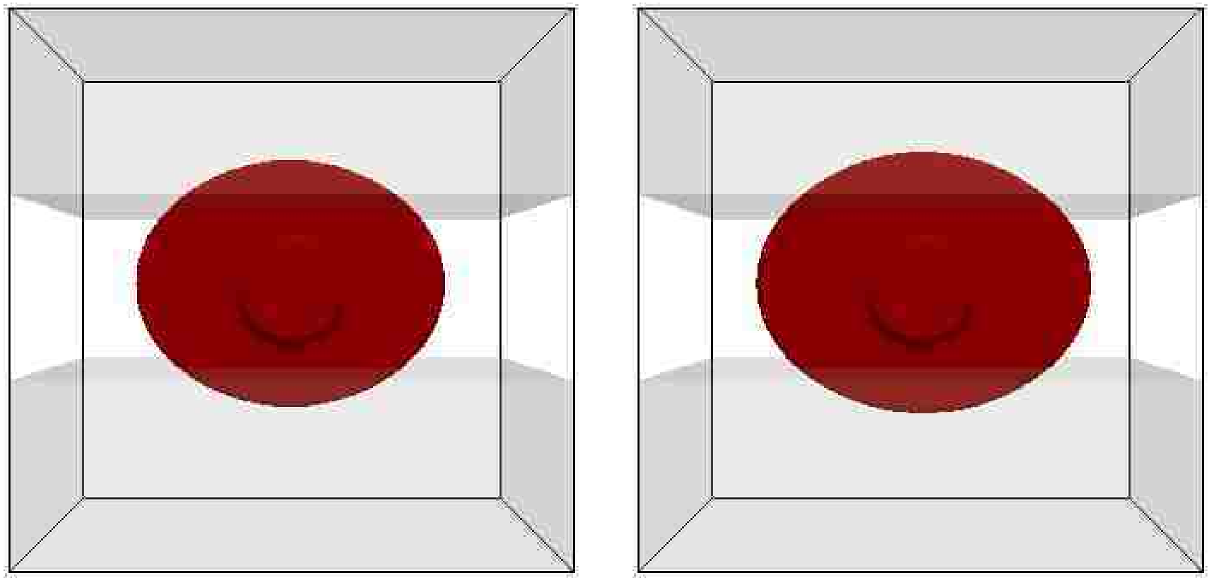

(a) $k_{ext} = 2.8 \times 10^{-25}$ m^2, $k_{mid} = 2.83 \times 10^{-27}$ m^2

(b) $k_{ext} = 2.3 \times 10^{-25}$ m^2, $k_{mid} = 2.83 \times 10^{-27}$ m^2

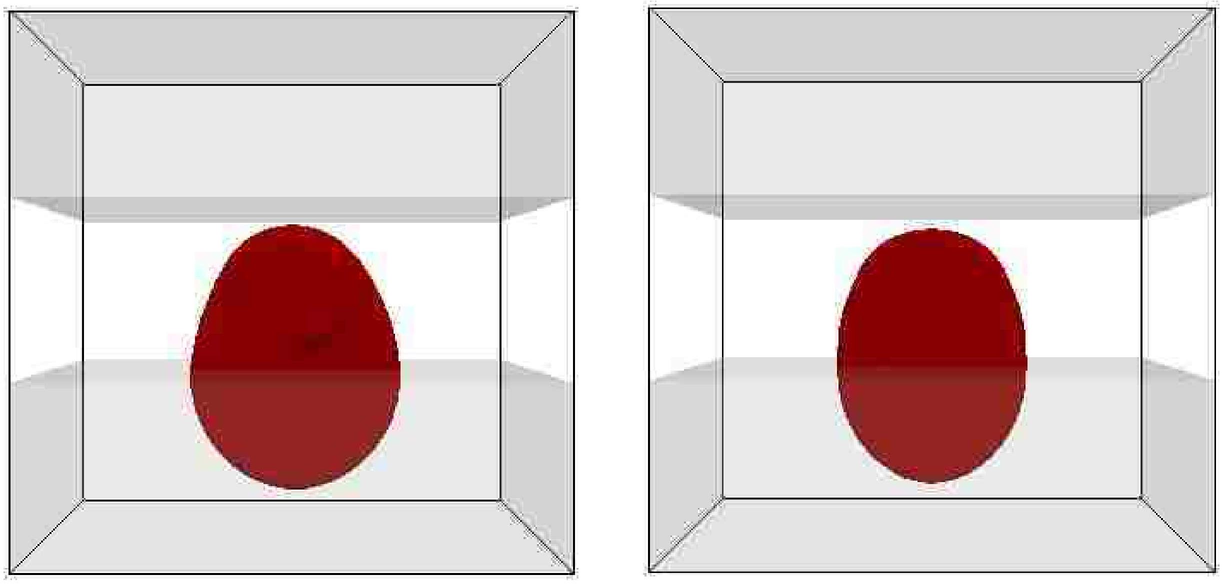

(c) $k_{ext} = 2.8 \times 10^{-27}$ m^2, $k_{mid} = 1.7 \times 10^{-25}$ m^2

(d) $k_{ext} = 2.83 \times 10^{-27}$ m^2, $k_{mid} = 2.83 \times 10^{-25}$ m^2

Figure 4.27: Propagated hydraulic fracture in the three layered reservoir with different permeabilities

more propagation in that layer with less extension in the vertical direction. As a result, the fracture has a higher length compared to its height.

One may have observed the non-symmetric propagation in the combination of reservoir properties that otherwise would have favored uniform and equal propagation into the external layers, as in Figures 4.25a, 4.25b, 4.26a, 4.26b, 4.27c and 4.27d. In these figures, the fracture extends more into the bottom layer than into the top layer. The evolution of these fractures is such that propagation is symmetric prior to reaching the boundary interfaces. However, due to floating point errors, the bottom part of the fracture reaches the lower interface before the top part reaches the top layer interface. Subsequent fluid injection favors fracture growth into the bottom layer. Although this geometry could have been reversed to favor growth into the top layer, the result show that it may be difficult to control hydraulic fracture growth in conditions where fractures propagate into layers with lower resistance to fluid flow and rock deformation.

Chapter 5

Conclusions and Recommendations

5.1 Conclusions

In this dissertation, a coupled model for simulating hydraulic fracturing in poroelastic media is developed and numerically implemented. The developed numerical model was used to study the effect of reservoir and flow properties on fracturing fluid pressure, fracture geometries (length, height, width, radius) and fracture propagation paths. The model is based on a phase field representation of fractures and the corresponding reformulation of the flow and mechanical models in terms on the phase field variable. This chapter summarizes and concludes all the work presented in this dissertation.

1. The dissertation started by highlighting the importance of incorporating poroelasticity in the flow and mechanical models used for simulating hydraulic fracturing. The variational fracture model was introduced as the mechanical model used in this dissertation. In the variational fracture approach, the deformed state of poroelastic media containing fractures is the solution of an optimization problem which involves minimizing the sum of the surface energy, elastic energy and work of pressure forces in the poroelastic media. Linear poroelasticity and linear elastic fracture mechanics are incorporated through the poroelastic energy and surface energy terms respectively.

2. Numerical implementation of fracture models used a smooth scalar phase field (v-field) that varies between 0 and 1, to represent fractures in the reservoir computational domain. The total energy functional was regularized in terms of the phase field variable. The regularized energy provided a single framework for modeling reservoir deformation and interaction and propagation of multiple hydraulic fractures. As a result, fracture propagation part does not need to be known a priori or restricted to any set of directions.

3. The variational fracture model was verified by simulating hydraulic fracturing propagation in impermeable poroelastic reservoirs. The analytical solutions for this problem were derived for pressure driven and volume driven hydraulic fracturing propagation. The analytical solution for pressure driven hydraulic fracture propagation showed that it is impossible to propagate fractures in a stable manner by arbitrarily increasing fluid pressure. The numerical simulation results verified the instability of this operation. Two and three dimensional volume driven hydraulic fracture propagation simulations were carried out and the numerical results were in good agreement with the analytical solutions. Numerical results produced of complex fracture patterns due to the presence of in-situ stresses and due to simultaneous propagation of multiple fractures.

4. The flow model component of the hydraulic fracturing model was developed by coupling Reynold's equation for flow in the fracture and the single phase continuity equation from poroelasticity theory. Given that fractures are considered as lower dimensional surfaces in the reservoir, the Reynold's equation was equipped with surface gradient and surface divergence operators to allow for fluid flow only within the plane of the fractures. Numerical analysis of the individual flow models provided a single coupled model to solve for fluid pressure in fracture and reservoir. The developed flow model was also regularized using the phase field variable. Fracture width and volumetric strain were the coupling terms between the flow and mechanical models. An algorithm to compute fracture width using the phase field and displacement variables was developed. The algorithm in its basic form introduces errors to the computed fracture width, especially around fracture tips. The tip errors which arises due to the fact that the phase field gradient makes no distinction between fracture tip and fracture surface, were removed by computing indicator functions that isolate fracture tips from the fracture surface. Numerical solution of the coupled flow and mechanical model used a modified fixed stress splitting scheme to improve the numerical stability. Mandel's and Terzaghi's consolidation problems were numerically solved to verify the coupled reservoir fluid

flow and deformation capabilities of the model.

5. Dimensional analysis of both the flow and mechanical models were carried out to derive their respectively dimensionless forms. All the numerical implementations were for the solution of the dimensionless models. The scaled model allows the use of arbitrary dimensionless reservoir and fluid parameters that improve the condition number of the numerical scheme. In addition, the numerical results can be scaled to solution values for realistic reservoir parameters using the derived scaling functions.

6. KGD hydraulic fracturing propagation in two dimensional poroelastic medium was solved to verify the coupled model. On studying the effects of reservoir permeability on the hydraulic fracturing process, high reservoir permeabilities resulted in high fluid losses, reducing fracture geometry and delaying the onset of fracture propagation. In the presence of anisotropic reservoir permeabilities, hydraulic fractures propagated in the direction with the least flow resistance. The use of high fluid viscosities for hydraulic fracturing resulted in higher injection pressures and shorter fractures compared to when low viscosity fluids were used. In addition, fracture width created from high fluid viscosities were larger than those from low viscosities. The stress shadow effect was captured by simulating the propagation of multiple fractures. In the simulation of two, three and four multiple fracture propagation, the stress shadow effect resulted in fracture tips of neighboring fractures propagating away from each other. The stress shadow effect of hydraulic fracturing interaction was found to decrease with increasing spacing between fractures and for decreasing permeability of the reservoir. The presence of in-situ stress produced fractures that propagated orthogonal to minimum stresses. The effect of reservoir laying was investigated by simulating penny-shaped hydraulic fracture propagation in layered reservoirs. For a penny-shaped fracture in the centre of a three-layered reservoir, layering was created by varying the mechanical and flow properties between three vertical sections of the reservoir. The external layers were considered to be the same, with equal reservoir properties. For some combination

of reservoir properties, the hydraulic fracture grew only within the bounded layer, with limited height growth which was controlled by the thickness of the middle layer. Other combinations of reservoir properties favored hydraulic fracture growth away from the middle layer into he bounding, external layers.

5.2 Recommendations for Future Work

Phase field based methods for hydraulic fracturing modeling is relatively new and this dissertation ranks amongst the early works in this area. The method will continue to attract research attention and see significant growth in the future. Based on the experiences gained during the course of this project, the recommendations for continued research on using the variational fracture method for modeling hydraulic fracturing are summarized as follows:

1. Given that fracture width is the primary coupling between the flow and mechanical models, the width computation can be improved through the development of a more robust algorithm that minimizes the tip errors. Although our width computation algorithm is programmed in parallel, its non-local structure increases the overall implementation time of the coupled model. The efficiency of the implementation can be improved. It is important to point that this is a computer science task.

2. Most of the numerical examples in this dissertation are two dimensional with some qualitative three dimensional computations in the last section of Chapter 4. The inability to perform quantitative simulations for three dimensional problems was due to the large computation cost involved. If the width computation algorithm is improved, more three dimensional computations should be carried out since they are a more realistic reflection of hydraulic fracturing in the subsurface.

3. Heat transfer, proppant transport and non-Newtonian fluids should be coupled to the developed model to study the effects of these additional phenomena on the hydraulic fracturing process.

References

Abousleiman, Y., A.H.-D. Cheng, L. Cui, E. Detournay, and J.-C. Roegiers. 1996. "Mandel's problem revisited." *Géotechnique* 46:187–195.

Adachi, J., E. Siebrits, and J. Desroches. 2007. "Computer simulation of hydraulic fractures." *Int. J Rock Mech & Mining Sci.* 44:739–757.

Advani, S.H., T.S. Lee, and J.K. Lee. 1990. "Three dimensional modeling of hydraulic fractures in layered media: Part I-Finite element formulations." *JPT* 112:1–9.

Aghighi, M.A. 2007. "Fully coupled fluid flow and geomechanics in the study of hydraulic fracturing and post-fracture production." Ph.D. diss., The University of New South Wales.

Albright, J., and C.F. Pearson. 1982. "Acoustic emissions as a tool for hydraulic fracture location: Experience at the Fenton Hill hot dry rock site." *SPEJ*, no. SPE-9509-PA.

Ambrosio, L., and V.M. Tortorelli. 1990a. "Approximation of functional depending on jumps by elliptic functional via t-convergence." *Communications on Pure and Applied Mathematics* 43 (8): 999–1036.

———. 1990b. *On the approximation of free discontinuity problems.* Scuola Normale Superiore.

Balay, S., K. Buschelman, V. Eijkhout, W. Gropp, D. Kaushik, M. Knepley, L.C. McInnes, B. Smith, and H. Zhang. 2011. *Petsc users manual.* 3.2. Math. & Comp. Sci. Div., Argonne Nat. Lab.

Barenblatt, G.I. 1962. "The mathematical theory of equilibrium cracks in brittle fracture." *Advances in applied mechanics* 7 (1): 55–129.

Barree, R.D. 1983. "A practical numerical simulator for three-dimensional fracture propagation in heterogeneous media." *SPE Reservoir Simulation Symposium.* San Francisco, CA.

Barter, B.J., J. Desroches, A.R. Ingraffea, and P.A. Wawrzynek. 2000. "Simulating fully 3D hydraulic fracturing." *Modeling in geomechanics*, pp. 525–557.

Batchelor, G.K. 1967. *An introduction to fluid dynamics.* Cambridge University Press.

Becker, A., and M.R. Gross. 1996. "Mechanisms for joint saturation in mechanical layered rocks: an example from southern Israel." *Tectonophysics* 257:223–237.

Biot, M.A. 1941. "General Theory of Three-Dimensional Consolidation." *Journal of Applied Physics* 12 (2): 155–164.

Boone, T.J., and A.R. Ingraffea. 1989. "An investigation of poroelastic effects related to hydraulic fracture propagation in rock and stress measurement techniques." *ARMA.*

———. 1990. "A numerical procedure for simulation of hydraulically driven fracture propagation in poroelastic media." *Int. J. Num. & Analytical. Meth. in Geomech.*

14:27–47.

Bourdin, B. 1998. “Une méthode variationelle en mécanique de la rupture, théorie et applications numériques.” Ph.D. diss.

Bourdin, B., C. Chukwudozie, and K. Yoshioka. 2012. “A variational approach to the numerical simulation of hydraulic fracturing.” *SPE ATCE 2012.*

Bourdin, B., G.A. Francfort, and J.-J. Marigo. 2000. “Numerical experiments in revisited brittle fracture.” *J. Mech. and Phys. of Solids* 48 (4): 797–826.

———. 2008. “The variational approach to fracture.” *Journal of Elasticity* 91 (1-3): 5–148.

Bourdin, B., J.-J. Marigo, C. Maurini, and P. Sicsic. 2014. “Morphogenesis and propagation of complex cracks induced by thermal shocks.” *Physical review letters* 112 (1): 014301.

Bui, H.D. 1977. “An integral equations method for solving the problem of a plane crack of arbitrary shape.” *J. Mech. Phys. Solids* 25:29–39.

Bunger, A.P., E. Detournay, and D.I. Garagash. 2005. “Toughness dominated hydraulic fracture with leak off.” *Int. J. Fracture* 134, no. 175-190.

Carrier, B., and S. Granet. 2012. “Numerical modeling of hydraulic fracture problem in permeable medium using cohesive zone model.” *Eng. Fracture Mech.* 79:312–328.

Chambolle, A., A. Giacomini, and M. Ponsiglione. 2008. “Crack initiation in elastic bodies.” *Arch. Ration. Mech. Anal.* 188 (2): 309–349.

Chukwudozie, C., B. Bourdin, and K. Yoshioka. 2013. “A variational approach to the modeling and numerical simulation of hydraulic fracturing under in-situ stresses.” *Proceedings of the 38th Workshop on Geothermal Reservoir Engineering.*

Chukwudozie, C., K. Yoshioka, T. Buchmann, and P. Connolly. 2013. “A new modeling approach to natural fracturing process.” *ARMA*, no. 13-100.

Clifton, R.J., and A.S. Abou-Sayed. 1981. “A variational approach to the prediction of the three-dimensional geometry of hydraulic fractures.” *SPE.*

Correa, M.R., and A.F.D. Loula. 2007. “Unconditionally Stable Mixed Finite Element Methods for Darcy Flow.” *LNCC Technical Reports* 197:1525–1540.

Coussy, O. 2004. *Poromechanics.* John Wiley & Sons, Ltd.

Dahi, A. 2009. “Analysis of hydraulic fracture propagation in fractured reservoirs: an improved model for the interaction between induced and natural fractures.” Ph.D. diss., The University of Texas at Austin.

Dean, R.H., X. Gai, C.M. Stone, and S.E. Minkoff. 2006. “A comparison of techniques for coupling porous flow and geomechanics.” *Spe Journal* 11 (01): 132–140.

Dean, R.H., and J.H. Schmidt. 2009. “Hydraulic-fracture predictions with a fully coupled geomechanical reservoir simulator.” *SPE Journal* 14 (04): 707–714.

Detournay, E. 1991. “Plane strain analysis of a stationary hydraulic fracture in a poroelastic medium.” *Int. J. Solids and Struct.* 27 (13): 1645–1662.

Detournay, E., and A.H.-D. Cheng. 1988. “Poroelastic response of a borehole in non-hydrostatic stress field.” *International Journal of Rock Mechanics and Mining Sciences and Geomechanics Abstract* 25:171–182.

———. 1993. “Fundamentals of Poroelasticity.” *Comprehensive Rock Engineering: Principles, Practices and Projects*, vol. II.

Detournay, E., and D.I. Garagash. 2003. “The near tip region of a fluid driven fracture propagating in a permeable elastic solid.” *J. Fluid Mech.* 494:1–32.

Dugdale, D.S. 1960. “Yielding of steel sheets containing slits.” *Journal of the Mechanics and Physics of Solids* 8 (2): 100–104.

EIA, US. 2014. “Annual energy outlook 2014.” *US Energy Information Administration, Washington, DC.*

Elman, H. C., J.D. Silvester, and A.J. Wathen. 2005. *Finite elements and fast iterative solvers.* Oxford University Press, USA.

Ern, A., and J.-L. Guermond. 2004. *Theory and Practice of Finite Elements.* Volume 159. Springer Science & Business Media.

Fakoya, M.F., and S.N. Shah. 2013. “Rheological properties of surfactant-based and polymeric nano-fluids.” *SPE/ICoTA Coiled Tubing & Well Intervention Conference & Exhibition.* Society of Petroleum Engineers.

———. 2014. “Enhancement of Filtration Properties in Surfactant-Based and Polymeric Fluids by Nanoparticles.” *SPE Eastern Regional Meeting.* Society of Petroleum Engineers.

Fomin, S., T. Hashida, A. Shimizu, K. Matsuki, and K. Sakaguchi. 2003. “Fractal concept in numerical simulation of hydraulic fracturing of the hot dry rock geothermal reservoir.” *Hydrological Processes* 17:2975–2989.

Francfort, G.A., and J.-J Marigo. 1998. “Revisiting brittle fracture as an energy minimization problem.” *J. Mech. and Phys. of Solids* 46 (8): 1319–1342.

Garagash, D.I. 2006. “Plane-strain propagation of a fluid-driven fracture during injection and shut-in: Asymptotics of large toughness.” *Engineering Fracture Mechanics* 73 (4): 456–481.

Geertsma, J., and F. de Klerk. 1969. “A rapid method of predicting width and extent of hydraulically induced fractures.” *JPT* 246 (2458): 1571–1581.

Ghassemi, A. 1996. “Three-dimensional poroelastic hydraulic fracture simulation using displacement discontinuity method.” Ph.D. diss., The University of Oklahoma.

Gidley, J.L. 1989. “Recent advances in hydraulic fracturing.”

Griffith, A.A. 1921. “The phenomena of rupture and flows in solids.” *Phil. trans. Roy. Soc. London*, no. A221:163–197.

Gross, M.R., M.P. Fischer, and T. Engelder. 1995. “Factors controlling joint spacing in interbedded sedimentary rocks: integrating numerical models with field observations from the Monterey formation, USA.” *Geol. Soc. Spec. Publ.*, no. 92:215–233.

Guo, L.L., J.-P. Xiang, and Q. Lei. 2013. “A numerical investigation of fracture and fracture aperture development in multi-layered rock using combined finite-element method.” *ARMA*, no. 13-686.

Gupta, P., and C. A. Duarte. 2014. “Simulation of non-planar three-dimensional hydraulic fracture propagation.” *Int. J. Numer. Anal. Meth. Geomech.*, no. doi: 10.1002/nag.2305.

Gupta, P., and C.A. Duarte. 2015. “Coupled formulation and algorithms for the simulation of non-planar three-dimensional hydraulic fractures using the generalized finite element method.” *International Journal for Numerical and Analytical Methods in Geomechanics.*

Hameyer, K., J. Driesen, H. De Gersem, and R. Belmans. 1999. “The classification of coupled field problems.” *Magnetics, IEEE Transactions* 35:1618–1621.

Hobbs, D.W. 1967. “The formation of tension joint in sedimentary rocks: an explanation.” *Geological Magazizne* 104:550–556.

Hu, J., and D.I. Garagash. 2010. “Plane-strain propagation of a fluid-driven crack in a permeable rock with fracture toughness.” *Journal of Engineering Mechanics.*

Huang, Q., and J. Angelier. 1989. “Fracture spacing and its relation to bed thickness.” *Geological Magazine* 126:355–362.

Hubbert, M.K., and D.G. Willis. 1957. “Mechanics of hydraulic fracturing.” *Petroleum Transactions AIME* 210:153–168.

Irwin, G.R. 1957. “Analysis of stresses and strains near the end of a crack traversing in a plate.” *J. Appl. Mech.* 24:361–364.

Jaeger, J.C., N.G.W. Cook, and R. Zimmerman. 2007. *Fundamentals of rock mechanics.* Wiley.

Jha, B., and R. Juanes. 2006. “A locally conservative finite element framework for the simulation of coupled flow and reservoir geomechanics.” *SPE ATCE San Antonio*, no. SPE 102812.

Ji, L., A. Settari, and R.B. Sullivan. 2009. “A novel hydraulic fracturing model fully coupled with geomechanics and reservoir simulation.” *SPEJ*, no. 110845.

Johnson, R.B., and J.V. DeGraff. 1988. *Principles of engineering geology.* Wiley.

Kim, J. 2010. “Sequential methods for coupled geomechanics and multiphase flow.” Ph.D. diss., Stanford University.

Kim, J., H.A. Tchelepi, and R. Juanes. 2009. “Stability, accuracy and efficiency of sequential methods for coupled flow and geomechanics." *SPE Reservoir Simulation Simposium, The Woodlands*, no. SPE 119084.

———. 2011. "Stability and convergence of sequential methods for coupled flow and geomechanics: Drained and undrained splits." *Comput. Methods Appl. Mech. Engrg.* 200:2094–216.

Kovalyshen, Y. 2010, February. "Fluid-driven fracture in poroelastic medium." Ph.D. diss., University of Minnesota.

Kristianovic, S., and Y. Zheltov. 1955. "Formation of vertical fractures by means of highly viscous fluids." *Proceedings of the Fourth World Petroleum Congress, Rome* II:579–586.

Kuuskraa, V.A., S.H. Stevens, and K. Moodhe. 2013. "EIA/ARI world shale gas and shale oil resource assessment." *Advanced Resources International INC.*

Ladeira, F.L., and N.J. Price. 1981. "Relationship between fracture spacing and bed thickness." *J. Struct. Geol.* 3:179–183.

Lee, I.S. 2008. "Computational techniques for efficient solution of discretized Biot's theory for fluid flow in deformable porous media." Ph.D. diss., Virginia Polytechnique Institue and State University.

Lewis, R.W. 1998. *The Finite Element Method in Static and Dynamic Deformation and Consolidation of Porous Media.* John Wiley and Sons, Ltd.

Lobão, M.C., R. Eve, D.R.J. Owen, and E.A. de Souza Neto. 2010. "Modelling of hydro-fracture flow in porous media." *Engineering Computations* 27 (1): 129–154.

Mandel, J. 1953. "Consolidation des sols (étude mathematique)." *Géotechnique* 30:287–299.

Martin, V., J. Jaffré, and J.E. Roberts. 2005. "Modeling fractures and barriers as interfaces for flow in porous media." *SIAM Journal on Scientific Computing* 26 (5): 1667–1691.

Masud, A., and T.J.R. Hughes. 2002. "A stabilized mixed finite element method for Darcy flow." *Comput. Methods Appl. Mech. Engr* 191 (191): 4341–4370.

Mesgarnejad, A. 2014. "Applications of the Variational Approach to Fracture Mechanics." Ph.D. diss., Louisiana State University, Baton Rouge, LA.

Mikelic, A., M.F. Wheeler, and T. Wick. 2013. "A phase field approach to the fluid filled fracture surrounded by a poroelastic medium." *ICES report*, pp. 13–15.

———. 2015. "A phase-field method for propagating fluid-filled fractures coupled to a surrounding porous medium." *Multiscale Modeling & Simulation* 13 (1): 367–398.

Minkoff, S.E., C.M. Stone, J.G. Arguello, Bryant S., Eaton J., M. Peszynska, and M. Wheeler. 1999. "Staggered In Time Coupling of Reservoir Flow Simulation and Geomechanical Deformation: Step 1-One-Way Coupling." *SPE Reservoir Simulation Symposium.* Citeseer.

Minkoff, S.E., C.M. Stone, S. Bryant, M. Peszynska, and M.F. Wheeler. 2003. "Coupled fluid flow and geomechanical deformation modeling." *Journal of Petroleum Science and Engineering* 38 (1): 37–56.

Mohammadnejad, T., and A.R Khoei. 2013. "An extended finite element method for hydraulic fracture propagation in deformable porous media with the cohesive crack model." *Finite Elements in Analysis and Design* 73:77–95.

Montgomery, C.T., and M.B. Smith. 2010. "Hydraulic fracturing - History of unending technology." *JPT*.

Morales, R.H. 1989. "Microcomputer analysis of hydraulic fracture behavior with a pseudo-three dimensional simulator." *SPE Production Engineering*, pp. 69–74.

Nakshatrala, K.B., D.Z. Turner, K.D. Hjelmstad, and A. Masud. 2006. "A stabilized mixed finite element method for Darcy flow based on a multiscale decomposition of the solution." *Comput. Methods Appl. Mech. Engrg* 195:4036–4049.

Nordgren, R.P. 1972. "Propagation of a vertical hydraulic fracture." *SPEJ*, no. 3009:306–314.

Perkins, T.K., and L.R. Kern. 1961. "Widths of hydraulic fractures." *JPT* 222:937–949.

Phillips, P.S. 2005. "Finite Element Methods in Linear Poroelasticity: Theoretical and Computational Results." Ph.D. diss., The University of Texas at Austin.

Ribeiro, L.H., and M.M. Sharma. 2012. "A New Three-Dimensional, Compositional, Model for Hydraulic Fracturing with Energized Fluids." *SPE Annual Technical Conference and Exhibition.* Society of Petroleum Engineers.

Rungamornrat, J., M.F. Wheeler, and M.E. Mear. 2005. "A numerical technique for simulating nonplanar evolution of hydraulic fractures." *Proceedings SPE Annual Tech. Conf. and Exhibition*, no. SPE 96968.

Santi, P.M., J. E. Holschen, and R.W. Stephenson. 2000. "Improving elastic modulus measurements for rock based on geology." *Environmental & Engineering Geoscience* 6 (4): 333–346.

Sarris, E., and P. Papanastasiou. 2012. "Modeling of hydraulic fracturing in a poroelastic cohesive formation." *International Journal Geomechanics* 12:160–167.

Savitski, A.A., and E. Detournay. 2002. "Propagation of a penny-shaped fluid driven fracture in an impermeable rock:asymptotic solutions." *Int. J. Solids and Struct.*, pp. 6311–6337.

Segura, J.M., and I. Carol. 2004. "On zero-thickness interface elements for diffusion problems." *International journal for numerical and analytical methods in geomechanics* 28 (9): 947–962.

———. 2008a. "Coupled HM analysis using zero-thickness interface elements with double nodes. Part I: Theoretical model." *International journal for numerical and analytical methods in geomechanics* 32 (18): 2083–2101.

———. 2008b. “Coupled HM analysis using zero-thickness interface elements with double nodesPart II: Verification and application.” *International journal for numerical and analytical methods in geomechanics* 32 (18): 2103–2123.

Serres, C., C. Alboin, J. Jaffre, and J. Roberts. 2002. “Modeling fractures as interfaces for flow and transport in porous media.” Technical Report, Inst. de Radioprotection et de Surete Nucleaire, Dept. d’Evaluation de Surete, 92-Fontenay aux Roses (France).

Settari, A., and M.P. Cleary. 1986. “Development and testing of a pseudo-three dimensional model of hydraulic fracture geometry.” *SPE Production Engineering*, pp. 449–466.

Settari, A., and H.S. Price. 1984. “Simulation of hydraulic fracturing in low-permeability reservoirs.” *Society of Petroleum Engineers Journal* 24 (02): 141–152.

Settari, A., and D.A. Walters. 2001. “Advances in coupled geomechanical and reservoir modeling with applications to reservoir compaction.” *SPE Journal* 6 (03): 334–342.

Shen, Y. 2014. “A variational inequality formulation to incorporate the fluid lag in the fluid driven fracture propagation.” *Computer Methods in Applied Mechanics and Engineering*, vol. 272.

Smith, M.B. 1985. “Stimulation design for short, precise hydraulic fractures.” *Society of Petroleum Engineers Journal* 25 (03): 371–379.

Smith, M.C. 1978/1979. “Heat extraction from hot, dry, crustal rock.” *Pure and Applied Geophysics* 117:290–296.

Sneddon, I.N., and H.A. Elliott. 1946. “The opening of a Griffith crack under internal pressure.” *Quarterly of Appl. Math.* 4, no. 262.

Sneddon, I.N., and M. Lowengrub. 1969. *Crack problems in the classical theory of elasticity.* John Wiley & Sons.

Tada, H., P.C. Paris, and G.R. Irwin. 2000. “The analysis of cracks handbook.” *New York: ASME Press* 2:1.

Tran, D., A.T. Settari, and L. Nghiem. 2013. “Predicting Growth and Decay of Hydraulic-Fracture Width in Porous Media Subjected to Isothermal and Nonisothermal Flow.” *SPE Journal* 18 (04): 781–794.

Underwood, C.A., M.L. Cooke, J.A. Simo, and M.A. Muldoon. 2003. “Stratigraphic controls on vertical fracture patterns in Silurian dolomite, northeastern Wisconsin.” *AAPG Bulletin* 87 (1): 121–142.

Vandamme, L., and E. Detournay. 1989. “A two-dimensional poroelastic displacement discontinuity method for hydraulic fracture simulation.” *International Journal for Numerical and Analytical Methods in Geomechanics* 13 (2): 215–224.

van de Hoek, P.J. 2000. “A simple and accurate description of non-linear fluid leak-off in high-permeable fracturing.” *SPE annual technical conference.*

Verruijt, A. 2013. “Theory and problems of poroelasticity.” Book in preparation.

Wan, J. 2002. “Stabilized finite element methods for coupled geomechanics and multiphase flow.” Ph.D. diss., Stanford University.

Wang, H. 2000. *Theory of linear poroelasticity with applications to geomechanics and hydrogeology.* Princeton University Press.

Wick, T., G. Singh, and M.F. Wheeler. 2014. “Pressurized-fracture propagation using a phasefield approach coupled to a reservoir simulator.” *SPE Hydraulic Fracturing Technology Conference, Woodlands,(SPE 168597-MS).*

Yuan, Y. 1997. “Simulation of penny-shaped hydraulic fracturing in porous media.” Ph.D. diss., The University of Oklahoma.

Zheng, Y., R. Burridge, and D.R. Burns. 2003. “Reservoir simulation with the finite element method using Biot poroelastic approach.” Technical Report, Massachusetts Institute of Technology. Earth Resources Laboratory.

Zyvoloski, G. 1985. “The sizing of a hot dry rock reservoir from a hydraulic fracturing experiment.” *ARMA.*

Appendix A
Scaling and Derivation of The Dimensionless Form of The Variational Fracture Model

$$\begin{aligned}\mathbf{F}_\varepsilon(\vec{u},v) = {} & \frac{1}{2}\int_\Omega \mathbf{A}\big(v\epsilon(\vec{u}) - \frac{\alpha}{3\kappa}\,\mathbb{I}p\big) : \big(v\epsilon(\vec{u}) - \frac{\alpha}{3\kappa}\,\mathbb{I}p\big)dV - \int_{\partial_N\Omega} \tau\cdot\vec{u}\,d\,s - \int_\Omega f\cdot\vec{u}\,dV \\ & + \frac{G_c}{4c_n}\int_\Omega \Big(\frac{(1-v)^n}{\varepsilon} + \varepsilon|\nabla v|^2\Big)dV + \int_\Omega p\,\vec{u}\cdot\nabla v dV\end{aligned} \tag{A.1}$$

where $\kappa = \frac{E}{3(1-2\nu)}$ The relevant parameters are G_c, E, $\vec{u}$, $\mathbf{A}$, p, κ, α, $\vec{f}$, $\vec{\tau}$ and $V$and are scaled as follows.

$$\begin{aligned} E &= E_o\tilde{E} \\ G_c &= G_{c_o}\tilde{G}_c \\ \vec{u} &= u_o\tilde{\vec{u}} \\ p &= p_o\tilde{p} \\ \kappa &= E_o\tilde{\kappa} \\ \alpha &= \alpha_o\tilde{\alpha} \\ \mathbf{A} &= E_o\tilde{\mathbf{A}} \\ \vec{f} &= f_o\tilde{\vec{f}} \\ \vec{\tau} &= p_o\tilde{\vec{\tau}} \\ V &= x_o^N\tilde{V} \end{aligned} \tag{A.2}$$

In addition, the variational fracture model parameters, ε and ∇v are represented as

$$\begin{aligned} \varepsilon &= x_o\tilde{\varepsilon} \\ \nabla v &= \frac{1}{x_o}\tilde{\nabla}v \end{aligned} \tag{A.3}$$

Substituting Equations A.2 and A.3 into Equation A.1, one obtains

$$\begin{aligned}\mathbf{F}_\varepsilon(\vec{u},v) = {} & \frac{E_o x_o^N}{2}\int_{\tilde{\Omega}} \tilde{\mathbf{A}}\big(\frac{u_o}{x_o}v\epsilon(\tilde{\vec{u}}) - \frac{\alpha_o p_o}{E_o}\frac{\tilde{\alpha}}{3\tilde{\kappa}}\,\mathbb{I}\tilde{p}\big) : \big(\frac{u_o}{x_o}v\epsilon(\tilde{\vec{u}}) - \frac{\alpha_o p_o}{E_o}\frac{\tilde{\alpha}}{3\tilde{\kappa}}\,\mathbb{I}\tilde{p}\big)d\tilde{V} \\ & - p_o u_o x_o^{N-1}\int_{\partial_N\tilde{\Omega}} \tilde{\vec{\tau}}\cdot\tilde{\vec{u}}\,d\tilde{s} - f_o u_o x_o^N\int_{\tilde{\Omega}} \tilde{\vec{f}}\cdot\tilde{\vec{u}}\,d\tilde{V} \\ & + p_o u_o x_o^{N-1}\int_{\tilde{\Omega}} \tilde{p}\,\tilde{\vec{u}}\cdot\tilde{\nabla}v\,d\tilde{V} + \frac{G_{c_o}\tilde{G}_c x_o^{N-1}}{4c_n}\int_{\tilde{\Omega}} \Big(\frac{(1-v)^n}{\tilde{\varepsilon}} + \tilde{\varepsilon}|\tilde{\nabla}v|^2\Big)d\tilde{V}\end{aligned} \tag{A.4}$$

$$
\begin{aligned}
\mathbf{F}_\varepsilon(\vec{u},v) = G_{c_o} x_o^{N-1}\Bigg[& \frac{E_o x_o^N u_o^2}{G_{c_o} x_o^{N-1} x_o^2}\frac{1}{2}\int_{\tilde{\Omega}} \tilde{\mathbf{A}}\big(v\epsilon(\vec{u}_D) - \frac{\alpha_o p_o x_o}{E_o u_o}\frac{\tilde{\alpha}}{3\tilde{\kappa}}\,\mathbb{I}\tilde{p}\big) : \big(v\epsilon(\vec{\tilde{u}}) - \frac{\alpha_o p_o x_o}{E_o u_o}\frac{\tilde{\alpha}}{3\tilde{\kappa}}\,\mathbb{I}\tilde{p}\big)d\tilde{V} \\
& - \frac{p_o u_o x_o^{N-1}}{G_{c_o} x_o^{N-1}}\int_{\partial_N\tilde{\Omega}} \vec{\tilde{\tau}}\cdot\vec{\tilde{u}}\,d\tilde{s} - \frac{f_o u_o x_o^N}{G_{c_o} x_o^{N-1}}\int_{\tilde{\Omega}} \vec{\tilde{f}}\cdot\vec{\tilde{u}}\,d\tilde{V} \\
& + \frac{p_o u_o x_o^{N-1}}{G_{c_o} x_o^{N-1}}\int_{\tilde{\Omega}} \tilde{p}\,\vec{\tilde{u}}\cdot\tilde{\nabla} v\,d\tilde{V}\Bigg] + \frac{\tilde{G}_c}{4c_n}\int_{\tilde{\Omega}}\Big(\frac{(1-v)^n}{\tilde{\varepsilon}} + \tilde{\varepsilon}|\tilde{\nabla} v|^2\Big)d\tilde{V}
\end{aligned}
\tag{A.5}
$$

To obtain a dimensionless form of the variational fracture model, all the products of the coefficient terms are set to 1. Therefore

$$
\begin{aligned}
\frac{E_o x_o^N u_o^2}{G_{c_o} x_o^{N+1}} = 1 \quad &\Rightarrow \quad u_o = \sqrt{\frac{G_{c_o} x_o}{E_o}} \\
\frac{p_o u_o x_o^{N-1}}{G_{c_o} x_o^{N-1}} = 1 \quad &\Rightarrow \quad p_o = \frac{G_{c_o}}{u_o} = \sqrt{\frac{G_{c_o} E_o}{x_o}} \\
\frac{f_o u_o x_o^{N}}{G_{c_o} x_o^{N-1}} = 1 \quad &\Rightarrow \quad f_o = \frac{G_{c_o}}{u_o x_o} = \sqrt{\frac{G_{c_o} E_o}{x_o^3}} \\
\frac{\alpha_o p_o x_o}{E_o u_o} = 1 \quad &\Rightarrow \quad \alpha_o = \frac{E_o u_o}{p_o x_o} = 1 \qquad \text{(this implies that } \alpha = \tilde{\alpha}\text{)}
\end{aligned}
\tag{A.6}
$$

Therefore, the variational fracture model in terms of the dimensionless variables and solved on the computational domain is

$$
\begin{aligned}
\mathbf{F}_\varepsilon(\vec{\tilde{u}},v) = \frac{1}{2}\int_{\tilde{\Omega}} \tilde{\mathbf{A}}\big(v\epsilon(\vec{\tilde{u}}) - \frac{\alpha}{3\tilde{\kappa}}\,\mathbb{I}\tilde{p}\big) : \big(v\epsilon(\vec{\tilde{u}}) - \frac{\alpha}{3\tilde{\kappa}}\,\mathbb{I}\tilde{p}\big)d\tilde{V} - \int_{\partial_N\tilde{\Omega}} \vec{\tilde{\tau}}\cdot\vec{\tilde{u}}\,d\tilde{s} \\
- \int_{\tilde{\Omega}} \vec{\tilde{f}}\cdot\vec{\tilde{u}}\,d\tilde{V} + \frac{\tilde{G}_c}{4c_n}\int_{\tilde{\Omega}}\Big(\frac{(1-v)^n}{\tilde{\varepsilon}} + \tilde{\varepsilon}|\tilde{\nabla} v|^2\Big)d\tilde{V} + \int_{\tilde{\Omega}} \tilde{p}\,\vec{\tilde{u}}\cdot\tilde{\nabla} v\,d\tilde{V}
\end{aligned}
\tag{A.7}
$$

Where $\mathbf{F}_\varepsilon(\vec{\tilde{u}},v) = \frac{1}{G_{c_o} x_o^{N-1}}\mathbf{F}_\varepsilon(\vec{u},v)$

The tilde also represents numerical simulation inputs or solutions. From these dimensionless model inputs and solution variables, the realistic reservoir parameters and solutions are obtained by scaling according to Equation A.2. The typical range of Young's modulus and Poisson's ratio for different reservoir rocks have been reported to be 2-100GPa and 0.01-0.46 respectively (Santi, Holschen, and Stephenson 2000; Johnson and DeGraff 1988) while the fracture toughness is less than 200 Pa m (Gidley 1989).

Appendix B
Scaling and Derivation of The Dimensionless Form of The Coupled Flow Model

Reservoir Flow Model

$$\frac{1}{M}\frac{\partial p_r}{\partial t} + \alpha\frac{\partial \nabla \cdot \vec{u}}{\partial t} - \nabla \cdot \frac{K}{\mu}\nabla p_r = Q_{rs}\delta \tag{B.1}$$

Integrating over V:

$$\int_{\Omega\backslash\Gamma} \frac{1}{M}\frac{\partial p_r}{\partial t}\, dV + \int_{\Omega\backslash\Gamma} \alpha\frac{\partial \epsilon_{vol}}{\partial t}\, dV - \int_{\partial_N\Omega} \frac{K}{\mu}\nabla p_r \cdot \vec{n}\, ds - \int_{\Gamma} q_l\, d\Gamma = Q_{rs} \tag{B.2}$$

Fracture Flow Model

$$\frac{\partial w}{\partial t} - \left[(\vec{n}_\Gamma \times \nabla) \cdot \frac{w^3}{12\mu}(\vec{n}_\Gamma \times \nabla_\Gamma p_f)\right] + q_l = Q_{fs}\delta_\Gamma \tag{B.3}$$

Integrating over Γ:

$$\int_{\Gamma} \frac{\partial w}{\partial t}\, d\Gamma - \int_{\Gamma} \left[(\vec{n}_\Gamma \times \nabla) \cdot \frac{w^3}{12\mu}(\vec{n}_\Gamma \times \nabla_\Gamma p_f)\right] d\Gamma + \int_{\Gamma} q_l\, d\Gamma = Q_{fs} \tag{B.4}$$

Coupled Reservoir and Fracture Flow Model

The coupled model is obtained by adding Equations 3.5 and B.4. Due to pressure continuity, we set $p_r = p_f = p$

$$\int_{\Omega\backslash\Gamma} \frac{1}{M}\frac{\partial p}{\partial t}\, d\Omega + \int_{\Omega\backslash\Gamma} \alpha\frac{\partial \nabla \cdot \vec{u}}{\partial t}\, d\Omega + \int_{\Gamma} \frac{\partial w}{\partial t}\, d\Gamma - \int_{\Gamma} \left[(\vec{n}_\Gamma \times \nabla) \cdot \frac{w^3}{12\mu}(\vec{n}_\Gamma \times \nabla_\Gamma p)\right] d\Gamma - \int_{\partial_N\Omega} \frac{K}{\mu}\nabla p \cdot \vec{n}\, ds = Q \tag{B.5}$$

Where, $Q = Q_{fs} + Q_{rs}$.

The relevant parameters are w, p, M, μ, K, Q, t and are scaled as follows.

$$\begin{aligned}
w &= u_o \tilde{w} \\
p &= p_o \tilde{p} \\
M &= m_o \tilde{M} \\
\mu &= \mu_o \tilde{\mu} \\
K &= k_o \tilde{K} \\
Q &= Q_o \tilde{Q} \\
t &= t_o \tilde{t} \\
\Gamma &= x_o^{N-1} \tilde{\Gamma} \\
V &= x_o^{N} \tilde{V}
\end{aligned} \tag{B.6}$$

Substituting the scalings of Equation B.6 into Equation B.5, one obtains

$$\begin{aligned}
&\frac{u_o x_o^{N-1}}{t_o} \int_{\tilde{\Gamma}} \frac{\partial \tilde{w}}{\partial \tilde{t}} \, d\tilde{\Gamma} + \frac{x_o^N p_o}{M_o t_o} \int_{\tilde{\Omega} \backslash \tilde{\Gamma}} \frac{1}{\tilde{M}} \frac{\partial \tilde{p}}{\partial \tilde{t}} \, d\tilde{V} + \frac{u_o x_o^N}{x_o t_o} \int_{\tilde{\Omega} \backslash \tilde{\Gamma}} \alpha \frac{\partial \nabla \cdot \vec{\tilde{u}}}{\partial \tilde{t}} \, d\tilde{V} - \\
&\qquad \frac{u_o^3 x_o^{N-1} p_o}{\mu_o x_o^2} \int_{\tilde{\Gamma}} \left[(\vec{n}_\Gamma \times \tilde{\nabla}) \cdot \frac{\tilde{w}^3}{12 \tilde{\mu}} (\vec{n}_\Gamma \times \tilde{\nabla}_\Gamma \tilde{p}) \right] d\tilde{\Gamma} - \frac{x_o^{N-1} K_o p_o}{\mu_o x_o} \int_{\partial_N \tilde{\Omega}} \frac{\tilde{K}}{\tilde{\mu}} \tilde{\nabla} \tilde{p} \cdot \vec{n} \, d\tilde{s} \\
&\qquad = Q_o \tilde{Q}
\end{aligned} \tag{B.7}$$

$$\begin{aligned}
&\int_{\tilde{\Gamma}} \frac{\partial \tilde{w}}{\partial \tilde{t}} \, d\tilde{\Gamma} + \frac{x_o p_o}{m_o u_o} \int_{\tilde{\Omega} \backslash \tilde{\Gamma}} \frac{1}{\tilde{M}} \frac{\partial \tilde{p}}{\partial \tilde{t}} \, d\tilde{V} + \int_{\tilde{\Omega} \backslash \tilde{\Gamma}} \alpha \frac{\partial \nabla \cdot \vec{\tilde{u}}}{\partial \tilde{t}} \, d\tilde{V} - \\
&\qquad \frac{u_o^2 t_o p_o}{\mu_o x_o^2} \int_{\tilde{\Gamma}} \left[(\vec{n}_\Gamma \times \tilde{\nabla}) \cdot \frac{\tilde{w}^3}{12 \tilde{\mu}} (\vec{n}_\Gamma \times \tilde{\nabla}_\Gamma \tilde{p}) \right] d\tilde{\Gamma} - \frac{k_o p_o t_o}{u_o \mu_o x_o} \int_{\partial_N \tilde{\Omega}} \frac{\tilde{K}}{\tilde{\mu}} \tilde{\nabla} \tilde{p} \cdot \vec{n} \, d\tilde{s} \\
&\qquad = \frac{Q_o t_o}{u_o x_o^{N-1}} \tilde{Q}
\end{aligned} \tag{B.8}$$

Again, setting all the coefficients are set to 1, the scaling parameters are

$$\begin{aligned}
\frac{Q_o t_o}{u_o x_o^{N-1}} = 1 \quad &\Rightarrow \quad t_o = \frac{u_o x_o^{N-1}}{Q_o} = \sqrt{\frac{G_{c_o} x_o^{2N-1}}{E_o Q_o^2}} \\
\frac{u_o p_o t_o}{\mu_o x_o^2} = 1 \quad &\Rightarrow \quad \mu_o = \frac{u_o^2 p_o t_o}{x_o^2} = \frac{G_{c_o}^2 x_o^{N-2}}{E_o Q_o} \\
\frac{k_o p_o t_o}{u_o \mu_o x_o} = 1 \quad &\Rightarrow \quad k_o = \frac{u_o \mu_o x_o}{p_o t_o} = \frac{u_o^3}{x_o} \\
\frac{x_o p_o}{m_o u_o} = 1 \quad &\Rightarrow \quad m_o = \frac{p_o x_o}{u_o} = E_o
\end{aligned} \tag{B.9}$$

The corresponding dimensionless coupled flow model is therefore,

$$\int_{\tilde{\Gamma}} \frac{\partial \tilde{w}}{\partial \tilde{t}}\, d\tilde{\Gamma} + \int_{\tilde{\Omega}\backslash\tilde{\Gamma}} \frac{1}{\tilde{M}} \frac{\partial \tilde{p}}{\partial \tilde{t}}\, d\tilde{V} + \int_{\tilde{\Omega}\backslash\tilde{\Gamma}} \alpha \frac{\partial \nabla \cdot \vec{\tilde{u}}}{\partial \tilde{t}}\, d\tilde{V} - \int_{\tilde{\Gamma}} \left[(\vec{n}_\Gamma \times \tilde{\nabla}) \cdot \frac{\tilde{w}^3}{12\tilde{\mu}} (\vec{n}_\Gamma \times \tilde{\nabla}_\Gamma \tilde{p}) \right] d\tilde{\Gamma} - \int_{\partial_N \tilde{\Omega}} \frac{\tilde{K}}{\tilde{\mu}} \tilde{\nabla} \tilde{p} \cdot \vec{n}\, d\tilde{s} = \tilde{Q} \quad \text{(B.10)}$$

Hydraulic fracturing is a common operation in unconventional reservoirs with permeabilities less than 0.1 mD.

Appendix C
Derivation of The Solution for Volume Driven Fracture Propagation

The volume of the line fracture in a 2D domain is

$$V_f = \pi b l \tag{C.1}$$

where

$$b = \frac{2\Delta p l}{E'} \tag{C.2}$$

and

$$E' = \frac{E}{(1-\nu^2)} \tag{C.3}$$

Thus, Eqn. C.1 becomess

$$V_f = \frac{2\pi \Delta p l^2}{E'} \tag{C.4}$$

Consider an existing line fracture with an initial length of l_o. Prior to fracture propagation, the fracture length does not change so that $l = l_o$. Since fracture length at the onset of propagation is l_o, critical fluid pressure (Sneddon and Elliott 1946) is

$$\Delta p_c = p_c - \sigma_{min} = \sqrt{\frac{G_c E'}{\pi l_o}} \tag{C.5}$$

Critical fracture volume at critical fluid pressure is obtained by substituting Eqn. C.5 into Eqn. C.4

$$V_{f_c} = \frac{2\,\pi \sqrt{\frac{G_c E'}{\pi l_o}} l_o^2}{E'} = \sqrt{\frac{4\pi l_o^3 G_c}{E'}} \tag{C.6}$$

Since Eqn. C.4 is fracture volume at all pressures and fracture lengths, prior to fracture propagation, $l = l_o$ and the fluid pressure in this regime becomes

$$p = \frac{V_f E'}{2\pi l_o^2} + \sigma_{min} \tag{C.7}$$

During quasi-static propagation of the fracture, the fracture is always in a critical state during each quasi-static step so that Eqn. C.5 applies in all of this regime at $l \geq l_o$. The fluid pressure and fracture length in this regime are

$$\Delta p = \sqrt{\frac{G_c E'}{\pi l}} \tag{C.8}$$

$$l = \frac{G_c E'}{\pi \Delta p^2} \tag{C.9}$$

To obtain the fluid pressure as the fracture propagates, substitute Eqn. C.9 into Eqn. C.4, we have

$$\begin{aligned} V_f &= \frac{2\,\pi\,\Delta p (\frac{G_c E'}{\pi \Delta p^2})^2}{E'} \\ &= \frac{2\,G_c^2 E'}{\pi\,\Delta p^3} \\ \pi\,\Delta p^3 V_f &= 2\,G_c^2 E' \\ \Delta p^3 &= \frac{2\,G_c^2 E'}{\pi\,V_f} \\ \Delta p &= \sqrt[3]{\frac{2\,G_c^2 E'}{\pi\,V_f}} \\ p &= \sqrt[3]{\frac{2\,G_c^2 E'}{\pi\,V_f}} + \sigma_{min} \end{aligned} \tag{C.10}$$

The fracture length during the propagation regime is obtained by substituting Eqn. C.15 into Eqn. C.4

$$\begin{aligned} V_f &= \frac{2\,\pi\,\sqrt{\frac{G_c E'}{\pi l}}\,l^2}{E'} \\ &= \sqrt{\frac{4\pi^2 G_c E'\,l^4}{\pi l E'^2}} \\ &= \sqrt{\frac{4\pi\,G_c\,l^3}{E'}} \\ 4\pi\,G_c\,l^3 &= E'\,V_f^2 \\ l &= \sqrt[3]{\frac{E'\,V_f^2}{4\pi\,G_c}} \end{aligned} \tag{C.11}$$

Derivation of Sneddon Based Solution For Volume Driven Penny-Shaped Fracture in 3D

Penny-shaped fracture volume is

$$V_f = \frac{4}{3}\pi R^2 w_0 \tag{C.12}$$

where

$$w_0 = \frac{4\Delta p R}{\pi\,E'} \tag{C.13}$$

Volume becomes

$$V_f = \frac{16\Delta p R^3}{3E'} \tag{C.14}$$

Thus, prior to propagation, $R = R_o$ and the fluid pressure is

$$p = \frac{3V_f E'}{16R_o^3} + \sigma_{min} \tag{C.15}$$

The critical fracture fluid pressure (Sneddon and Elliott 1946) is

$$\Delta p_c = p_c - \sigma_{min} = \sqrt{\frac{\pi G_c E'}{4R_o}} \tag{C.16}$$

Critical fracture volume is obtained by substituting Eqn. C.16 into Eqn. C.14

$$V_{f_c} = \frac{16\sqrt{\frac{\pi G_c E'}{4R_o}} R_o^3}{3E'} = \sqrt{\frac{64\pi R_o^5 G_c}{9E'}} \tag{C.17}$$

At the critical conditions during fracture propagation, fluid pressure and fracture radius are,

$$\Delta p = \sqrt{\frac{\pi G_c E'}{4R}} \tag{C.18}$$

$$R = \frac{\pi G_c E'}{4\Delta p^2} \tag{C.19}$$

To obtain fluid pressure during propagation, substitute Eqn. C.19 into Eqn. C.14

$$\begin{aligned} V_f &= \frac{16\Delta p\,(\frac{\pi G_c E'}{4\Delta p^2})^3}{3E'} \\ &= \frac{\pi^3\, G_c^3 {E'}^3}{12\Delta p^5} \\ 12\Delta p^5 V_f &= \pi^3\, G_c^3 {E'}^3 \\ p &= \sqrt[5]{\frac{\pi^3\, G_c^3 {E'}^3}{12 V_f}} + \sigma_{min} \end{aligned} \tag{C.20}$$

The evolution of fracture radius during propagation is obtained by substituting Eqn. C.16

into Eqn. C.14

$$\begin{aligned}
V_f &= \frac{16\sqrt{\frac{\pi G_c E'}{4R}}\,R^3}{3E'} \\
&= \sqrt{\frac{64\pi G_c E' R^5}{9E'}} \\
64\pi G_c E' R^5 &= 9{E'}^2 V_f^2 \\
R &= \sqrt[5]{\frac{9E' V_f^2}{64\pi G_c}}
\end{aligned} \tag{C.21}$$

Appendix D
Identities Used in Weak Form of Fracture Flow Model

For scalar ψ, vectors $\vec{F}$ and $\vec{G}$ and surface $\Gamma \subset \mathbb{R}^1$ in $\Omega \subset \mathbb{R}^2$, the following identities have been used in this chapter.

Curl of product of scalar and vector

$$\nabla \times (\psi\, \vec{F}) = \psi \nabla \times \vec{F} + \nabla\psi \times \vec{F} \tag{D.1}$$

Triple scalar product

$$\vec{u} \cdot (\vec{v} \times \vec{w}) = (\vec{v} \times \vec{w}) \cdot \vec{u} = (\vec{w} \times \vec{u}) \cdot \vec{v} = (\vec{u} \times \vec{v}) \cdot \vec{w} \tag{D.2}$$

Triple cross product

$$\vec{u} \times (\vec{v} \times \vec{w}) = (\vec{u} \cdot \vec{w})\, \vec{v} - (\vec{u} \cdot \vec{v})\vec{w} \tag{D.3}$$

Surface divergence

$$\nabla_\Gamma \cdot \vec{F} = \vec{n} \cdot \nabla \times (\vec{n} \times \vec{F}) = (\vec{n} \times \nabla) \cdot (\vec{n} \times \vec{F}) \quad \text{(Eqn. D.2)} \tag{D.4}$$

Surface gradient

$$\begin{aligned} \nabla_\Gamma\, \psi &= [\nabla\psi - \vec{n}\,(\vec{n} \cdot \nabla\psi)] = \big(\mathbf{I} - \vec{n} \otimes \vec{n}\big)\nabla\psi \\ &= -\vec{n} \times (\vec{n} \times \nabla\psi) \qquad \text{(Eqn. } D.3) \end{aligned} \tag{D.5}$$

Stokes theorem

$$\int_\Gamma (\nabla \times \vec{G}) \cdot \vec{n}\, dA = \oint_{\partial\Gamma} \vec{G} \cdot \vec{t}\, ds \tag{D.6}$$

Alternate form.

$$\int_\Gamma \nabla_\Gamma \cdot \vec{F}\, dA = \oint_{\partial\Gamma} \vec{F} \cdot \vec{m}\, ds \tag{D.7}$$

Proof of alternative form.

$$\begin{aligned}\int_S \nabla_\Gamma \cdot \vec{F}\, dA &= \int_\Gamma \vec{n} \cdot \nabla \times (\vec{n} \times \vec{F})\, dA = \int_\Gamma (\vec{n} \times \nabla) \cdot (\vec{n} \times \vec{F})\, dA \\ &= \int_\Gamma \vec{n} \cdot (\nabla \times \vec{G}) dA; \quad \text{where} \quad \vec{G} = \vec{n} \times \vec{F} \\ &= \int_\Gamma (\nabla \times \vec{G}) \cdot \vec{n}\, dA = \int_\Gamma (\nabla \times \vec{G}) \cdot d\vec{A} \\ &= \oint_{\partial\Gamma} \vec{G} \cdot \vec{t}\, ds \\ &= \oint_{\partial\Gamma} \vec{t} \cdot (\vec{n} \times \vec{F})\, ds = \oint_{\partial\Gamma} (\vec{t} \times \vec{n}) \cdot \vec{F}\, ds \\ &= \oint_{\partial\Gamma} \vec{F} \cdot \vec{m}\, ds \end{aligned} \tag{D.8}$$

$\vec{n}$ is unit normal vector to the Γ, $\vec{t}$ is unit vector tangent to the curve (boundary of Γ) while $\vec{m}$ is unit vector tangent to the Γ, perpendicular to the curve and pointing directly outside Γ. Also, A is the area of Γ and s is the length of the boundary of Γ. Fracture has only one boundary, $\partial\Gamma$, which is a point in two dimensions and an arc in three dimensions.

Appendix E
Nomenclature

Roman Symbols

M	Unit of mass
L	Unit of length
T	Unit of time
t	Time, [T]
$\vec{u}$	Displacement
v	Phase field variable for fracture representation
w	Fracture width, [L]
p	Fluid pressure, $[\mathrm{ML}^{-1}\mathrm{T}^{-2}]$
p_r	Reservoir pore pressure, $[\mathrm{ML}^{-1}\mathrm{T}^{-2}]$
p_f	Fracture fluid pore pressure, $[\mathrm{ML}^{-1}\mathrm{T}^{-2}]$
p_c	Critical fracture pressure, $[\mathrm{ML}^{-1}\mathrm{T}^{-2}]$
$\bar{p}$	Average fracture pressure
$\vec{q}_f$	Fracture flow rate, $[\mathrm{ML}^{-1}\mathrm{T}^{-2}]$
$\vec{q}_r$	Reservoir flow rate, $[\mathrm{ML}^{-1}\mathrm{T}^{-2}]$
q_l	Leak-off term, $[\mathrm{ML}^{-1}\mathrm{T}^{-2}]$
E	Young's modulus, $[\mathrm{ML}^{-1}\mathrm{T}^{-2}]$
E'	Plane strain Young's modulus, $[\mathrm{ML}^{-1}\mathrm{T}^{-2}]$
$\mathbf{A}$	Elasticity matrix, $[\mathrm{ML}^{-1}\mathrm{T}^{-2}]$
$\mathbf{W}$	(Poro)Elastic energy density function,
K_T	Bulk modulus of poroelastic media, $[\mathrm{ML}^{-1}\mathrm{T}^{-2}]$
K_s	Bulk modulus of solid grains, $[\mathrm{ML}^{-1}\mathrm{T}^{-2}]$
K_f	Bulk modulus of fluid, $[\mathrm{ML}^{-1}\mathrm{T}^{-2}]$
K_{dr}	Drained bulk modulus, $[\mathrm{ML}^{-1}\mathrm{T}^{-2}]$
M	Biot's modulus $[\mathrm{ML}^{-1}\mathrm{T}^{-2}]$
K	Reservoir permeability, $[\mathrm{L}^{-2}]$
k_f	Fracture permeability, $[\mathrm{ML}^{-1}\mathrm{T}^{-2}]$
μ	Fluid viscosity $[\mathrm{ML}^{-1}\mathrm{T}^{-1}]$
$\vec{g}$	Acceleration due to gravity, $[\mathrm{MT}^{-2}]$

q_{rs}	Reservoir source term, [LT^{-1}]
q_{fs}	Fracture source term, [LT^{-1}]
$q_{fs_{\varepsilon}}$	Reservoir source term, [LT^{-1}]
$\mathcal{P}$	Potential energy
$\mathcal{F}$	Total energy
$\mathcal{E}$	Elastic energy
$\mathbf{F}_{\varepsilon}$	Regularized total energy
G_c	Fracture toughness, [MT^{-2}]
G	Energy release rate, [MT^{-2}]
G_I	Mode I energy release rate, [MT^{-2}]
G_{II}	Mode II energy release rate, [MT^{-2}]
G_{III}	Mode III energy release rate, [MT^{-2}]
K_c	Critical stress intensity factors [ML$^{-1/2}$T^{-2}]
K_I	Mode I stress intensity factors [ML$^{-1/2}$T^{-2}]
K_{II}	Mode II stress intensity factors [ML$^{-1/2}$T^{-2}]
K_{III}	Mode III stress intensity factors [ML$^{-1/2}$T^{-2}]
l	Line fracture length, [L]
$\dot{l}$	Rate of change in fracture length, [LT^{-1}]
R	Radius of penny-shaped fracture, [L]
$\mathcal{H}^{N-1}(\Gamma)$	Measure of fracture surface area L^2
$[\![\,]\!]$	Jump/change in quantity
V_f	Fracture volume, [L^3]
V_{f_c}	Fracture volume, [L^3]
V_{inj}	Injected fluid volume, [L^3]
$\mathbf{n}$	Normal vector
$\vec{n}_{\Gamma}$	Normal to fracture surface
h	Finite element resolution
x, y, z	Coordinates, L

Greek Symbols

α	Biot's coefficient
ν	Poisson's ratio
μ	Fluid viscosity, $[\mathrm{ML}^{-1}\mathrm{T}^{-1}]$
ρ_b	Bulk density of reservoir, $[\mathrm{ML}^{-3}]$
ρ_s	Density of solid grains, $[\mathrm{ML}^{-3}]$
ρ_f	Fluid density, $[\mathrm{ML}^{-3}]$
ϕ	Porosity
ε	Phase field length parameter, [L]
ϵ	Linear strain
ϵ_{vol}	Volumetric strain
σ	Stress, $[\mathrm{ML}^{-1}\mathrm{T}^{-2}]$
σ_c	Critical stress, $[\mathrm{ML}^{-1}\mathrm{T}^{-2}]$
σ'	Stress, $[\mathrm{ML}^{-1}\mathrm{T}^{-2}]$
σ^{vol}	Volumetric Stress, $[\mathrm{ML}^{-1}\mathrm{T}^{-2}]$
σ_{max}	Maximum in-situ stress, $[\mathrm{ML}^{-1}\mathrm{T}^{-2}]$
σ_{min}	Minimum in-situ stress, $[\mathrm{ML}^{-1}\mathrm{T}^{-2}]$
ψ	Finite element test function
$\boldsymbol{\tau}$	Traction on boundary, $[\mathrm{ML}^{-1}\mathrm{T}^{-2}]$
Ω	Full dimensional computational domain
Γ	Fracture domain
θ	Time discretization weighting parameter
δ	Dirac delta function
Δ	Change in a quantity

Vita

Chukwudi Chukwudozie was born in Abuja Nigeria to Patrick and Comfort Chukwudozie Okoli. He had his Pre-College education in Abuja and obtained a Bachelors in Chemical Engineering from the Federal University of Technology, Minna, Niger State Nigeria in January 2006. He obtained a Masters of Science in Petroleum Engineering in the Spring of 2011 and another Masters of Science in Applied Mathematics in the Fall of 2015, all from the Louisiana State University. He is currently a candidate for the degree of Doctor of Philosophy in Petroleum Engineering to be awarded in August 2016.